ISSN 1811-1165 (Print)
ISSN 2413-2179 (Online)

EURASIAN PHYSICAL TECHNICAL JOURNAL

VOLUME 19, NO. 2(40), 2022

phtj.buketov.edu.kz

EURASIAN PHYSICAL TECHNICAL JOURNAL

p - ISSN 1811-1165
e - ISSN 2413-2179

Volume 19, No. 2(40), 2022

1st issue – March, 2004

Journal Founder:

E.A. BUKETOV KARAGANDA UNIVERSITY

Е.А.БӨКЕТОВ АТЫНДАҒЫ ҚАРАҒАНДЫ УНИВЕРСИТЕТІ

КАРАГАНДИНСКИЙ УНИВЕРСИТЕТ имени Е.А.БУКЕТОВА

Contact information:
Editorial board of EAPhTJ (Build. 2, room 216)
E.A. Buketov Karaganda University
Universitetskaya Str.28, Karaganda,
Kazakhstan, 100028
Subscription index: 75240

Tel: +7(7212) 77-04-03
Fax: +7(7212) 77-03-84
E-mail: ephtj@mail.ru

Signed to print on **15.06.2022**
Format 60x84 1/8. Offset paper.
Volume **14.88 p.sh.** Circulation 300 copies.
Agreed price. Order No. 89.

Басуға **15.06.2022**ж. қол қойылды.
Пішімі 60×84 1/8. Офсеттік қағазы.
Көлемі **14.88** ес.-б.т. Таралымы 300 дана.
Бағасы келісім бойынша. Тапсырыс № 89**.**

Подписано к печати **15.06.2022**.
Формат 60 × 84 1/8. Офсетная бумага.
Объем **14.88** печ.л. Тираж 300 экз.
Цена договорная. Заказ № 89.

Printed in the Publishing House
of the E.A.Buketov KarU

Е.А. Бөкетов атындағы ҚарУ баспасының баспаханасында басылып шықты

Отпечатано в Издательстве
КарУ имени Е.А.Букетова

Registration Certificate No.4382-Zh, November 7, 2003.
Re-registration Certificate No.KZ50VPY00027647, October 6, 2020 issued by Information Committee of the Ministry of Information and Public Development of the Republic of Kazakhstan

Eurasian Physical Technical Journal, 2022, Vol. 19, No. 2(40)

CONTENTS

Dear authors and readers!
Dear Colleagues!

In accordance with the requirements since 2022, the acceptance and preparation of articles for publication in the Eurasian Physical Technical Journ is carried out online through an updated interactive site such as OJS – https://phtj.buketov.edu.kz/index.php/EPTJ/index The site has all the necessary instructions for authors and a convenient way to search for information for readers.

The Eurasian Physical Technical Journal is continued to be indexed in the Scopus database. As of June 6, 2022, the Cite Score Tracker is 0.9, but percentile on the Energy has decreased from 23% to 18% compared to 2021. We are proud that at the results of 2021 on the analytical SJR platform, the Eurasian phys. tech. j. has an H-index 4! Moreover, on the Energy and Engineering, journal is included in the Q3 quartile - https://www.scimagojr.com/journalrank.php?category=2101&area=2100&country=KZ&openaccess=true&type These indicators were achieved thanks to our authors, who provided in their articles the results of scientific research on topical problems of technical physics, and thanks to the work of editors, experts and reviewers, who contributed to improving the quality of articles.

Some important events

12th International Scientific Conference “Chaos and Structures in Nonlinear Systems. Theory and Experiment” was held in June 2022. More than 130 scientists, teachers, doctoral students and undergraduates from universities and research centers of Kazakhstan, Russia, USA, Ukraine, Poland, Uzbekistan, etc. took part in the conference. Reports were presented with the results of research on topical issues of physics, nanotechnology, thermal physics, energy, fractal engineering, radio-electronics, astrophysics, etc. Under the leadership of the board chairman - Rector of the "Toraighyrov University", professor Sadykov E.T. organizers provided comfortable conditions for discussion meetings in university and for relaxing of participants on the magnificent Zhasybay lake in Bayanaul.

The 12th conference was timed to coincide with the celebration of the 80th anniversary of Professor Zhanabaev Z.Zh., who from the beginning is its initiator and organizer. The 25-year history of the conference is a clear confirmation of the correctness his choice of the nonlinear systems physics ideology to the understanding and describtion of many physical and technical phenomena study results using modern apparatus of the information analysis.

On the eve of his anniversary, professor Zhanabaev Z.Zh. came up with new important results in the study of the physics of exciton formations in nanoelectronics, in neuro-dynamics: an equation was obtained for the fractal evolution of a physical quantity; the possibility of describing the energy of excitons and the action potential of neurons in the form of a fractal measure is shown; an experimentally confirmed theory of the nanostructured semiconductors electrical properties had been constructed, ect.

Professor Zhanabaev Z. developed the theory of self-affine fractals, successfully applied his theory in digital processing and filtering of gravitational waves. He used it own method of recognition and identification of voices and images in the creation of a radio engineering generator of dynamic chaos with phase control. The peculiarity of this generator that it can implement interleaved, ultra-wideband signals with fractal properties, which allows it to be effectively used in information security, in wireless multichannel communication technology.

Professor Zhanabaev Z.Zh. successfully carries out work on the preparation of scientific and pedagogical personnel of the highest qualification. Under his leadership, 9 PhD theses, 3 doctoral dissertations, 13 doctoral PhD dissertations of international level and more than a hundred undergraduates

were defended. Among more than 300 publications of Professor Zhanabaev Z.Zh. has 10 patents, including a patent for its own model of a fractal antenna called ZhF-antenna for a nanosatellite.

Zeinulla Zhanabayevich's creative activity and devotion to science, as a teacher and as a remarkable scientist, have been noted many times at the highest level. In honor of the 80th anniversary for an invaluable contribution to the training and education of highly qualified specialists and for outstanding services in the development of physics science, professor Zhanabaev Z.Zh. is awarded the highest university award - is awarded the "Al-Farabi Big Gold Medal"!

Professor Zhanabaev Z.Zh. has been actively working in the editorial board of the journal since its foundation (since 2003). He analyzes each article very carefully, and his objective opinion, as a rule, is correct and decisive. We congratulate Zeinulla Zhanabayevich and wish you good health, creative ideas and great success, personal happiness and inexhaustible enthusiasm!

You know that the composition of the editorial board of the Eurasian Physical Technical Journal is constantly updated. In this issue, we are pleased to introduce a new member of the editorial board - a scientist - astrophysicist, doctor of physical and mathematical sciences, professor Miroshnichenko Anatoly Sergeevich.

In 1983, Anatoly Sergeevich graduated from Leningrad State University with a degree in astronomy. In 2008 he defended his doctoral dissertation at the Special Astrophysical Observatory of the Russian Academy of Sciences. He has extensive experience working in well-known scientific centers such as the Pulkovo Observatory (St. Petersburg, Russia), the University of Toledo (Ohio, USA), the Institute of Radio Astronomy. Max Planck (Bonn, Germany), University of North Carolina at Greensboro (North Carolina, USA).

Miroshnichenko A.S. is a professor at the Department of Physics and Astronomy at the University of North Carolina at Greensboro, USA, has an h-index according to SCOPUS 24, according to WoS - 25. Scientific interests are related to the study of stars of early spectral classes (Be and B[e]), circumstellar shells, binary systems, fundamental parameters of stars, etc.

Professor Miroshnichenko A.S. is the supervisor of PhD applicants. He conducts research on joint projects with the Pulkovo Observatory, al-Farabi Kazakh National University, National Autonomous University of Mexico, Institute named after V.G. Fesenkov, Almaty, Kazakhstan, etc. There is no doubt that the work of Professor Miroshnichenko A.S. as a member of the editorial board will contribute to the expansion of scientific relations between scientists, which will improve the quality and further development of our journal.

In this issue, we bring to the attention of readers interesting articles with the latest results of research aimed at solving modern topical problems in physics and technology of physics.

We hope that the proposed scientific articles will interest our readers.

And we will be glad to see you among our authors of the next issues.

Best regards,

ch. editor, prof. Saule Sakipova

June, 2022

DOI 10.31489/2022No2/6-12
UDC: 621.793.3

X-RAY PHASE AND MICROSTRUCTURAL ANALYSIS OF HARDENING COATINGS OBTAINED BY SELF-PROPAGATING HIGH-TEMPERATURE SYNTHESIS IN COMBINATION WITH HEATING OF A MIXTURE OF $Al + B_2O_3$ BASED ON HIGH-FREQUENCY CURRENT TREATMENT

Ishkov A.A.[1], Malikov V.N.[2], Tikhonsky N.D.[2], Gulyarenko A.A.[3], Remshev E.Yu.[4], Voinash S.A.[5], Sokolova V.A.[6], Orekhovskaya A.A.[7]*

[1] Altay State Agrarian University, Barnaul, Russia
[2] Altai State University, Barnaul, Russia
[3]Seifullin Kazakh Agro Technical University NJSC, Nur-Sultan, Kazakhstan,
[4] Baltic State Technical University "Voenmeh", Saint Petersburg, Russia
[5] PRO FERRUM Limited Liability Company, St. Petersburg, Russia
[6] Military Academy of Communications named after Marshal of the Soviet Union S.M. Budyonny, Saint Petersburg, Russia
[7] Belgorod State Agricultural University named after, Belgorod Region, Russia, orehovskaja_aa@bsaa.edu.ru

The paper describes the results of studies of hardening boride coatings obtained during the implementation of the process of self-propagating high-temperature synthesis. These coatings were composite materials based on aluminum oxide and boron. The obtained coatings were subjected to X-ray phase and microstructural analysis, which showed the main components of the resulting compositions and made it possible to assess the thickness and structure of the coating-base metal transition area. The different content of silicon and iron makes it possible to assess the occurrence of surface chemical and metallurgical processes during self-propagating high-temperature synthesis when heating of the base mixture samples on high-frequency current treatment. The expediency of using high-frequency current treatment in combination with the process of self-propagating high-temperature synthesis for better-quality spattering of the hardening coating is shown. The appearance of two areas in the coating with different thickness and structure of the coating is established.

Keywords: steel hardening, microstructure analysis, self-propagating high-temperature synthesis, coatings, high-frequency currents.

Introduction

An increase in the strength of steels and alloys can be obtained by creating ideal structures through targeted process exposure. According to the operating conditions, many products should have high surface hardness and strength, and a ductile core. This combination of properties is achieved by surface plasma or laser hardening of 65G steel. As is known, instead of the widely used 65G steel, manufacturers in the last 3-5 years have been increasingly using boron-containing 30MnB5 steel for the manufacture of working machine bodies (mainly for the working machine bodies), and tungsten-containing 5-6XB2C steel is recommended to replace the said steel in cutting elements (blades). At the same time, oxides which significantly reduce the wear resistance of cutting tools made of high-speed steel, are generated on the working surfaces of these materials in the process of cutting in the high-temperature areas (up to 620–630ºC). To increase the wear resistance of the tool, various methods of hardening are used, including the application of protective coatings [1-3]. To strengthen the cutting edge of the parts under study using modern technologies, methods of applying various hard, wear-resistant, and functional coatings are widely used, e.g. flame, arc, laser and plasma weld surfacing, induction (HFC) weld surfacing, creation of bimetallic elements on the cutting edge using cladding, etc.

Self-propagating high-temperature synthesis (SHS) of solid chemical compounds is a new technological process for obtaining hardening coatings, which is based on carrying out an exothermic chemical reaction of the interaction of initial reagents in the form of combustion [1-2]. As a result of this process, a layer with very good properties, such as high microhardness, good wear resistance, and corrosion resistance, can be obtained [4-7]. Due to the acicular microstructure, the borated layer is characterized by good adhesion to the

steel substrate. However, despite these multiple advantages, the borated layers are rather brittle. This disadvantage can manifest itself in the form of chips and peeling from the substrate [4]. At the same time, there are many methods for increasing the strength and stability of such layers [8-11]. One of such methods is heating using HFC during the formation of a diffusion borated layer [7,8]. Therefore, a layer is obtained with a changed microstructure and new properties, such as high hardness, strength, wear resistance, and corrosion resistance [12]. However, most of the currently known methods of borating steel (furnace, gas, or electrolytic) are long-lasting, labor-intensive, non-automated, and poorly integrated into the process schemes of modern production. A significant intensification of borating occurs during high-speed HFC heating of the steel surface under a layer of a special borated charge material [13, 14].

It is assumed that conducting a combined process of applying a functional coating on the surface of steel parts with the joint implementation of SHS, HFC heating, and the method of high-speed HFC borating, which we are developing, is capable of providing better characteristics of the obtained boride coatings and achieving a significant increase in the strength of the steel part. Carrying out studies of SHS processes in the basic model system and its modified versions is required to establish the laws of initiation and combustion of a charge material of various compositions, as well as to control this process with the possibility of further obtaining high-quality hardening boride coatings on the surface of a steel part with a thickness of at least 150-200 microns and to develop a prototype of the existing technology.

In addition, it is required to experimentally test the possibility of obtaining such coatings on hardening HFC installations, which make up the main equipment fleet of operating agricultural machine-building enterprises. Theoretically, such a possibility is predicted since the maximum temperature reached on such installations on the surface of the part T_{hard} = 850-950°C (due to the limited power of the generators, the element base usedб and the design specifics of the inductors), which is insufficient for the implementation of the high-speed HFC borating process (T_{bor} = 1150-1250°C), can be increased due to the heat released during the combustion of the exothermic Al+B_2O_3 mixture.

To obtain a qualitative result and a sufficient amount of experimental data, it is required to perform work on the study of the main characteristics of SHS processes in a model system suitable for obtaining hardening, mainly boride coatings (study of the conditions for initiation of SHS and the stability of the process, determination of the combustion rate, the maximum temperature of the process, thermal structure combustion waves, structure and phase product composition, etc.).

1. Materials and Methods

A high-temperature redox reaction in the B_2O_3+Al system was chosen as a model system for the implementation and study of SHS processes. The chemical interaction of the components in this system can be described by the following stoichiometric equation:

$$B_2O_3 + 2Al = 2B + Al_2O_3, \ \Delta H_p < 0 \quad (1)$$

As a result of the chemical interaction in the B_2O_3+Al system, a component is generated, which, during HFC heating in the presence of the P-0.66 borate flux, can interact with the steel surface of the part, thus forming boride wear-resistant and hardening compounds in the Fe-B system of various compositions.

The B_2O_3+Al model system is sensitive to moisture content, which is caused by the interaction of boric anhydride with water and the generation of metaboric acid, and, after that, orthoboric acid:

$$B_2O_3 + 3H_2O = 2H_3BO_3$$

Therefore, before preparing the initial charge material, it is required to dehydrate thoroughly the available boric anhydride or to have a freshly synthesized product. For dehydration, the available boric anhydride was crushed and placed in a stainless steel tray, which was closed with a perforated lid capable of passing vapors of crystallization and chemically bound water. The tray was installed in a SNOL-type muffle furnace heated to 120-150°C for 1-2 hours. During this time, all crystallization water escaped from boric anhydride. After that, the temperature in the furnace rose to 750-800°C and upon reaching it, boric anhydride was soaked for another 1-2 hours. During this time, almost all chemically bound water escaped from the product. After the end of calcination and cooling, the tray was removed from the muffle, where the resulting glassy mass was recovered from it. The resulting product was crushed in a jaw crusher and then ground in a ball mill. After sieving, a powder of dehydrated boric anhydride of the required fractional composition was

.

obtained. To prepare experimental samples for studying the main parameters of SHS processes in the model system, the following method was used: a small amount of the initial charge material was moistened with alcohol or alcohol-acetone mixture to a mushy state and thoroughly mixed. A 10 mL disposable injection syringe with a cut-off bottom was filled with the resulting wet mixture; the syringe was placed with its open part on filter paper and the mass was tapped; the plunger was inserted and loaded for 2-3 sec without removing the syringe from the paper. Then, raising the syringe, the resulting cylindrical sample was carefully pushed out onto paper and dried in the air until the smell of alcohol disappeared. The final drying of the sample took 2-3 hours.

The previously obtained dried cylindrical sample was placed on a ceramic support. 4-5 turns of a nichrome coil connected to the laboratory transformer were placed on its upper base and the coil was pressed to the end of the cylinder so that the turns were 1/3 immersed in the charge material, after which the current was passed along the spiral, gradually increasing the voltage on the autotransformer. mAs soon as a stable combustion zone was initiated at the end of the sample, the current from the coil was turned off and the propagation of the SHS front was monitored. If the case of the need for the study of the SHS process during high-speed HFC heating, a dried cylindrical sample was placed on the surface of a steel plate with dimensions of 20*50*5 mm, which was in turn placed in a single-loop inductor connected to an HFC generator. The generator was turned on and the steel was heated until the onset of SHS on the lower base of the sample. As soon as a stable combustion zone is initiated at the end of the sample, the inductor current is switched off and the propagation of the SHS front is monitored. For the study, prepared samples of the basic composition in the form of molded cylinders (No.1, 3) with a diameter of 10 mm and a length of 20-30 mm, as well as in the form of a powder (No. 2), were used.

The SHS process was initiated in all cases by high-frequency heating of samples installed on the surface of steel plates with dimensions of 10-20*30-50 mm and thicknesses of 3-6 mm, made of structural alloyed steels of domestic (65G) and imported (S355) production. The molded cylindrical specimens were freely installed on horizontally fixed plates, after which they were heated using HFC until the occurrence of the SHS process, which was visually registered (bright flash) and further until the plate material reached a temperature of 1,100-1,200°C (white-yellow heat). The powder of the basic composition was moistened with alcohol to a mushy consistency and freely applied to a previously prepared (cleaned) plate with a layer of 2-3 mm thick, and then dried. The SHS process and HFC heating of the powder sample (coating) were initiated similarly to the molded samples.

2. Experimental Results

Combustion products of cylindrical molded and powder samples are black, easily crumbling sinter close to the original sample in dimensions and shape. Combustion products are weakly bound to the steel substrate. In the places where the base composition is applied on steel plates, after its combustion, surface changes associated with the formation of coatings and the melting of the base metal are visible. The combustion products of the basic composition obtained during the SHS process were subjected to X-ray phase analysis (XPA) using a powder method on a Shimadzu XRD 6000 diffractometer (equipment of the GOSNITI Nanocenter, Moscow). According to the results of the XPA of the charge material, the diffraction patterns shown in Fig. 1 were obtained. Fig. 1 shows that the diffraction patterns of all three samples coincide; therefore, the composition was determined only for one of them. The determination was carried out by the computer program of the device by comparing the most intense peaks and their groups with the built-in database. The results of determining the composition of the SHS products in the base mixture during HFC heating are shown in Fig. 2. As follows from the data in Fig. 2, the SHS products of the samples contain aluminum oxide, aluminum nitride, and boron (identified by the operator as zirconium boride) as the main components, which confirms the occurrence of the SHS process in the basic composition according to reaction equation 1. It should also be noted that it is difficult to identify the phase composition of the products by the selected method of physicochemical analysis since the main reflexes of the main phases coincide. Only the Al_2O_3 and AlN phases are reliably identified.

The generation of a significant amount of aluminum nitride, AlN, is explained by the occurrence at a high SHS temperature of the interaction reaction of a part of the initial aluminum with nitrogen in the air according to the following scheme:

$$2Al + N_2 = 2AlN$$

Figure 2.a shows a diffractogram of one of the studied samples (Raw Data) with a reflection of the observed reflexes (Peak Data, Figure 2.b) and Miller indices. The diffraction peaks of Al_2O_3 from the ICDD database (Card Data, Fig. 2.d) are also presented. Entry Data (Fig. 2.c) shows a comparison of the observed reflexes of the test sample with the database, Different colors of reflexes on the Entry Data graph show the coincidence of peaks with different substances in the database: Al_2O_3, AlN, ZrB, $Li_4P_4O_{12}$+2H_2O.

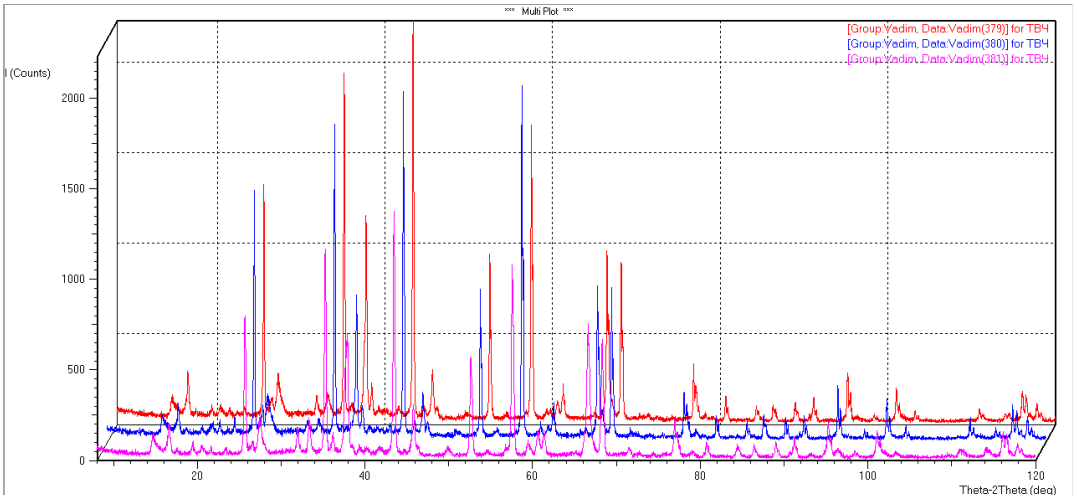

Fig.1. Diffraction patterns of combustion products of samples No.1-3

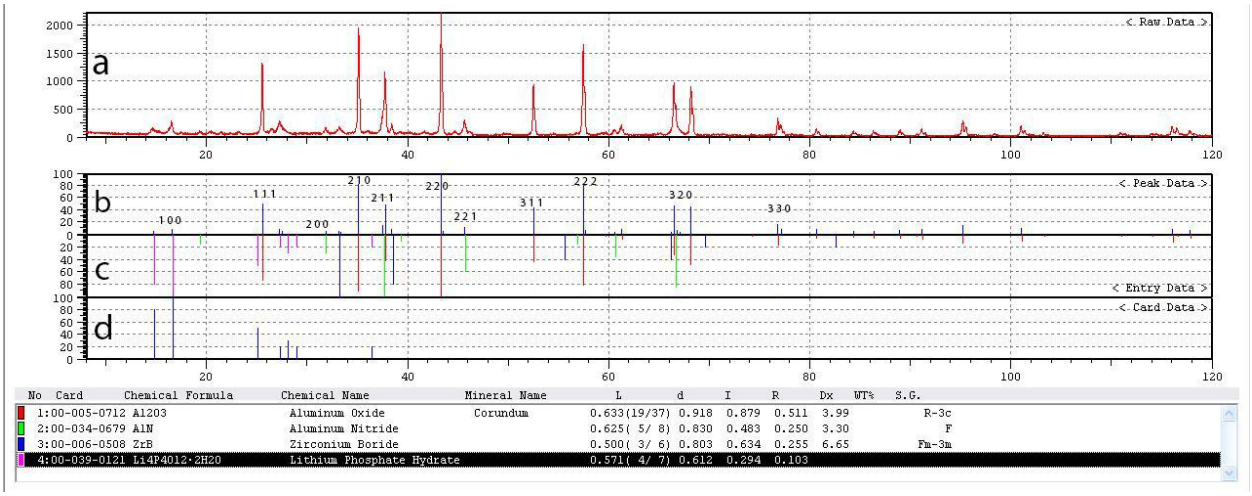

Fig.2. An example of decoding the diffraction pattern of SHS products of sample No.1

This should be taken into account when calculating the composition of the modified mixture for the future coating technology, increasing the aluminum in content. The low reliability of the determination of boron in the SHS products of the base mixture may be associated with its release under the reaction conditions in the amorphous state, possible partial burnout by the reaction

$$4B^* + 3O_2 = 2B_2O_3,$$

As well as diffusion and interaction with the surface of the steel part with the generation of target products, iron borides, iron carbo borides, and Fe-B, Fe-B-C eutectics.

These processes should also be taken into account when calculating the composition of the modified mixture by introducing various fluxes and additives. Samples for the study were prepared from steel plates with surface changes in the places of application of the base mixture, which had appeared after the SHS process during HFC heating. The structure of the samples in the areas of surface changes (presumably

.

formed coatings) and borated layer thickness was studied and determined. Figures 3-6 show the results of the study of the structure of the coating obtained in the SHS process during the high-frequency heating of sample No.1 mounted on a plate made of S355 steel at various magnifications.

As follows from Fig. 3, when the SHS process is carried out during HFC heating of the cylindrical sample No.1, which is molded from the base mixture, at the place of its installation on the surface of a plate made of S355 steel, the formation of a coating with a complex structure of the transition area, which contains several components and porosity, is indeed observed. The thickness of the resulting coating ranges from 150 to 250 microns. The complex structure of the coating-base metal transition area, multi component nature, and porosity of the resulting coating are clearly visible at higher magnification in polarized light (see Fig. 4).

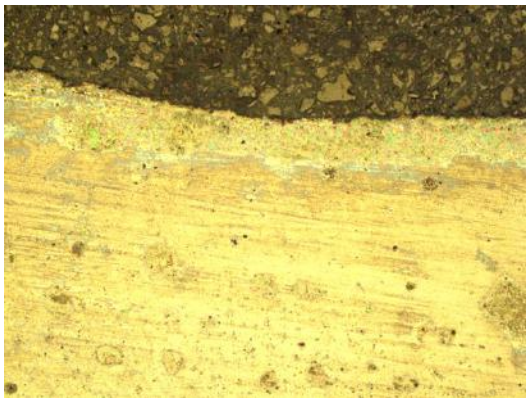

Fig. 3. Microstructure of the coating obtained on S355 steel in the SHS process during HFC heating of sample No.1 (general view, ×100 magnification).

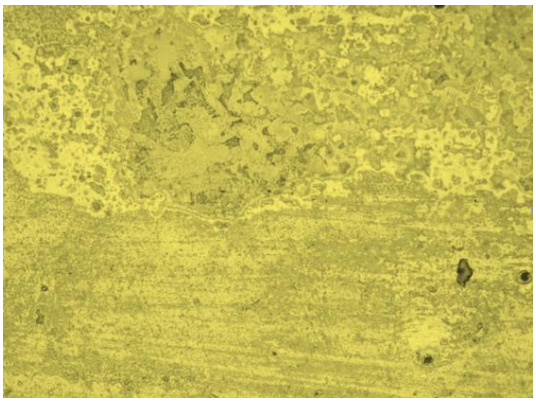

Fig. 4. Microstructure of the coating obtained on S355 steel in the SHS process during HFC heating of sample No.1 (transition area, ×500 magnification).

Structures similar to those observed above were obtained also on S355 steel and in the SHS-process during high-frequency heating of sample No.3, which was placed on the surface of the steel plate, with the only difference that their thickness was 70-100 microns. A decrease in the thickness of the coatings formed in the SHS process during high-frequency heating of sample No.3 is explained by its lower height (volume, mass), as a result of which a smaller amount of surface-active products generated during combustion is observed. The coatings obtained in the SHS process during HFC heating of sample No.2 (sheath) have a completely different structure (Fig. 5, 6).

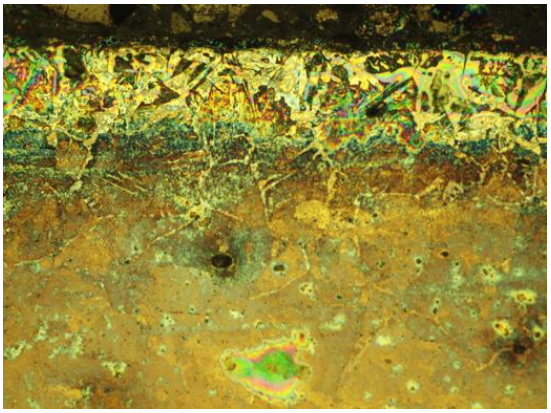

Fig. 5. Microstructure of the coating obtained on S355 steel in the SHS process during HFC heating of sample No.2 (section 1, coverage, ×500 magnification).

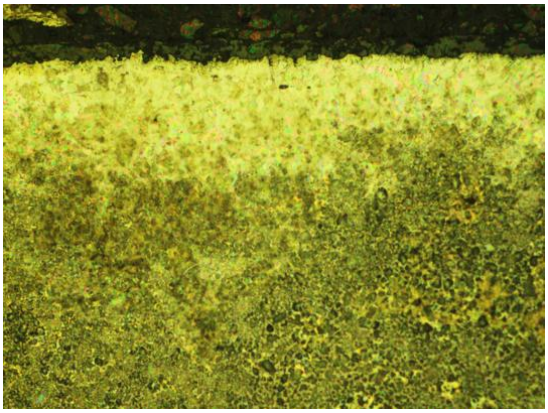

Fig. 6. Microstructure of the coating obtained on S355 steel in the SHS process during HFC heating of sample No.2 (section 2, coverage, ×500 magnification).

Fig. 5-6 clearly show two areas (zones) with different thicknesses and structures of the coating are formed in the coating formed in the SHS process during HFC heating of sample No.2 with a thickness of 2-3 mm, of the base composition applied to the surface of S355 steel. The central coverage area (section 1) is

formed in the place that was subjected to the strongest HFC heating of a steel plate coated with a sheath from the base composition; the peripheral coating area (section 2) is formed along the edges of the boundaries of sheath application, in the areas subjected to the lowest heating. The obtained images show that the microstructure of the coating of the periphery area is similar to the microstructure of the coating obtained in the SHS process during high-frequency heating of samples Nos.1, 3 (see Fig. 6, section 2). The microstructure and composition of the coating of the central area differ from the previously obtained coatings (see Fig. 5, section 1). The coating of area No.1 has a minor thickness (50-70 microns) and a structure characteristic of boride phases is noticeable, i.e. closed dark carbide regions, light interlayers of iron-boride and iron-carbo-boride eutectic.

The study of macrophotographs (50) of the grinding of reinforcing coatings allows the morphology of their most typical areas to identify the main structures (characteristic phases) that make up the coating and determine their characteristics. In all coatings modified with boron, its spherical inclusions are found, the hardness of which reaches values of 1620-1970 HV. Also, in all coatings, regions (phases) are detected, represented by fine eutectic of the Fe-C-B system, the hardness of which exceeds the value of the unmodified boron phases by 1.2-1.5 times, reaches 1080-1110 HV.

The common features of modified coatings are the melting of their boundary with the base metal, and in non-modified ones - the presence of dendritic regions (phases) with a hardness reduced to 500-700 HV. The main material on all samples has a microhardness of 400-450 HV. Table 1. provides summary information on the characteristic phases of reinforcing coatings obtained on 65G steel, HDPE surfacing by various methods and from various charge materials.

Table 1. Description of characteristic phases of coatings and their properties

Method, charge	Coating phases	Structure type, morphology	Microhardness, HV
Sample 1	1	Fine-dispersed boride eutectic, weakly delimited gray areas with inclusions of octahedral fused and crushed carbides	1080-1100
	2	Melted ledeburite-like eutectic, dark and gray with a fine structure	640-660
	3	Structureless spherical inclusions with a clear boundary	1900-2000
	4	Dendritic structures, columnar, even and branched light formations on the border with the base metal	500-700
	5	Boride eutectic, light areas on the border with the base metal	900-1000
	6	Weakly delimited light areas with needle inclusions	800-900
Sample 2	1	Weakly delimited gray areas with needle inclusions	900-950
	2	Fused boride eutectic, light areas on the border with the base metal	850-900
	3	Structureless spherical inclusions with a clear boundary, cracks	1600-1700
	4	Boride eutectic, light areas on the border with pores and inclusions of boron carbide	1000-1100
Sample 3	1	Boride eutectic, the main type of structure in the deposited layer	700-750
	2	Dendritic structures, columnar, even and branched light formations on the border with the base metal	500-550
	3	Weakly delimited gray areas with octahedral and needle inclusions	900-1000
	4	Needle-like structures in a gray field between dendrites	700-750

The chemical composition of the coatings obtained on various samples was studied using a portable X-ray fluorescence spectrometer NITON (equipment of the GOSNITI Nanocenter, Moscow). The chemical element boron belongs to the "lungs" and is not determined by the X-ray fluorescence method. The results of the study of the chemical composition of the coatings are presented in Table 2.

Conclusion

Therefore, it can be concluded that a significant content of aluminum in the form of oxide is observed in all coatings. The different contents of silicon and iron indicate the passage of surface chemical and metallurgical processes in the implementation of SHS processes during high-frequency heating of samples of the base mixture on the surface of S355 steel, as well as segregation and redistribution of steel components on the surface.

.

Table 2. Chemical composition of charge coatings.

Element	Content of the element, %		
	Sample 1	Sample 2	Sample 3
Al	65.52±3.27	69.40±3.20	35.65±2.50
Si	13.68±1.75	19.23±2.66	25.17±2.60
Fe	16.13±2.66	6.39±1.09	7.60±1.26
Cu	1.41±0.32	3.45±0.73	2.09±0.41
Pb	2.88±0.68	1.47±0.35	4.55±0.97

The resulting coatings are composite materials based on aluminum oxide, SHS products in the base mixture, generated through SHS with boron, but due to the high content of aluminum oxide and the occurrence of side reactions, they have a porous inhomogeneous structure, insufficient thickness, and low hardness. The use of HFC heating significantly improves the microstructure of the obtained coatings and provides a better-quality spattering of the coating on the steel part. Obtaining more homogeneous, extended, and harder coatings is possible only when modifying the base mixture, i.e. increasing the aluminum content therein, introducing fluxes, and adjusting the fractional and chemical composition of the powder material.

Acknowledgments

The tests were carried out on the equipment of the Shared Use Center "Materials Research Center".
The work was performed within the framework of project No. AP08052699 «Development and creation of an experimental site for hardening heavy-loaded parts of soil-cutting machines using innovative plasma technology».
The experimental study of boriding mixtures was carried out at the expense of a grant from the President of the Russian Federation for state support of young Russian scientists No. MK-3213.2022.4.

REFERENCES

1 Campos I., Bautista O., Ramírez G., et al. Effect of boron paste thickness on the growth kinetics of Fe_2B boride layers during the boriding process. *Appl. Surf. Sci.*, 2005, Vol. 243, pp. 429–436.

2 Campos I., Palomar M., Amador A., et al. Evaluation of the corrosion resistance of iron boride coatings obtained by paste boriding process. *Surf. Coat. Technol.* 2006, Vol. 201, pp. 2438–2442.

3 Vorob'eva G.A., Remshev E.Yu. Effect of the Parameters of Aero thermo acoustic Treatment of 40Kh Steel on the Acoustic Emission Parameters. *Russian Metallurgy*. 2016, No. 3, pp. 215–218.

4 Krukovich M.G., Prusakov B.A., Sizov I.G. Plasticity of Boronized Layers. *Springer Series in Materials Science*, 2016, Vol. 237, ISBN 978-3-319-40012-9 (eBook).

5 Muhammad W. Boriding of high carbon high chromium cold work tool steel. *Mater. Sci. Eng.*, 2014, Vol.60, pp. 1-6.

6 Calik A., Simsek M., Karakas M.S., Ucar N. Effect of boronizing on microhardness and wear resistance of steel AISI 1050 and chilled cast iron. *Met. Sci. Heat Treat.,* 2014, Vol. 56, pp. 89 – 92.

7 Jurči P., Hudáková M. Diffusion boronizing of H11 hot work tool steel. *Mater. Eng. Perform*, 2011, Vol.20, pp. 1180-1187.

8 Balandin Yu. A. Surface hardening of die steel by diffusion boronizing, borocopperizing, and borochromizing in a fluidized bed. *Met. Sci. Heat Treat*., 2005, Vol. 47, pp. 103-106.

9 Bartkowska A., et al. Laser production of B-Ni complex layers. *Surf.Coat.Technol.,* 2014, Vol.248, pp. 23-29.

10 Bartkowska A., Swadźba R., Popławski M., Bartkowski D. Microstructure, microhardness, phase analysis and chemical composition of laser remelted FeB-Fe_2B surface layers produced on Vanadis-6 steel. *Opt. Laser Technol*., 2016, Vol. 86, pp. 115–125.

11 Safonov A.N. Special features of boronizing iron and steel using a continuous-wave CO_2 laser. *Met. Sci. Heat Treat.* 1998, Vol. 40, No.1 - 2, pp. 6 – 10.

12 Dombrovskii Yu.M., Stepanov M.S. Creation of composite diffusion boride coatings with microarc hardening in powder media. *Izv. Volgograd. Gos. Tekh. Univ.,* 2014, Vol.10, No.23, pp. 41–42.

13 Report on the Project no. AP08052699 *Development and creation of an experimental site for strengthening heavy-loaded parts of soil-cutting machines using innovative plasma technology*, Nur-Sultan, S.Seifullin Kazakh Agro Technical University, 2020, 89p.

14 Ishkov A.V., Malikov V.N. The study of the wear of the control knives of the straw chopper *Journal of Physics: Conference Series*. 2020, 1515 (5), pp. 052026.

Article accepted for publication 23.02.2022

DOI 10.31489/2022No2/13-18

UDC 538.971

INFLUENCE OF PHASE FORMATION PROCESSES IN LITHIUM ZIRCONATE CERAMICS ON STRENGTH AND THERMAL PROPERTIES

Kozlovskiy A.L.[1,2]*, Abyshev B.[1], Zhumadilov K.Zh.[1], Shlimas D.I.[1,2]

[1]L.N. Gumilyov Eurasian National University, Nur-Sultan, Kazakhstan, kozlovskiy.a@inp.kz

[2]Institute of Nuclear Physics, Almaty, Kazakhstan

The article is devoted to the study of the properties of lithium zirconate ceramics obtained by solid-phase synthesis. The choice of lithium zirconate ceramics as objects of study is due to the great prospects for their use as materials for tritium propagation. Results of a study of the influence of the $LiO/ZrO_2/Li_2ZrO_3 \rightarrow LiO/Li_2ZrO_3 \rightarrow Li_2ZrO_3$ type phase transformations in ceramics, depending on the annealing temperature, on the strength and thermophysical parameters of ceramics are obtained. During the studies, it was found that the change in hardness and crack resistance are directly dependent on the phase composition and concentration of impurity phases in the composition of ceramics. It has been determined that the displacement of lithium oxide and zirconium dioxide impurity phases leads to an increase in hardness and an increase in resistance to cracking under single compression. It has been established that at annealing temperatures above 900°C, the change in strength and thermophysical parameters is minimal. At the same time, a change in the phase composition of the $LiO/ZrO_2/Li_2ZrO_3 \rightarrow Li_2ZrO_3$ type ceramics leads to an increase in the thermal conductivity coefficient by (15-20)%.

Keywords: lithium-containing ceramics, phase transformations, hardness, thermal conductivity, nuclear materials

Introduction

In recent years, much attention has been paid to the study of new types of lithium-containing ceramics, as well as their thermophysical and mechanical properties. The interest in these studies is due to the great demand for tritium, which is one of the alternative energy sources, the accumulation of which is required to maintain the efficiency of thermonuclear fusion and the operation of thermonuclear reactors, including TOKAMAK or ITER [1–3]. As is known, traditional methods for producing tritium today cannot meet the demand for it, which requires additional research in ways to obtain it [4,5]. One such way is to reproduce the classical nuclear reaction of the $^6Li + n \rightarrow He + T$ type, which makes it possible to obtain tritium from lithium, with its subsequent accumulation to support thermonuclear fusion. At the same time, as shown in a number of scientific papers [6-10], the tritium production is usually accompanied by the release of helium and other products of nuclear reactions, which leads to the material degradation, as well as a decrease in its resistance to external influences and a deterioration in strength properties.

In this regard, when developing a technology for creating lithium-containing ceramics, much attention should be paid to studying the effect of the phase composition on the strength and thermal properties of ceramics, since these parameters play a very important role in determining the performance of ceramics during their operation [11-15]. As is known, the phase composition of ceramics, as well as the presence of impurities in the composition of ceramics, can have both a positive and a negative effect on the strength properties of ceramics, including the resistance to compression and external pressure. In turn, the presence of impurities can have a significant effect on heat transfer in the material, thereby reducing the efficiency of heat removal from ceramics and the occurrence of overheating [16-18].

Based on the foregoing, the purpose of this work is to study the effect of the phase composition of Li_2ZrO_3 ceramics obtained by solid-phase synthesis and annealed at different annealing temperatures in the range from 600 to 1100°C on the strength and thermophysical parameters of ceramics. This work is part of a cycle of works devoted to the study of the Li_2ZrO_3 ceramic properties and evaluation of the possibility of their use as blanket materials for tritium propagation, which is one of the promising research areas in modern energy [18-20]. Li_2ZrO_3 ceramics were chosen as objects of study, which, as was shown earlier in [18-20], are highly resistant to radiation damage.

.

Experimental part

Synthesis of Li_2ZrO_3 ceramics was carried out by the method of solid-phase synthesis with further thermal annealing of the resulting mixtures in a muffle furnace (RusUniversal, Russia) at temperatures of 600-1100°C. $LiClO_4 \cdot 3H_2O$ and ZrO_2 powders (Sigma Aldrich Saint Louis, Missouri, USA), whose chemical purity was 99.95 %, were used as initial components. As a result of thermal annealing in the temperature range of 600-1100°C, it was found that with an increase in the annealing temperature, phase transformations of the following type $LiO/ZrO_2/Li_2ZrO_3 \rightarrow LiO/Li_2ZrO_3 \rightarrow Li_2ZrO_3$ are observed [19]. At the same time, at an annealing temperature above 900°C, the structure of ceramics is single-phase Li_2ZrO_3 ceramics with a monoclinic structure type.

Study of strength properties was carried out using the indentation method, which was implemented using a LECO LM 700 microhardness tester (LECO Corporation, USA). A Vickers pyramid was used as an indenter, with an indenter load of 10 N. Determination of resistance to single compression was carried out by testing the compression of samples in a press with a compression rate of 0.1 mm/min. Thermal conductive characteristics were evaluated using formula (1), which makes it possible to determine the value of the thermal conductivity coefficient.

$$\lambda = \frac{q\delta}{t_{c1} - t_{c2}}, \tag{1}$$

where q is the heat flux density, W/m^2; t_{c1} and t_{c2} are sample temperatures on both sides, K; δ is the sample thickness.

Results and discussion

One of the important conditions for the applicability of lithium-containing ceramics as blanket materials for tritium propagation is their mechanical strength and resistance to external mechanical influences that may occur during operation, as well as due to a change in the material volume, which can lead to additional pressure and deformation. As a rule, the strength properties of materials are determined by measuring the hardness indices by indentation methods, and the difference in values may reflect the processes of hardening or softening of materials. At the same time, several factors affect the hardness of the material, including density, phase composition, and dislocation concentration play an important role in these characteristics. The combination of these factors can have a very significant effect on the strength characteristics of ceramics. Figure 1 shows the results of changes in the microhardness of Li_2ZrO_3ceramics depending on the phase composition of the ceramics.

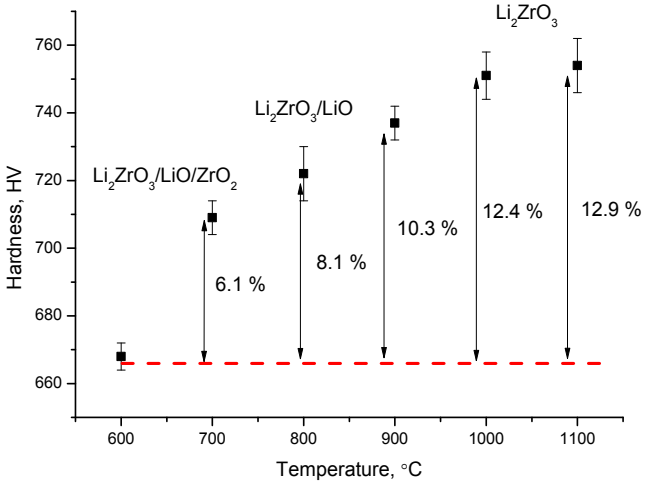

Fig.1. Results of measuring the Li_2ZrO_3 ceramic microhardness depending on the phase composition of ceramics

As can be seen from the presented data, an increase in the annealing temperature, which leads to a change in the phase composition of the ceramics, leads to an increase in the hardness indices, which indicates the effect of strengthening the ceramics associated with a change in the crystal structure of the samples under study. At the same time, in the case of specimens containing LiO and ZrO_2 impurity phases in the

composition of ceramics, the hardness values are rather low compared to pure ceramics. The displacement of impurity inclusions from the composition of ceramics, as well as an increase in the structural ordering degree, leads to an increase in the strength and hardness of ceramics. However, it should be noted that the complete displacement of impurity phases from Li_2ZrO_3 ceramics at annealing temperatures of 1000-1100°C does not lead to a significant increase in strength, which may be evidence of the saturation effect of ceramic consolidation, which does not lead to serious hardening and is associated only with a change in the concentration of point structural defects.

Figure 2 shows the results of changes in the resistance of ceramics to cracking under single compression, which characterizes the properties of ceramics to external pressures. As can be seen from the data presented, a change in the phase composition of ceramics leads not only to an increase in hardness, but also to an increase in crack resistance. At the same time, the change in crack resistance has a similar trend with changes in the hardening and hardness of ceramic samples.

However, if the displacement of impurity phases from the ceramic structure leads to the strengthening of ceramics by 10-12 %, in the case of resistance to cracking of these data, the effect of displacement of impurity phases leads to an increase in resistance by 40-60 %. At the same time, an increase in the annealing temperature from 900 to 1100°C does not lead to large changes, which indicates that the main effect in hardening is associated with a change in the phase composition of ceramics, while for single-phase ceramics obtained at temperatures of 1000-1100°C the change in strength characteristics is insignificant.

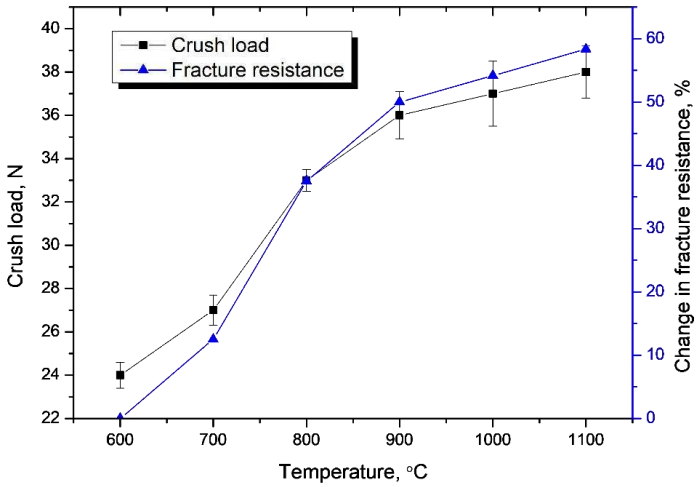

Fig.2. Results of change in the resistance to single compression of ceramics

Figure 3 presents the results of a comparative analysis of changes in the ceramic hardening and consolidation trends associated with a change in density values, which was determined using the X-ray diffraction method by analyzing data on changes in the crystal lattice volume. The general form of changes indicates a significant difference in trends, associated with a difference in changes in the measured values. In the case of changes in the consolidation value, the trend of changes depending on temperature is close to linear, which indicates that the main contribution to consolidation is made by structural ordering caused by a change in the defect structure, as well as partial annihilation of defects as a result of thermal annealing.

In the case of hardening of ceramics, the trend of changes in this value is non-linear and has a pronounced dependence on the phase composition of ceramics, which is reflected in the following facts. The presence of impurity phases in ceramics obtained at an annealing temperature of 600°C leads to the fact that the values of hardness and stability are quite small, which indicates a low resistance to external influences. Displacement of impurity phases with an increase in the annealing temperature leads to a sharp increase in strength and hardness, which is reflected in a change in the trend. However, complete displacement of impurity phases at annealing temperatures of 1000-1100°C, accompanied by structure ordering, does not lead to significant changes in strength characteristics.

One of the factors that make it possible to explain this nature of changes in strength properties, in addition to the phase composition and its changes depending on the annealing temperature, is changes in the

.

dislocation density of ceramics due to changes in the grain size. Figure 4 shows the results of changes in the dislocation density of ceramics depending on the annealing temperature.

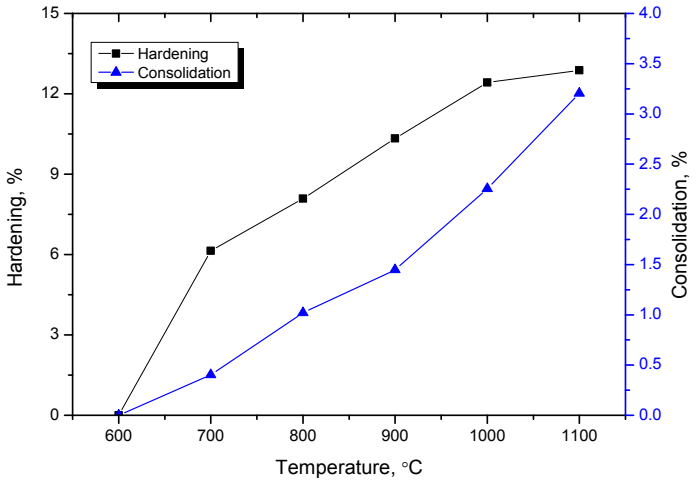

Fig.3. Results of a comparative analysis of changes in the ceramic hardening and consolidation trends

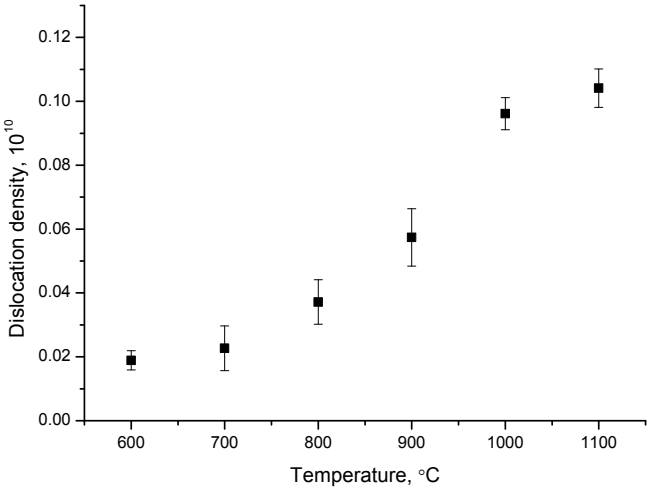

Fig.4. Results of changes in the density of ceramics depending on the annealing temperature

As can be seen from the data presented, the change in dislocation density has a similar trend to changes in strength characteristics and a pronounced nature associated with changes in the phase composition of ceramics. At the same time, the displacement of impurity phases leads to a decrease in the grain size, which in turn leads to an increase in the dislocation density, the changes of which have an inverse quadratic dependence on the grain size. In the case typical for ceramics obtained at a temperature of 1000-1100°C, for which no changes in size were observed, the dislocation density values are also practically unchanged. Thus, we can conclude that the hardening of ceramics is related to the dislocation density, as well as the phase composition of ceramics. As is known, at certain values of the dislocation density, the effects of hardening of materials are observed, as well as an increase in the resistance to destruction under external influences, which is an important factor for materials subjected to mechanical stress, as well as deformation processes.

An important factor determining applicability of ceramics as breeder materials in combination with the mechanical and strength properties of ceramics is their thermophysical characteristics, which characterize the ability to remove heat from the system. At the same time, it is necessary that the materials retain their heat-conducting characteristics over a wide temperature range. Figure 5 shows the results of changes in the thermal conductivity coefficient depending on the heating temperature in the range from 400 to 800°C.

As can be seen from the data presented, a change in the phase composition leads to a sharp increase in the thermal conductivity of ceramics, which is due to a decrease in deformation contributions and cavities

that prevent heat transfer. At the same time, it should be noted that the thermal conductivity of ceramics is maintained over the entire measured temperature range, which indicates the stability of heat transfer. It should also be noted that the structural ordering observed for samples annealed at a temperature of 1000-1100°C does not lead to a significant change in the thermal conductivity, which, as in the case of strength properties, indicates that the change in thermophysical parameters is more related to the phase composition of ceramics, as well as impurity inclusions in the form of LiO and ZrO_2 phases, the displacement and phase transformation of which at annealing temperatures above 800°C leads to an increase in thermal conductivity by 15-20 %. Figure 6 shows results of the dependence of ceramics porosity change and average thermal conductivity value. The porosity value was determined by evaluating changes in the ceramic density depending on the annealing temperature.

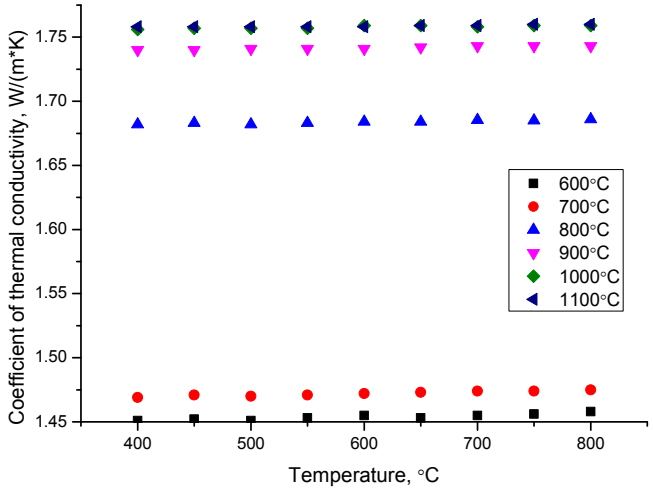

Fig.5. Results of change in the thermal conductivity coefficient

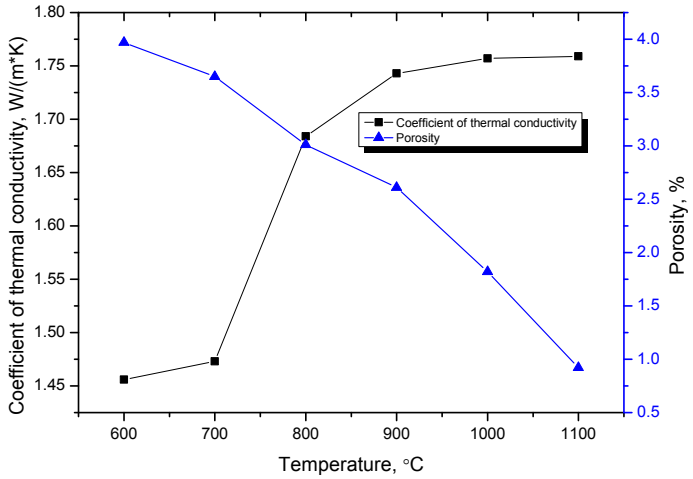

Fig.6. Dependence of the change in the thermal conductivity coefficient and porosity of ceramics

The general trend of changes in the thermal conductivity has a strongly pronounced dependence on the phase composition, as mentioned above. Thus, in the presence of impurity inclusions in the structure, the thermal conductivity is significantly small, which, in addition to the influence of the presence of impurity phases, can also be due to structural distortions that occur during the formation of a complex crystal structure. At the same time, the displacement of impurity inclusions leads to an increase in thermal conductivity, as well as a significant change in porosity, in view of its decrease due to structural ordering. However, the complete displacement of impurity phases from the structure of ceramics does not lead to a significant change in thermal conductivity, the change in which in the annealing temperature range of 900-1100°C does not exceed 1.0-1.5%. At the same time, structural ordering has a significant effect on the ceramic porosity, and a decrease in its value by more than 2.5-3 times compared with the same value for ceramics annealed at a temperature of 600-700°C.

.

Conclusion

Thus, it can be concluded from the experimental work carried out that the structural ordering and phase transformations associated with the displacement of impurity inclusions in Li_2ZrO_3 ceramics have a significant effect on the strength and thermophysical parameters of ceramics. At the same time, the greatest contribution to changes in the strength and thermophysical properties of ceramics is made by phase transformations associated with the formation of an ordered Li_2ZrO_3 phase in the structure of ceramics. In the case of complete formation of the Li_2ZrO_3 phase and further structural ordering, not at high annealing temperatures above 1000°C, does not lead to significant changes in the thermophysical and strength properties. In the case of the complete formation of the Li_2ZrO_3 phase and further structural ordering at high annealing temperatures above 1000°C, it does not lead to significant changes in the thermophysical and strength properties.

Funding

This research was funded by the Science Committee of the Ministry of Education and Science of the Republic of Kazakhstan (No. BR11765580).

REFERENCES

1 Lulewicz J.D., et al. Behaviour of Li_2ZrO_3 and Li_2TiO_3 pebbles relevant to their utilization as ceramic breeder for the HCPB blanket. *Journal of nuclear materials*. 2000, Vol. 283, pp. 1361-1365.

2 Martínez-dlCruz L., Pfeiffer H. Toward understanding the effect of water sorption on lithium zirconate (Li2ZrO3) during its carbonation process at low temperatures. *The Journal of Physical Chemistry C*. 2010. Vol. 114, №. 20, pp. 9453-9458.

3 Kordatos A., et al. Defect processes in Li2ZrO3: insights from atomistic modeling. *Journal of Materials Science: Materials in Electronics*, 2017. Vol. 28, №. 16. pp. 11789-11793.

4 Mukai K., Sanchez F., Knitter R. Chemical compatibility study between ceramic breeder and EUROFER97 steel for HCPB-DEMO blanket. *Journal of Nuclear Materials*. 2017, Vol. 488. pp. 196-203.

5 Carella E., et al. Tritium modelling in HCPB breeder blanket at a system level. *Fusion Engineering and Design*. 2017, Vol. 124, pp. 687-691.

6 Novoselov I.Yu, Shrager E.R., Tikhonov A. Synthesis of uranium-thorium oxide powders in low-temperature plasma of high frequency torch discharge. *Eurasian Physical Technical Journal*, 2022, Vol. 19(1), pp. 50-54

7 Hernandez F.A., et al. An enhanced, near-term HCPB design as driver blanket for the EU DEMO. *Fusion Engineering and Design*. 2019, Vol. 146, pp. 1186-1191.

8 Ciampichetti A., et al. Conceptual design of tritium extraction system for the European HCPB test blanket module. *Fusion Engineering and Design*. 2012, Vol. 87, №. 5-6, pp. 620-624.

9 Rakhadilov B.K., et al. Effect of the structure formed after bulk and surface hardening on the hardness and wear resistance of $20Cr_2Ni_4A$ steel. *Eurasian Physical Technical Journal*, 2022, Vol.19(1), pp. 20-25

10 Dell'Orco G., et al. Experimental tests on Li-ceramic breeders for the helium cooled pebble bed (HCPB) blanket design. *Fusion engineering and design*. 2003, Vol. 69, №. 1-4, pp. 233-240.

11 Rao G. J., et al. Fabrication of Li_4SiO_4-Li_2ZrO_3 composite pebbles using extrusion and spherodization technique with improved crush load and moisture stability. *Journal of Nuclear Materials*. 2019, Vol. 514, pp. 321-333.

12 Cipa J., et al. X-ray induced defects in advanced lithium orthosilicate pebbles with additions of lithium metatitanate. *Fusion Engineering and Design*. 2019, Vol. 143, pp. 10-15.

13 Rex K.A., et al. Defect Properties and Lithium Incorporation in Li_2ZrO_3. *Energies*. 2021, Vol. 14, №. 13, pp. 3963-3970.

14 Kulsartov T., et al. Modeling of hydrogen isotopes release from lithium ceramics Li_2TiO_3 during in-situ experiments using vacuum extraction method. *Fusion Engineering and Design*. 2021, Vol. 170, pp. 112705.

15 Gong Y., et al. Improvement of crushing strength and thermal conductivity by introduction of hetero-element Al into Li_4SiO_4.*Ceramics International*. 2019, Vol. 45, №. 18, pp. 24564-24569.

16 Yang M., et al. Tritium release behavior of Li_4SiO_4 and Li_4SiO_4+ 5 mol% TiO_2 ceramic pebbles with small grain size. *Journal of Nuclear Materials*. 2019, Vol. 514, pp. 284-289.

17 Piazza G., et al. Behaviour of ceramic breeder materials in long time annealing experiments. *Fusion engineering and design*, 2001, Vol. 58. pp. 653-659.

18 Abyshev B., et al. Study of Radiation Resistance to Helium Swelling of $_{Li2ZrO3}$/LiO and Li_2ZrO_3 Ceramics. *Crystals*, 2022, Vol. 12, №. 3. pp. 384-390.

19 Zdorovets M.V., et al. Study of Phase Formation Processes in Li_2ZrO_3 Ceramics Obtained by Mechanochemical Synthesis. *Crystals*. 2021, Vol. 12, №. 1. pp. 21-30.

20 Shlimas D., Kozlovskiy A. L., Zdorovets M. Study of Corrosion Resistance and Degradation Mechanisms in $LiTiO_2$-Li_2TiO_3 Ceramic. *Crystals*. 2021, Vol. 11, №. 7, pp. 753.

Article accepted for publication 14.04.2022

DOI 10.31489/2022No2/19-29

UDC 539.199, 544.723.2

MODELING OF CONFORMATIONAL CHANGES OF POLYELECTROLYTES ON THE SURFACE OF A TRANSVERSELY POLARIZED METAL NANOWIRE IN AN EXTERNAL ELECTRIC FIELD

Kucherenko M.G., Kruchinin N.Yu.*, Neyasov P. P.

Center of Laser and Informational Biophysics, Orenburg State University, Orenburg, Russia, clibph@yandex.ru, kruchinin_56@mail.ru

Gold nanowires with polyelectrolytes adsorbed on their surface are widely used in various biomedical research. In this work, for the first time, conformational changes in polyelectrolytes on the surface of a gold nanowire transversely polarized in an external electric field were considered. The properties of a specially created analytical model of conformational rearrangements of a Gaussian macromolecular chain adsorbed on the surface of a cylindrical metal nanowire in an external electric field transverse to the axis of the nanowire were investigated. Conformational changes of uniformly charged polypeptides on the surface of a transversely polarized gold nanowire have been studied using molecular dynamics simulation. On the basis of the analytical model and the results of molecular dynamics simulation, the spatial distributions of the density of polyelectrolyte units on the surface of the nanowire were constructed. With an increase in the strength of the external electric field, an asymmetric stretching of the polyelectrolyte fringe in the direction of the dipole moment of the transversely polarized nanowire was observed.

Keywords: metal nanowire, polyelectrolyte, conformational changes, molecular dynamics

Introduction

Plasmonic nanorods and nanowires with polymer molecules adsorbed on their surface are widely used for biological nanoprobes based on the effect of surface-enhanced Raman scattering, as well as for creating various chemical sensors [1–7]. In this case, of particular interest is the control of conformational changes in adsorbed macrochains under the influence of an external electric field in order to create similar nanoprobes and sensors with controlled characteristics [8–14].

Previously, the authors studied electrically induced conformational changes in macromolecular chains on the surface of gold nanoobjects of spherical [15–17] and cylindrical [18–20] shapes, as well as on the surface of gold prolate nanospheroids [21–23] and the flat surface of a gold crystal. It was shown that under the influence of both a static external electric field and microwave electromagnetic radiation, the conformational structure of polyelectrolyte chains adsorbed on the surface of metal nanoobjects changes significantly, and at the same time depends on the shape of the nanoobject. At the same time, it is of interest to study conformational changes in polyelectrolytes with a uniform distribution of charges of the same sign along the entire macrochain on the surface of a metal cylindrical nanowire or nanorod polarized in the transverse direction in a static electric field, which was not disclosed in previously published works [18-20].

Therefore, the purpose of this work is to study the conformational changes of uniformly charged polyelectrolytes on the surface of a metal nanowire transversely polarized in an external electric field. For this, two approaches will be used: a statistical description of the macromolecular fringe layer and molecular dynamics (MD) simulation.

1 Formation of a macromolecular fringe layer on the surface of a cylindrical nanowire: a mathematical model

1.1 Mathematical model of formation of the fringe layer of a polyelectrolyte macromolecular chain on the surface of a transversely polarized nanowire

A change in the conformations of macrochains of a polyelectrolyte adsorbed on a nanowire can be carried out by an external electric field that polarizes the conductor. In the simplest model, polymer molecules are represented as ideal Gaussian chains, but the attraction of links to the surface of the adsorbent

.

is taken into account. The intensity of the quasi-static field outside the cylinder of radius *R*, i.e. when $r > R$ and placed in the field $\mathbf{E}_0$ has the form [24] ($\mathbf{n}_x, \mathbf{n}_y$ are the unit vectors of the Cartesian coordinate system)

$$\mathbf{E}_2(r,\varphi) = E_0\mathbf{n}_x + E_0\frac{\varepsilon_1(\omega)-\varepsilon_2}{\varepsilon_1(\omega)+\varepsilon_2}\frac{R^2}{r^2}\left[(1-2\sin^2\varphi)\cdot\mathbf{n}_x + \sin 2\varphi\cdot\mathbf{n}_y\right]. \quad (1)$$

The adsorption potential of the surface of a circular nanowire in the case of van der Waals adsorption can be effectively represented by a combination of the simplest model potentials "solid wall–delta functional well": $V_1(r) = V_\infty(R) - \alpha\delta(r-r_0)$ [18]. When a nanowire is placed in a uniform electric field, its potential becomes dependent on the angular variable φ in the cross-sectional plane as a result of conductor polarization. Then the potential of the total field in the space outside the nanowire with the polarized component $\mathbf{E}_x(t)$ can be written as the sum

$$V(\mathbf{r}) = V_1(r) + V_2(r,\varphi) = V_\infty(R) - \alpha\delta(r-r_0) - eE_0 r\cos\varphi + V_p(r,\varphi), \quad (2)$$

where

$$V_2(r,\varphi) = -eE_0 r\cos\varphi + \frac{\varepsilon_1(\omega)-\varepsilon_2}{\varepsilon_1(\omega)+\varepsilon_2}R^2 eE_0\frac{\cos\varphi}{r} \quad (3)$$

– the energy of interaction of a polyelectrolyte unit carrying a charge *e* with the primary external electric field and the polarization field of the wire. The dielectric constants $\varepsilon_1(\omega), \varepsilon_2$ in (3) characterize the nanowire metal and the environment, respectively.

To study the spatial structure of the macrochain, a conformational function $\psi(\mathbf{r})$ is introduced that satisfies a Schrodinger-type differential equation [25]

$$\frac{a^2kT}{6}\nabla^2\psi(\mathbf{r}) = [V(\mathbf{r})-\varepsilon]\psi(\mathbf{r}), \quad (4)$$

where *a* is the size of the chain link; *T* is the temperature of the colloidal solution. In the case of a sufficiently weak external field, potential (3) can be taken into account in the framework of perturbation theory. Equation (4) with potential (2) contains an angular variable, so it should be written in the form

$$\frac{a^2kT}{6}\left[\frac{1}{r}\frac{\partial}{\partial r}r\frac{\partial}{\partial r} + \frac{1}{r^2}\frac{\partial^2}{\partial\varphi^2}\right]\psi(\mathbf{r}) = [V(\mathbf{r})-\varepsilon]\psi(\mathbf{r}). \quad (5)$$

Solution (5) can be represented as $\psi(\mathbf{r}) = F(r)\Phi_m(\varphi)$, where $\Phi_m(\varphi)$ is the eigenfunction of the projection operator of the quantum orbital angular momentum with integer *m*: $\Phi_m(\varphi) = 1/\sqrt{2\pi}\exp(im\varphi)$.

For the radial function $F_m(r)$ (5), we obtain the equation [19]

$$\frac{a^2kT}{6}\left[\frac{1}{r}\frac{d}{dr}r\frac{d}{dr} - \frac{m^2}{r^2}\right]F_m(r) = [V(r)-\varepsilon_m]F_m(r). \quad (6)$$

Here in (6) the radial potential $V(r) = V_1(r) + V_2(r)$, and $V_2(r)$ is defined by the relation $V_2(r,\varphi) = V_2(r)\Phi_1(\varphi)$, or

$$V_2(r,\varphi) = -\left[1-\alpha'(\omega)\left(\frac{R}{r}\right)^2\right]rE_0\cos\varphi$$

$$V_2(r,\varphi) = -eE_0 r\cos\varphi + \frac{\varepsilon_1(\omega)-\varepsilon_2}{\varepsilon_1(\omega)+\varepsilon_2} R^2 eE_0 \frac{\cos\varphi}{r}$$

The equation for the function $F_m(r)$ without taking into account the polarization part $V_2(r)$ of the potential is obtained from (5), and can be written in the form

$$F_m''(r) + \frac{1}{r}F_m'(r) - \frac{m^2}{r^2}F_m(r) = \frac{6}{a^2 kT}\left[V_1(r) - \varepsilon_m\right]F_m(r). \quad (7)$$

In the absence of a potential $V_1(r) = V_\infty(R) - \alpha\delta(r - r_0)$, equation (7) is the Bessel equation for cylindrical functions $Z_m(\xi)$. Thus, the solution to (7) are the Bessel functions of the imaginary argument $I_m(q_m r)$ и $K_m(q_m r)$, $\xi = q_m r$, $q_m^2 = -\frac{6\varepsilon_m}{a^2 kT}$. Then, as solutions of equation (4) with a certain index *m* in the field $V(r) = V_1(r)$, decaying at infinity, we can write the following expressions

$$\begin{cases} F_m^I(r) = A_m I_m(q_m r) + B_m K_m(q_m r), & R < r < r_0 \\ F_m^{II}(r) = C_m K_m(q_m r), & r_0 < r < \infty \end{cases}. \quad (8)$$

The constants A_m, B_m and C_m are found from the following boundary conditions and conjugation conditions that the functions $\psi(r)$ must satisfy

$$\psi_I(R) = 0, \quad \psi_I(r_0) = \psi_{II}(r_0), \quad \psi_{II}'(r_0) - \psi_I'(r_0) = -\frac{6\alpha}{a^2 kT}\psi_{II}(r_0). \quad (9)$$

The last equation in (9) allows us to determine the only discrete level of the spectrum ε_m for each integer index *m* [19]. For *m* =0, we arrive at the problem with circular symmetry of the distribution density $n(r) = \psi^2(r)$ of links, which we have already studied earlier in a number of papers.

In the general case of an arbitrary index *m*, to determine the parameters q_m and ε_m it is necessary to use the equation

$$\frac{d}{dr}F_m^{II}(r)\big|_{r=r_0} - \frac{d}{dr}F_m^I(r)\big|_{r=r_0} = -\frac{6\alpha}{a^2 kT}F_m^{II}(r_0), \quad (10)$$

and from the other two equalities (9) there are relations between the constants A_m and two other constants B_m and C_m.

Then solutions (8) take the form

$$\begin{cases} F_m^I(r) = A_m\left[I_m(q_m r) - \frac{I_m(q_m R)}{K_m(q_m R)}K_m(q_m r)\right], & R < r < r_0 \\ F_m^{II}(r) = A_m\left[\frac{I_m(q_m r_0)}{K_m(q_m r_0)} - \frac{I_m(q_m R)}{K_m(q_m R)}\right]K_m(q_m r), & r_0 < r < \infty \end{cases}. \quad (11)$$

Substituting (11) into (10) we obtain the general transcendental equation for the eigenvalues q_m

$$\frac{a^2 kT}{6\alpha r_0} = I_m(q_m r_0)K_m(q_m r_0) - K_m^2(q_m r_0)\frac{I_m(q_m R)}{K_m(q_m R)}. \quad (12)$$

.

It was shown in [19] that the functions (11) with m=0 and m=1 are especially important for constructing the first-order perturbation theory. In this case, the density $n(r,\varphi)=\psi^2(r,\varphi)$ of links of the adsorbed macrochain will still be determined by functions (8) or (11) with index m=0, and eigenvalues ε_0. The first-order corrections to the eigenvalue ε_0, when perturbations $V_2(r,\varphi)=-eE_0 r\cos\varphi+V_P(r,\varphi)$ are taken into account, are equal to zero for states (8) or (11) [19]. However, the correct use of the Rayleigh-Schrodinger perturbation theory requires taking into account states (11) with m=1 to clarify the basic states $F_0^I(r)$, $F_0^{II}(r)$ in the field of a polarized nanowire.

1.2 Calculations based on the conformational model of an adsorbed Gaussian chain on the surface of a transversely polarized nanowire

Based on the results of calculations using formulas (1)–(12), spatial distributions of the density of polyelectrolyte units on the surface of a transversely polarized metal nanowire were constructed. All link density distributions are presented normalized to the value of the local density maximum.

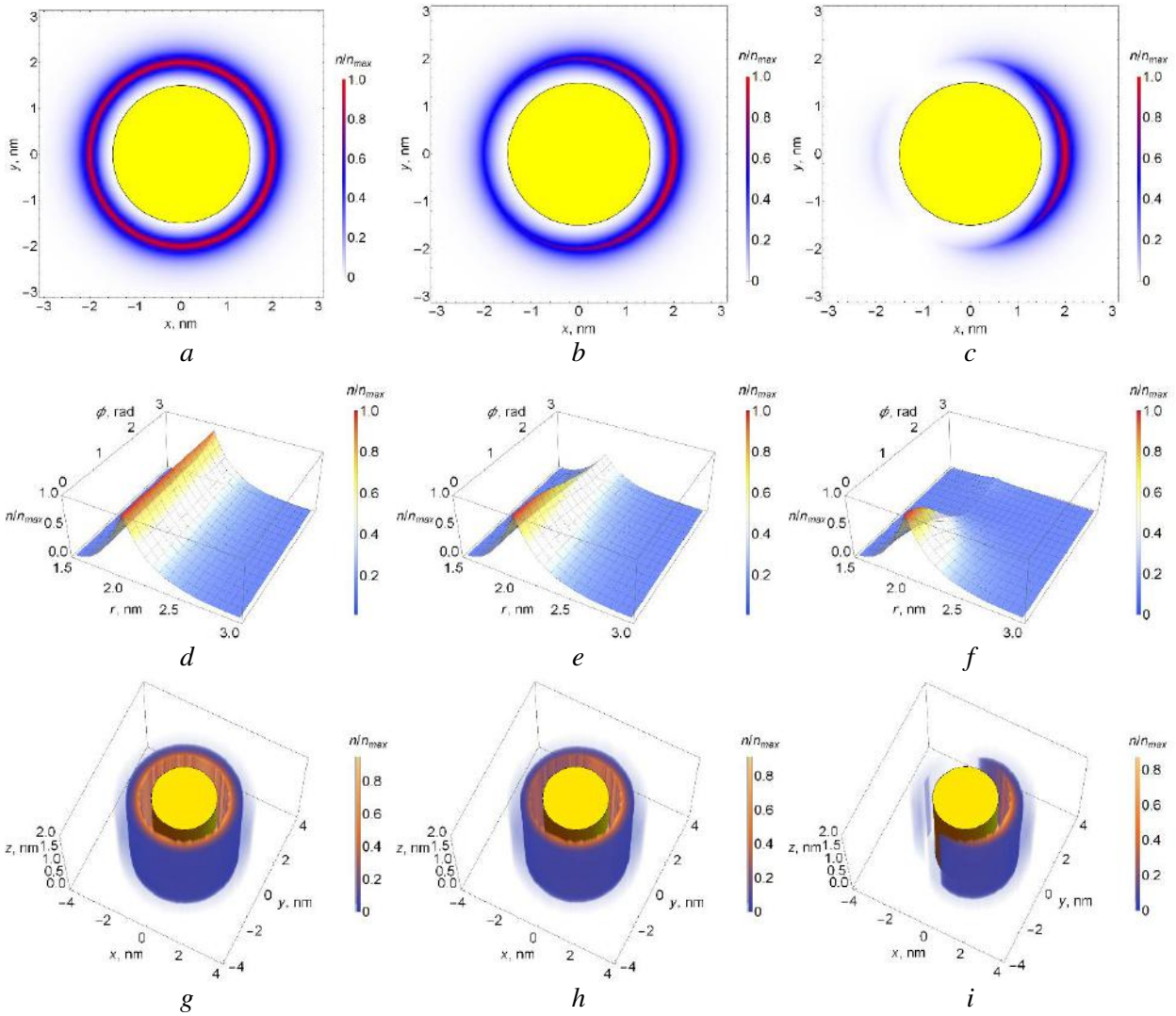

Fig. 1. Spatial distributions of the density of polyelectrolyte units on the surface of a transversely polarized nanowire at different external electric field strengths E_0 (directed along the x axis): 10^4 (a, d, g), 10^5 (b, e, h), 10^6 V/cm (c, f, i). Other parameters: e'= - 0.1 $|e|$, R=1.5 nm, r_0=2 nm, α=5·10^{-3} eV·nm, T=300 K, a =0.5 nm.

Figure 1 shows the spatial distributions of the density of polyelectrolyte units at different external electric field strengths E_0: 10^4 (Fig. 1a, 1d and 1g), 10^5 (Fig. 1b, 1e and 1h) and 10^6 V/cm (Fig. 1c, 1f and 1i). In this case, the following parameters were set in expressions (1-14): link charge e'= - 0.1 $|e|$, nanowire

radius R=1.5 nm, location of the potential well from the nanowire axis r_0=2 nm, potential well depth α=5·10^{-3} eV·nm, temperature T=300 K and link size a=0.5 nm. As can be seen from Figures 1a–1c, with an increase in the strength of the electric field directed from left to right, the links of the polyelectrolyte macrochain are shifted to the right positively charged region of the transversely polarized metal nanowire. At a low electric field strength, the polyelectrolyte almost uniformly envelops the nanowire (Figs. 1a, 1d, and 1g). At the same time, the higher the electric field strength, the stronger the differences in the density of polyelectrolyte units over the cross section of the nanowire (Fig. 1d-1f) for fields of different strengths, and the more the edge of the macrochain shifted to the positively charged region of the polarized nanowire.

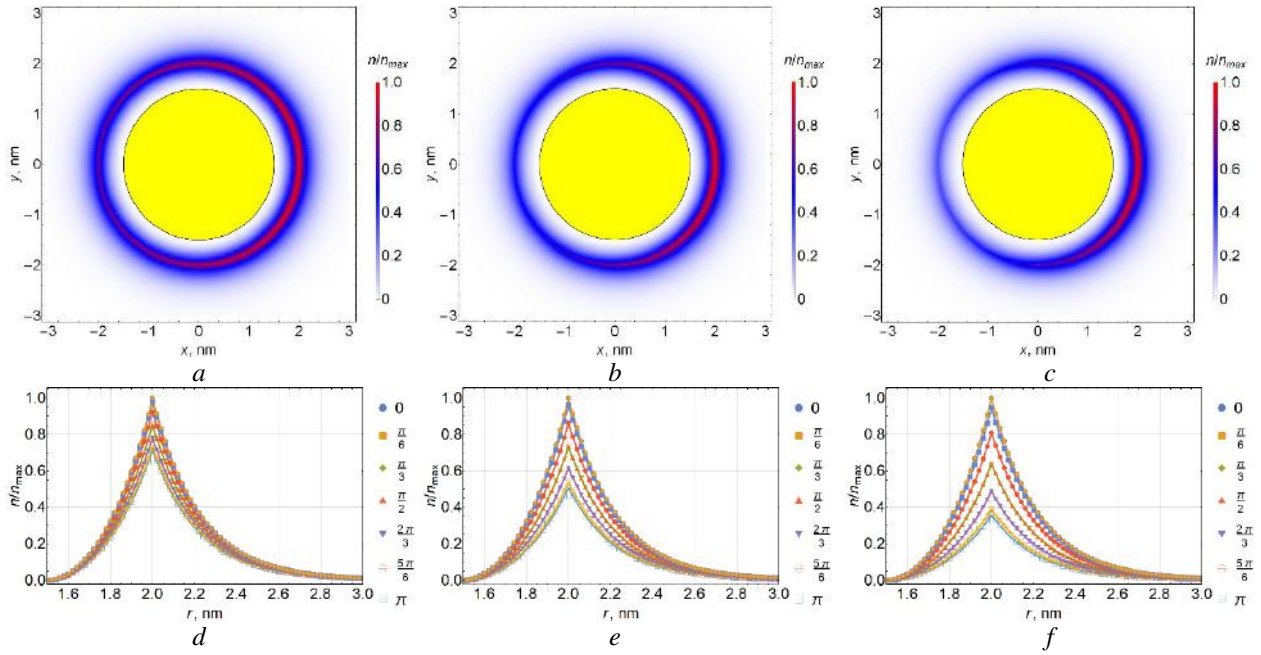

Fig. 2. Spatial distributions of the density of polyelectrolyte units on the surface of a transversely polarized nanowire at different charges of its unit e: - 0.05 (a, d), - 0.1 (b, e), - 0.15 |e| (c, f) Other parameters: R=1.5 nm, r_0=2 nm, α=5·10^{-3} eV·nm, T=300 K, a =0.5 nm, E_0=10^5 V/cm (directed along the axis x).

Figure 2 shows the spatial distributions of the density of the polyelectrolyte units for different values of the charge of the polyelectrolyte unit: - 0,05 |e| (Fig. 2a and 2d), - 0.1 |e| (Fig. 2b and 2e) and - 0.15 |e| (Fig. 2c and 2f) and a constant value of the external electric field E_0=10^5 V/cm. The following parameters were used in expressions (1)-(12): R=1.5 nm, r_0=2 nm, , α=5·10^{-3} eV·nm, T=300 K, a=0.5 nm. It can be seen that as the charge of the polyelectrolyte link increases, the fragments of the macromolecule in the cross section of the nanowire are increasingly shifted towards the positively charged pole. At the same time, the density of macrochain links in the positively and negatively charged regions of the transversely polarized nanowire differs the more, the greater the absolute value of the charge of the polyelectrolyte link (Fig. 2d-e). This is due to the fact that with an increase in the absolute value of the macrochain charge, the electrostatic forces of interaction between the macromolecule and the polarized nanowire increase at a constant potential well depth α, which leads to a displacement of the edge of the charged polyelectrolyte into the oppositely charged region of the nanowire.

In addition, when modeling on the basis of expressions (1)–(12), the influence of variations of other theory parameters on the structural rearrangement of the fringe of a polyelectrolyte molecule adsorbed on the surface of a transversely polarized nanowire was estimated. Figure 3 shows the spatial distributions of the density of polyelectrolyte units at different temperatures: 250 (Fig. 3a), 300 (Fig. 3b) and 350 K (Fig. 3c) with unchanged parameters: e'=- 0.1 |e|, R=1.5 nm, r_0=2 nm, α=5·10^{-3} eV·nm, E_0=105 V/cm, a =0.5 nm. It can be seen from the figure that, at a constant external electric field strength, an increase in the temperature of the colloid leads to the fact that the polyelectrolyte units move freely over the surface of the nanowire and the macrochain uniformly envelops the nanowire. This is due to the fact that the kinetic energy of the macrochain links exceeds the potential barriers caused by attraction to the surface of the nanowire. The same effect takes place when the depth of the potential well α decreases. Thus, when the depth of the potential well decreases from 6·10^{-3} eV·nm to 4·10^{-3} eV·nm and the values of the parameters in expressions (1)-(12)

.

equal to e'= - 0.1 $|e|$, R= 1.5 nm, r_0=2 nm, T=300 K, E_0=10^5 V/cm, a =0.5 nm, the fringe around the nanowire also took a shape similar to the case of high temperature (Fig. 3c), i.e. uniformly enveloping the nanowire. The same effect was caused by a decrease in the nanowire radius from 1.7 nm to 1.3 nm or an increase in the link size from 0.45 nm to 0.55 nm with unchanged parameters: e'= -0.1 $|e|$, α=5·10^{-3} eV·nm, T= 300 K, E_0=10^5 V/cm.

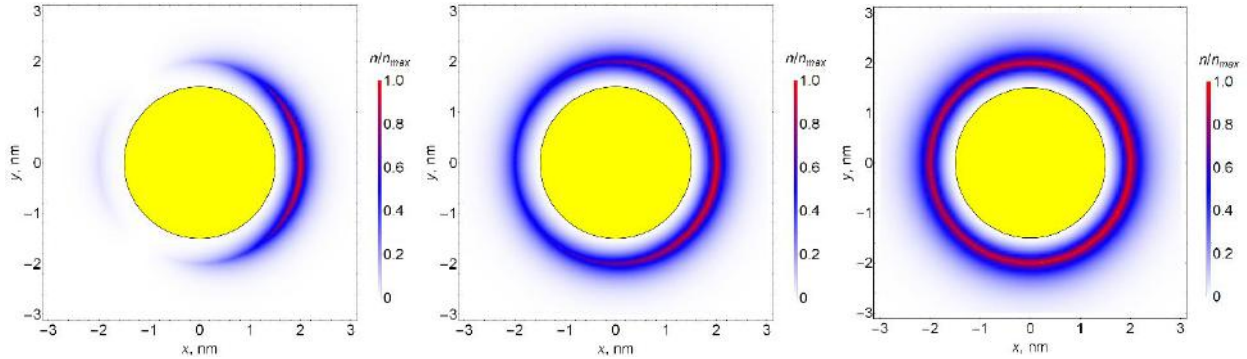

Fig. 3. Spatial distributions of the density of polyelectrolyte units on the surface of a transversely polarized nanowire at different temperatures T: 250 (a), 300 (b), 350 K (c) Other parameters: e'=- 0.1 $|e|$, R =1.5 nm, r_0=2 nm, α=5·10^{-3} eV·nm, a =0.5 nm, E_0=10^5 V/cm (directed along the axis x).

2 Molecular dynamics simulation

In this work, MD simulation of uniformly charged polypeptides consisting of 800 amino acid residues was performed on the surface of a cylindrical gold nanowire polarized in the transverse direction in an external electric field. The model of a gold nanowire was obtained by cutting a cylinder with a radius of 1.5 nm and a length of 15.5 nm from a gold crystal, and its atoms remained fixed during the MD simulation.

The following negatively charged polypeptides have been considered:

1) polypeptide $(A_{10}DA_9)_{40}$, consisting of 760 Ala units (A, neutral) with uniformly distributed 40 Asp units (D, charge -1e), the total macrochain charge was -40e;

2) polypeptide $(A_5DA_4)_{80}$, consisting of 720 Ala units with 80 Asp units uniformly distributed (total macrochain charge -80e);

3) polypeptide $(A_2DA_2)_{160}$, consisting of 640 Ala units with 160 Asp units uniformly distributed (total macrochain charge -160e).

MD simulation was performed using the NAMD 2.13 software package [25]. For polypeptides, the CHARMM22 force field was used [27]. Non-covalent interactions with a gold nanowire were described by the Lennard-Jones potential parameterized in [28]. The Van der Waals potential was cut off at a distance of 1.2 nm using a smoothing function between 1.0 and 1.2 nm. Electrostatic interactions were calculated directly at a distance of 1.2 nm, and at greater distances, we used Ewald's particle–mesh approach (PME) [29] with a grid step of 0.11 nm. The entire nanosystem was placed in a cube with 24 nm edges filled with TIP3P water molecules [30]. To control the obtaining of equilibrium conformations, the change in the root-mean-square distance between polypeptide atoms in different conformations (RMSD) was monitored. MD simulation was performed at a constant temperature at 900 K with a subsequent reduction to 300 K.

First, such conformational structures of macrochains were obtained, in which the polypeptide enveloped the surface of the nanowire. For this purpose, MD simulation of negatively charged polypeptides on the surface of a positively charged gold nanowire (surface charge density +3.3e/nm^2) was carried out. Three starting conformational structures of each polypeptide were obtained for MD simulation on the surface of a transversely polarized gold nanowire.

If the external electric field vector is directed transversely with respect to the axis of a cylindrical metal nanowire, then electric charges will be induced on the surface of the nanowire with a surface density proportional to the cosine of the angle between the directions of the electric field vectors **E** and the normal to the surface [31]:

$$\sigma = \frac{E}{2\pi}\cos\theta \qquad (13)$$

Therefore, the local electric field of a nanowire polarized in the transverse direction was set by assigning partial charges to nanowire atoms located on its surface according to the cosine law (13). The following values of the induced dipole moment of the nanowire per unit of its length were obtained: 0.75, 1.5, and 3 kD/nm. In this case, on the surface of the nanowire, the maximum value of the induced partial charge of the atom in the positively charged region of the polarized nanowire was +0.125*e*, +0.25*e*, and +0.5*e*, respectively.

2.1 MD simulation results

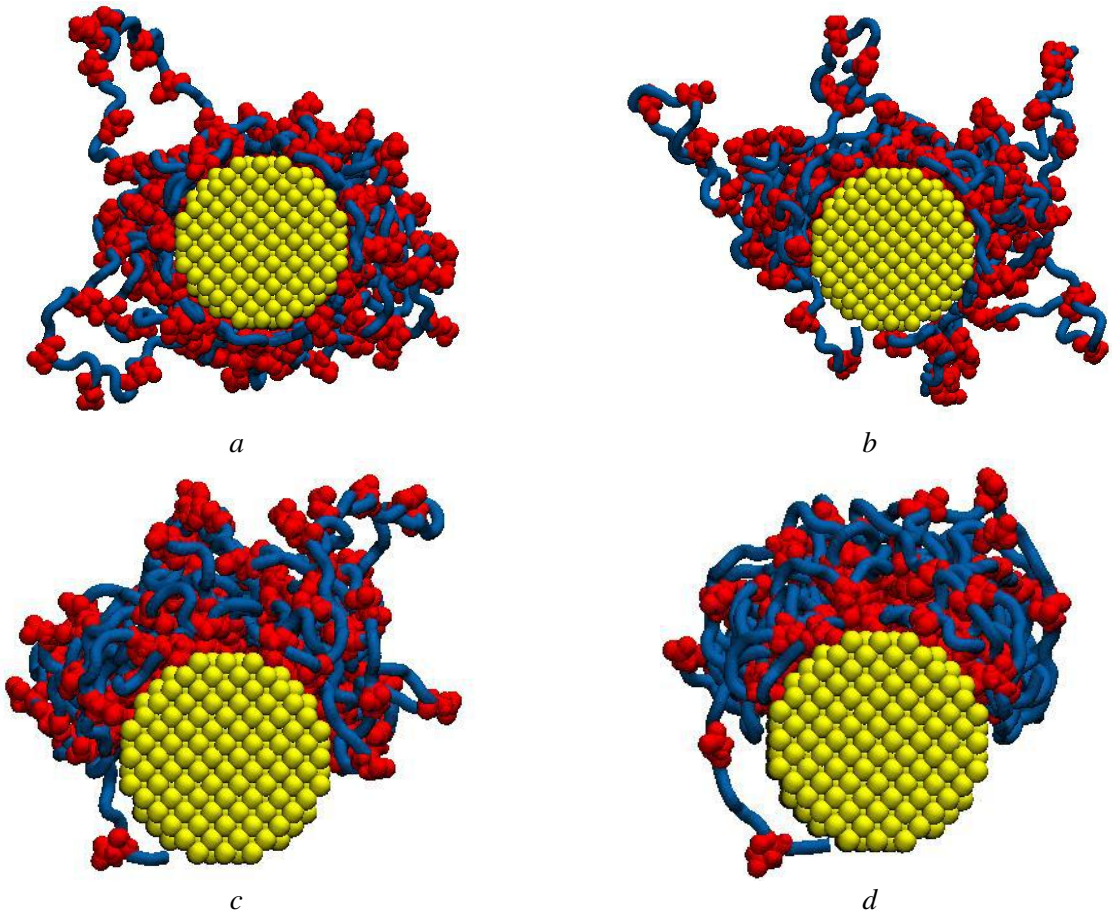

Fig. 4. Polypeptide $(A_2DA_2)_{160}$ in the starting conformation (a), as well as on the surface of a transversely polarized gold nanowire with a dipole moment (directed upwards): 0.75 (b), 1.5 (c) and 3 (d) kD/nm (the blue tube and red symbols denote Ala and Asp residues, respectively).

Figure 4a shows the starting conformational structure of the $(A_2DA_2)_{160}$ polypeptide, which was obtained at the end of MD simulation on a positively charged nanowire, with the macromolecular chain as a whole uniformly enveloping the nanowire. Figures 4b–4d show that as the dipole moment of the nanowire increases in the transverse direction, the macromolecular chain shifts more and more to the positively charged region of the nanowire (in the upper half of the cross section). At the maximum value of the dipole moment of the nanowire (Fig. 4d), almost all amino acid residues are located in the upper positively charged region of the nanowire. An exception is the only positively charged N-terminus of the polypeptide, which remained in the negatively charged region of the nanowire. A similar picture of displacement of negatively charged macrochain units to the positively charged region of the transversely polarized nanowire was observed for polypeptides $(A_{10}DA_9)_{40}$ and $(A_5DA_4)_{80}$.

Figure 5 shows the average angular dependences of the distribution of atoms of the polypeptide $(A_2DA_2)_{160}$, which were calculated with a step of 10 degrees along the cross section (a negatively charged pole in the nanowire cross section corresponds to an angle of 180 degrees, and a positively charged pole corresponds to an angle of 0 degrees). This figure shows that, in the starting conformation (curve 1), a generally uniform distribution of atoms of uniformly charged polypeptides around the nanowire is observed. At the value of the dipole moment of the nanowire equal to 0.75 kD/nm, a small part of the polypeptide

.

atoms shifted to the positively charged region of the nanowire (curve 2), and already at the value of the dipole moment of the nanowire equal to 1.5 kD/nm (curve 3), most of the amino acid residues of the polypeptide shifted to the positively charged region. nanowire area. Similar mean angular distributions of atoms were also observed for other considered polypeptides.

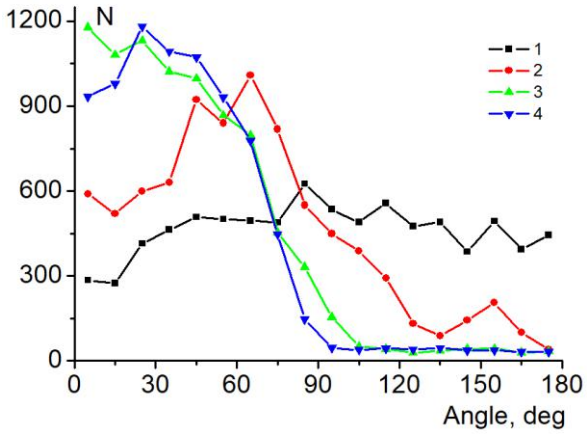

Fig. 5. Average angular dependences of the distribution of atoms of the polypeptide $(A_2DA_2)_{160}$ on the surface of a transversely polarized gold nanowire. In the figure, the numbers denote the values of the dipole moment of the nanowire: 1) – 0, 2) – 0.75, 3) – 1.5 and 4) – 3 kD/nm.

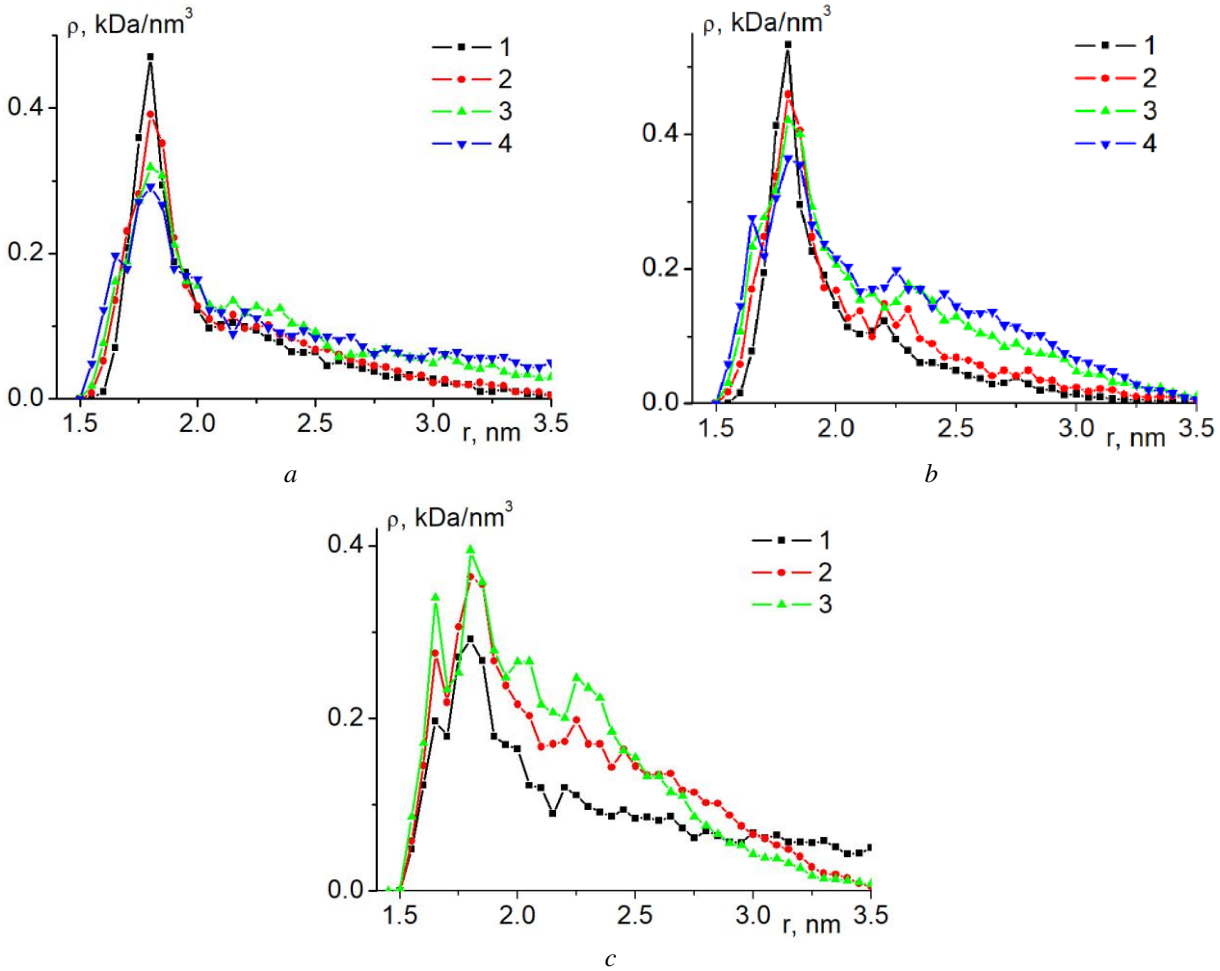

Fig. 6. Radial dependences of the average density of atoms of the polypeptide $(A_{10}DA_9)_{40}$ (a) and $(A_5DA_4)_{80}$ (b) on the surface of the positively charged half of the transversely polarized nanowire at dipole moment values: 1) – 0, 2) – 0.75, 3) – 1.5 and 4) – 3 kD/nm. Radial dependences of the average atomic density of polypeptides $(A_{10}DA_9)_{40}$ (c, 1), $(A_5DA_4)_{80}$ (c, 2), and $(A_2DA_2)_{160}$ (c, 3) on the surface of a positively charged region of a transversely polarized gold nanowire at a dipole moment of 3 kD/nm.

Figure 6 shows the radial dependences of the average density of polypeptide atoms on the surface of a positively charged region of a transversely polarized nanowire for various values of its dipole moment. It can be seen that as the dipole moment of the transversely polarized nanowire increases (Figs. 6a and 6b), the density of polypeptide atoms near the surface decreases more and more. This is due to the fact that when similarly charged units are displaced to the upper region and, accordingly, their number increases there, the polyelectrolyte fringe swells due to bulk interactions between macromolecule units. It is also seen in Fig. 3c that at the maximum value of the dipole moment of the nanowire considered for the polypeptide $(A_{10}DA_9)_{40}$ with the lowest density of charged units per macrochain length unit, the curve of the radial dependence of the density of polypeptide atoms is significantly lower than for the other two polypeptides. This is due to the fact that with an increase in the number of charged units per unit length of the polypeptide, the force of electrostatic attraction between the positively charged region of the transversely polarized nanowire and the negatively charged polypeptide increases.

Conclusion

Based on the expressions of the analytical model for the formation of a macromolecular fringe layer on the surface of a cylindrical metal nanowire, the conformational changes in the uniformly charged polyelectrolyte adsorbed on it under the action of a transversely directed external electric field were calculated. As the strength of the external electric field increased, an asymmetric stretching of the polyelectrolyte fringe was observed in the direction of the dipole moment of the transversely polarized nanowire. In this case, the links of the macrochain of the charged polyelectrolyte shifted to the oppositely charged pole along the cross section of the nanowire, and the like-charged pole became exposed relative to the charged macromolecule. An increase in the macrochain charge per unit of its length at a constant strength of the external transverse electric field led to an ever greater displacement of the polyelectrolyte fringe into the oppositely charged region of the transversely polarized nanowire. The influence of other parameters included in the obtained expressions of the mathematical model on changes in the polymer fringe of the adsorbed polyelectrolyte of the transversely polarized nanowire was evaluated. An increase in temperature, a decrease in the depth of the potential well, a decrease in the nanowire radius, and an increase in the link size led to the fact that the asymmetry of the pattern for the polyelectrolyte fringe disappeared and the macromolecular chain uniformly enveloped the transversely polarized nanowire.

The obtained picture of the density distribution of macrochain units is in qualitative agreement with the conformational structures of uniformly charged polypeptides adsorbed on a gold, transversely polarized nanowire, which appear as a result of the performed MD simulation. In the case of MD simulation, the asymmetric stretching of the polypeptide fringe in the direction of the dipole moment of the transversely polarized nanowire also occurred. In this case, the higher the value of the dipole moment of the gold nanowire and the greater the number of charged amino acid residues of the same sign per unit length of the polypeptide, the stronger the macrochain shifted to the oppositely charged region of the transversely polarized nanowire. In this region of the nanowire, the macromolecular fringe gradually swelled due to bulk interactions between the charged units of the macromolecule.

The asymmetric stretching of the polyelectrolyte fringe with an increase in the strength of the external electric field is due to its effect on the charged links of the macrochain. Under the influence of an external force, which leads to a decrease in the possible conformations of the macrochain, elastic forces arise that prevent such a rearrangement of the macromolecule and are of an entropic nature [25]. As the possible conformations of a macromolecule decrease, its conformational entropy also decreases. With an increase in the strength of the external electric field, the forces acting on the charged macrochain increase, which begins to shift to the oppositely charged region of the transversely polarized nanowire. In this case, the elastic forces, which are of an entropic nature, prevent this and tend to return the shape of such a fringe that evenly envelops the nanowire. In MD simulation, in addition to the entropy factor, the shape of the polyelectrolyte fringe on the surface of the transversely polarized nanowire is also affected by the force factor associated with volumetric interactions of macromolecule units with each other.

Such a rearrangement of the conformational structure of adsorbed uniformly charged macromolecules adsorbed on the surface of a metal nanowire, which occurs under the influence of an external, transversely directed electric field, can find practical application in the creation of new or modification of existing bionanoprobes and sensors that based on the effect of surface-enhanced Raman scattering and are sensitive to exposure to an external electric field.

.

We can also note further prospects for such studies of conformational changes in adsorbed polyelectrolytes on the surfaces of gold nanoparticles. Of great interest, in addition to spherical [15–17] and cylindrical [18–20] nanoobjects, is the study of conformational rearrangements on the surface of spheroidal gold nanoparticles with different anisotropy in order to obtain nanosystems with tunable plasmon characteristics. On the surface of a prolate [21–23] or oblate spheroidal nanoparticle, both charged and polarized along the rotation axis, the distribution of electric charges differs significantly from the cases of charge distribution on the surface of polarized spherical or cylindrical nanoobjects. Such an inhomogeneous distribution of charges on the surface will lead to the fact that on the surface of both charged and placed in a static or alternating electric field nanospheroids, the polyelectrolyte fringe will have a unique shape, depending on the ratio between the lengths of the major and minor axes of the nanospheroids.

Acknowledgements

This work was supported by the Ministry of Science and Higher Education of the Russian Federation within the framework of project no. FSGU-2020-0003.

REFERENCES

1 Pardehkhorram R., Alshawawreh F., Gonçales V.R., et al. Gooding. functionalized gold nanorod probes: a sophisticated design of SERS immunoassay for biodetection in complex media. *Anal. Chem*., 2021, Vol. 93, pp. 12954-12965. https://doi.org/10.1021/acs.analchem.1c02557.

2 Sankari S.S., Dahms H., Tsai M., et al. Comparative study of an antimicrobial peptide and a neuropeptide conjugated with gold nanorods for the targeted photothermal killing of bacteria. *Colloids and Surfaces B: Biointerfaces*, 2021, Vol. 208, pp. 112117. https://doi.org/10.1016/j.colsurfb.2021.112117.

3 Ferhan A.R., Hwang Y., Ibrahim M.S.B., et al. Ultrahigh surface sensitivity of deposited gold nanorod arrays for nanoplasmonic biosensing. *Applied Materials Today*, 2021, Vol. 23, pp. 101046. https://doi.org/10.1016/j.apmt.2021.101046.

4 Nguyen V., Li Y., Henry J., et al. Gold nanorod enhanced photoacoustic microscopy and optical coherence tomography of choroidal neovascularization. *ACS Appl. Mater. Interfaces*, 2021, Vol. 13, pp. 40214-10228. https://doi.org/10.1021/acsami.1c03504.

5 Sheng G., Ni J., Xing K., et al. Infection microenvironment-responsive multifunctional peptide coated gold nanorods for bimodal antibacterial applications. *Colloid and Interface Science Communications*, 2021, Vol. 41, pp. 100379. https://doi.org/10.1016/j.colcom.2021.100379.

6 Creyer M.N., Jin Z., Moore C., et al. Modulation of gold nanorod growth via the proteolysis of dithiol peptides for enzymatic biomarker detection. *ACS Appl. Mater. Interfaces*, 2021, Vol. 13, pp. 45236-45243. https://doi.org/10.1021/acsami.1c11620.

7 Dong X., Ye J., Chen Y., et al. Intelligent peptide-nanorods against drug-resistant bacterial infection and promote wound healing by mild-temperature photothermal therapy. *Chemical Engineering Journal*, 2022, Vol. 432, pp. 134061. https://doi.org/10.1016/j.cej.2021.134061.

8 Kyaw H.H., Boonruang S., Mohammed W.S., Dutta J. Design of electric-field assisted surface plasmon resonance system for the detection of heavy metal ions in water. *AIP Advances*, 2015, Vol. 5, pp. 107226. https://doi.org/10.1063/1.4934934.

9 Chen Y., Cruz-Chu E.R., Woodard J., et al. Electrically induced conformational change of peptides on metallic nanosurfaces. *ACS Nano*, 2012, Vol. 6, pp. 8847-8856. https://doi.org/10.1021/nn3027408.

10 Bekardb I., Dunstan D.E. Electric field induced changes in protein conformation. *Soft Matter*, 2014, Vol.10, pp. 431-437. https://doi.org/10.1039/C3SM52653D.

11 Wu X., Liu Z., Zhu W. External electric field induced conformational changes as a buffer to increase the stability of CL-20/HMX cocrystal and its pure components. *Materials Today Communications*, 2021, Vol. 26, pp. 101696. https://doi.org/10.1016/j.mtcomm.2020.101696.

12 Mayya K.S., Schoeler B., Caruso F. Preparation and organization of nanoscale polyelectrolyte-coated gold nanoparticles. *Advanced Functional Materials*, 2003, Vol. 13: pp. 183-188. https://doi.org/10.1002/adfm.200390028.

13 Dobrynin A.V., Rubinstein M. Theory of polyelectrolytes in solutions and at surfaces. *Progress in Polymer Science,* 2005, Vol. 30, pp. 1049-1118. https://doi.org/10.1016/j.progpolymsci.2005.07.006.

14 Chong G., Hernandez R. Adsorption dynamics and structure of polycations on citrate-coated gold nanoparticles. *The Journal of Physical Chemistry C,* 2018, Vol. 122, 19962-19969. https://doi.org/10.1021/acs.jpcc.8b05202.

15 Kruchinin N.Yu., Kucherenko M.G. Conformational rearrangements of polyampholytic polypeptides on metal nanoparticle surface in microwave electric field: molecular-dynamics simulation. *Colloid Journal*, 2020, Vol. 82, pp. 392-402. https://doi.org/10.1134/S1061933X20040067.

16 Kruchinin N.Yu., Kucherenko M.G., Neyasov P.P. Conformational changes of uniformly charged polyelectrolyte chains on the surface of a polarized gold nanoparticle: molecular dynamics simulation and the theory of a Gaussian chain in a field *Russian Journal of Physical Chemistry A*, 2021, Vol. 95, pp. 362-371. https://doi.org/10.1134/S003602442102014X.

17 Kruchinin N.Yu. Molecular dynamics simulation of uniformly charged polypeptides on the surface of a charged metal nanoparticle in an alternating electric Field *Colloid Journal*, 2021, Vol. 83, pp. 326-334. https://doi.org/10.1134/S1061933X2102006X.

18 Kruchinin N.Yu., Kucherenko M.G. Rearrangements in the conformational structure of polypeptides on the surface of a metal nanowire in rotating electric field: molecular dynamics simulation *Colloid Journal*, 2021, Vol. 83, pp. 79-87. https://doi.org/10.1134/S1061933X20060083.

19 Kruchinin N.Yu., Kucherenko M.G. Rearrangement of the conformational structure of polyampholytes on the surface of a metal nanowire in a transverse microwave electric field. *Eurasian Physical Technical Journal,* 2021, Vol.18, pp. 16-28. doi:10.31489/2021No1/16-28.

20 Kruchinin N.Yu., Kucherenko M.G. Rearrangements in the conformational structure of polyampholytic polypeptides on the surface of a uniformly charged and polarized nanowire: Molecular dynamics simulation. *Surfaces and Interfaces*, 2021, Vol. 27, pp. 101517. https://doi.org/10.1016/j.surfin.2021.101517.

21 Kruchinin N.Yu., Kucherenko M.G. Molecular dynamics simulation of conformational rearrangements in polyelectrolyte macromolecules on the surface of a charged or polarized prolate spheroidal metal nanoparticle. *Colloid Journal*, 2021, Vol. 83, pp. 591-604. https://doi.org/10.1134/S1061933X21050070

22 Kruchinin N.Yu., Kucherenko M.G. Modeling the conformational rearrangement of polyampholytes on the surface of a prolate spheroidal metal nanoparticle in alternating electric field. *High Energy Chemistry,* 2021, Vol. 55, pp. 442-453. https://doi.org/10.1134/S0018143921060084.

23 Kruchinin N.Yu., Kucherenko M.G. Molecular dynamics simulation of the conformational structure of uniform polypeptides on the surface of a polarized metal prolate nanospheroid with varying pH. *Russian Journal of Physical Chemistry A*, 2022, Vol. 96, pp. 624-632. https://doi.org/10.1134/S0036024422030141.

24 Novotny L., Hecht B. *Principles of nanooptics*. 2006, Cambridge: Cambridge University Press. 564p.

25 Grosberg A.Y., Khokhlov A.R. *Statistical Physics of Macromolecules*. 1994, AIP Press, New York. 347p

26 Phillips J.C., Braun R., Wang W., et al. Scalable molecular dynamics with NAMD. *J Comput Chem*. 2005, Vol. 26, pp. 1781-1802. https://doi.org/10.1002/jcc.20289.

27 MacKerell A.D. Jr., Bashford D., Bellott M., et al. All-atom empirical potential for molecular modeling and dynamics studies of proteins *J. Phys. Chem*. B. 1998, Vol. 102, pp. 3586-3616. https://doi.org/10.1021/jp973084f.

28 Heinz H., Vaia R.A., Farmer B.L., Naik R.R. Accurate simulation of surfaces and interfaces of face-centered cubic metals using 12−6 and 9−6 Lennard-Jones potentials. *J. Phys. Chem*. C. 2008, Vol. 112, pp. 17281-17290. https://doi.org/10.1021/jp801931d.

29 Darden T., York D., Pedersen L. Particle mesh Ewald: An N·log(N) method for Ewald sums in large systems *J. Chem. Phys*. 1993, Vol. 98, pp. 10089-10092. https://doi.org/10.1063/1.464397.

30 Jorgensen W.L., Chandrasekhar J., Madura J.D., et al. Comparison of simple potential functions for simulating liquid water. *J. Chem. Phys*. 1983, Vol. 79, pp. 926-935. https://doi.org/10.1063/1.445869.

31 Landau L.D., Pitaevskii L.P., Lifshitz E.M. *Electrodynamics of Continuous Media*, 2nd Edition, Elsevier Ltd., 1984, 460 p.

Article accepted for publication 23.03.2022

.

DOI 10.31489/2022No2/30-34

UDC 535.37

THE EFFECT OF LASER ENERGY DENSITY ON THE PROPERTIES OF GRAPHENE DOTS

Seliverstova E.V.*, Ibrayev N. Kh., Alikhaidarova E.Zh.

Institute of Molecular Nanophotonics, Buketov Karaganda University, Karaganda, Kazakhstan, genia_sv@mail.ru

The structural and optical properties of dots based on graphene oxide (GO) obtained by laser ablation method with various energy densities of radiation were studied. It was shown that after laser ablation, the average lateral size of GO sheets was decreased from 1280–1900 nm to 230±95 nm and 110±42 nm for samples prepared at a laser radiation with energy density of E~15 and 21 mJ/cm^2, respectively. Raman spectroscopy data showed that after ablation, the I_D/I_G ratio decreased from 1.04 to 0.97, indicating an increase in the number of sp^2-hybridized domains in GO after ablation. A change in the energy density has practically no effect on a change in its functionalization, as well as the ordering of sp^2 domains inside a GO sheet. The optical density of GO dispersions and the intensity of their fluorescence depend on the ablation conditions. For non-ablated dispersions along with the luminescence band at 450 nm, additional band appears in the spectrum with a maximum at about 600 nm. After ablation the distribution of particles becomes more uniform, as evidenced by both the change in the shape of the GO luminescence band and the constancy of the fluorescence lifetime upon registration at different wavelength.

Keywords: graphene oxide, graphene dots, laser ablation, structure, optical properties.

Introduction

Laser ablation in a liquid is a reliable and simple method for the preparation of nanosized objects and nanoparticles [1–3], carbon and graphene dots [4]. It is known that, under the influence of laser radiation, a laser-induced breakdown occurs on the surface of the sample in a liquid. As a result, shock waves are formed, and the resulting plasma expands and cools. Then the cavitation bubble expands and collapses, releasing a large amount of energy and breaking the substance into smaller fragments [5]. The properties of the resulting nanomaterials depend on the parameters of laser radiation (wavelength, energy and pulse duration, exposure time) and the properties of the ablated dispersion [6].

Currently, this method is a good alternative for the preparation of graphene luminescent dots. By changing the radiation characteristics during laser ablation, it is possible to obtain graphene dots of various shapes and sizes, which exhibit unusual photoluminescence associated with a circular polygonal shape and corresponding edge effects [7]. In particular, the laser ablation method was used in Ref. [8] to obtain graphene oxide (GO) nanostructures. It was shown that during the ablation process, nanostructures of various shapes are formed: ribbons, flakes, and quantum dots with simultaneous photoreduction of graphene oxide. Graphene oxide dots exhibit blue photoluminescence. By changing the ablation time, it is possible to achieve different fluorescence quantum yields of graphene dots [9, 10]. It is known that the power of laser radiation directly affects the mechanism of material ablation. For example, it was shown in Refs. [11–14] that at high laser radiation energy densities (>10 J/cm^2), the ablation mechanism changes from melting to explosive boiling or fragmentation, which do not lead to the formation of nanoparticles.

The aim of the present work is studying of the effect of laser pulse energy density on the properties of GO in aqueous dispersions. This will open up possibilities for controlling the optical and luminescent properties of graphene dots by changing the conditions for their synthesis. Graphene and carbon dots [15] can be used in various fields, such as energy storage [16], photovoltaics [17], photoelectrochemical [18] and photocatalytic [19–22] generation of hydrogen/hydrocarbon fuels, and photocatalysis of organic pollution [23]. In addition, their high photostability and biocompatibility make them a good alternative to conventional semiconductor quantum dots.

1. Experimental part

To prepare and study dispersions of graphene oxide the method and equipment described in Refs. [9, 10] were used. Briefly, single layer graphene oxide (GO, Cheaptubes) [24] was dispersed in deionized water (AquaMax) by sonication for 30 min. The solution was then centrifuged at 6000 rpm for 1 hour. The height of the ablated liquid was equal to 0.8 cm. During laser ablation, the dispersion was continuously stirred. The Nd:YAG laser with λ_{gen}=532 nm, τ=10 nm and pulse energy density equal to E~15 and 21 mJ/cm^2 was chosen as the radiation source. Previous studies have shown that after 20 min of ablation, GO is reduced and graphitized, which leads to an increase in the average crystallite size of sp^2 carbon domains and a decrease in the number of GO layers in the obtained particles [9]. Based on this, the ablation time was chosen equal to 30 minutes.

According to data obtained with a Zetasizer Nano S90 analyzer (Malvern), the particle size of GO was estimated. To study the particle morphology, the dispersion was spreaded onto the surface of silicon wafers. The images were registered with a scanning electron microscope Mira-3 LMU (Tescan). The Raman spectra of the prepared samples were recorded using a Confotec MR520 (3D Scanning Raman Confocal Microscope, Sol Instruments) with laser excitation at a wavelength of 532 nm. Absorption spectra were measured on a Cary-300 spectrometer (Agilent). Fluorescence was recorded using an Eclipse (Agilent) spectrofluorimeter. Fluorescence decay kinetics of graphene dots were measured by using TCSPC (time-correlated single photon counting) system (Becker&Hickl) at excitation wavelength λ_{exc}= 375 nm. All measurements were carried out at room temperature in 1 cm quartz cells.

2. Results and discussion

Measurements of the particle size of graphene oxide by dynamic light scattering showed that, before ablation in solution, about half of the particles are larger than 1 μm (1280–1900 nm). After ablation at 15 mJ/cm^2, the average particle size was noticeably decreased from 1575 nm to 230±95 nm. An increase in the ablation power leads to a further decrease in the particle size of graphene oxide to 110±42 nm (Fig. 1).

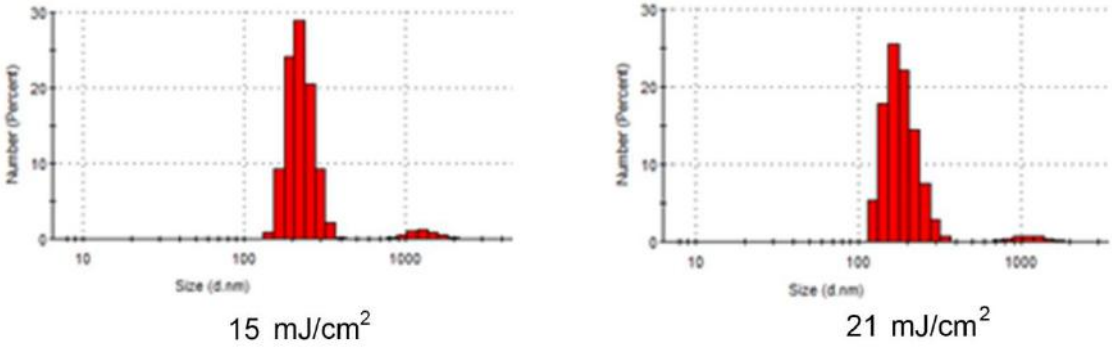

Fig. 1. Size distribution of GO after ablation at various laser radiation energy densities

SEM studies have shown (Fig. 2) that on the substrates GO dispersion forms a film consisting of both single-layer and multi-layer GO sheets. In multilayer particles, graphene oxide is prone to the formation of folds and wrinkles.

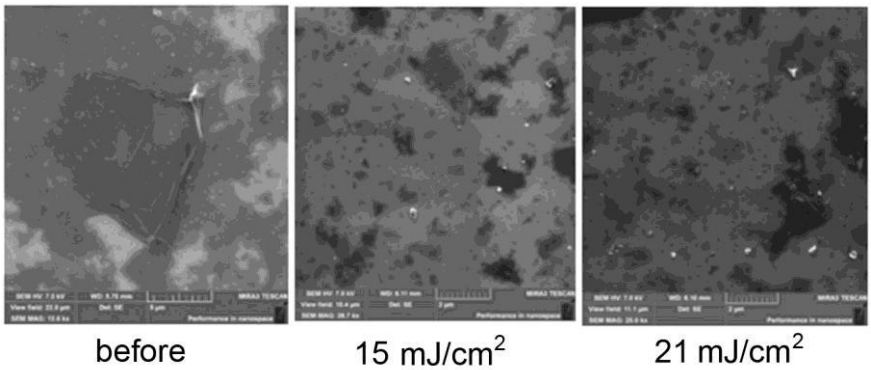

Fig. 2. SEM images of GO before and after ablation at various laser radiation energy densities

.

After laser processing, smaller particles are visualized on SEM images. At an energy density of 21 J/cm^2 the size of particles is smaller and they are uniformly distributed over the surface. The SEM data correlate well with the results obtained by dynamic light scattering, showing that the size distribution of graphene dots decreases with changing in the E from 15 to 21 mJ/cm^2.

It can be seen from the Raman spectroscopy data (table 1) that the maximum of the G-band of GO is shifted to higher frequencies compared to the band for graphene, which indicates the presence of C=O bonds in the structure of the GO sheet [25]. At the same time, the I_D/I_G ratio decreased markedly from 1.04 to 0.97 after ablation of the GO dispersion. A change in the radiation energy density has almost no effect on the change in its functionalization, as well as the ordering of the sp^2 domains inside the GO sheet.

Table 1. Position and intensity Raman bands of GO in dispersion after ablation at different laser radiation energy densities

	E, mJ/cm^2	D, cm^{-1}	I, r.u.	G, cm^{-1}	I, r.u.	I_D/I_G	2D, cm^{-1}	I, r.u.	I_{2D}/I_G
Before ablation	–	1360	18895	1602	18109	1.04	2734	11249	0.62
After ablation	15	1360	42482	1602	43738	0.97	2740	24413	0.56
	21	1368	26100	1602	27140	0.96	2740	15906	0.59

Studies of the optical properties of graphene dots showed (Fig. 3) that an increase in the energy density of laser radiation leads to a slight increase in the optical density (D) of GO at the maximum of the absorption band (~228 nm, Fig. 3a). It should be noted that, compared with the optical density of solutions before ablation, the value of D increased by almost 80%, which indicates an increase in the number of absorbing particles.

However, such an increase leads to the effect of self-quenching of the GO luminescence [26], which is clearly seen in Fig. 3b. Along with the luminescence band at 450 nm, additional band appears in the spectrum in the form of a shoulder with a maximum at about 600 nm. After laser treatment of the GO dispersion, the shape of the fluorescence spectrum changes and exhibits only one maximum at 490 nm. As it was shown by the recorded excitation spectra, the deformation of the GO luminescence band in dispersions before ablation is associated with the presence of several luminescence centers, because the curve shows maxima at 340 and 370 nm.

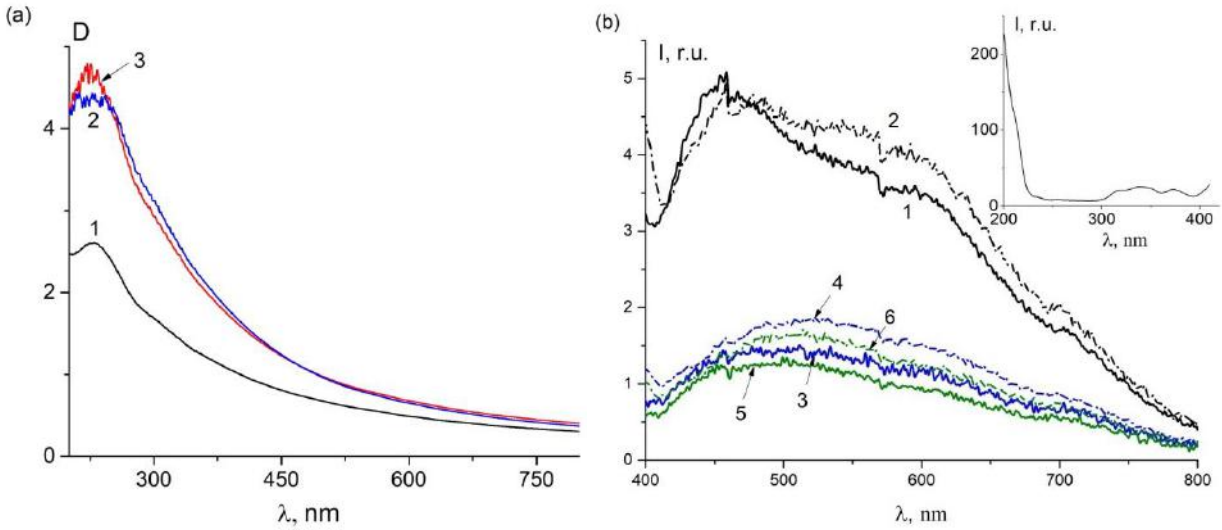

Fig. 3. Absorption (a) and fluorescence (b) spectra of GO before and after ablation at different laser energy densities E, mJ/cm^2: 1 – 0; 2 – 15; 3 – 2. Fluorescence spectra were recorded at λ_{exc}=320 nm – 1, 3, 5; λ_{exc}=350 nm – 2, 4, 6. On the inset: excitation spectra of GO before ablation at λ_{reg}=480 nm.

Figure 3b shows that as the excitation wavelength increases, the GO fluorescence spectra shift bathochromically and have different intensities. This may be due to the luminescence of various centers or the localization of electron-hole pairs in isolated sp^2 clusters in the sp^3 matrix. After ablation, the particles become more uniform both in size and composition. In this case the shape of the band does not change upon

the changing in the power density of laser irradiation, and the intensity of the fluorescence GO is only on 10% higher for dots, prepared at 21 mJ/cm^2 compared to 15 J/cm^2.

The lifetimes estimated from the fluorescence decay kinetics are presented in table 2. The decay kinetics can be described with using a biexponential equation with different contributions from the first and second components.

However, as can be seen from the data, the presence of a long-lived component has almost no effect on $<\tau>$ the average GO fluorescence lifetime. At the same time, the fluorescence lifetimes of GO particles after ablation slightly decreased, however, they are the same when λ_{reg} was changed.

Table 1. Fluorescence lifetimes of GO ablated at different laser energy densities

λ_{reg}, nm	$<\tau>$, ns	τ_1, ns	σ_1, %	τ_2, ns	σ_2, %
Before ablation					
450	0.36	0.26	92	1.55	8
511	0.34	0.30	96	1.40	4
21 mJ/cm^2					
450	0.34	0.26	94	1.57	6
511	0.31	0.28	97	1.18	3
15 mJ/cm^2					
450	0.32	0.28	92	1.13	8
511	0.32	0.28	97	1.57	3

Conclusion

The studies performed have shown that an increase in the energy density of laser radiation leads to a decrease in the size of graphene oxide particles after ablation. At the same time, no noticeable changes in the morphology and structure of the particles were registered.

A slight increase in both the optical density and fluorescence intensity was registered for graphene oxide dots obtained at 21 mJ/cm^2, relative to these parameters recorded for dots that were synthesized at 15 mJ/cm^2. In this case, the distribution of particles becomes more uniform, as evidenced by both the change in the shape of the GO luminescence band and the constancy of the fluorescence lifetime upon registration at different λ_{reg}.

The results obtained can be used to create organic luminescent materials, in optical nanotechnologies, as well as in photovoltaics, biophysics, and bioimaging.

Acknowledgments

This work was carried out as part of the research project AP08052672,
funded by the Ministry of Education and Science of the Republic of Kazakhstan.

REFERENCES

1 Kim H.J., Bang I.C., Onoe J. Characteristic stability of bare Au-water nanofluids fabricated by pulsed laser ablation in liquids, *Opt. Lasers Eng*. 2009, Vol. 47, pp. 532–8.

2 Ganeev R.A, Baba M., Ryasnyansky A.I., Suzuki M., Kuroda H. Characterization of optical and nonlinear optical properties ofsilver nanoparticles prepared by laser ablation in various liquids. *Opt. Commun.* 2004, Vol. 240, pp. 437–48.

3 Moniri S., Ghoranneviss M., Hantehzadeh M.R., Asadabad M.A. Synthesis and optical characterization of copper nanoparticlesprepared by laser ablation, *Bull. Mat. Sci*. 2017, Vol. 40, pp. 37–43.

4 Atiaf K.J., Abbas Q.A. Synthesis of graphene oxide nanoparticles by laser ablation system. *Iraqi J. Sci*. 2020, Vol. 61(9), pp. 2241–2250.

5 Dell'Aglio M., Gaudiuso R., De Pascale O., De Giacomo A. Mechanisms and processes of pulsed laser ablation in liquids duringnanoparticle production. *Appl. Surf. Sci.* 2015, Vol. 348, pp. 4–9.

6 Amendola V., Meneghetti M. Laser ablation synthesis in solution and size manipulation of noble metal nanoparticles. *Phys.Chem. Chem. Phys*. 2009, Vol. 11, pp. 3805–3821.

7 Kim S., Hwang S.W., Kim M., Shin D.Y., Shin D.H. Anomalous behaviors of visible luminescence from graphene quantum dots: interplay between size and shape. *ACS Nano*, 2012, Vol. 6, pp. 8203–8208.

8 Lin T.N., Chih K.H., Yuan C.T., Shen J.L., Lince C.A.J., Liud W.R. Laser-ablation production of graphene

.

oxide nanostructures: from ribbons to quantum dots. *Nanoscale*, 2015. Vol. 7, pp. 2708–2715.

9 Seliverstova E., Ibrayev N., Menshova E. Modification of structure and optical properties of graphene oxide dots, prepared by laser ablation method. *Fullerenes, Nanotubes, Carbon Nanostruct*., 2022, Vol. 30(1), pp.119-125.

10 Seliverstova E., Ibrayev N., Menshova E., Alikhaidarova E. Laser modification of structure and optical properties of N-doped graphene oxide. *Mater. Res. Express*, 2021, Vol. 8(11), pp. 115601(1-5).

11 Zhu S., Song Y., Zhao X., Shao J., Zhang J., Yang B. The photoluminescence mechanism in carbon dots (graphene quantum dots, carbon nanodots, and polymer dots): current state and future perspective. *Nano Res.*, 2015, No. 2, pp. 355–381.

12 Ganash E.A., Al-Jabarti G.A., Altuwirqi R.M. The synthesis of carbon-based nanomaterials by pulsed laser ablation in water. *Mater. Res. Express*, 2019, No. 1, pp. P. 015002 (1–10).

13 Hoffman J., Chrzanowska J., Kucharski S., Moscicki T., Mihailescu I.N., Ristoscu C., Szymanski Z. The effect of laser wavelength on the ablation rate of carbon. *Appl. Phys. A*, 2014, Vol. 117, pp. 395–400.

14 Hoffman J. The effect of recoil pressure in the ablation of polycrystalline graphite by a nanosecond laser pulse. *J. Phys. D: Appl. Phys*., 2015, Vol. 48, pp. 235201 (1–8).

15 Ibrayev N.Kh., Dzhanabekova R.Kh., Amanzholova G.S. Spectral and luminescent properties of carbon quantum dots functionalized with N- and S-contaning groups. *Euras. Phys. Tech. J*., 2021, Vol. 18, No.2(36), pp. 12-17.

16 Wang D.H., Choi D.W., Li J., Yang Z.G., Nie Z.M., Kou R. Self-assembled TiO_2-graphene hybrid nanostructures for enhanced Li-Ion insertion, *ACS Nano*, 2009, Vol. 3, pp. 907–914.

17 Wang X., Zhi L., Muellen K. Transparent, conductive graphene electrodes for dye-sensitized solar cells, *Nano Lett*., 2008, Vol. 8, pp. 323–327.

18 Ng Y.H., Lightcap I.V., Goodwin K., Matsumura M., Kamat P.V. To what extent do graphene scaffolds improve the photovoltaic and photocatalytic response of TiO_2 nanostructured films. *J. Phys. Chem. Lett*., 2010, Vol. 15, pp. 2222–2227.

19 Li Q., Guo B.D., Yu J.G., Ran J.R., Zhang B.H., Yan H.J., Gong J.R. Highly efficient visible-light-driven photocatalytic hydrogen production of CdS-cluster-decorated graphene nanosheets. *J. Am. Chem. Soc*., 2011, Vol. 133, pp. 10878–10884.

20 Ozer L.Y., Garlisi C., Oladipo H., Pagliaro M., Sharief S.A., Yusuf A., Almheiri S., Palmisano G. Inorganic semiconductors-graphene composites in photo(electro)catalysis: synthetic strategies, interaction mechanisms and applications. *J. Photochem. Photobiol. C*, 2007, Vol. 33, pp. 132–164.

21 Zhang Z., Wang C., Zakaria R., Ying Y. Role of particle size in nanocrystalline TiO_2–based photocatalysts. *J. Phys. Chem.: B*, 1998, Vol. 102, pp. 10871–10878.

22 Dubey P.K., Tripathi P., Tiwari R.S., Sinha A.S.K., Srivastava O.N. Synthesis of reduced graphene oxide-TiO2 nanoparticle composite systems and its application in hydrogen production. *Int. J. Hydrogen Energ*., 2014, Vol. 39, pp. 16282–16292.

23 Thakur K., Kandasubramanian B. Graphene and graphene oxide-based composites for removal of organic pollutants: a review. *J. Chem. Engineer. Data*, 2019, Vol. 64(3), pp. 833-867.

24 Zhumabekov A.Zh., Ibrayev N.Kh., Seliverstova E.V. Investigation of photocatalytic activity of TiO_2–GO nanocomposite. *Euras. Phys. Tech. J*., 2019, Vol. 16, No. 1, pp. 42–46.

25 Jorio A., Dresselhans M., Saito R., Dresselhaus G.F. *Raman spectroscopy in graphene related systems*. Verlag: Wiley-VCH, 2011, 356 p.

26 Parker C. *Photoluminescence of solutions*. Mir, 1972, 510 p. [In Russian]

Article accepted for publication 28.04.2022

DOI 10.31489/2022No2/35-41

UDC 538.9; 535.215; 539.23; 535.3

EFFECT OF ALCOHOL SOLVENTS ON THE STRUCTURAL, OPTICAL AND ELECTRICAL CHARACTERISTICS OF PEDOT:PSS POLYMER FILMS ANNEALED AT LOW ATMOSPHERIC PRESSURE

Aimukhanov A.K.[1], Rozhkova X.S.[1*], Ilyassov B.R.[2], Omarbekova G.I.[1], Seisembekova T.E.[1]

[1]Scientific Center for Nanotechnology and Functional Nanomaterials, Buketov University, Karaganda, Kazakhstan, ksusharogovaya@mail.ru
[2]Astana IT University, Nur-Sultan, Kazakhstan

The paper presents the results of a study of the effect of alcohol solvents on the surface structure, optical and electrical characteristics of a Poly(3,4-ethylenedioxythiophene) polystyrene sulfonate films annealed at a low atmospheric pressure of 10^{-3} millimeters of mercury. It has been found that the modification of the surface of a polymer film with ethyl and isopropyl alcohols leads to a change in the surface morphology, optical and electrical transport properties of the polymer. It is shown that when the Poly(3,4-ethylenedioxythiophene) polystyrene sulfonate film is modified with alcohol solvents, the absorption spectra show a decrease in the absorption of the polystyrene sulfonate aromatic fragment. It is shown that the structural features of the Poly(3,4-ethylenedioxythiophene) polystyrene sulfonate surface morphology affect the electrical transport parameters of films, such as the resistance of the Poly(3,4-ethylenedioxythiophene) polystyrene sulfonate film, the charge carrier transfer resistance at the Poly(3,4-ethylenedioxythiophene) polystyrene sulfonate/electrode interface, the effective extraction rate, and the effective time of flight of charge carriers. The optimal technological parameters for the production of films have been determined, at which the electrical transport properties of Poly(3,4-ethylenedioxythiophene) polystyrene sulfonate films annealed at low atmospheric pressure increase.

Keywords: PEDOT:PSS, Izopropanol, Ethanol, low atmospheric pressure, surface morphology, optical spectroscopy, impedance spectroscopy

Introduction

PEDOT:PSS is traditionally used as a hole transport layer in organic solar cells (OSC) due to its high transparency in the visible light range, good film formation during dissolution, and high work function [1,2]. The properties of the PEDOT:PSS layer can definitely affect the performance of the OSC. It can be used as a potential alternative to both traditional solid substrate electrodes such as conductive electrode (ITO, FTO) and metal electrodes (Au, Pt, Cu, etc.) [3-4].

However, defects of microstructure in the PEDOT:PSS film morphology can lead to inefficient hole transport within the PEDOT:PSS layer [5-8], causing unbalanced charge carrier transport, which ultimately results in low FF and high current leakage [9-12]. Thus, the uniformity of the PEDOT:PSS layer is important for PSC performance.

Currently, there are several methods for improving the electrical and optical properties of a PEDOT:PSS film: post-processing, doping and creating composites [5]. One of the main ways to improve the conductivity of PEDOT:PSS is the addition of organic solvents, including alcohol ones [13–17]. It is known that solvents affect the conductivity and structure of the film [18, 19], however, in the works of the authors, due attention is not paid to the processes of generation and transport of charge carriers in films of the modified PEDOT:PSS.

Previously, we studied the effect of modification of the structure of the PEDOT:PSS polymer with hole conductivity on the optical, electrical transport and photovoltaic properties of an organic solar cell based on a P3HT:PC60BM bulk heterojunction [20]. It was shown that thermal treatment with the addition of isopropyl alcohol to the PEDOT:PSS polymer solution leads to a change in the structural and optical properties of the films. It has been established that the efficiency of charge

.

carrier transfer and the efficiency of a polymer solar cell depend on the structural features of PEDOT:PSS.

Thus, it can be noted that studies on the effect of structural changes in the PEDOT:PSS polymer on its morphological, optical and electrical transport parameters remain relevant.

In this work, we will investigate the effect of modification of a conductive PEDOT:PSS polymer with organic alcohol solvents on the morphological, optical and electrical transport characteristics of a PEDOT:PSS polymer with hole conductivity annealed at low atmospheric pressure.

1. Experimental

We used PEDOT:PSS (1%, Ossila Al4083), Izopropanol, Ethanol (pure 99.9% Sigma Aldrich). To change the surface morphology, the PEDOT:PSS hole-conducting polymer was diluted with a certain concentration of alcohol (ethyl, isopropyl), placed in a vacuum furnace (YHCHEM, Shanghai Yuanhuai Industrial Co) and annealed at 120°C for 10 minutes. A comparative analysis of the modified PEDOT:PSS film was carried out by comparing the structure of the surface morphology, optical and electrical properties. The structural formulas of the compounds are shown in Figure 1. The preparation of the substrates was carried out according to the procedure [21]. Before starting the experiments, the PEDOT:PSS solution was filtered through a 0.45 micrometer filter. PEDOT:PSS films were obtained on the surface of quartz glass by centrifugation (on a SPIN150i centrifuge manufactured by Semiconductor Production System) at a rotation speed of 5000 rpm.

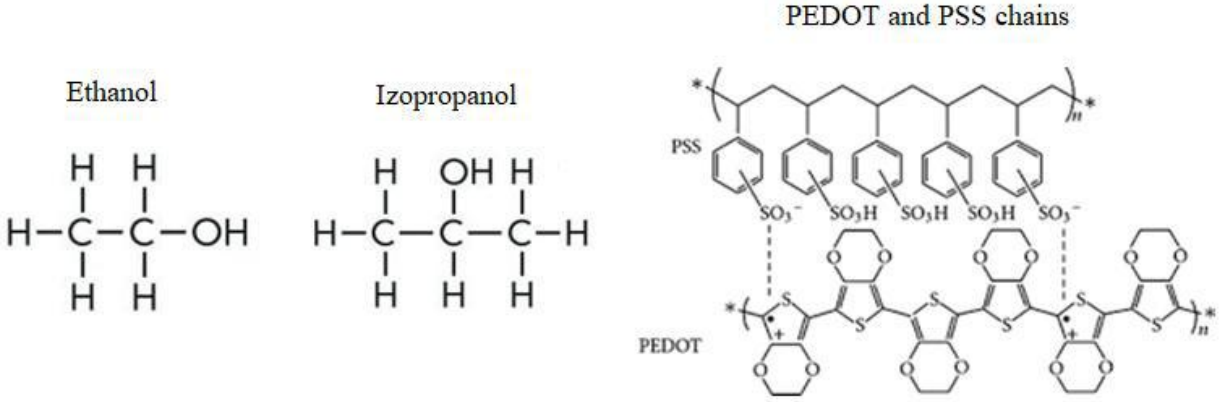

Fig. 1. Chemical structure of Ethanol, Izopropanol, PEDOT and PSS

The surface topography of the samples was studied using a high-resolution atomic force microscope (AFM) JSPM-5400 (JEOL, Japan). The AFM images were processed using a special modular program for analyzing scanning probe microscopy data (Win SPMII Data-Processing Software). The surface morphology and roughness of PEDOT:PSS thin films were analyzed from AFM images. The images of the surface of the PEDOT:PSS films were obtained in the mode of the semicontact scanning method. The absorption spectra of the studied samples were recorded on an AvaSpec-ULS2048CL-EVO spectrometer manufactured by Avantes, which records absorption spectra in the range of 200-1100 nm and has an optical resolution of 0.04 nm. The impedance spectra were measured using a measuring system P-45X (Elins) with an additionally installed FRA-24M frequency analyzer module. Fitting and analysis of the spectrum parameters were carried out using the EIS-analyzer software package, according to the procedure [22].

2. Results and Discussion

Images of the surface morphology of PEDOT:PSS films with different ratios of ethyl and isopropyl alcohols are shown in Figure 2. Table 1 shows the roughness values of PEDOT:PSS films. Figure 2 shows that the PEDOT:PSS film without the addition of alcohols after thermal annealing has a rather pronounced relief. In this case, the surface morphology has a pronounced heterogeneity, the surface roughness is 0.64 nm. In a PEDOT:PSS film prepared in ethanol in a ratio of 80% PEDOT:PSS/20% ethanol, after thermal annealing at a temperature of 120°C, a decrease in surface roughness to a value of 0.58 nm is observed. A further increase in the concentration of alcohol in a ratio of 70% PEDOT:PSS/30% ethanol leads to a reduction in the surface roughness of the film to 0.54 nm. At a ratio of 50% PEDOT:PSS/50% ethanol, the surface roughness of the film is reduced to a value of 0.45 nm.

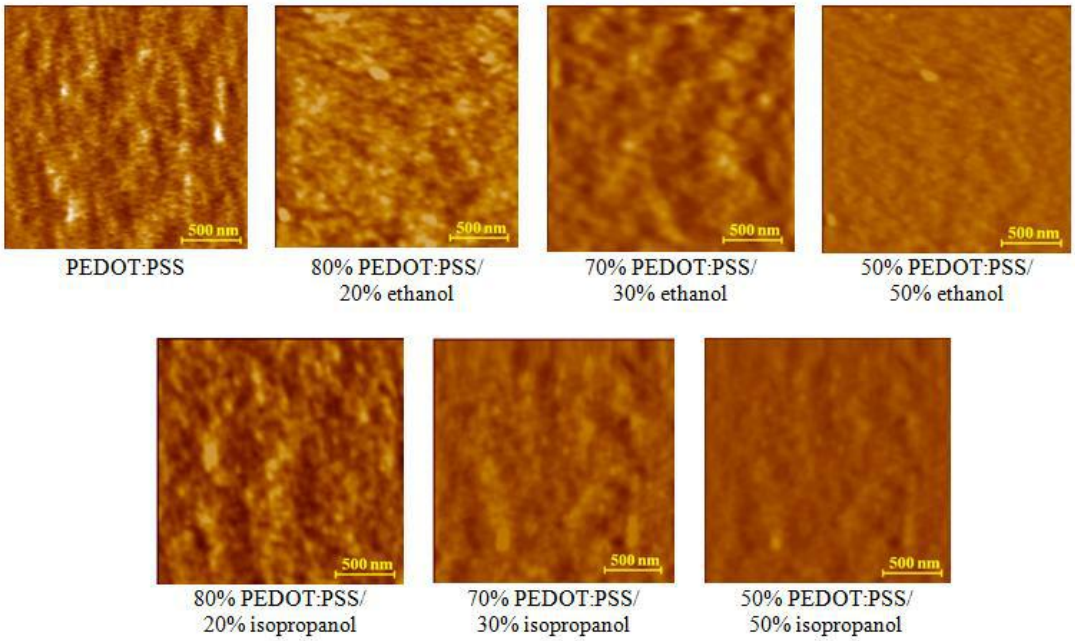

Fig. 2. Surface morphology images of PEDOT:PSS films

For a qualitative analysis of studies, the effect of the ratio of isopropyl alcohol on the morphology of the PEDOT:PSS polymer was studied. From the obtained results it can be seen that the roughness of the PEDOT:PSS film in a ratio of 80% PEDOT:PSS/20% isopropanol was 0.54 nm. This value is not very different from the roughness value obtained for ethyl alcohol. At a ratio of 70% PEDOT:PSS/30% isopropanol, the film roughness also decreases to a value of 0.49 nm. Increasing the proportion of isopropyl alcohol to 50% in the film resulted in smoothing of the film surface with a roughness of 0.43 nm. Comparative analysis of changes in surface roughness showed that in the process of film preparation with the addition of various concentrations of ethyl alcohol, the surface roughness decreases by 1.4 times, and isopropyl alcohol by 1.5 times.

Table 1. Surface roughness of PEDOT:PSS films with different concentrations of alcohols

Sample	R_a, nm
PEDOT:PSS	0.64
80% PEDOT:PSS/20% ethanol	0.58
70% PEDOT:PSS/30% ethanol	0.54
50% PEDOT:PSS/50% ethanol	0.45
80% PEDOT:PSS/20% isopropanol	0.54
70% PEDOT:PSS/30% isopropanol	0.49
50% PEDOT:PSS/50% isopropanol	0.43

.

Figure 3 shows the absorption spectra of PEDOT:PSS films with different ratios of ethyl and isopropyl alcohol, annealed at low atmospheric pressure at T=120C°. It can be seen from the figure that the initial PEDOT:PSS film has a maximum at a wavelength of λ_1 = 214 nm with a spectral half-width of 10.2 nm. In the absorption spectra of all films, a shoulder λ_2 is observed with a maximum at 227 nm, which is associated with the absorption of the PSS - poly(styrenesulfonate) [20,23]. When ethyl alcohol is added to the film during preparation, the positions of the maxima in the absorption spectra do not change, only a decrease in the optical density values and a decrease in the half-width are observed (Figure 3a). The value of the maximum at a wavelength of 214 nm decreased by 1.2 times, and at a wavelength of 227 nm - by 1.6 times.

The absorption spectra of PEDOT:PSS films annealed at T=120C° with different ratios of isopropyl alcohol are shown in Figure 3b. A comparison of the shapes and positions of the absorption spectra maxima of films with isopropyl and ethyl alcohol showed no visible changes. The half-width of the absorption spectrum remained within the same range as for ethyl alcohol. The values of the optical density at the absorption maxima decrease. The value of the maximum at a wavelength of 214 nm decreased by a factor of 1.7, and at a wavelength of 227 nm, by a factor of 2.2. Table 2 lists the characteristics of the absorption spectra of PEDOT:PSS films prepared with various concentrations of alcohol solvents and annealed at low atmospheric pressure.

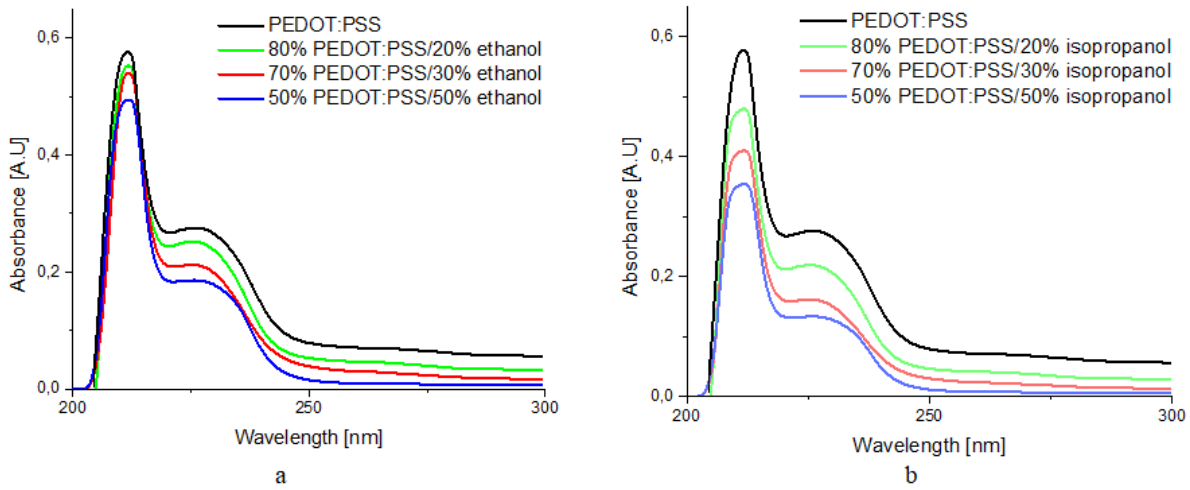

Fig. 3. The absorption spectra of PEDOT:PSS/ethanol (a) and PEDOT:PSS/isopropanol (b) films

It should be noted that a comparative analysis of the change in the values of optical density at the absorption maxima of the films shows that for isopropyl alcohol a greater decrease in absorption is observed than for ethyl alcohol.

Table 2. Characteristics of absorption spectra of PEDOT:PSS films

Sample	Absorption peaks		D_1	D_2	FWHM, nm
	λ_1, nm	λ_2, nm			
PEDOT:PSS	214	227	0.58	0.28	10.2
Ethanol					
80% PEDOT:PSS/20% ethanol	214	227	0.55	0.25	9.5
70% PEDOT:PSS/30% ethanol	214	227	0.54	0.21	9.1
50% PEDOT:PSS/50% ethanol	214	227	0.49	0.18	8.5
Isopropanol					
80% PEDOT:PSS/20% isopropanol	214	227	0.48	0.22	10.1
70% PEDOT:PSS/30% isopropanol	214	227	0.41	0.16	10.1
50% PEDOT:PSS/50% isopropanol	214	227	0.35	0.13	9.7

Next, using the method of impedance spectroscopy, we studied the effect of modification of the PEDOT:PSS structure annealed at low atmospheric pressure with alcohol solvents on the parameters of charge carrier transport in the cells of the ITO/PEDOT:PSS/Al structure. The analysis of the results was carried out according to the diffusion-recombination model with an equivalent chain, shown in Figure 4a [24]. Here R_1 is the PEDOT:PSS film resistance, R_2 is the charge carrier transfer resistance at the PEDOT:PSS/Al interface, CPE is a constant phase element, is an equivalent electrical circuit component that simulates the behavior of a double layer, but is an imperfect capacitor. From the impedance spectra, the main electrical transport parameters were calculated (Table 3), where: R_h and R_{ext} correspond to R_1 and R_2, τ_{eff} is the effective transit time through PEDOT:PSS, k_{eff} is the effective charge carrier extraction rate from PEDOT:PSS. The scheme of charge transport in the ITO/PEDOT:PSS/Al cell is shown in Figure 4b.

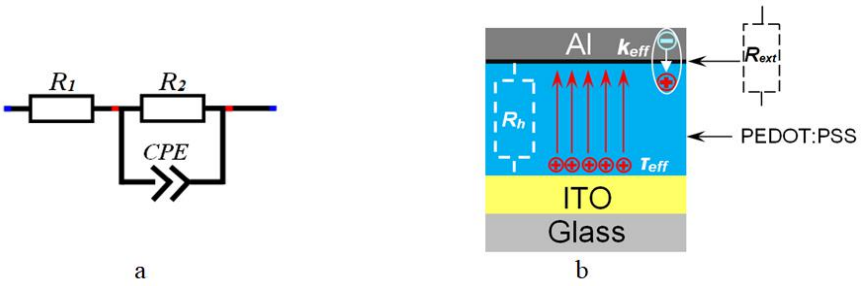

Fig. 4. Equivalent electrical circuit (a) and circuit of charge transport in the cell (b)

The impedance spectra of PEDOT:PSS films with different concentrations of alcohol solvents annealed at low atmospheric pressure are shown in Figure 5. Table 3 shows the values of the electrical transport parameters of the films. As can be seen from Table 3, the modification of PEDOT:PSS with organic solvents affects the transport of charge carriers in PEDOT:PSS. Table 3 shows that cells based on films obtained from solutions with alcohol solvents have better electrical transport properties compared to the original PEDOT:PSS film. The best transport parameters are achieved with a maximum concentration of 50% alcohol solvent. The addition of ethanol significantly reduces the resistance of the PEDOT:PSS (R_h) film by a maximum of 1.8 times and the resistance of the PEDOT:PSS/Al (R_{ext}) interface by a factor of 3.8, which increases the efficiency of hole transport from ITO to Al through PEDOT:PSS. However, when using isopropyl alcohol, the decrease in R_h and R_{ext} is more significant: R_h decreased by 2.7 times, while R_{ext} by 4.2 times compared to the original PEDOT:PSS.

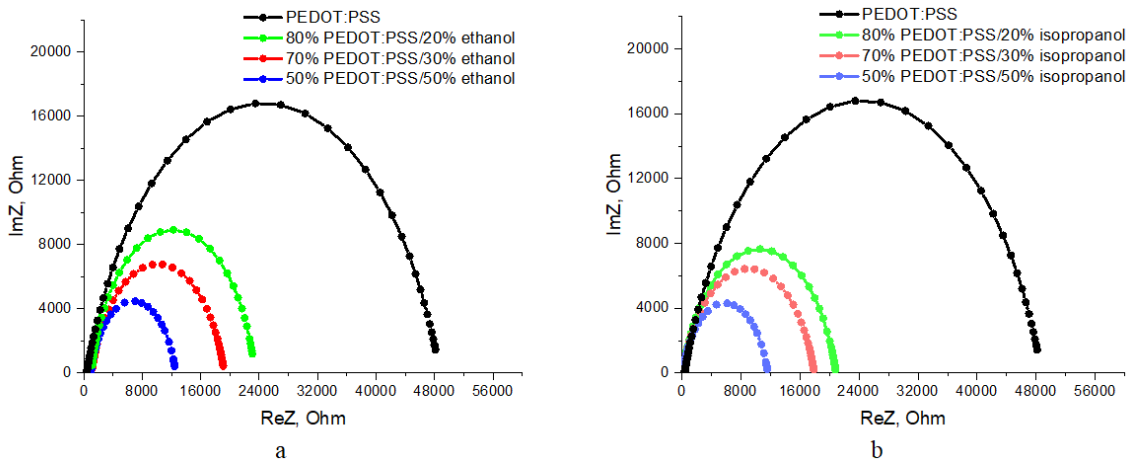

Fig.5. The impedance spectra of PEDOT:PSS/ethanol (a) and PEDOT:PSS/isopropanol (b) films

The values k_{eff} and τ_{eff} characterize the efficiency of carrier extraction with PEDOT:PSS and the effective charge transit time in PEDOT:PSS. As can be seen from Table 3, the addition of ethyl and isopropyl alcohol to PEDOT:PSS has a noticeable positive dynamic in k_{eff} and τ_{eff}. However, the best results are shown by films prepared with the addition of isopropyl alcohol.

Effective charge carrier extraction rate from PEDOT:PSS films obtained from a solution with isopropyl alcohol increased by more than three times, and the effective transit time decreased inversely. Holes injected into PEDOT:PSS diffuse to the electrode where they recombine with electrons. Fast transport of injected holes to the outer electrode is very important, since this reduces the probability of their reverse recombination. In our case, fast hole transport is provided by improving the structure of PEDOT:PSS after adding isopropyl alcohol to the initial solution, which leads to an improvement in the quality of the PEDOT:PSS/ITO interface [20].

Table 3. Electrical transport parameters of PEDOT:PSS films annealed at low atmospheric pressure

Sample	R_h, Ω	R_{ext}, Ω	k_{eff}, s^{-1}	τ_{eff}, ms
PEDOT:PSS	268.7	48745	157.5	6.4
Ethanol				
80% PEDOT:PSS/20% ethanol	248.3	23854	259.4	3.9
70% PEDOT:PSS/30% ethanol	204.7	19887	348.1	2.9
50% PEDOT:PSS/50% ethanol	148.5	12769	425.1	2.4
Isopropanol				
80% PEDOT:PSS/20% isopropanol	197.8	21748	357.2	2.8
70% PEDOT:PSS/30% isopropanol	104.2	18374	483.9	2.1
50% PEDOT:PSS/50% isopropanol	98.5	11478	601.8	1.7

Conclusions

An analysis of the experiments showed that the addition of an alcohol solvent affects the surface structure of PEDOT:PSS films annealed at low atmospheric pressure, which, in turn, affects the process of charge carrier transport. It has been found that the addition of alcohol to the PEDOT:PSS polymer leads to a decrease in surface roughness. Upon modification of the PEDOT:PSS surface, a decrease in the absorption of the PSS aromatic fragment is observed in the absorption spectra. It is shown that changes in the structure and morphology of the PEDOT:PSS surface affect the electrical transport parameters of the films. It has been found that the surface of the PEDOT:PSS film annealed at low atmospheric pressure and modified in isopropyl alcohol has the lowest resistance parameters R_h and R_{ext} and the highest k_{eff}, at which, due to the change in the PEDOT:PSS surface structure, the fastest charge carriers transport is ensured.

Solar cells based on modified PEDOT:PSS films, as a rule, have lower resistance values compared to the original films, which is due to the faster transport of injected holes to the outer electrode. Thus, this study showed the possibility of optimizing the electrical transport parameters of solar cells by modifying the PEDOT:PSS hole-transport layer.The electrical transport characteristics of the modified PEDOT polymer can be used in the development of organic light-emitting devices and photoconverters.

Acknowledgments

This research is funded by the Science Committee of the Ministry of Education and Science of the Republic of Kazakhstan (Grant № AP08856176).

REFERENCES

1 Anrango-Camacho C., Pavón-Ipiales K., Frontana-Uribe B.A., Palma-Cando A. Recent Advances in Hole-Transporting Layers for Organic Solar Cells. *Nanomaterials*, 2022, Vol. 12, No 443, pp. 1-54. DOI:10.3390/nano12030443.

2 Wen Y., Xu J. Scientific Importance of Water-Processable PEDOT–PSS and Preparation, Challenge and New Application in Sensors of Its Film Electrode: A Review. *J. Pol. Sci. Part A: Pol. Chem.*. 2017, Vol. 55, pp.1121-1150. doi: 10.1002/pola.28482.

3 Roh E., Hwang B.U., Kim D., Kim B.Y., Lee N.E. Stretchable, Transparent, Ultrasensitive, and Patchable Strain Sensor for Human-Machine Interfaces Comprising a Nanohybrid of Carbon Nanotubes and Conductive Elastomers. *ACS Nano*, 2015, Vol. 9, pp. 6252-6261. doi:10.1021/acsnano.5b01613

4 Choong C.L., Shim M.B., Lee B.S., Jeon S., et al. Highly Stretchable Resistive Pressure Sensors Using a Conductive Elastomeric Composite on a Micropyramid Array. *Adv. Mat.*, 2014, Vol.26, Is.21, pp. 3451–3458. doi:10.1002/adma.201305182.

5 Xia Y., Dai S. Review on applications of PEDOTs and PEDOT:PSS in perovskite solar cells. *J. Mater. Sci. Mater. Electron*, 2021, Vol. 32, pp. 12746-12757. doi:10.1007/s10854-020-03473-w.

6. Ouyang J., Chu C.W., Chen F.C., Xu Q., Yang Y. High-conductivity poly(3,4-ethylenedioxythiophene):poly(styrene sulfonate) film and its application in polymer optoelectronic devices. *Adv. Funct. Mater.,* 2005, Vol.15, Is.2, pp. 203-208. doi: 10.1002/adfm.200400016.

7. Lim F.J., Ananthanarayanan K., Luther J., Ho G.W. Influence of a novel fluorosurfactant modified PEDOT:PSS hole transport layer on the performance of inverted organic solar cells. *J. Mater. Chem*., 2012, Vol. 22, pp. 25057-25064. doi: 10.1039/C2JM35646E.

8. Mihailetchi V.D., Duren J.K.V., Blom P.W., Hummelen J.C., et al. Electron transport in a methanofullerene. *Adv. Funct. Mater.,* 2003, Vol. 13, Iss. 1, pp. 43-46. doi:10.1002/adfm.200390004.

9 Lee D.Y., Na S.I., Kim S.S. Graphene oxide/PEDOT:PSS composite hole transport layer for effcient and stable planar heterojunction perovskite solar cells. *Nanoscale*, 2016, 8, pp. 1513-1522. doi:10.1039/C5NR05271H.

10 Giuri A., Masi S., Colella S., Kovtun A., Dell'Elce S., et al. Cooperative Effect of GO and Glucose on PEDOT:PSS for High V_{OC} and Hysteresis-Free Solution-Processed Perovskite Solar Cells. *Adv. Funct. Mater*., 2016, Vol. 26, Is. 38, pp. 6985-6994. doi:10.1002/adfm.201603023.

11 Huang D., Goh T., Kong J., Zheng Y., Zhao S., Xu Z., Taylor A. Perovskite solar cells with a DMSO-treated PEDOT:PSS hole transport layer exhibit higher photovoltaic performance and enhanced durability. *Nanoscale*, 2017, Vol. 9, pp. 4236-4243. doi:10.1039/C6NR08375G.

12 Hu L., Sun K., Wang M., Chen W., et al. Inverted Planar Perovskite Solar Cells with a High Fill Factor and Negligible Hysteresis by the Dual Effect of NaCl-Doped PEDOT:PSS. *ACS Appl. Mater. Interfaces,* 2017, Vol. 9, Is. 50, pp. 43902-43909. doi:10.1021/acsami.7b14592.

13 Rwei S.P., Lee Y.H., Shiu J.W., Sasikumar R., Shyr U.T. Characterization of Solvent-Treated PEDOT:PSS Thin Films with Enhanced Conductivities. *Polymers,* 2019, Vol. 11, Is. 134, pp. 1-10. doi:10.3390/polym11010134.

14 Ouyang J. "Secondary doping" methods to significantly enhance the conductivity of PEDOT:PSS for its application as transparent electrode of optoelectronic devices. *Displays*, 2013, Vol. 34, Is. 5, pp. 423-436. DOI:10.1016/j.displa.2013.08.007

15 Shi H., Liu C.C., Jiang Q.L., Xu J.K. Effective approaches to improve the electrical conductivity of PEDOT:PSS: A review. *Adv. Electron. Mater.*, 2015, Vol. 1, Is.4, pp. 1500017. doi:10.1002/aelm.201500017

16 Xiong J., Jiang F., Zhou W., Liu C., Xu J. Highly electrical and thermoelectric properties of a PEDOT:PSS thin-film via direct dilution-filtration. *RSC Adv.*, 2015, Vol. 5, pp. 60708-60712. doi:10.1039/C5RA07820B.

17 Xia Y., Ouyang J. Anion effect on salt-induced conductivity enhancement of poly(3,4-ethylenedioxythiophene):poly(styrenesulfonate) films. *Org. Electron.*, 2010, Vol. 11, pp. 1129–1135. doi:10.1016/j.orgel.2010.04.007.

18 Namkoong G., Younes E.M., Abdel-Fattah T.M., El-Maghraby E.M, et al. Aging process of PEDOT:PSS dispersion and robust recovery of aged PEDOT:PSS as a hole transport layer for organic solar cells. *Org. Electron.*, 2015, Vol. 25, pp. 237-244. doi:10.1016/j.orgel.2015.06.049.

19 Jewłoszewicz B., Bogdanowicz K.A., Przybył W., et al. PEDOT:PSS in Water and Toluene for Organic Devices-Technical Approach. Polymers, 2020, Vol. 12, Is. 3, pp. 565 (1-19). doi:10.3390/polym12030565.

20 Aimukhanov A.K., Rozhkova X.S., Ilyassov B.R., Zeinidenov A.K., Nuraje N. The influence of structural and charge transport properties of PEDOT:PSS layers on the photovoltaic properties of polymer solar cells, *Polym. Adv. Technol*., 2021, Vol. 32, pp. 49-504. doi:10.1002/pat.5102.

21 Kim K., Ihm K., Kim B. Surface property of indium tin oxide (ITO) after various methods of cleaning. *Acta Phys. Pol. A*, 2015, Vol. 127, No. 4, pp. 1176-1179. doi:10.12693/APhysPolA.127.1176.

22 Bisquert J., Mora-Sero I., Fabregat-Santiago F. Diffusion-recombination impedance model for solar cells with disorder and nonlinear recombination. *ChemElectroChem*, 2014, Vol. 1, Is. 1, pp. 1-9. doi:10.1002/celc.201300091.

23 Xia Y, Sun K, Ouyang J. Highly conductive poly(3,4-ethylenedioxythiophene):Poly(styrene sulfonate) films treated with an amphiphilic fluoro compound as the transparent electrode of polymer solar cells. *Energy Environ. Sci*., 2012, Vol. 5, Is. 1, pp. 5325-5332. doi:10.1039/c1ee02475b.

24 Zeinidenov A.K., Abisheva A.K., Ilyassov B.R., Aimukhanov A.K., Abilmazhinov S.E. Influence of structural features of ZnO films on optical and photoelectric characteristics of inverted polymer solar elements. *Eurasian Phys. Tech. J.,* 2021, Vol.18, No.36, pp. 40-46. doi: 10.31489/2021No2/40-46.

Article accepted for publication 31.03.2022

.

DOI 10.31489/2022No2/42-47

UDC 621.386.8:385.592+537.226+537.226.1

ELECTROPHYSICAL PROPERTIES OF NEW NANOSTRUCTURED COPPER-ZINC MANGANITE OF LANTHANUM AND MAGNESIUM

Kasenov B.K.[1], Kasenova Sh.B.[1], Sagintaeva Zh.I.[1], Kuanyshbekov E.E.[1], Bekturganov Zh.S.[2], Zeinidenov A.K.[2]

[1]Abishev Chemical-Metallurgical Institute, Karaganda, Kazakhstan, kasenov1946@mail.ru
[2]E.A. Buketov Karaganda University, Karaganda, Kazakhstan

The polycrystalline copper-zinc manganite was synthesized by the solid-phase interaction in the range of 800-1200 °C of oxides of lanthanum (III), copper (II), zinc (II), manganese (III) and magnesium carbonate, thus its nanostructured particles were first obtained by grinding on the vibrating mill "Retsch" (Germany). The X-ray investigations determined that the nanostructured manganite is crystallized in the cubic syngony. On the LCR-7817/827 device (Company «Good Will Instrument Co., Ltd., Taiwan») in the range of 293-483 K at frequencies equal to 1.5 and 10 kHz, the dielectric constant and electrical resistance were investigated and it was found that this compound at 293-353 K has the semiconductor conductivity, at 353-373 K - metal and at 373-483 K - semiconductor conductivity again. The band gap widths were calculated. The permittivity at 483 K reaches gigantic values at all frequencies. Referring to the above, the objective of this paper is to study the temperature dependence of the dielectric constant and the electrical resistance of a new nanostructured copper-zinc manganite of lanthanum and magnesium.

Keywords: copper-zinc manganite, lanthanum, magnesium, nanostructured particles, electron microscopy, X-ray, electrophysics, semiconductor.

Introduction

Manganites of the rare-earth elements doped with oxides of alkaline-earth metals with effects of the giant and colossal magnetic resistance can be used in the magnetic field sensors, reading heads for the magnetic recording of high density and sensors of the moved temperature [1]. In addition, manganites can have the semiconductor, ferroelectric, radioluminescent and other properties [2-4]. It should also be noted that recently similar new compounds, based on nickelates of lanthanum and strontium, were obtained. They have the giant values of the dielectric constant, which are of interest as materials with the high values of working memory [5]. It should also be noted that these materials are not only promising, but in some cases used as electrodes for high-temperature fuel cells, catalysts for afterburning exhaust gases, oxygen membranes, thermistors, sensors [6]. Perovskites, which include oxides of manganese, rare earth and alkaline earth metals, are also of interest as an anode material for a solid oxide fuel cell [7]. Based on the foregoing, the study of the physicochemical properties of new analogous compounds has a certain scientific and practical interest.

1 Experimental technique

The starting materials to synthesize this compound were La_2O_3 ("puriss. spec."), ZnO, Mn_2O_3, $MgCO_3$ (qualification ("p.a.")), their stoichiometric amounts were thoroughly mixed, milled and annealed in the range of 800-1200 °C for 30 h. The mixture was cooled at 800 °C, 1000 °C and 1200 °C with the repeated mixing and milling. The low-temperature annealing was made at 400 °C for 10 h [8]. Then, on the vibration mill "Retsch" (Germany), the polycrystals of the formed alloy were ground to nanostructured particles, their sizes were determined on MJRA electron microscope, 3LMU Tescan (Fig.1). The X-ray phase analysis of nanostructured $LaMgCuZnMnO_6$ was performed on a diffractometer DRON-2,0 under conditions: CuK_α - radiation, U = 30 kV, J = 10 mA, rotation speed - 1000 pulses per second, time constant t = 5 sec, angle interval - 2θ from 10 to 90°.

The intensity of diffraction maxima was estimated on 100-point scale. The X-ray patterns were indicated by the analytical method [9]. The pycnometric density was determined according to [10]. Toluene

was used as the indifferent liquid. Figure 2 shows the diffractogram of the nanostructured $LaMgCuZnMnO_6$. Similarly, we synthesized copper-zinc manganites of lanthanum and alkali metals [11].

The study of the electrophysical properties (dielectric constant, electric resistance) was performed by the measuring of the electric capacity of a sample on LCR-7817/827 device with a basic error of 0.05% (Company «Good Will Instrument Co., Ltd., Taiwan ») at frequencies of 1, 5 and 10 kHz. The plan-parallel samples were previous made as discs (diameter - 10 mm, thickness - 1.3 mm) with a binder.

Pressing was performed at pressure of 20 kg/cm^3. The resulting discs were baked at temperature of 400 °C in SNOL furnace for 6 h. Further, their thorough double-sided grinding was made. The two-electrode system was used. The dielectric constant was determined from the electric capacitance. Sawyer-Tower circuit was used to obtain the dependence between the electric induction and electric field intensity [12].

The value of the dielectric constant (ε) was determined by the formula:

$$C = \varepsilon_0 \cdot \varepsilon \cdot S/h, \quad (1)$$

where ε_0 – is the electrical constant, S – is the area, h – is the thickness of the sample, C – is the electric capacitance. In its turn $\varepsilon = C \cdot h/\varepsilon_0 \cdot \varepsilon$; $\varepsilon_0 = 8.85 \cdot 10^{-12}$ Ф/м; $S = \pi \cdot d^2/4$.

The electrophysical investigations were tested by measuring of the dielectric constant (ε) of the standard $BaTiO_3$ at frequencies of 1 and 5 kHz and 293 K, equal to 1296 and 1220 and which were satisfactorily with its recommended value of 1400 ± 250 [12-15].

2 Results and discussion

As can be seen from Fig. 1 the nanostructured $LaMgCuZnMnO_6$ is characterized by the following particle sizes of 122.65, 138.43, 159.34, 162.02 and 214.90 nm. Referring to [16], if a nanoparticle has a complex shape and structure, then a linear size of a particle as a whole are not studied, but a size of its structural element is exanimated as characteristic. Such particles, as a rule, are called nanostructured, and their linear sizes can significantly exceed 100 nm [16].

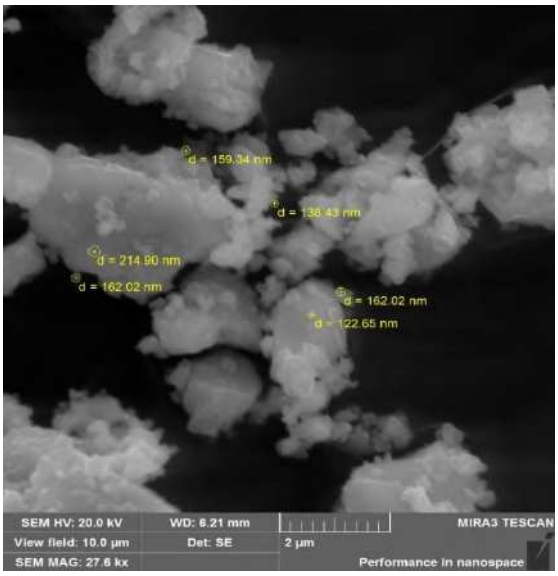

Fig. 1. The electron microscopy of the nanostructured $LaMgCuZnMnO_6$

Based on the results of the X-ray investigations, it was determined that the nanostructured $LaMgCuZnMnO_6$ crystallizes in the cubic syngony with the following lattice parameters: a = 13.53 ± 0.02 Å, V^o = 2476.81 ± 0.06 Å^3, Z = 4, $V^o_{elec.cell}$ = 619.20 ± 0.02 Å^3, $\rho_{roent.}$= 4.52; ρ_{pick} = 4.50 ± 0.01 g/cm^3 [8]. The correctness and reliability of the obtained results were confirmed by the satisfactory agreement of the experimental and calculated values of $10^4/d^2$, as well as a good coincidence of the X-ray and picnometer densities.

.

The investigation of the electrophysical properties of $LaMgCuZnMnO_6$ in the range of 293-483 K showed that its electrical resistance at transition from 293 K to 483 K decreases by 58.5 times (at 1 kHz), by 48 times (at 5 kHz) and by 39.6 times (at 10 kHz). This compound in the range of 293-353 K has the semiconductor conductivity, at 353-373 K - metallic and at 373-483 K - semiconductor conductivity again. Calculations of the gap width showed that they in the range of 293-353 K are 0.83 eV, and at 373-483 K - 0.80 eV, and this material can be attributed to the narrow-probe semiconductors. There is also a decrease in the electrical resistance with an increase in frequency from 1 to 10 kHz. Table and Figure 2 show the results of measurement of the dielectric constant and electrical resistance of nanostructured $LaMgCuZnMnO_6$.

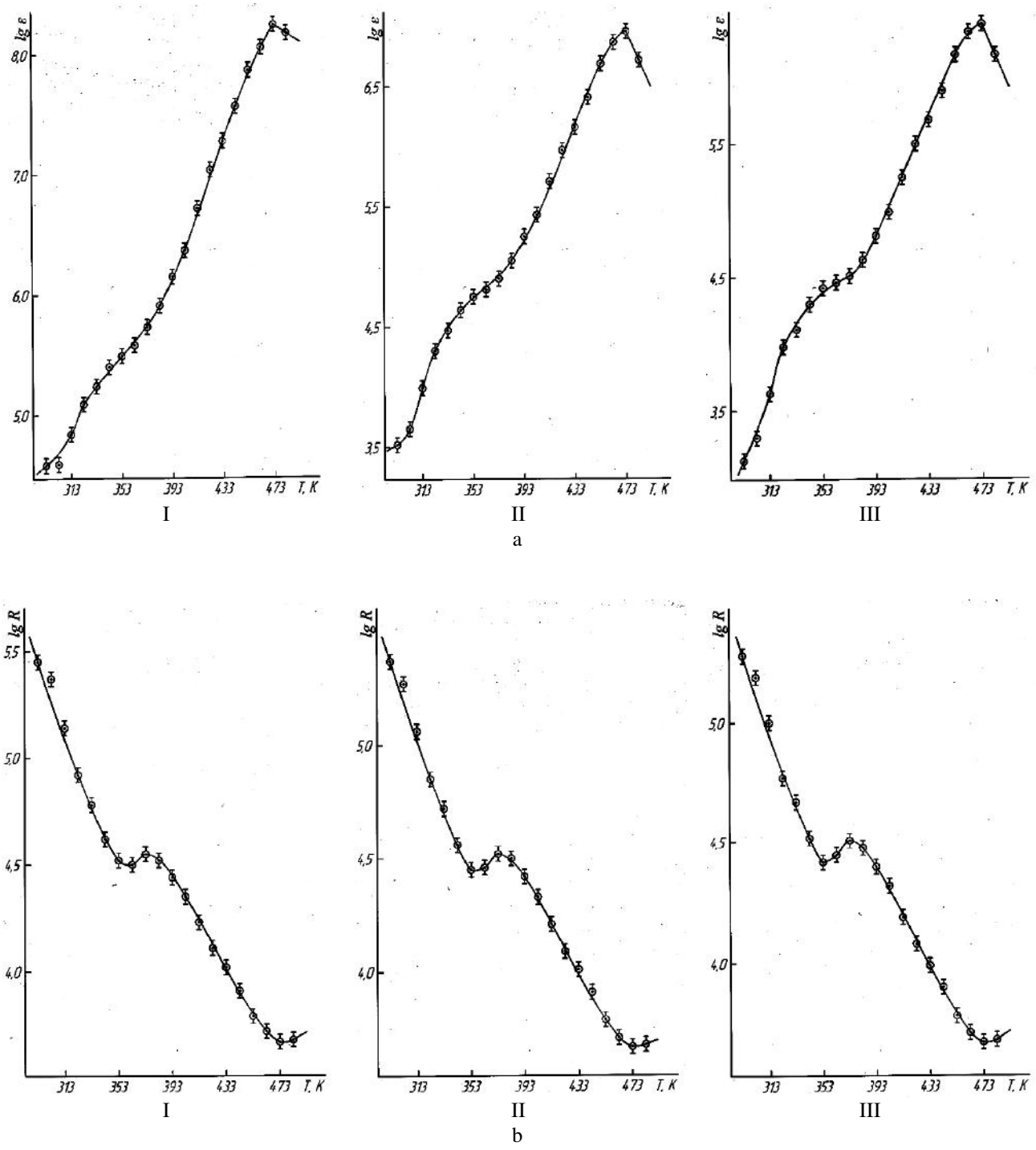

Fig. 2. Dependence of dielectric constant (a) and electric resistance (b) of $LaMgCuZnMnO_6$ on temperature and frequencies equal to 1 kHz (I), 5 kHz (II) and 10 kHz (III)

Table 1. The electrical resistance (R) and dielectric constant (ε) of $LaMgCuZnMnO_6$ in the range of 293-483 K and at frequencies equal to 1 kHz (I), 5 kHz (II) and 10 kHz (III)

T, K	**ε**	**lg ε**	**R, Ohm**	**lg R,**
1	2	3	4	5
		I		
293	38373	4.58	281200	5.45
303	38907	4.59	235600	5.37
313	69267	4.84	137600	5.14
323	123013	5.09	83160	4.92
333	172773	5.24	60410	4.78
343	249329	5.40	41380	4.62
353	310274	5.49	32830	4.52
363	376458	5.58	31690	4.50
373	543143	5.73	35290	4.55
383	811040	5.91	33360	4.52
393	1418691	6.15	27330	4.44
403	2361222	6.37	22560	4.35
413	5188888	6.72	16940	4.23
423	10868329	7.04	12870	4.11
433	18885890	7.28	10580	4.02
443	36933319	7.57	8201	3.91
453	73942927	7.87	6222	3.79
463	115858793	8.06	5206	3.72
473	178977293	8.25	4701	3.67
483	149764295	8.18	4804	3.68
		II		
293	3331	3.52	232600	5.37
303	4475	3.65	187400	5.27
313	9882	3.99	114500	5.06
323	19861	4.30	70110	4.85
333	29214	4.47	51900	4.72
343	43594	4.64	35920	4.56
353	56719	4.75	28460	4.45
363	64649	4.81	28960	4.46
373	80017	4.90	33270	4.52
383	111505	5.05	31390	4.50
393	175883	5.25	26230	4.42
403	270971	5.43	21600	4.33
413	510893	5.71	10330	4.01
423	933391	5.97	12410	4.09
433	1436252	6.16	10340	4.01
443	2563820	6.41	8047	3.91
453	4882148	6.69	6130	3.79
463	7374141	6.87	5151	3.71
473	9155421	6.96	4684	3.67
483	5263953	6.72	4804	3.68
		III		
293	1370	3.14	191800	5.28
303	1991	3.30	153700	5.19
313	4288	3.63	99010	5.00
323	9538	3.98	59400	4.77
333	13006	4.11	47140	4.67
343	20013	4.30	32950	4.52
353	26317	4.42	26410	4.42
363	28552	4.46	27940	4.45
373	32123	4.51	32260	4.51
383	42851	4.63	30270	4.48

.

Table continuation

1	2	3	4	5
393	65084	4.81	25080	4.40
403	97125	4.99	20930	4.32
413	178668	5.25	15640	4.19
423	314822	5.50	12020	4.08
433	482378	5.68	9841	3.99
443	801036	5.90	7855	3.90
453	1464248	6.17	6052	3.78
463	2183670	6.34	5095	3.71
473	2500774	6.40	4676	3.67
483	1474252	6.17	4837	3.68

The dependence of the electrical resistance on the reciprocal temperature in the range of 293-343 K is described by the equation:

$$\lg R = -0{,}05 + 1573 / T, \quad (2)$$

and in the range 373-483 K:

$$\lg R = 0{,}35 + 1575 / T, \quad (3)$$

by the solution of which the activation energies of conduction were calculated, equal to 30.12 kJ/mol (ΔT = 293-343 K) and 30.16 kJ/mol (ΔT = 373-483 K), respectively.

The dielectric constant in a small narrow temperature range of 293 K to 483 K increases very rapidly from $3.8 \cdot 10^4$ to $1.5 \cdot 10^8$ (1 kHz), $3.3 \cdot 10^3$ to $5.3 \cdot 10^6$ (5 kHz) and $1.4 \cdot 10^3$ to $1.5 \cdot 10^6$. Large values of the permittivity at 293-483 K can be caused, according to [17], by high dielectric losses. Giant values of permittivity ($\varepsilon = 10^5$-10^6) for $La_{15/8}Sr_{1/8}NiO_4$ ceramics were established in [5] and they also explain the nature of this phenomenon in terms of the theory of the Maxwell-Wagner effect, according to which dielectric losses are large in the region of intermediate frequencies, t .to. the period of oscillations of the electric field strength was compared with the relaxation time of the surface polarization. In our case, the investigated area of the object is in the range of 1-10 kHz, which can also be attributed to intermediate frequencies. It should also be noted that a decrease in values of dielectric constant was observed with the increasing frequency. These results show that in the indicated narrow temperature range this compound is, in our view, of interest for microcondensator technology.

Conclusions

The nanostructured copper-zinc manganite of lanthanum and magnesium of $LaMgCuZnMnO_6$ was first obtained. In the range of 293-483 K and at frequencies equal to 1, 5 and 10 kHz, the electrical resistance and dielectric constant of the copper-zinc manganite were investigated. It was determined that this compound in the range of 293-353 K has the semiconductor conductivity, metal conductivity in the range of 353-373 K, and semiconductor conductivity in the range of 373-483 K. The widths of band gap equal to 0.83 eV (293-353 K) and 0.80 eV (373-483 K) were calculated. The activation energies of conduction were calculated in the intervals 293-343 K and 373-483 K, equal to 30.12 and 30.16 kJ/mol, respectively. The dielectric constant of $LaMgCuZnMnO_6$ at a relatively low temperature of 483 K reaches up to $1{,}5 \cdot 10^8$ (1 kHz), $5{,}3 \cdot 10^6$ (5 kHz) and $1{,}5 \cdot 10^6$ (10 kHz). The research results presented in this paper show that the nanostructured $LaMgCuZnMnO_6$ is of interest for the semiconductor and microcondensator technology.

Acknowledgments

This research was funded by the Science Committee of the Ministry of Education and Science of the Republic of Kazakhstan (Grant No. AP08855601).

REFERENCES

1 Tretyakov Yu.D., Brylyov O.A. New generations of inorganic functional materials. *Journal of the Russian Chemical Society named after D.I. Mendeleev,* 2000, Vol. 44, No. 4, pp. 10-16. [in Russian].

2 Kasenov B.K., Kasenova Sh.B., Sagintaeva Zh.I., Ermagambet B.T., Bekturganov N.S., Oskembekov I.M. *Double and triple manganites, ferrites and chromites of alkali, alkaline earth and rare earth metals.* Moscow, Nauchnyi mir, 2017, 416 p. [in Russian].

3 Solin N.I., Naumov S.V. Magnetic and electrical properties of weakly doped manganese-deficient $La_{1x}Ca_xMn_{1z}O_3$ manganites. *Journal of Experimental and Theoretical Physics,* 2013, Vol. 116, No. 1, pp. 145-158. https://doi.org/10.1134/s1063776113010172

4 Golenishchev-Kutuzov A.V., Golenishchev-Kutuzov V.A., Ismagilov I.R., etc. Magnetically controlled structural, Yang-Teller, dielectric, and transport effects $La_{0,875}Sr_{0.125}MnO_3$. *Izvestiya RAS. Physics Series,* 2015, Vol. 79, No. 6, pp. 768-770 [in Russian].

5 Erin Yu. Substance with high value of dielectric capacitivity was found. *Chemistry and Chemists,* Part 1, 2009. *Available at the:* http://chemistry-chemists.com/N1_2009/16-22.pdf [in Russian].

6 Aksenova T.V., Gavrilova L.Ya, Cherepanov V.A. Crystal structure and physicochemical properties of doped lanthanum manganites. *Russian Journal of Physical Chemistry A,* 2012, Vol. 86, pp. 1862-1868. https://doi.org/10.1134/S0036024412120023

7 Ivanov A.I., Agarkov D.A., Burmistrov I.N., Kudrenko E.A., Bredikhin S.I., Kharton V.V. Synthesis and Properties of Fuel Cell Anodes Based on $(La_{0,5+x}Sr_{0.5-x})_{1-y}Mn_{0.5}Ti_{0,5}O_{3-\delta}$ (x = 0-0.25, y = 0-0.03). *Russian Journal of Electrochemistry*, 2014, Vol. 50, No 8, pp. 730-736. https://doi.org/10.1134/S1023193514080047

8 Kasenova Sh.B., Sagintaeva Zh.I., Kasenov B.K., Turtubaeva M.O., Nukhuly A., Kuanyshbekov Ye.Ye., Issabaeva M.A. New nanostructured manganites of $LaMe^{II}CuZnMnO_6$ (Me^{II} – Mg, Ca, Sr, Ba). *Bulletin of the Karaganda University. Chemistry Series,* 2021, Vol. 103, No. 3, pp. 60-66. https://doi.org/10.31489/2021ch3/60-66

9 Kovba L.M., Trunov V.K. *X-ray phase analysis*. Moscow, 1976, 256 p. [in Russian].

10 Kivilis S.S. *Technique of measuring of the density of liquids and solids*. Moscow, 1959, 191 p. [in Russian].

11 Kasenov B.K., Kasenova Sh.B., Sagintaeva Zh.I., Nukhuly A., Turtubaeva M.O., Bekturganov Zh. S., Zeinidenov A.K., Kuanyshbekov E.E., Issabaeva M.A. Synthesis and X-ray investigation of novel nanostructured copper-zinc manganites of Lanthanum and alkali metals. *Eurasian Physical Technical Journal*, 2021, Vol. 18, No. 1, pp. 29-33. https://doi.org/10.31489/2021no1/29-33

12 Okadzaki K. *Technology of ceramic materials.* Moscow, 1976, 256 p. [in Russian].

13 Fesenko E.G. *Perovskite family and ferroelectricity.* Moscow, 1972, 248 p. [in Russian].

14 Venevcev Yu.N., Politova E.D., Ivanov S.A. *Ferroelectric and antisegnetoelectrics of the barium titanate family*. Moscow, 1985, 256 p. [in Russian].

15 Kassenova Sh.B., Sagintayeva Zh.I., Kassenov B.K., Kuanyshbekov E.E, Bekturganov Zh.S., Zeinidenov A.K. Electrophysical characteristics of nanodimensional cobalte-cuprate-manganite $LaNa_2CoCuMnO_6$ and nickelite-cuprate-manganite $LaNa_2NiCuMnO_6$. *Bulletin of the Karaganda University. Physics Series,* 2020, Vol. 98, No. 2, pp. 43-49. https://doi.org/10.31489/2020ph2/43-49

16 Tretyakov Yu.D. Problem of development of nanotechnology in Russia and abroad. *Bulletin of the Russian Academy of Sciences,* 2007, Vol. 77, No 1, pp. 3-10. [in Russian].

17 Barfoot J. *Introduction to the physics of ferroelectric phenomena.* Moscow, 1970, 352 p. [in Russian].

Article accepted for publication 05.05.2022

DOI 10.31489/2022No2/48-57

UDC 536.7, 536.245

DEVELOPMENT AND RESEARCH OF THE TOPOLOGY OF COOLING BAFFLES FOR BLADES OF THE AXIAL CARBON DIOXIDE TURBINES

Komarov I.I., Vegera A.N., Bryzgunov P.A.*, Makhmutov B.A., Smirnov A.O.

National Research University "Moscow Power Engineering Institute", Moscow, Russian Federation,
BryzgunovPA@mpei.ru

Currently, there is an increase in average annual temperature and climate change across the various continents. Carbon dioxide emissions from energy facilities contributed to this condition. Implementation of oxy-fuel cycles is a promising solution for reducing carbon dioxide emissions from the energy sector. To date, the most efficient oxy-fuel cycle is the Allam cycle. In this cycle supercritical carbon dioxide acts as a working fluid of the cycle, wherein CO_2's temperature upstream of the turbine is 1,150 °C and the pressure is 30 MPa. Due to the high temperature of the working fluid, it is necessary to cool first stages of the carbon dioxide turbine. The feature of considered cooling system in this turbine is that carbon dioxide being used as a refrigerant too. This paper investigated two topologies of convective cooling systems in the carbon dioxide turbine's nozzle blade as well as considers an option for increasing the intensity of heat exchange through the use of helical ribbing in the cylindrical cooling baffle. Numerical simulation involving the ANSYS software package was performed for two topologies of the cooling baffles arrangement in the nozzle blade body: configuration 1 - with 17 baffles of 1 mm diameter, configuration 2 - with three baffles of the blade profile shape. Configuration 1 proved to be more efficient: the Nusselt number has a value of 117, and average value of the heat transfer coefficient on the refrigerant side is 6,413 W/m^2·K. The effect of using helical ribbing in the cooling cylindrical baffle of the blade under study was investigated, which enabled to reduce the metal temperature by 54 °C on average and doubled the heat transfer coefficient.

Keywords: cooling blade, supercritical carbon dioxide, oxy-fuel combustion power cycle, carbon dioxide turbine, rib turbulators, heat transfer.

Introduction

One of the main causes of global warming and climate change in the world is the burning of fossil fuel such as oil, coal, gas, to generate electricity [1]. Combustion of various fuels generates the greenhouse gas - carbon dioxide (CO_2). Due to economic growth, the need for electricity increases every year, [2] leading to higher consumption of natural resources. To curb the rise in average annual temperature and reduce greenhouse gas emissions, an international agreement has been adopted to limit temperature increase by 2°C by 2040 [3]. Presently, main processes to reduce the carbon dioxide emissions include: commissioning of renewable energy sources and cut down the number of power plants operating on fossil fuels; commissioning of nuclear power plants, implementation of CO_2 capture procedures. Each of the above processes has its own disadvantages. For instance, the amount of electricity generated by wind and solar power plants is highly dependent on external weather conditions [4]. These plants also face problems with integration into power network [5]. Besides, there are complications with disposal of solar batteries and blades of wind generators. Nuclear power plants have no harmful effects on climate change, but after operation the fuel must be disposed of since there is still no technology for complete recycling of the fuel [6]. Decarbonization technology (CCS) imposes high capital and operating costs on energy facilities [7]. Application of the oxygen-fuel cycles is an alternative option for reducing CO_2 emissions [8, 9]. Allam cycle is the most promising and efficient.

Based on the Brayton cycle, the Allam cycle's working fluid is the supercritical carbon dioxide. The Allam cycle power plant consists of compressor, pump, combustion chamber, carbon dioxide turbine and regenerative heat exchanger. A distinctive feature of this cycle's combustion chamber is the presence of three inlet streams: natural gas (fuel), oxygen (oxidizer) and carbon dioxide (maximum temperature limiter). Another feature of the combustion chamber is zero nitrogen content to prevent generation of NO_x. Air separating unit is used for the generation of oxygen. Downstream of the combustion chamber the combustion products consisting mainly of CO_2 at a temperature of 1,150 ° C and a pressure of 30 MPa, enter the turbine

rotating the electric generator [10]. Downstream of the turbine, the exhausted carbon dioxide enters the regenerative heat exchanger, and then into the water separator, where the condensed steam is removed. Then, one portion of the gas is returned to the cycle, and another portion is sent for disposal [11,12]. Thus, no CO_2 greenhouse gas emissions take place.

Allam cycle's carbon dioxide turbine is notable for parameters of working fluid upstream of the first stage. Pressure of the combustion products corresponds to parameters of steam turbines at supercritical parameters, and the working fluid temperature is similar to gases at the gas turbine inlet. Due to these parameters it is necessary to apply additional cooling of the turbine rotor, nozzle and rotating blades of first stages [13]. The turbine cooling is notable for using CO_2 as a refrigerant. Unlike air, carbon dioxide has a higher density (by 35%) and this must be taken into account when designing the turbine cooling system, because due to the higher density it may be difficult to form a film on the blade wall. Toshiba Company, being designer of combustion chamber and carbon dioxide turbine of the Allam cycle for blade cooling, suggests the loop convective cooling circuit without film cooling and with further refrigerant ejection through the blade periphery [14].

Presently, there are few publicly available studies on carbon dioxide flow in the blade cooling baffles. Main CO_2 studies cover the application of various heat exchange intensifiers [15] or analysis of gas dynamic properties of the working fluid in inter-blade baffles of the carbon dioxide turbine [16]. There are many papers on the study of various topologies of convective blade cooling systems, but air [17,18]or steam is considered as a refrigerant [19,20].

There is a large quantity of works related to studying of heat exchange intensifiers. The paper [21] contains large study of different rib shapes with various installation angles in the baffle. V-rib with 60° installation angle shows the highest thermal-hydraulic performance. The article [22] compares thermal hydraulic properties of round, oval, ellipsoid and drop-shaped pins. The drop-shaped pin is the most efficient under the same conditions. Paper [23] gives a brief overview of commonly used heat transfer intensifiers, suggesting the use of slots and curved ribs as an alternative to inclined ribs and pins. In the considered articles on heat exchange intensifiers the studies are conducted in rectangular baffles. Not much work has been done in circular baffles, although the shape of the cooling baffle may greatly influence the flow of refrigerant in it. The paper [24] studies ribs installed at right angles in baffle with the circular cross section. Thanks to the ribbing under review, it was possible to increase the heat transfer coefficient by the flow transition and increasing the area of heated surface. Similar paper is given in the article [25], only the configuration with ribs located along the baffle was investigated. Use of ribs in the cooling baffle has increased the cooling efficiency of the turbine blade. The article [26] studied two baffles: one with oblique ribs and the other with V-shaped ribs. The average Nusselt number is much higher in the configuration with V-shaped ribs due to the formation of many vortices, while in the configuration with oblique ribs only one vortex is formed.

This paper deals with the study of two different topologies for convective cooling of carbon dioxide turbine blades. Cooling system designs will differ in the location and size of baffles in the blade body. Also, to increase the intensity of convective heat transfer, a new design of intensifier was developed and tested: helical ribbing. The study was conducted for a baffle similar to the baffle of the cooled configuration 1 blade. Carbon dioxide will be used as a refrigerant with parameters corresponding to parameters of the Allam CO_2 cycle.

1 Geometry

Two topologies for the arrangement of cooling baffles in the nozzle blade were designed for the study: a configuration with 17 baffles having diameter of 1 mm spaced 5 mm apart (configuration 1) and a configuration with three baffles the shape of which is the same as shape of the blade profile (configuration 2). Profile of the C-9015A nozzle set has been selected for accommodation of baffles in the blade body. The wall thickness between cooling baffles and the outer wall of the blade airfoil is 1 mm in both cases. Basic geometry, such as chord and blade height, are also equal and shown in Table 1. The cross-sectional area of the cooling space in the configuration with three baffles is 200 mm^2, while in the baffle of 1 mm diameter it is 13.4 mm^2. Schematic designs of both configurations are shown in Figures 1 and 2.

Due to economic growth, the need for electricity increases every year, [2] leading to higher consumption of natural resources. To curb the rise in average annual temperature and reduce greenhouse gas emissions, an international agreement has been adopted to limit temperature increase by 2°C by 2040 [3].

.

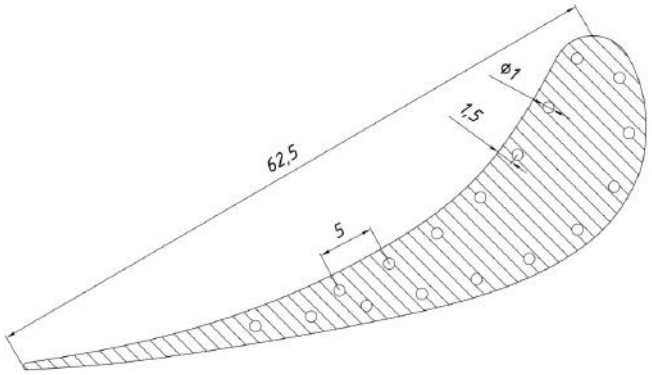

Fig.1. Cross-section of the blade under study with baffles of 1 mm diameter.

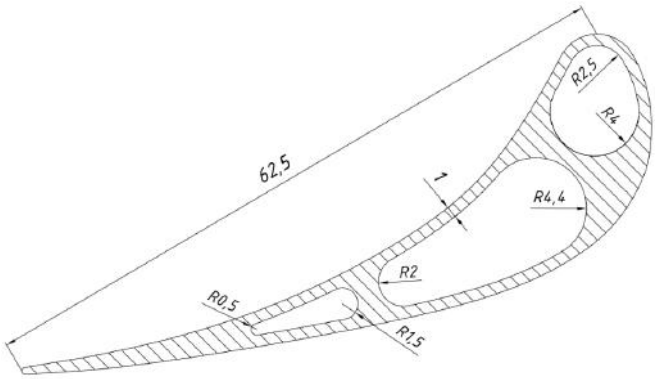

Fig.2. Cross-section of the blade with three baffles under study.

Table 1. Basic geometry of blades under study.

Type of design	Diameter of baffles, mm	Baffles pitch, mm	Number of baffles	Wall thickness, mm	Profile chord, mm	Blade height, mm
Configuration 1	1	5	17	1	62.5	25
Configuration 2	-	-	3			

To increase the efficiency of cooling in the configuration 1 blade, the effect of heat transfer intensification inside the cylindrical baffle was studied. Use of the heat exchange intensifiers results in flow mixing and transition, thus improving heat transfer from the hot walls of the blade metal to the refrigerant.

To define the increase in cooling efficiency when using intensification in the cylindrical baffle, two baffle topologies were calculated: smooth baffle and similar baffle with helical ribbing. Dimensions of the studied baffles correspond to baffles of the configuration 1 blade. Schematic designs of the studied channel models are shown in Figure 3, and Table 2 shows their basic geometrical characteristics.

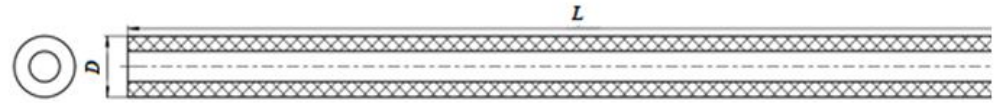

a) sketch of the circular smooth baffle

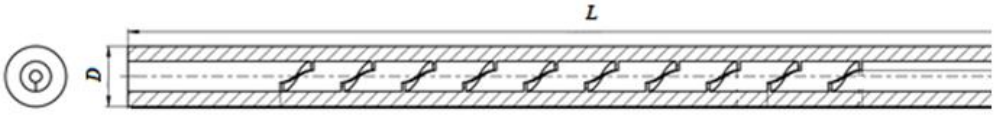

b) sketch of the circular baffle with helical ribbing

Fig.3. Geometry of studied baffles.

Table 2. Geometry parameters of studied baffles.

Parameter	Value
Baffle length, mm	25
Baffle diameter, mm	1
Wall thickness, mm	1
Helical ribbing height, mm	0.3
Helical ribbing thickness, mm	0.1
Pitch, mm	1

2 Mesh

The modelling was performed in the coupled formulation. To implement this method, a separate grid was constructed for each volume element of the model: for the blade body, for the main flow of supercritical CO_2, for the cooling baffles with supercritical CO_2. The nozzle blade body grid is entirely made of tetrahedron-shaped elements. The grid of gas flows is combined: elements of the main flow have a tetrahedron shape and the near-wall elements are prismatic in shape for more accurate calculation in the boundary layer zone. Indicator of grid quality in the boundary zone is the y^+ value, which should be close to 1. For similar conditions at the stage inlet the CO_2 density is twice higher than air density, at the average. As a result, height of the first boundary layer in grid near the blade wall of turbine operating on supercritical carbon dioxide is twice less than for conventional gas turbines with the same y^+ [16]. To achieve a low y^+ value, a grid model with a large number of elements is required. To speed up the calculation and reduce the number of grid elements at the upper and lower flow boundaries, no additional prismatic boundary layers which significantly increase the volume of the grid model, were created. Main characteristics of the calculation model grid with 1 mm diameter baffles and of the computational model with three baffles in the form of blade profile are presented in Table 3. Figure 4 shows the computational grid of the configuration 1 blade.

The Ansys software package was used to study the effect of heat exchange intensification in the cylindrical baffle. The computational grid is volumetric, unstructured, tetrahedral. Method for designing the computational grid of models under study is Delaunay. Prismatic boundary layer is modeled on the baffle walls and on helical ribbing. Figure 5 shows the computational grid of the baffle with helical ribbing.

Table 3. Main characteristics of the studied topologies computational grids.

Parameter	Value	
	Configuration 1	Configuration 2
Number of grid elements, mln.	8,028	7,698
Blade body		
Global size of the grid, mm	0.33	0.23
Working fluid flow		
Global size of the grid, mm	0.58	0.55
Prismatic layer design procedure	First Layer Thickness	
First prismatic layer thickness, mm	0,017	0,007
Number of prismatic layers	13	14
Growth rate	1.26	1.3
Boundary layer design algorithm	Pre	
Cooling baffles		
Global size of the grid, mm	0.1	0.18
Prismatic layer design procedure	First Layer Thickness	
First prismatic layer thickness, mm	0,006	0,0045
Number of prismatic layers	10	12
Growth rate	1.2	1.28
Boundary layer design algorithm	Pre	

.

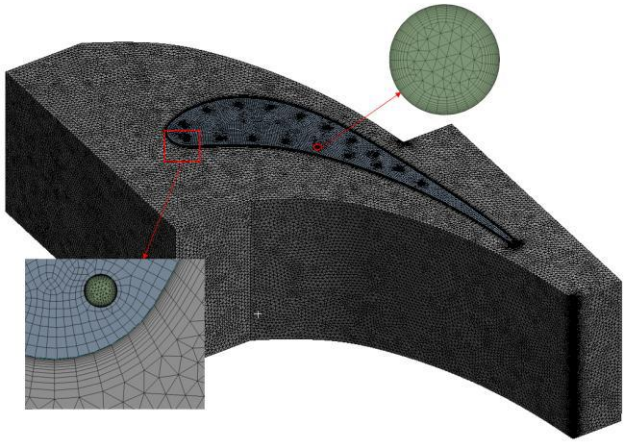

Fig.4. Reference Grid of the Configuration 1 blade.

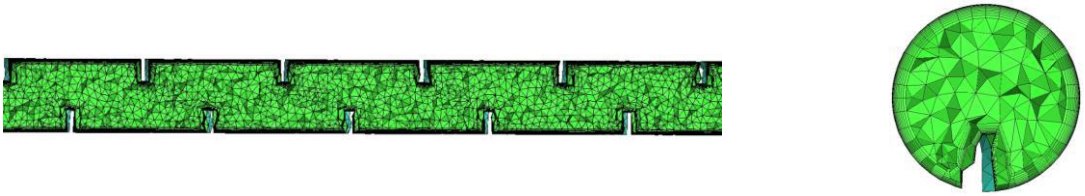

a) Longitudinal Section b) Lateral Section

Fig.5. Reference Grid of the Baffle with Helical Ribbing.

3 Boundary and Physical Conditions

The boundary conditions in use herein are compliant with the fluid parameters of the Allam cycle carbon dioxide turbine [8]. The full braking pressure and temperature are set for the primary carbon dioxide flow in the inter-blade baffle while the static pressure is set for the output. The full braking pressure and temperature are also set for the input cooling baffles while the total coolant consumption is set for the baffle outputs. In addition to physical parameters of the fluid, the density of the blade material equal to 8050 kg/m^3, the specific heat equal to 573 J/kg·K, and the heating constant equal to 22.1 W/m·K were set. These material specifications correspond to the nickel-based Alloy 740. For the primary specifications of the boundary conditions, see Table 4. The periodic boundaries were set for the side surfaces of the primary carbon dioxide flow. Figure 6 shows the reference model for research of the blade with cooling baffles 1 mm in diameter under the set boundary conditions. The calculation uses the turbulence model k-ω SST.

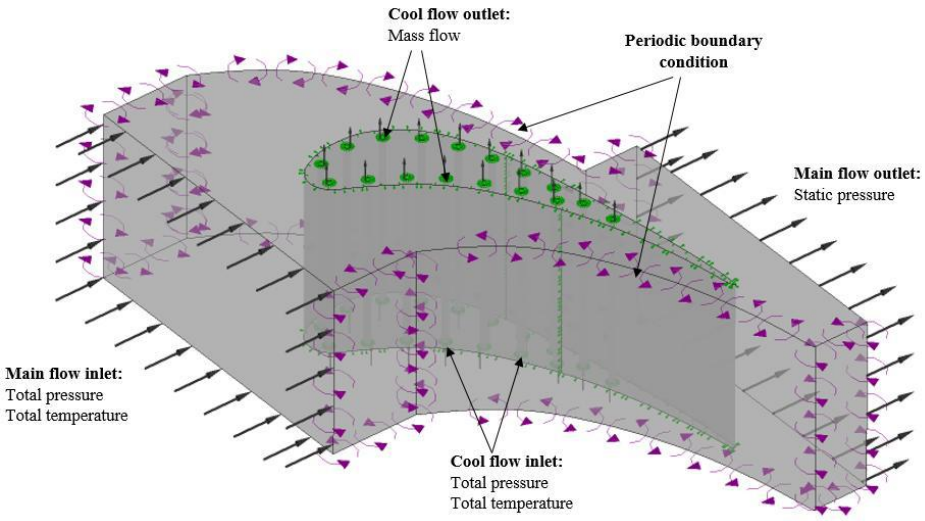

Fig.6. Boundary Conditions of the Reference Model

Table 4. Reference Boundary Conditions.

Parameter	Value
Primary Flow Input Pressure, MPa	30
Primary Flow Input Temperature, K	1373.15
Primary Flow Output Pressure, MPa	25
Cooling Baffle Input Pressure, MPa	30
Cooling Baffle Input Temperature, K	473.15
Total Coolant Consumption at Cooling Baffle Outputs, kg/sec	0.0224
Primary Flow and Coolant Material	S-CO2
Blade Body Material	Alloy 740
Turbulence Model	SST

The boundary conditions for the mathematical model of the cylindrical baffles on review were selected in accordance with the carbon dioxide parameters of the Allam cycle carbon dioxide turbine. Carbon dioxide flow modelling used the Ansys CFX mathematical package. For the boundary conditions of the reference model, see Table 5. The *k-ω* SST was used as the turbulence model. Mean outer wall temperatures were set for modelling heat and hydrodynamic processes of the baffles on review. The full braking pressure and the flow temperature were set for the baffle input while the coolant consumption depending on the Reynolds number was set for the output section. The calculations were conducted within the *Re* number range from 20000 to 100000 in increments of 20000.

Table 5. Boundary Conditions for Cylindrical Baffle Calculations.

Parameter	Value
Fluid	CO_2
Baffle Input CO2 Temperature, °C	200
Baffle Input Pressure, MPa	30
Wall Temperature, °C	850
Reynolds Number	20000, 40000, 60000, 80000, 100000
Turbulence Model	SST

4 Methods

The thermal transmittance value was calculated to analyze the influence of helical ribbing usage in the cylindrical cooling baffle on the blade metal temperature. The inputs for the analysis were the Ansys CFX computational flow dynamics results for the cooled configuration 1 blade. To calculate the coolant thermal transmittance value, the baffle was selected which is located in the immediate proximity of the most heat-loaded zone while the wall element between two baffles throughout the blade height was selected in the same zone to calculate the fluid thermal transmittance value.

First, the thermal transmittance values were determined for the coolant and for the hot gasses. After the thermal transmittance values were determined, the heating constant was determined for the design with smooth baffles and for the baffle with helical ribbing subject to variations of the thermal transmittance value directly proportional to the Nusselt number. Finally, we were able to compute the wall temperature resulting from usage of helical ribbing in cylindrical cooling baffles of the nozzle blade.

5 Results and Discussion

This study provides mathematical modelling of two convective cooling configurations for the nozzle blade of the carbon dioxide turbine. The least blade metal temperatures are achieved under the topology with 17 cooling baffles 1 mm in diameter. The mean volumetric temperature of the metal is achieved under configuration 1 and equals 1218 K while in configuration 2, the mean temperature equals 1331 K or 9.5 % higher than that of configuration 1. The minimum metal temperature in the 17-baffle configuration equals 978 K or 12.2 % lower than that of the three-baffle configuration (Figure 7).

The 17-baffle convective cooling system also demonstrates higher heat exchange intensity versus the three-baffle configuration. In configuration 1, the *Nu* value equals 117 while in configuration 2, it equals 68 (42 % lower). The thermal transmittance value is also higher for the topology with cooling baffles 1 mm in

.

diameter and it is as high as 6400 W/m^2·K. In the topology with three cooling baffles, the thermal transmittance value equals 520 W/m^2·K or 12.3 times lower versus configuration 1 (Figure 8).

The obtained results are associated primarily with the Reynolds number value of the nozzle blade cooling baffles. The Nusselt number and the thermal transmittance values are directly proportional to the *Re* value of the baffle. The higher the coolant velocity in the cooling baffles is, the higher the Reynolds number value is. It results into increasing heat exchange intensity and thermal transmittance value.

Ceteris paribus, the topologies of blade convective cooling systems on review have materially different values of significant baffle dimensions. The clear area of baffles 1 mm in diameter is significantly lower than the clear area of baffles of the configuration 2 blade. Therefore, subject to the continuity equation and under the same coolant consumption values, the velocity in the configuration 1 baffles is much higher than in the three-baffle configuration baffles. For the 17-baffle blade, the coolant velocity equals 4.2 m/sec while it is 15 times lower for the three-baffle blade and equals 0.28 m/sec. The Reynolds number of the carbon dioxide flow in the configuration 1 cooling baffles equals 23200 while it equals 12850 for the configuration 2 baffles or 45 % lower versus the first topology. For the three-baffle blade to achieve the same Reynolds number value in its cooling baffles as the configuration with 17 baffles 1 mm in diameter, the coolant consumption must be 1.8 times higher.

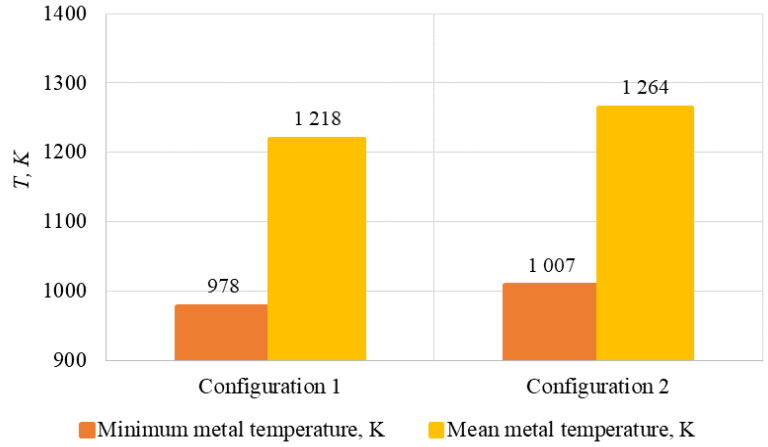

Fig.7. Dependency of the Blade Metal Temperature on the Topology of the Cooling Baffles.

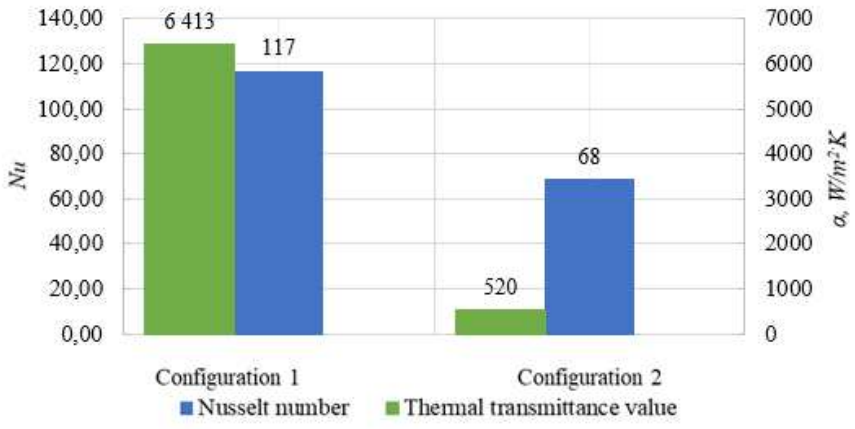

Fig.8. Dependency of the Nusselt Number and the Thermal Transmittance Values on the Topology of the Blade Cooling Baffles.

Figure 9 shows metal temperature profiles for significant sections along the blade height such as the root, middle and peripheral sections. Referring to the figure, it will be seen that it is possible to limit the influence of high primary carbon dioxide flow temperature on the airfoil interior where the lowest temperatures for the entire blade volume are achieved for the configuration 1 blade by positioning the cooling baffles along the blade profile 1 mm away from the profile wall. This topology allows to reduce the

wall temperature by 100 K on the average for the concavity but not for the back and the leading edge of the blade where the wall temperature is as high as 1350 K. It is associated with the primary flow velocity along the blade back exceeding the one along the concavity, which increases the thermal transmittance value on part of hot gasses. It may also be associated with an insignificantly greater distance between the cooling baffles and the profile wall on the profile back side in the half-interval zones between the baffles. Decreasing heat exchange intensity and cooling performance are observed throughout the blade height due to the coolant heating. To increase the profile convexity cooling performance for the nozzle blade on review with this cooling baffle positioning configuration, one must reduce the intervals between the cooling baffles along the back.

Configuration 2 shows high heating of all outer walls of the blade profile. It is possible to reduce the temperature materially between the root section cooling baffles themselves only. Throughout the blade height and due to low velocity in the cooling baffles, the coolant heats rapidly and the walls between the baffles are cooled insignificantly in the middle section already. This cooling system configuration must have higher coolant consumption to achieve normal flow velocities in the baffles, and the cooling baffle walls may have heat exchange intensifiers.

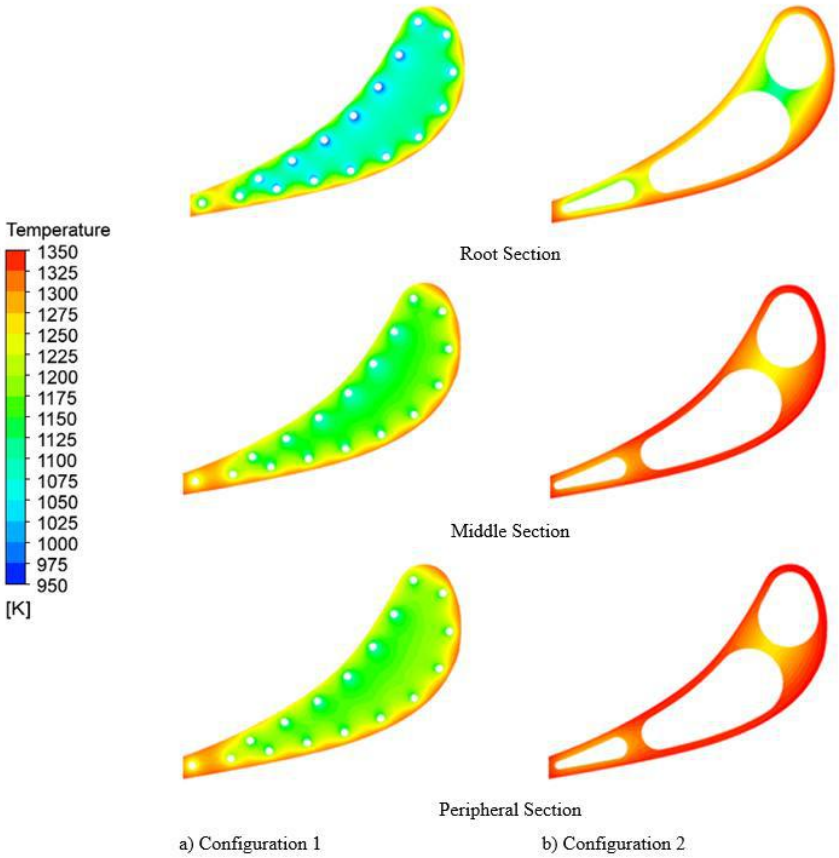

Fig.9. Temperature Profiles.

Circular baffle study results are shown as diagrams of dependency of the Nusselt number (Figure 10) and linear hydraulic loss ratio (Figure 11) on the Reynolds number. Using helical ribbing allows to increase the heat exchange intensity by 91% on the average throughout the Reynolds number range on review. The Nusselt number increases due to the coolant flow turbulence and the increasing heat exchange contact area. However, using helical ribbing increases the losses associated with the hydraulic loss ratio. In this connection, as the Reynolds number increases the hydraulic loss ratio of the cylindrical baffle with ribbing decreases by 10% due to decreasing thickness of the boundary layer. The *Re* number equals 23240 for the cooling baffle in the calculations for the configuration 1 blade. At this Reynolds number, the Nusselt number is 2 times higher for the baffle with helical ribbing, which causes the baffle thermal transmittance value to increase 2 times as well.

.

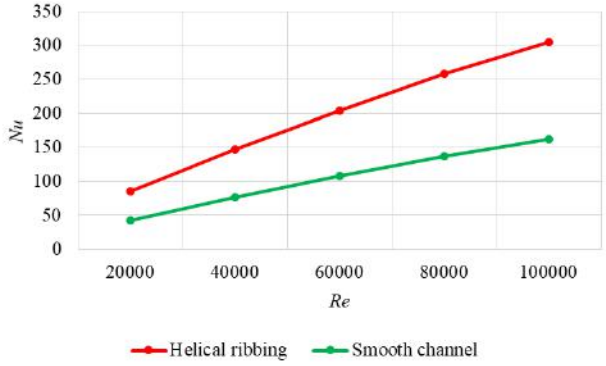

Fig.10. Diagram of Dependency of the Nusselt Number on the Reynolds Number for the Baffles on Review.

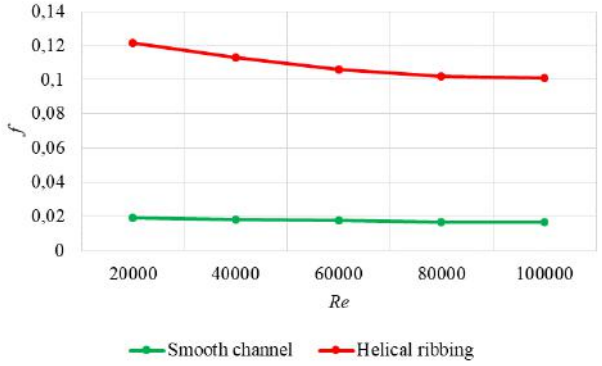

Fig.11. Diagram of Dependency of the Hydraulic Loss Ratio on the Reynolds Number for the Baffles on Review.

Using heat exchange intensification in the form of helical ribbing of the cooling baffles of the nozzle blade on review caused the wall temperature in the most heat loaded area to decrease by 54 °C. It also allowed to increase the thermal transmittance value by 33%. Due to the increasing thermal transmittance value, the helical ribbing may be used to reduce the coolant consumption for cooling at the constant blade metal temperature, which, in its turn, would cause the cycle performance to increase.

Conclusions

The following conclusions may be drawn from the completed studies:

1) The design with 17 baffles 1 mm in diameter ensures more efficient cooling of the blade than the three-baffle structure. The first topology ensures lower metal temperatures throughout the blade volume. Design 1 also has higher values of the Nusselt number (42 % higher versus configuration 2) and thermal transmittance (12 times higher). It is associated with a higher differential velocity of the coolant in the baffles of the topologies on review and thus with different Reynolds number values for them.

2) For the configuration 2 blade to achieve the similar Reynolds number value for its cooling baffles as the blade with 17 baffles, the coolant consumption must be 1.8 times higher. Therefore, the configuration ensures coolant savings, which allows to decrease the carbon dioxide turbine losses materially.

3) The 17-baffle topology clearly demonstrates non-homogeneity of cooling along the blade profile. This topology ensures much better reduction of the wall concavity temperature versus the back and the leading edge of the blade. It is associated with a higher primary flow velocity along the back of the profile versus the concavity, which increases the thermal transmittance value on part of hot gasses. It may also be associated with an insignificantly greater distance between the cooling baffles and the profile wall on the profile back side in the half-interval zones between the baffles.

4) The influence of the heat exchange intensification in the form of helical ribbing of the cylindrical baffle was studied using the computational flow dynamics inputs for the configuration 1 blade. It was possible to double the Nusselt number and the thermal transmittance values and to reduce the wall temperature by 54 °C in the most heat-loaded zone.

5) Using helical ribbing in the cylindrical baffle allowed to increase the thermal transmittance value by 33%, which may be used to reduce coolant consumption, which, in its turn, would result into greater cycle performance.

Acknowledgments

This study conducted by the Moscow Power Engineering Institute was financially supported by the Ministry of Science and Higher Education of the Russian Federation (project no. FSWF-2020-0020).

REFERENCES

1 Araujo G., Robalino-López A., Tapia N. Energy foresight: Exploration of CO_2 reduction policy scenario for Ecuador during 2016–2030. *Energetika.* 2019. Vol. 65, No 1, pp. 51 – 70.

2 Bariss U., Laicane I., Blumberga D. Analysis of factors influencing energy efficiency in a Smart Metering Pilot. *Energetika*. 2014. Vol. 60, No 2, pp. 125 – 135.

3 Energy I. World Energy Outlook 2014. International Energy Agency (IEA). OECD. Paris. IEA Publications, 2014. Available at: https://www.iea.org/reports/world-energy-outlook-2014

4 Kádár P. Pros and cons of the renewable energy application. *Acta Polytech. Hung*. 2014. Vol. 11, No 4, pp.211–224.

5 Phuangpornpitak N., Tia S. Opportunities and challenges of integrating renewable energy in smart grid system. *Energy Procedia*. 2013. Vol. 34, pp. 282 – 290.

6 Adar E. The State of the Art of Nuclear Energy: Pros and Cons. *EurAsia Waste Management Symposium*. Istanbul, 2020. pp. 26 – 28.

7 Boot-Handford M.E., et al. Carbon capture and storage update. *Energy Environ. Sci. Royal Society of Chemistry.* 2014. Vol. 7, No 1, pp. 130 – 189.

8 Rogalev A., et al. Research and Development of the Oxy-Fuel Combustion Power Cycles with CO2 Recirculation. *Energies.* 2021. Vol. 14, No 10, pp. 2927.

9 Scaccabarozzi R., Gatti M., Martelli E. Thermodynamic Optimization and Part-load Analysis of the NET Power Cycle. *Energy Procedia*. 2017. Vol. 114, pp. 551 – 560.

10 Rogalev A. et al. The flow path characteristics analysis for supercritical carbon dioxide gas turbines. *E3S Web of Conferences*, 2019. Vol. 124, pp. 01006.

11 Iwai Y. et al. Development Approach to the Combustor of Gas Turbine for Oxy-Fuel, Supercritical CO2 Cycle. *ASME Turbo Expo 2015*. Montreal, 2015. Vol. 9, pp. 1–7.

12 Allam R.J. et al. The Oxy-Fuel, Supercritical CO2 Allam Cycle: New Cycle Developments to Produce Even Lower-Cost Electricity From Fossil Fuels Without Atmospheric Emissions. *ASME Turbo EXPO 2014*. Düsseldorf, 2014. Vol 3B, pp. 1 – 9.

13 Allam R. et al. Demonstration of the Allam Cycle: An Update on the Development Status of a High Efficiency Supercritical Carbon Dioxide Power Process Employing Full Carbon Capture. *Energy Procedia*. 2017. Vol. 114, pp.5948–5966.

14 Sasaki T. et al. Development of Turbine and Combustor for a Semi-Closed Recuperated Brayton Cycle of Supercritical Carbon Dioxide. *ASME Turbo Expo 2017.* Charlotte, 2017. Vol. 1, 8 p.

15 Kindra V. et al. An experimental and numerical study of flow and heat transfer in cooling channels with pin fin-dimple and pin fin-groove arrays. *13 th European Conference on Turbomachinery Fluid dynamics & Thermodynamics*. Lausanne, 2018, pp. 1 – 10.

16 Ying Q. et al. Vortex Patterns Investigation and Enstrophy Analysis in a Small Scale S-CO2 Axial Turbine. *Energies*. 2021. Vol. 14, No 19, pp. 1 – 22.

17 Rahimi J., Poursaeidi E., Khavasi E. Stress analysis of a second stage gas turbine blade under asymmetric thermal gradient. *Mech. Ind. EDP Sciences.* 2019. Vol. 20, No 6, pp. 607.

18 Kim K.M. et al. Analysis of conjugated heat transfer, stress and failure in a gas turbine blade with circular cooling passages. *Eng. Fail. Anal*. 2011. Vol. 18, No 4, pp. 1212 – 1222.

19 Bohn D., Ren J., Kusterer K. Cooling Performance of the Steam-Cooled Vane in a Steam Turbine Cascade. *Turbo Expo 2005*. Reno, 2005. Vol 3, pp. 217 – 226.

20 Wróblewski W. Numerical evaluation of the blade cooling for the supercritical steam turbine. *Appl. Therm. Eng*. 2013. Vol. 51, No 1 – 2, pp. 953 – 962.

21 Kaewchoothong N. et al. Effect of inclined ribs on heat transfer coefficient in stationary square channel. *Theor. Appl. Mech. Lett*. 2017. Vol. 7, No 6, pp. 344–350.

22 Jin W. et al. Effect of shape and distribution of pin-fins on the flow and heat transfer characteristics in the rectangular cooling channel. *Int. J. Therm. Sci.* 2021. Vol. 161, 106758 p.

23 Gupta S., Chaube A., Verma P. Review on Heat Transfer Augmentation Techniques: Application in Gas Turbine Blade Internal Cooling. *J. Eng. Sci. Technol. Rev.* 2012. Vol. 5, No 1, pp. 57 – 62.

24 Aljibory M.W., Rashid F.L., Alais S.M.A. An Experimental and numerical investigation of heat transfer enhancement using annular ribs in a tube. *IOP Conference Series: Materials Science and Engineering*. 2018. Vol. 433, No 1, pp. 012057.

25 Yousefi A., Nejat A., Sabour M.H. Ribbed channel heat transfer enhancement of an internally cooled turbine vane using cooling conjugate heat transfer simulation. *Therm. Sci. Eng. Prog*. 2020. Vol. 19, pp. 100641.

26 Zheng N. et al. Effects of rib arrangements on the flow pattern and heat transfer in an internally ribbed heat exchanger tube. *Int. J. Therm. Sci. Elsevier*. 2016. Vol. 101, pp. 93–105.

Article accepted for publication 16.03.2022

.

DOI 10.31489/2022No2/58-64

UDC 574.56

PERFORMANCE SIMULATION OF ECO-FRIENDLY SOLAR CELLS BASED ON $CH_3NH_3SnI_3$

Omarova Zh.[1], Yerezhep D.[1]*, Aldiyarov A.[1], Golikov O.[1], Tokmoldin N.[2]

[1*] Faculty of Physics and Technology, Al Farabi Kazakh National University, Almaty Kazakhstan, darhan_13@physics.kz

[2] Optoelectronics of Disordered Semiconductors, Institute of Physics and Astronomy, University of Potsdam, Germany.

Large-scale deployment of the perovskite photovoltaic technology using such high-performance materials as $CH_3NH_3PbI_3$ may face serious environmental issues in the future. Implementation of perovskite solar cell based on Sn could be an alternative solution for commercialisation. This paper presents the results of a theoretical study of a lead-free, environmentally-friendly photovoltaic cell using $CH_3NH_3SnI_3$ as a light-absorbing layer. The characteristics of a photovoltaic cell based on perovskite were modelled using the SCAPS-1D program. Various thicknesses of the absorbing layer were analysed, and an optimised device structure is proposed, demonstrating a high power conversion efficiency of up to 28% at ambient temperature. The analysis of the thicknesses of the $CH_3NH_3SnI_3$ absorbing layer revealed that at a thickness of 500 nm, performance is demonstrated with an efficiency of 27.41 %, a fill factor of 85.92 %, a short circuit current density of 32.60 mA/cm^2 and an open-circuit voltage of 0.98 V. The obtained numerical results indicate that the $CH_3NH_3SnI_3$ absorbing layer may be a viable replacement for the standard materials and may form the basis of a highly efficient technology of the environmentally-friendly perovskite solar cells.

Keywords: lead-free, electron-transport layer, hole-transport layer, absorption layer, SCAPS-1D.

Introduction

With the rapid economic development, the demand for energy is increasing, as evidenced by the studies of the World Energy Resources, which predicted that the world's oil, gas and coal reserves will be exhausted in about 100 years. In addition, a growing number of studies have shown that problems such as environmental pollution and global warming are the consequences of burning fossil fuels [1]. Along with the problem of the depletion of fossil fuels, pollution and global warming pose significant challenges to the production of energy [2,3]. Thus, finding an alternative source that will be clean, renewable and sustainable to replace fossil fuels is an urgent task today. One of the solutions for the production of energy is the conversion of solar energy as photovoltaics is renewable and pure [4]. Besides, it can be converted into many other types of energy for various purposes. Compared with other alternative energy sources, such as hydropower, wind power, bioenergy, geothermal and nuclear power, photovoltaics is available in larger amounts and is more abundant [5].

A photovoltaic cell is an important energy conversion device that uses solar energy [6,7]. The first solar cell was manufactured using a single crystal of silicon at Bell Laboratories, which demonstrated an energy conversion efficiency (PCE) of 6% in 1954 [8]. However, silicon-based photovoltaic cells had their disadvantages, such as high cost and low PCE, but photovoltaic cells based on perovskite prevent all of these disadvantages [9]. Perovskite solar cells (PSC) based on organometallic lead halides quickly emerged as the fourth generation of photovoltaic technology, featuring high PCE [10]. This advantage made them the strongest competitor of silicon-based photovoltaic cells. To date, the PCE of a photovoltaic converter based on perovskites has reached ~ 26 % in a laboratory environment [11–13].

Recently, much attention has been paid to planar perovskite structures (n-i-p or p-i-n) due to the simplicity of the device architecture and, above all, the manufacturability at low temperatures. It allows to facilitate the use of flexible structures as most flexible substrates, such as poly(ethylene 2,6-naphthalate) and poly(ethylene terephthalate), are damaged by the high temperature required for a mesoscopic configuration [14].

Usually, a perovskite photovoltaic material has the following structure: ABX_3, where A is an organic compound CH_3NH_3, B is Pb or Sn, and X_3 is a halide anion (for example, I^-). The most widespread perovskite is $CH_3NH_3PbI_3$, also referred to as MAPI, or a methylammonium lead triiodide. However, perovskites based on MAPI are toxic due to the presence of Pb, which may destabilise the further commercialization of this material [15]. One of the alternative perovskite materials containing tin instead of lead is methylammonium tin triiodide ($CH_3NH_3SnI_3$ or MASI).

A significant amount of research is being dedicated to developing lead-free PSC, with the tin halide perovskite being one of the most promising alternatives [16]. Tin is widely distributed in nature and has similar electronic properties to lead, since it is a member of the same group in the periodic table. In addition, perovskites based on tin halide have excellent light absorbing properties and high carrier mobilities [17]. Additionally, tin-based perovskites provide a high theoretical PCE due to a smaller band gap than the equivalent lead-based perovskites [18].

The transport layer plays a vital role in determining the PCE of a photovoltaic cell. The materials used as the transport layer must fulfil a number of requirements. Firstly, the transport layer must have high transparency for the charge transfer so that the maximum amount of energy enters the perovskite layer. Secondly, it is necessary to have such a material in which the electrons are holes moving fast enough to ensure a rapid charge transfer from one layer to another. It is also necessary to employ a material with good chemical and physical stability in the environment so that it does not react with the other layers of the photovoltaic cell. To collect charge carriers efficiently, it is common to use additional layers such as ETL and HTL. The functional purpose of the ETL is to block holes, collect electrons from the perovskite layer and then deliver them to the anode. Besides, the ETL must have a high transmittance from ultraviolet to the visible regions so that all photons passing through this layer are maximally absorbed by the perovskite. Today, materials used as the ETL include TiO_2, SnO_2, SiO_2, ZnO, etc. In this research, TiO_2 was taken as the ETL since it was possible to achieve the maximum PCE by using this material. Similarly, the functional purpose of the HTL is to block electrons, collect holes from the perovskite layer and then deliver them to the cathode. In this research, Spiro-OMETAD was used as an HTL as this material is widely used as an HTL since the emergence of the first solid perovskite. The key issue for polymer photovoltaic cells based on perovskites is the mobility of the charge carriers. In a photovoltaic cell with a bulk heterojunction, the electron-to-hole mobility ratio can be controlled by replacing one of the donor or acceptor materials.

It should be noted that the experimental research of photovoltaic cell devices is an expensive and laborious process. Therefore, it is common in many scientific fields to perform simulations to obtain an effective structure of a photovoltaic cell. Numerical studies provide opportunities to solve these kinds of problems and help predict/optimize the performance of the device. In this paper, a photovoltaic cell based on perovskites will be modelled using the SCAPS-1D program, which is based on the continuity equations for holes and electrons, as well as the Poisson equation.

Methodology

The simulated photovoltaic cell is shown in Fig. 1 and consists of three main layers: TiO_2 (electron transport layer (ETL))/$CH_3NH_3SnI_3$ (perovskite light-absorbing layer)/Spiro-OMeTAD (hole transport layer (HTL)). It should be noted that recently the numerical analysis in the SCAPS-1D program (version 3.3.09) has become popular as it has proven its effectiveness in various scientific works [19–22]. SCAPS-1D operates by solving the Poisson equation and the continuity equation for electrons and holes. The Poisson equation states:

$$\frac{d^2}{dx^2}\psi(x) = \frac{e}{\varepsilon_0 \varepsilon_r}\left(p(x) - n(x) + N_D - N_A + \rho_p - \rho_n\right), \quad (1)$$

where ψ is the electrostatic potential; e is the elementary charge; ε_0 and ε_r are the dielectric constant in vacuum and the relative dielectric constant of a material; p and n are the concentrations of holes and electrons, respectively; N_D and N_A are the donor and acceptor impurities; ρ_P and ρ_n are the distributions of holes and electrons, respectively.

To describe the dependence of electrons and holes, the following continuity equation is used:

$$\frac{dJ_n}{dx} = G - R, \quad (2)$$

.

$$\frac{dJ_p}{dx} = G - R, \tag{3}$$

where J_n and J_p are the current density of the electrons and holes; R is the recombination rate; G is the generation rate.

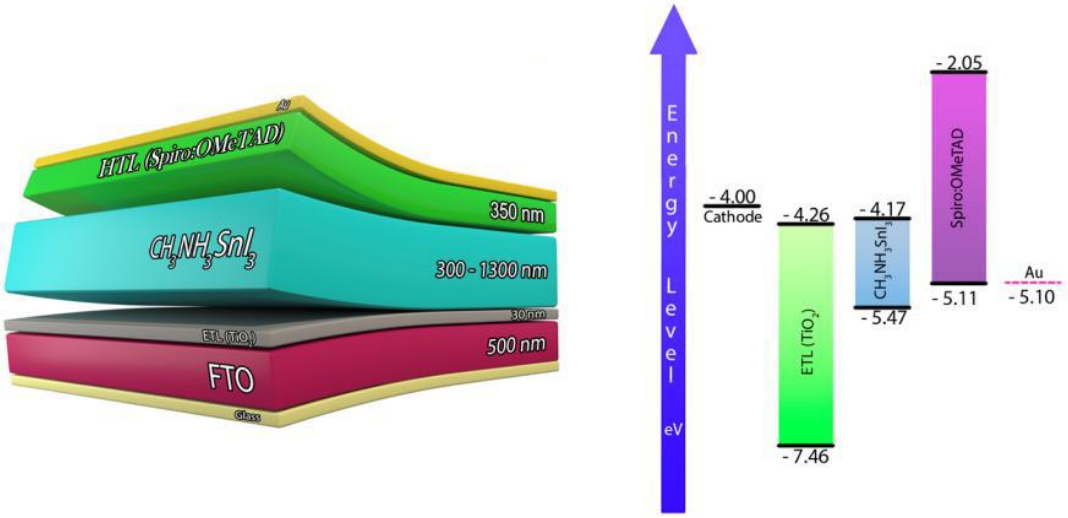

Fig.1. Initial structure of the simulated solar cell

Drift and diffusion move carriers in semiconductors, which can be represented using the equations:

$$J = J_n + J_P, \tag{4}$$

$$J_n = D_n \frac{dn}{dx} + \mu_n n \frac{d\psi}{dx}, \tag{5}$$

$$J_p = D_p \frac{dp}{dx} + \mu_p p \frac{d\psi}{dx}, \tag{6}$$

where J - is the current density; J_n and J_p are the current density of the electrons and holes; D_n and D_p are the diffusion coefficients for electrons and holes; $\frac{dn}{dx}$ and $\frac{dp}{dx}$ are the concentration gradients for electrons and holes; n and p - electron and hole concentrations, μ_n and μ_p - electron and hole mobilities.

The initial technological and geometric parameters of the simulated solar cell were taken from the experimental photovoltaic cell and are presented in Table 1 [19–21]. Table 1 shows the parameters of the semiconductor of each layer as well as the electrical properties of the contacts used in the simulation in this research.

Results and discussion

It should be noted that the optical-electrical characteristics of an organic photovoltaic cell are more dependent on the thickness of the perovskite (absorber) layer. When the thickness of the photovoltaic cell changes, such parameters of the device as short-circuit current, generation and recombination of carriers, mechanism of charge transfer, etc. change as well. Thus, a thicker perovskite layer absorbs more light and generates more electron holes. However, it should be noted that in a thicker layer, the recombination rate increases due to the longer path travelled by the charges, which reduces the PCE of a photovoltaic cell. In this research, the influence of the thickness of the perovskite layer ($CH_3NH_3SnI_3$) on the PCE of a photovoltaic cell was studied through computer simulation. Numerical research was carried out in the AM1.5G solar spectrum at a power of P=1000W/m^2.

Table 1. Parameters of solar cells [19–21].

Parameters	**FTO**	**TiO_2**	**$CH_3NH_3SnI_3$**	**Spiro-OMETAD**
Thickness (nm)	500*	30*	300-1300*	350*
Band gap (eV)	3.50	3.20	1.30	3.06
Electron affinity (eV)	4.00	4.26	4.17	2.05
Dielectric permittivity	9.0	32.0	8.2	3.0
CB effective density of states (cm^{-3})	2.20×10^{18}	1×10^{19}	1×10^{18}	2.20×10^{18}
VB effective density of states (cm^{-3})	1.80×10^{19}	1×10^{19}	1×10^{18}	1.80×10^{19}
Electron thermal speed (cm/s)	1×10^{7}	1×10^{7}	1×10^{7}	1×10^{7}
Hole thermal speed (cm/s)	1×10^{7}	1×10^{7}	1×10^{7}	1×10^{7}
Electron mobility (cm^2/Vs)	20.0	20.0	1.6	2×10^{-4}
Hole mobility (cm^2/Vs)	10.0	10.0	1.6	2×10^{-4}
Shallow donor density N_D (cm-3)	10^{19}	10^{17}	0	0
Shallow acceptor density N_A (cm^{-3})	0	0	1×10^{14}	2×10^{18}
Defect density N_t (cm^{-3})	1.0×10^{14}	1.0×10^{14}	2.5×10^{13}	1.0×10^{15}
*in this research				

Optimisation of the photovoltaic cell was carried out by changing the thickness of the absorbing layer $CH_3NH_3SnI_3$ 300 nm, 500 nm, 700 nm, 900 nm, 1100 nm and 1300 nm at a fixed temperature of 300K, keeping all other parameters and layer thicknesses the same. Considering the complexity of the device and the large choice of materials for PSC, the use of numerical calculation methods allows obtaining important information on the main solar characteristics of the modified PSC. Modelling in SCAPS-1D was done using the parameters shown in Table 1, based on earlier theoretical and experimental works. In this work, the thicknesses of the transport layers were fixed, and special attention was paid to the perovskite absorbing layer. Transport layers play an important role in PSC, because they not only carry cations from the absorbing layer to the electrode, but also act as a separator.

Accordingly, the series resistance of the PSC increases with the increase in the thickness of the charge transport layer, which leads to charge recombination, as it becomes more difficult for holes and electrons to reach the anode and cathode, respectively. Thus, the optimal ETL thickness should be as small as possible to provide good blocking properties at the tops of the layers, resulting in fast electron transfer and low resistive losses [23]. For HTL, the layer thickness is also of great importance, since the minimum time for the charge to pass through the layers will increase the main characteristics of the PSC by increasing the conductivity and reducing the probability of recombination [24–27].

The changes in the thickness of the absorbing layer help determine the best performance of the photovoltaic cell, which can be a decisive factor. Fig. 2 shows the current-voltage characteristics due to different thicknesses of the $CH_3NH_3SnI_3$ absorbing layer.

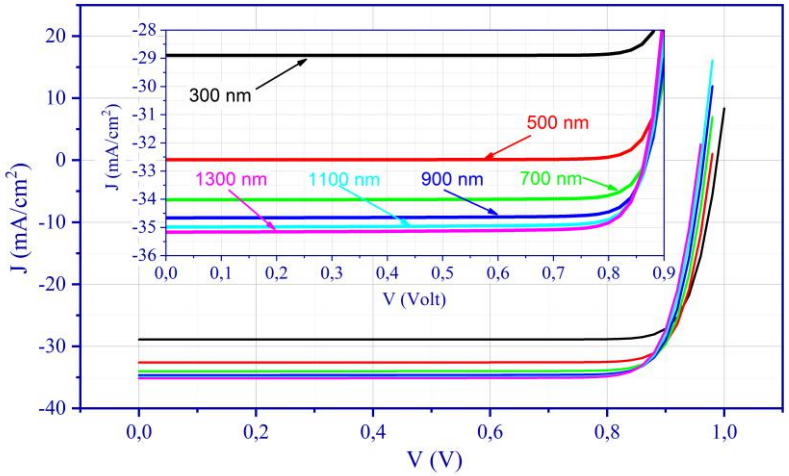

Fig.2. Current-voltage characteristic of a simulated solar cell FTO/TiO_2/$CH_3NH_3SnI_3$/Spiro-OMETAD/Au with different thicknesses of the absorbing layer

It should be noted that the short-circuit current for the absorber layer thickness of 1100-1300 nm is the highest one compared with the other thicknesses. Fig. 3 demonstrates the comparison of the short-circuit current and open-circuit voltage of a tin-based perovskite cell for the thicknesses ranging from 300 nm to 1300 nm.

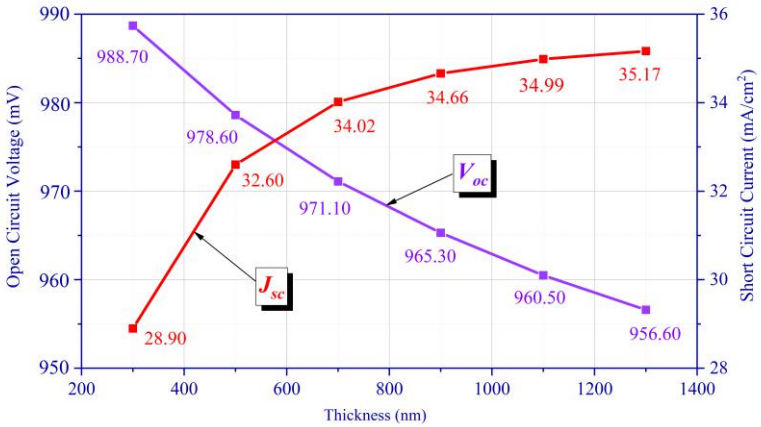

Fig.3. Dependence of the short-circuit current and open-circuit voltage on the thickness

The thickness of the absorber layer plays a significant role in determining the quality and performance of a thin-film PSC. Fig. 4 depicts the changes in the fill factor and PCE with the various thicknesses of the absorbing layer. As can be seen from the figure, the PCE increases with the increase in the thickness of the perovskite layer. However, starting from a thickness of 900 nm, the PCE reaches a plateau and is equal to ~ 29%. It can be seen that as the thickness of the perovskite layer increases, a significant increase in PCE and J_{SC} is observed. This observation can be explained by an increase in the light absorption in the absorbing layer. It facilitates the production of excitons and, therefore, leads to an increase in PCE. However, a further increase in the thickness of the absorber layer to 900 nm leads to higher resistance and higher recombination rates. At first, it leads to a plateau and then to a decrease in the corresponding parameters.

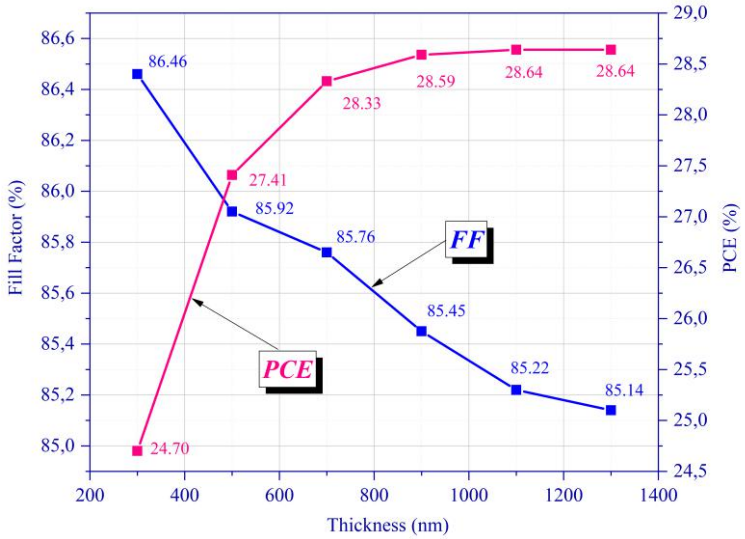

Fig.4. Dependence of the fill factor and PCE on the thickness of the absorbing layer

To prove the reliability of the simulated solar cell, a comparison with the other works on PSCs based on $CH_3NH_3SnI_3$ is shown in Table 2. The analysis of the PCE and the other parameters of the simulated photovoltaic cells the previous studies demonstrated in combination with the results of this research allows to conclude that the model used in this research is reliable. Analyzing works [28–31], one can draw some conclusions regarding the change in the thickness of the absorber layer, in particular, with an increase in the thickness of the absorber, PCE PSC increases, and one can also notice a tendency towards a decrease in FF. This can be explained by the fact that in the case of an increase in the thickness of the absorbing layer, the

energy absorption also increases due to the generation of a larger number of electron-hole pairs. Basically, the decrease in FF is due to the internal recombination of the PSC, which most likely occurs due to the short lifetime of charge carriers (electrons and holes), which leads to a short time for the creation of a conduction band in the PSC.

Table 2. Performance comparison of simulated tin-based PSCs with various device architectures.

Structure	Optimized thickness of the absorber layer (nm)	V_{OC}, V	J_{SC}, mA/cm^2	FF, %	PCE, %	Ref.
TCO//TiO_2/$CH_3NH_3SnI_3$/Spiro-OMETAD/Anode	350	0.67	17.60	44.20	5.15	[28]
FTO/TiO_2/$CH_3NH_3SnI_3$/ Spiro-OMeTAD/Au	350	0.67	16.99	47.67	5.42	[29]
FTO/TiO_2/$CH_3NH_3SnI_3$/ Spiro-OMeTAD/Au	1000	0.91	32.47	65.82	19.51	[30]
FTO/TiO_2/$FASnI_3$/Spiro-OMETAD/Au	2000	1.81	31.20	33.72	19.08	[31]
FTO/TiO_2/$CH_3NH_3SnI_3$/Spiro-OMETAD/Au	1100	0.96	34.99	85.22	28.64	This work

In general, by optimizing the parameters it is possible to achieve a PCE value of ~ 28%, which is an increased PCE value compared to previous works. The simulation results of this work provide the best indicators of the main characteristics of the PCE, which can then be used to predict the efficiency of PSC devices.

Conclusion

In this study, we simulated a lead-free PSC using the structure FTO/TiO_2/$CH_3NH_3SnI_3$/Spiro-OMETAD/Au by means of the SCAPS-1D simulation kit to investigate the performance limit of the given perovskite absorber layer. Particularly, the influence of the active layer thickness on the PCE of the photovoltaic cell was analysed, and the device structure was optimised accordingly. We observe a trade-off between increasing the short-circuit current by enhancing light absorption for the thicker absorber layer and minimizing the loss in the open-circuit voltage and fill factor through carrier recombination for the thinner layer. As a result, this trade-off yields the optimised thickness of the "ideal" perovskite layer free of traps and defects in the range of 1100-1300 nm. This results in the following maximum output cell parameters: J_{SC} = 35.17 mA/cm^2, V_{OC} = 0.96 V, *FF* = 85.14 %, *PCE* = 28.64 %. For comparison, the proposed model of a tin-based PSC with an absorbing layer thickness of 500 nm, which is more standard in terms of fabrication, demonstrates a *PCE* of 27.41 %, a short-circuit current density of 32.60 mA/cm^2, an open-circuit voltage of 0.98 V and a *FF* of 85.92 %. The presented model is intended for further application in the development of environmentally-friendly and lead-free PSCs.

Acknowledgments

These studies have been carried out with the financial support of the Ministry of Education and Science of the Republic of Kazakhstan under grant AP08855738.

The authors acknowledge the provision of SCAPS-1D software by Prof. Marc Burgelman.

REFERENCES

1 Klöckner K., Letmathe P. Is the coherence of coal phase-out and electrolytic hydrogen production the golden path to effective decarbonisation? *Applied Energy*, 2020, Vol. 279, pp. 115779. doi: 10.1016/j.apenergy.2020.115779.

2 Carneiro A.L. et al. Energy consumption and carbon footprint of perovskite solar cells. *Energy Reports*, 2022, Vol. 8, pp. 475–481. doi: 10.1016/j.egyr.2022.01.045.

3 Gür T.M. Carbon Dioxide Emissions, Capture, Storage and Utilization: Review of Materials, Processes and Technologies. *Progress in Energy and Combustion Science*, 2022, Vol. 89, pp. 100965.

4 Martinho F. Challenges for the future of tandem photovoltaics on the path to terawatt levels: a technology review. *Energy & Environmental Science*, 2021, Vol. 14, No. 7, pp. 3840–3871. doi: 10.1039/D1EE00540E.

5 Cousse J. Still in love with solar energy? Installation size, affect, and the social acceptance of renewable

.

energy technologies. *Renewable and Sustainable Energy Reviews*, 2021, Vol. 145, pp. 111107.

6 Jena A.K., Kulkarni A., Miyasaka T. Halide Perovskite Photovoltaics: Background, Status, and Future Prospects. *Chemical Reviews*, 2019, Vol. 119, No. 5, pp. 3036–3103. doi: 10.1021/acs.chemrev.8b00539.

7 Reddy S.H., Di Giacomo F., Di Carlo A. Low-Temperature-Processed Stable Perovskite Solar Cells and Modules: A Comprehensive Review. *Advanced Energy Materials*, 2022, Vol. 12, No. 13, pp. 2103534.

8 Chapin D.M., Fuller C.S., Pearson G.L. A New Silicon p-n Junction Photocell for Converting Solar Radiation into Electrical Power. *Journal of Applied Physics*, 1954, Vol. 25, No. 5, pp. 676–677. doi: 10.1063/1.1721711.

9 Green M.A. et al. Solar cell efficiency tables (Version 53). *Progress in Photovoltaics: Research and Applications*, 2019, Vol. 27, No. 1, pp. 3–12. doi: 10.1002/pip.3102.

10 Zu F. et al. Illumination-Driven Energy Level Realignment at Buried Interfaces between Organic Charge Transport Layers and a Lead Halide Perovskite. *Solar RRL*, 2022, pp. 2101065. doi: 10.1002/solr.202101065.

11 Jeong M. et al. Stable perovskite solar cells with efficiency exceeding 24.8% and 0.3-V voltage loss. *Science*, 2020, Vol. 369, No. 6511, pp. 1615–1620. doi: 10.1126/science.abb7167.

12 Min H. et al. Perovskite solar cells with atomically coherent interlayers on SnO2 electrodes. *Nature*, 2021, Vol. 598, No. 7881, pp. 444–450. doi: 10.1038/s41586-021-03964-8.

13 Park S.Y., Zhu K. Advances in SnO 2 for Efficient and Stable n–i–p Perovskite Solar Cells. *Advanced Materials*, 2022, pp. 2110438. doi: 10.1002/adma.202110438.

14 Herterich J. et al. Ion Movement Explains Huge V OC Increase despite Almost Unchanged Internal Quasi-Fermi-Level Splitting in Planar Perovskite Solar Cells. *Energy Technology*, 2021, Vol. 9, No. 5, pp. 2001104.

15 Morana M., Malavasi L. Pressure Effects on Lead-Free Metal Halide Perovskites: a Route to Design Optimized Materials for Photovoltaics. *Solar RRL*, 2021, Vol. 5, No. 11, pp. 2100550. doi: 10.1002/solr.202100550.

16 Ghimire S. et al. Structural Reconstruction in Lead-Free Two-Dimensional Tin Iodide Perovskites Leading to High Quantum Yield Emission. *ACS Energy Letters*, 2022, Vol. 7, No. 3, pp. 975–983.

17 Wuttig M. et al. Halide Perovskites: Advanced Photovoltaic Materials Empowered by a Unique Bonding Mechanism. *Advanced Functional Materials*, 2022, Vol. 32, No. 2, pp. 2110166. doi: 10.1002/adfm.202110166.

18 Meier F. et al. Charge Carrier Dynamics of Multiple-Cation Mixed-Halide Perovskite Thin Films. *The Journal of Physical Chemistry C*, 2021, Vol. 125, No. 31, pp. 17411–17417. doi: 10.1021/acs.jpcc.1c04302.

19 Deepthi Jayan K., Sebastian V. Comprehensive device modelling and performance analysis of MASnI3 based perovskite solar cells with diverse ETM, HTM and back metal contacts. *Solar Energy*, 2021, Vol. 217, pp. 40–48.

20 Patel P.K. Device simulation of highly efficient eco-friendly CH3NH3SnI3 perovskite solar cell. *Scientific Reports*, 2021, Vol. 11, No. 1, pp. 3082. doi: 10.1038/s41598-021-82817-w.

21 Singh A.K. et al. Performance optimization of lead free-MASnI3 based solar cell with 27% efficiency by numerical simulation. *Optical Materials*, 2021, Vol. 117, pp. 111193. doi: 10.1016/j.optmat.2021.111193.

22 Kanoun A.-A. et al. Toward development of high-performance perovskite solar cells based on CH3NH3GeI3 using computational approach. *Solar Energy*, 2019, Vol. 182, pp. 237–244. doi: 10.1016/j.solener.2019.02.041.

23 Tariq Jan S., Noman M. Influence of layer thickness, defect density, doping concentration, interface defects, work function, working temperature and reflecting coating on lead-free perovskite solar cell. *Solar Energy*, 2022, Vol. 237, pp. 29–43. doi: 10.1016/j.solener.2022.03.069.

24 Zeinidenov A. et al. The effect of MoO3 interlayer on electro-physical characteristics of the perovskite solar cells. *Synthetic Metals*, 2021, Vol. 281, pp. 116903. doi: 10.1016/j.synthmet.2021.116903.

25 Aimukhanov A.K. et al. Influence of surface structure and morphology of PEDOT: PSS on its optical and electrophysical characteristics. *Bulletin of the Karaganda University. Physics series.*2021, Vol. 103, No. 3, pp. 93–100.

26 Rombach F.M., Haque S.A., Macdonald T.J. Lessons learned from spiro-OMeTAD and PTAA in perovskite solar cells. *Energy & Environmental Science*, 2021, Vol. 14, No. 10, pp. 5161–5190. doi: 10.1039/D1EE02095A.

27 Aimukhanov A.K. et al. The influence of structural and charge transport properties of <scp>PEDOT</scp> : <scp>PSS</scp> layers on the photovoltaic properties of polymer solar cells. *Polymers for Advanced Technologies*, 2021, Vol. 32, No. 2, pp. 497–504. doi: 10.1002/pat.5102.

28 Salem M.S. et al. Analysis of Hybrid Hetero-Homo Junction Lead-Free Perovskite Solar Cells by SCAPS Simulator. *Energies*, 2021, Vol. 14, No. 18, pp. 5741. doi: 10.3390/en14185741.

29 Abdelaziz S. et al. Investigation of lead-free MASnI3-MASnIBr2 tandem solar cell: Numerical simulation. *Optical Materials*, 2022, Vol. 123, pp. 111893. doi: 10.1016/j.optmat.2021.111893.

30 Deepthi Jayan K., Sebastian V. Comprehensive device modelling and performance analysis of MASnI3 based perovskite solar cells with diverse ETM, HTM and back metal contacts. *Solar Energy*, 2021, Vol. 217, pp. 40–48.

31 Kumar M. et al. An optimized lead-free formamidinium Sn-based perovskite solar cell design for high power conversion efficiency by SCAPS simulation. *Optical Materials*, 2020, Vol. 108, pp. 110213.

Article accepted for publication 25.03.2022

DOI 10.31489/2022No2/65-70

UDC 536.24:532.526

LOCAL APPROACH TO IMPROVE THE AERODYNAMIC CHARACTERISTICS OF THE FINAL DRYING PROCESS

Suprun T.T.

Institute of Engineering Thermophysics, National Academy of Sciences of Ukraine, Kyiv,
suprun@secbiomass.com

Energy-saving technologies are widely used in various technological processes, in particular for the final drying of plant waste. The purpose of the study is to ensure optimal flow distributions and making targeted changes in the design of the coolant supply system based on measurements of local velocities at characteristic points in space, using the methods of hot-wire anemometry. The measurements were carried out in stages and covered eight modifications of the installation. Based on the analysis of the data obtained, specific measures were developed to improve the design of the coolant supply system.

Keywords: coolant supply system, local aerodynamic characteristics

Introduction

Currently energy-saving technologies are widely used in various technological processes, in particular, in drying processes. One of these technologies is the use of a jet system. Impact jets are often used in industry to dry, cool or heat a variety of products. Impact drying and cooling is especially common for continuous sheets such as paper, textiles, and metals. For example, results described in [1] for heat transfer mechanism of a slit jet impingement, will help to optimize cooling equipment and controlled parameters for the industrial-scale hot steel strip/plate cooling technology.

Another drying technology using a jet system has been developed at the Institute of Engineering Thermophysics (IET) of NASU. This technology was used for the secondary processing of waste of the original product, in particular plant raw materials. The use of dried plant waste as additional products for the food, pharmaceutical, and tobacco industries is a significant factor in energy saving. In this technology the final drying of plant raw materials with subsequent technological conditioning is carried out in a single-tier conveyor drying unit by vertical blowing of the coolant in a thin layer of the processed material.

One of the criteria for ensuring the high quality of the resulting product is the organization of the optimal flow distribution of the coolant along the entire working line in the presence of a layer of plant raw materials that is being processed. A significant role in the organization of such a flow distribution is assigned to the coolant supply system, which in this case was formed by rows of slots through which vertical jets flow, blowing a conveyor working line. The intensity of the heat and mass transfer process is determined precisely by the parameters of the coolant supply system (velocity and temperature), as well as by the flow conditions around the layer of the processed product.

The organization of the optimal coolant flow distribution was carried out using the local approach adopted at the IET NASU [2]. The main parameters characterizing the flow distribution are the absolute values of the average velocity and the degree of local velocity field non-uniformity at the characteristic points of the working zone. The values of these parameters are set based on a preliminary assessment of the intensity of heat and mass transfer, taking into account the upper velocity limit, which ensures high quality of the processed material and does not move the material outside the working line. For this installation, the recommended values are U_{av}~0.5-0.8 m/s with a permissible degree of non-uniformity 0.6-1.8.

Despite the fact that the design of the installation is preceded by an aerodynamic calculation of the coolant supply system, the influence of the structural elements of the installation on the hydrodynamic structure of the flow is not sufficiently taken into account. As a result, in practice, deviations from the calculation results are observed.

To study the processes of heat and mass transfer occurring in difficult conditions, typical for various heat and power equipment, physical modeling is one of the most successful methods [3]. Therefore, to test

.

the installation before its commissioning on a full-scale model, pilot tests are carried out on an experimental model, during which the discovered shortcomings are eliminated.

The article presents the results of a local approach in aerodynamic tests of an experimental model of an installation for final drying and technological conditioning of plant raw materials, the purpose of which was to ensure optimal flow distributions based on measurements of local velocities at characteristic points in space and making targeted changes in the design of the coolant supply system. Taking into account the obtained experimental data, specific measures were developed to improve the system for supplying the coolant to the working line. As a result, it was possible to significantly improve the design of the installation and provide the required flow distribution parameters.

Experimental technique

This section describes the design of a specially made experimental model, which fully reproduces the operating conditions of the installation in terms of geometric parameters and the air supply system. The main difference was that the experiments were carried out without heating the coolant (air) and with a fixed working line. The processed material was located on a horizontal working line in the form of a thin layer and was blown with vertical air jets. To assess the uniformity of the flow velocity field, the hot-wire method of measurements was used. Such method is commonly applied to study the structure of complex flows in a wide range of velocities [4], starting from 0.1 m/s, as was the case in the present setup. The calibrations of the hot-wire anemometer sensors were carried out in a special low-speed calibration device developed by IET of NASU. This device allows calibration in the velocity range starting from 0.1 m/s. Simultaneously with the values of the time-average velocity (U , m/s) the hot-wire method makes it possible to determine the value of longitudinal pulsations ($^{u'}/_{U}$, %), which, as is known [5], has a significant effect on the intensity of heat and mass transfer processes.

As can be seen from Fig. 1, the original plant material (1) is placed on a fixed working line, which is a thin metal plate (2) perforated with holes 4 mm in diameter. The working line is blown with vertical air jets flowing from the system of longitudinal slots (3). The slots were formed using corners (4) with movable walls (5) fixed in the air distribution box, which made it possible to independently adjust the slot width over a wide range (from 3 to 14 mm) to ensure the required flow rate through each slot. On the surface of the air distribution box with an area of 1.5x2 m^2 33 rows of slots were placed, the distance between the axes of which was 59 mm. To improve the mixing of the jets 33 cylindrical rods with a diameter of 8 mm were placed behind the slots.

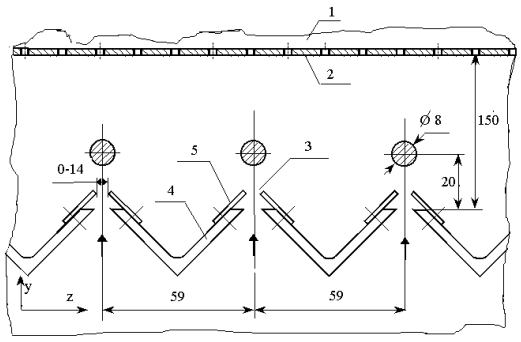

Fig. 1. Scheme of air supply to the working line: 1 - plant material; 2 - perforated metal plate; 3 - a system of longitudinal slots; 4 - corners; 5 - movable walls;

As shown in Fig. 2, the distribution box consisted of two parts: the input and the main one, where the rows of slots were located. The rows were counted along the flow in the z direction. The beginning of each row was counted from the main part of the box in the x direction, and the end corresponded to the dead end zone of the main part. In this case, y was measured behind a specific element (slot, cylinder, or working line) in the vertical direction, i.e. in the direction of the jets flowing from the slots. Both parts of the box were confused, which was supposed to provide the necessary amount of air to the periphery, i.e.to the last rows and to the end of all rows of slots.

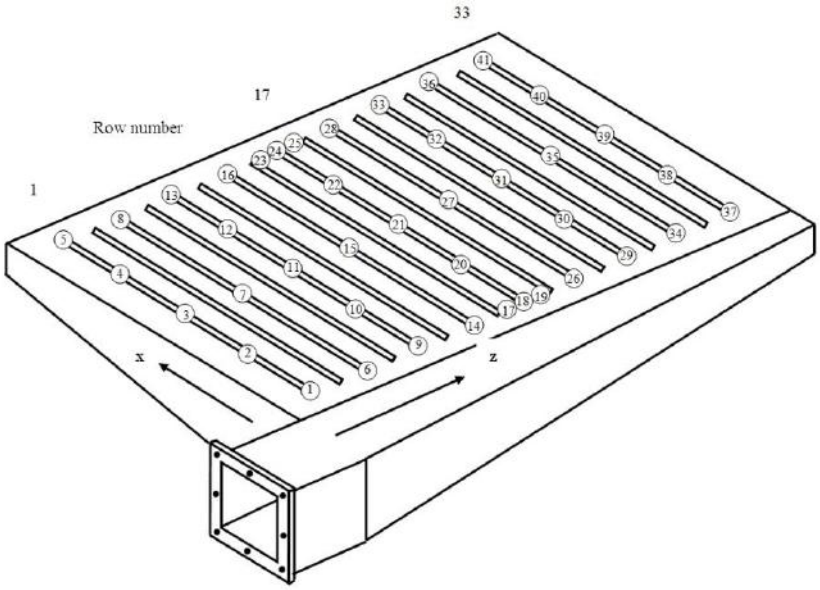

Fig.2. Location of rows and measurement points

The hot-wire anemometer sensor was installed in a special coordinate device, which allows it to be moved along the coordinate axes and fixed at a selected point in the measuring space. The non-uniformity of the flow velocity field was estimated based on the results of measurements at various points in space. For convenience, the measurement points were chosen above the odd rows. The location of the 41 measurement points is shown in Fig. 2, where only the odd rows of slots are shown.

Results and Discussion

Analysis of the measurement results using the local approach gave a complete picture of the spatial non-uniformity of the flow in the entire measuring volume. Based on local flow control, it was possible to carry out targeted measures to change airflow rates. In total, eight design modifications were tested and specific measures were developed to improve the coolant supply system.

To assess the non-uniformity of the velocity field, the so-called non-uniformity coefficient k was introduced, representing the ratio of the local velocity at a given point U to the average velocity U_{av}:

$$k = {}^{U}/_{U_{av}}, \tag{1}$$

where U_{av} were determined from n measurement data:

$$U_{av} = \sum_1^n {}^{U}/_{n}. \tag{2}$$

To obtain a general idea of the initial non-uniformity of the flow distribution, the measurement results of modification 1 were used. As can be seen from the analysis of the data presented in Fig. 3, the velocity field was characterized by a significant non-uniformity.

In the first measuring section, located near the beginning of the rows (x =40 mm), the velocities varied from 0.343 m/s in the last row to 0.76 m/s in the 17th central row, with the velocity maximum located in the central row (z =1000 mm). In the second measuring section (x =750 mm) the picture changed qualitatively: the velocity maxima took place in the first and last rows at a higher velocity level (from 1.1 to 2.3 m/s). In the last section (x =1460 mm) the velocity maximum took place in the last row (3.56 m/s), while in the first row the velocity was 1.4 m/s. At the same time, the velocity field non-uniformity along the length of the rows was much greater, reaching ~10 times in the last row. The average velocity calculated from the results of measurements at 13 points was U_{av} =1.6 m/s. The difference in velocities on both sides of the central slot indicated the propagation of the central jet at a certain angle to the working line. It can be caused both by the design of the slot itself and by the influence of the cylinder installed behind it.

.

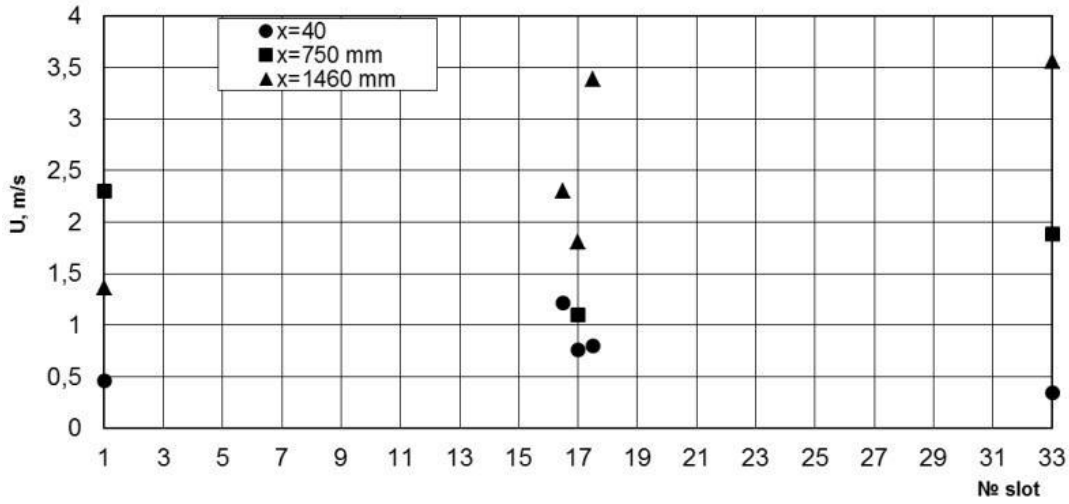

Fig.3. Velocity distribution in modification 1

Based on the obtained measurements, the following main conclusions were drawn:

– velocity distributions are non-uniform, as evidenced by the change in k within the same order;

– in general, higher velocities are observed at the periphery (i.e. in the last row and at the end of the rows);

Thus, based on the local approach, it was confirmed that the initial design of the installation does not satisfy the optimal parameters of the coolant supply system. The obtained experimental data on the non-uniformity of the velocity field formed the basis for measures to improve the installation. In particular, the increase in velocities at the periphery (i.e., in the last row and at the end of all rows) was associated, first of all, with a significant compression of the flow in the confusers of the inlet and main parts of the box. Since the design of the box could not be changed, it was decided to eliminate this defect by adjusting the width of the slots. The general trend of this measure is to widen the slots at the beginning of the rows to increase velocity and narrow them at the end of the rows to decrease it (Table 1).

Table 1. Width of the slots (mm)

Row number	1	2	3	4	5	6	7	8	9	10	11	12	13	14	15	16
x =0 mm	14	14	14	14	14	9	9	9	9	9	9	9	9	9	9	9
x =750 mm	7	7	7	7	9	9	9	9	9	9	9	9	9	9	9	9
x =1500 mm	4	4	4	4	4	4	4	4	4	4	4	4	4	4	4	4

continuation

Row number	17	18	19	20	21	22	23	24	25	26	27	28	29	30	31	32	33
x =0 mm	9	9	9	13	13	13	13	13	13	13	13	14	14	14	14	14	14
x =750 mm	9	9	9	8	8	8	8	8	8	7	7	7	7	8	8	8	8
x =1500 mm	4	4	4	4	4	4	4	4	4	4	4	4	3	3	3	3	3

Another measure to improve the non-uniformity of the velocity field was the partial covering of the slots at the ends of the rows.

Based on the measurements, air leaks through the leaky parts of the main box in the area of the first and last rows ends were also diagnosed and then eliminated.

The next measure to improve the aerodynamic characteristics of the installation was the elimination of cylindrical rods, which were originally installed to improve the mixing of jets. It should be noted that the presence of rods in the air supply system:

– generally complicate the air supply system;

– makes it difficult to clean the cracks due to the ingress of plant materials particles into them;

– rods create additional aerodynamic resistance;

– contribute to flow instability and to form the so called “Von Karman” vortex street;

– Lack of strict rules for fixing rods can cause curvature of the flow path.

Based on the known literature data on jet flows (see, for example, [6] and references to it), a preliminary calculation of a system of flat jets was carried out for a given blower capacity of 5000 m^3/h. The calculation results showed that the system of flat jets at a distance of about 30 calibers from the exit of the slot creates a velocity field with a non-uniformity k ≤2.4 at a maximum velocity of 1.3 m/s. These data on the absolute value of the velocity and the non-uniformity of the velocity field correspond to the flow distribution necessary for the reliable operation of the installation. Therefore, it was decided to improve the design of the air supply system by eliminating cylindrical rods.

To confirm the correctness of this measure, control measurements were carried out behind the slots above the working line in the absence of cylindrical rods (modification 8). The measurement results are shown below. In the entire measuring volume (Fig. 4), the velocity field non-uniformity coefficient k changed by no more than ~1.8 at an average velocity U_{av}=0.77 m/s. Thus, in modification 8, compared with the original version 1, a significant improvement in the velocity field was observed both along the rows and along their length.

Comparative analysis of the obtained results with similar data for the modification in the presence of rods makes it possible to detect an increase of up to 35% in the average velocity with the same non-uniformity coefficient. However, this increase in velocity does not move the material from the working line. Visual observations allow us to conclude that in modification 8 the flow conditions have been achieved, which ensure high-quality processing of the material. Fragments of plant material move, lift slightly above the surface of the working line, but practically do not detach from it and are not carried out by the flow into the surrounding space. The measurement results also showed that in modification 8 there is an increase in the degree of flow turbulence, reaching at some points $u'/_U$ = 52% at an average level of ~30% (Fig. 5).

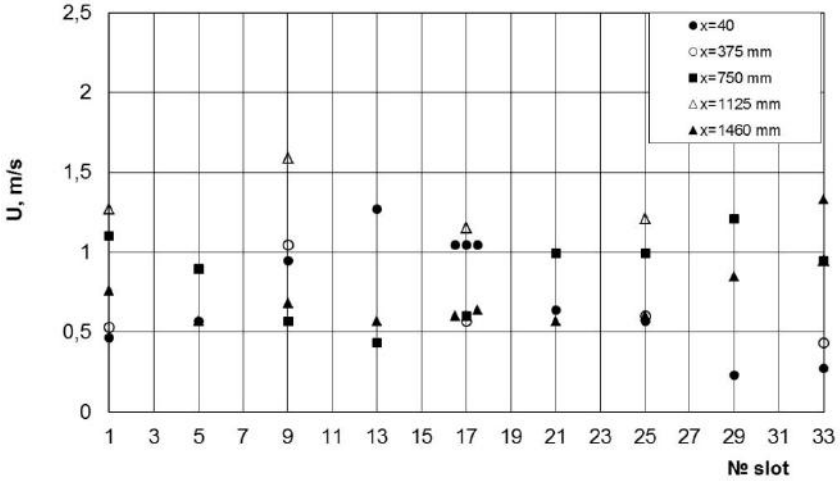

Fig.4. Velocity distribution in modification 8

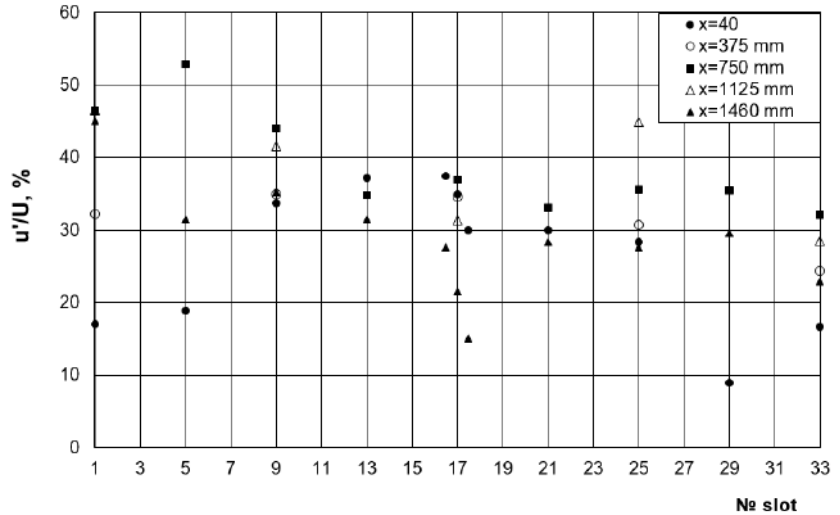

Fig.5. Longitudinal pulsations distribution in modification 8

.

As shown in [5], an increase in both the average flow velocity of the coolant and its degree of turbulence contributes to the intensification of the heat and mass transfer process. This will improve the quality of the product and reduce the drying time. Thus, based on the use of a local approach to obtain the optimal distribution of the coolant flow, specific measures were developed to improve the design of the installation.

Conclusion

The expediency of using a local approach to control the transfer processes in thermal power equipment for various purposes, developed at the ITTF NASU, was also confirmed during aerodynamic studies of the coolant supply system in the technology of final drying and technological conditioning of plant materials. Using hot-wire measurement technique, the values of average velocities and non-uniformity in the distributions of local velocities, as well as the degree of turbulence at characteristic points of the working space, were estimated.

The paper considers the results of aerodynamic testing of eight modifications of the installation. Specific measures are proposed to improve the design of the coolant supply system, namely:

- significant changes have been made to the size of the slots;
- at the ends of the rows, the sections of the slots are partially covered;
- minimized leakage in the distribution box;
- rows of cylindrical rods were eliminated;

As a result of the measures taken it was possible to achieve the optimal values of the average velocity U_{av} ~0.8 m/s with a coefficient of non-uniformity k =0.6-1.8, which provides the required quality of material processing without removing fragments of plant material outside the working line.

The introduction of an improved coolant supply system contributes to its productivity while reducing the time of drying and conditioning processes by intensifying heat and mass transfer because of increasing the average velocity of the highly turbulent coolant flow. Aerodynamic tests have confirmed the necessity of carrying out of the finishing experiments on prototypes in full-scale conditions before commissioning a specific installation. Such experiments make it possible to eliminate the existing shortcomings, work out a more efficient version of the designs, and ensure the reliability of the installation during operation.

REFERENCES

1 Bingxing Wang, Zhixue Liu, Bo Zhang, Zhaodong Wang, Guodong Wang. Heat Transfer Characteristic of Slit Nozzle Impingement on High-temperature Plate Surface. *ISIJ International*. 2019, Vol. 59, Issue 5, pp. 900-907 https://doi.org/10.2355/isijinternational.ISIJINT-2018-576

2 Suprun T.T. Local approach for evaluating heat transfer of prismatic elements on a flat surface. *Eurasian phys. tech. j.* 2021, Vol.18, No. 3 (37), pp. 43-47. doi: 10.31489/2021No3/43-47.

3 Suprun T. Physical modeling the unsteady flow with wakes. *Eurasian phys. tech. j.* 2017, Vol.14, No. 2(28), pp. 113 - 119. http://phtj.ksu.kz/files_phtj/2018.01/19.pdf

4 Bradshaw P. *An Introduction to Turbulence and its Measurement*. Mir, Moscow, 1974, 345 p. [in Russian]

5 Epik E.Ya., Suprun T.T. Impulse and heat transport processes at bypass transition. *Eurasian phys. tech. j.* 2007, Vol.4, No.1(7), pp. 52-57

6 Dyban E.P., Mazur A.I. *Convective heat transfer in jet stream flow of bodies*. Naukova Dumka, Kiev,1982, 303 p. [in Russian]

Article accepted for publication 06.04.2022

DOI 10.31489/2022No2/71-74

UDC 536.629.7

MAIN CHARACTERISTICS OF THE HEAT FLOW METER

Karabekova D.Zh.[1], Kissabekova P.A.[1]*, Kucheruk, V. Yu.[2], Mussenova E.K.[1], Azatbek Sh.[1]

[1] E.A. Buketov Karaganda University, Karaganda, Kazakhstan, pika_1666@mail.ru
[2] Vinnytsia National Technical University, Vinnytsia, Ukraine

The problems and prospects of application of non-destructive testing methods for technical diagnostics of the thermal networks state and various technological objects are discussed. The recording of the temperature state of thermal processes by using a flow meter is due to its sensitivity to the change of thermophysical characteristics and the ability to control without the use of an external energy source, etc. The description of the developed device to measuring of the heat flow using of a thermoelectric heat flow converter of a special design is shown. A distinctive feature of the device is the heating element that installed on an insulating layer serving as a support surface. Calibration of the device is proposed to be carried out by replacing the heat flow from the investigated object with the heat flow released in the heating element when an electric current passes through it. The developed device can register the changes in the heat flux density in the range of (25-100) W/m2, which allows it possible to detect the smallest thermal insulation defects.

***Keywords**:* heat flow meter, thermoelectric battery converter, integral sensitivity of heat flow meters, copper-constantan thermocouple, thermal energy.

Introduction

Energy conservation is one of the priorities of the state policy of Kazakhstan. The strategy «Kazakhstan-2050» presented a program of socio-economic development of the Republic of Kazakhstan, aimed at improving energy security. Over the past decade, due to population growth and the rapid industrial development, energy consumption has increased by more than 2 times. The shortage of energy leads to a shift in the worse of socio-economic stability and deterioration of the development of the state as a whole. The main energy problems caused by economic growth, excessive and extremely uneven use of energy resources, and the energy burden of infrastructure on the environment are related to thermal energy. Heating and power generation costs account for up to 45% of the total energy produced in the country. At the same time, more than half of these resources are accounted for by utilities, which are a fundamental component of the development of the economy and the main factor in ensuring the normal life of citizens [1, 2].

In these conditions, measurements, operational control and regulation of thermal parameters are essential, among which a significant place is occupied by heat flow, which has become today the same informative parameter as temperature, pressure, flux, etc. Measurements of heat flows characterizing heat leaks are carried out by a direct method using contact heat flow meters (HFM) of the «auxiliary wall» type [3]. Heat flow meters have a number of advantages over other non-destructive testing methods. They are characterized by high sensitivity to changes in the thermophysical characteristics of the control objects, the possibility of control without using an external energy source, economy, compactness and simplification of its operation. In this regard, of particular interest is development and creation of heat flow devices for heat supply systems are. As the results of numerous studies of thermal insulation of underground heating networks show, the most effective is the method of non-destructive testing based on a comparison of calculated and experimental values of the temperature distribution on the ground surface over heating networks [4-6].

1. Experimental part

Some modifications of heat flow devices are developed in the laboratory «Measurement of thermophysical quantities» of the Department of Engineering Thermophysics named after professor Zh.S. Akylbayev of the E.A. Buketov Karaganda University. The distinctive design of the heat flow device is that it contains a thermoelectric battery converter and a receiving plate, additionally equipped with a temperature-dependent and heating element. In this case, the thermoelectric battery converter is combined with the

.

heating element, and its «active» junctions are combined with the receiving plate, the «passive» junctions are in thermal contact with the heating element. In one of the modifications, the heat flow meter HFM-1M comprises a heating element, which performs the function of a receiving plate, a thermal battery, a thermoelectric battery converter of heat flow, a thermoelectric refrigerator, radiator, an electronic unit for converting and measuring the signal [7,8].

The developed device for measuring heat flow contains an insulating layer 1, which serves as a reference surface on which a heating element 2, a thermoelectric battery converter of heat flow 3, a thermoelectric refrigerator 4, a radiator 5, a measuring unit 6 (figure 1), [9].

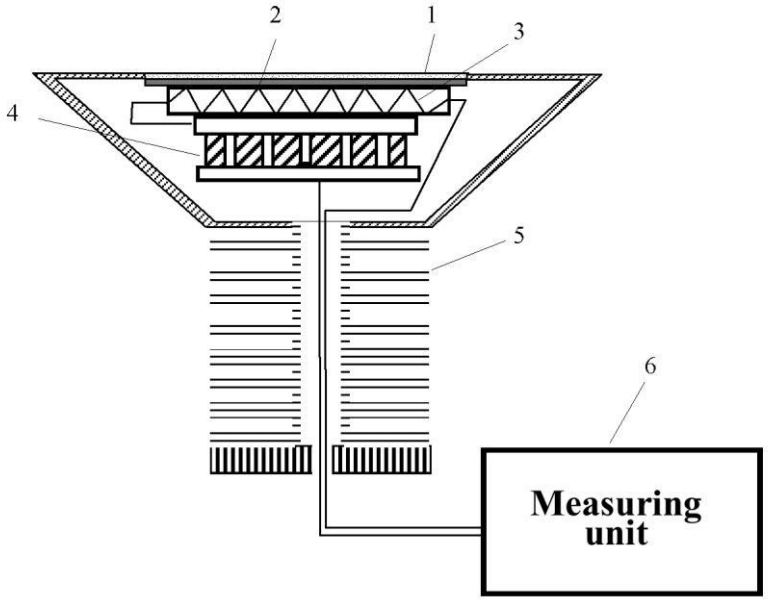

Fig.1. Schematic representation of the device for measuring heat flow:
1 - insulation layer; 2 - heating element; 3 - thermoelectric battery converter of heat flow;
4 - thermoelectric refrigerator; 5 - radiator; 6 - measuring unit

The closest in technical essence to the achieved result to the model is a thermoelectric battery of heat flow converter containing a thermoelectric element battery made of a thermoelectronic wire in the form of a flat spiral, composed of alternating half-turns, covered with a paired thermoelectrode material, a copper constantan, spaced to the thickness of the thermobattery, connected to the recording device. This thermoelectric battery converter of heat flow has high sensitivity, which allows it to be used for measuring heat fluxes not only high, but also low intensities.

On the insulated reference surface 1, a heating element 2 is installed, that in thermal contact with the «hot junctions» of the thermoelectric battery converter 3, the «cold junctions» of which are in contact with the «hot junctions» of the thermoelectric refrigerator 4, and the cold junctions» of the thermoelectric refrigerator are in contact with the radiator 5, while «hot junctions» are sealed between the heating element 2 and the thermoelectric battery converter 3, and the cold junctions» are in thermal contact with the housing of the device having an ambient temperature. The output signal from the thermoelectric battery converter of heat flow 3, the heating element 1 and the thermoelectric refrigerator 4 is transmitted to the measuring unit 6. The device for measuring the heat flow works as follows. An electric current of such magnitude is passed through the heating element so that the released power is obviously greater than the possible heat flow from the object under study. A signal appears at the output of the thermoelectric battery converter. In this case, the signal at the output of the thermoelectric battery converter will be proportional to the heat flow diverted from the converter by the thermoelectric refrigerator, and the temperature of the heating element is close to the temperature of the environment. The device is in working mode.

The device is brought to the object under study in an area where there are no defects. We bring the heat flow meter to the object under study in the field of the presence of a defect. By changing the signal at the output of a thermoelectric battery converter, the presence of a defect is judged.

2. Results and discussion

The principle of operation of the device is based on the substitution of the effect of incident radiation by the effect of Joule heat released in the calorimetric load when an electric current is passed during calibration. The role of the calorimetric load is performed by the heating element [10]. In order to calibrate the developed device for measuring heat flow, studies were conducted with the HFM-1M heat flow meter and the results are shown in fig. 2 and in table 1.

Table 1. Calibration table

t,^{0}C	HFM-1M ε, mV	Device for measuring heat flow ε, mV
20	0.44	0.76
25	0.80	1.16
30	1.20	1.57
35	1.61	1.98
40	2.02	2.39
45	2.43	2.81
50	2.85	3.22
55	3.26	3.64
60	3.68	4.06
65	3.81	4.52
70	3.94	4.85

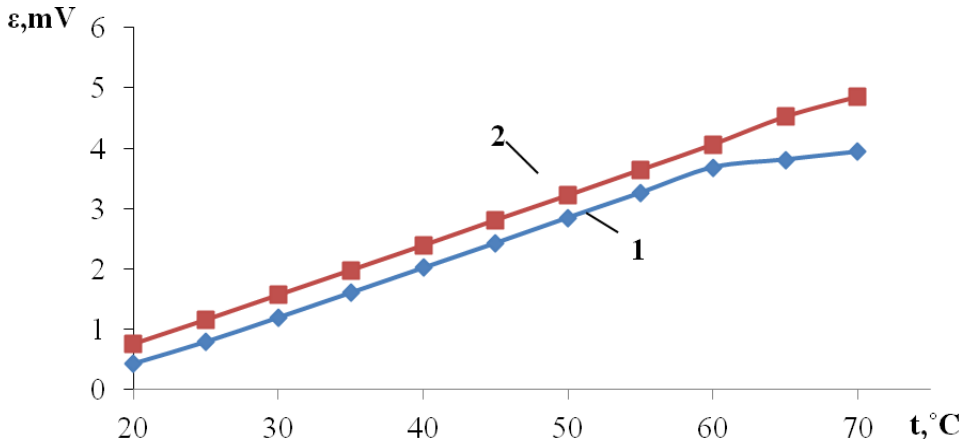

Fig.2. Graph of the dependence of the thermal EMF on temperature changes:
1 - HFM-1M, 2 - device for measuring heat flow.

The data obtained show that the thermal-EMF of the device for measuring heat flow exceeds 1.5 - 2 times. This is due to the fact that the sensitivity of the device the total value of the thermal-EMF in the thermal battery circuit is N times greater than in the HFM-1M thermoelectric converter, that is, the sensitivity of the device increases, and the resulting thermal-EMF. This is due to the fact that the sensitive element in the device for measuring heat flow is made in the form of a spiral of metal wire in an insulating layer, the non-radiated surface of which is controlled by hot thermal battery junctions. To reduce the heterogeneity of the zonal sensitivity, the hot junctions of the thermal battery were distributed according to a special technique. This technique is based on the condition that the total reactions received from each zone of the sensitive element are equal to each other, i.e. the identity must be fulfilled:

$$\frac{n_0 U_0}{F_0} = \frac{n_i U_i}{F_i} \qquad (1)$$

.

where n_0, U_0 and F_0 – the number of thermocouples, the reaction from each thermocouple and the area of the central or zero zone, respectively, a F_i - the same parameters of the i-th zone.

The application of condition (1) for the number of thermocouple junctions by zones made it possible to obtain receivers with zonal sensitivity, the spread of values of which does not exceed 2%. In general, the sensitive elements are multi-layered: black coating, calorimetric load, heat-sensitive elements, alternating lacquer and adhesive layers. That is, the sensitive elements are inhomogeneous, both in the direction perpendicular to the irradiated surface and in parallel. The heterogeneity in the first case is due to the multi-layered of the sensing element. Knowledge of the temperature profile inside the multi-layer sensitive element is necessary in determining the error due to the non-equivalence of heat losses in radiant and electric heating.

Conclusion

The objectives of research require the measurement of the heat flux density, the determination of the parameters of the heat flow and temperature, which vary depending on the degree of damage to the pipeline from 20 to 100 W/m^2 temperature from 5 to 20 ^{0}C, in case of violation of the thermal insulation structure between 25 and 35 W/m^2, The calculation of all the data to obtain the necessary sensitivity, which ensures the measurement of these flows with great accuracy, showed that the heat-sensitive element must be made with a height of 1.5 mm, a diameter of the receiving area of 80 mm from a wire with a cross section of 0.05 mm. In this case, the value of the working coefficient of the converter should be in the range from 4.0 to 12.0 W/(m^2·mV), and the value of the electrical resistance of the converter should be in the range of 12-20 kOhm.

This type of converter is relatively simple and easy to use, it has small dimensions. It's not selective in a wide spectral range (from 1.0 to 25.0 μm). Moreover, the developed devise has high sensitivity (from 10 W/(m^2·mV), and reliably works in harsh operating conditions.

REFERENCES

1 Akhmetzhanova S.B., Tusupbekov M.B., Stroeva G.V., Kysykov A.B. *Problems of development of the heat supply system and the scope of application of existing approaches to heat conservation in the Republic of Kazakhstan.* Astana: PROON/GEF, 2007, 21 p. [in Russian]

2 *The program of modernization of housing and communal services of the Republic of Kazakhstan for 2011-2020: approved on April 30*, 2011. No 473. [in Russian]

3 Ivanov V.V., Shkrebko S.V., Chernyshova L.A., et al. Qualitative forecasting of the condition of sections of underground heating mains. *Heat supply news*, 2001, No 3, pp. 27-28. [in Russian]

4. Nesteruk D.A., Vavilov V.P. *Teplovoj kontrol' i diagnostika. (Thermal monitoring and diagnostics).* Tomsk: TPU, 2007, 104 p. [in Russian]

5 Gerashchenko O. A., Grishchenko T. G. *Devices for Thermophysical Measurements.* Chas, Kiev, 1991, 162 p. [in Russian]

6 Gerashchenko O.A. *Fundamentals of heat metering system.* Kiev, 1984, 1971 p. [in Russian]

7 Varganov I.S., Lebedev G.T., Konpov V.V. Current state and main problems of thermal non-destructive testing methods. *Prom. teplotechnika,* 1983, Vol. 6, No2, pp. 80-93. [in Russian]

8 Karabekova D.Zh., Khassenov A.K, Kissabekova P.A., Satybaldin A.Zh., Tungushbekova M.K. Variation of spatially heterogeneous radiation by coordinate-sensitive receiver. *Eurasian Physical Technical Journal*, 2020, Vol.17, No.1(33), pp. 113-118.

9 Karabekova D. Zh., Kissabekova P.A., Khassenov A. K., Azatbek Sh. Device of measuring heat flow. Republic of Kazakhstan. Patent number: 6393. Date of publication: 03.09.21.

10 Kissabekova P.A., Karabekova D.Zh., Nussupbekov B.R., Khassenov A.K. Analysis of the Insulation State of Underground Pipelines in the Heating Network. *Thermal Engineering,* 2021, Vol. 68(10), pp. 802–805.

Article accepted for publication 07.04.2022

DOI 10.31489/2022No2/75-85

UDC 621.311, 621.311.001.57

STUDY OF ALGORITHM SYNTHETIC INERTIA FUNCTIONING IN ELECTRIC NETWORKS OF DIFFERENT DENSITY

Rudnik V.E., Suvorov A.A., Razzhivin I.A., Ruban N.Yu., Andreev M.V.

National Research Tomsk Polytechnic University, Tomsk, Russia, ver3@tpu.ru

The ability to use the algorithm synthetic inertia (SI) is one of the most important properties of renewable energy sources (RES) generating units connected to the network via a power converter (GUPC). Through the use of SI algorithm there is an opportunity to increase the inertia and damping properties of such plants. The effectiveness of the SI algorithm depends on the mains frequency input value, which is formed by the phase locked loop (PLL), which is an integral part of the power converter control system. However, the operation of the PLL can lead to oscillations with different frequencies when the GUPC is installed in weak electrical networks and, accordingly, adversely affect the performance of the SI algorithm. The studies have shown that the PLL in the photovoltaic plant (PV) control system allows to influence the performance of the SI algorithm, but the nature of this influence depends on the electric network density and can be positive or negative. The influence obtained on the test EPS is also confirmed for the power system of large-scale.

Keywords: phase locked loop, synthetic inertia, photovoltaic plant, renewable energy sources, electric power system

Introduction

Currently, there is a trend of ever-increasing energy consumption. Many leading countries are interested in decarbonization, based on the reduction of traditional generation based on fossil fuels. One of the main directions of development of the global energy sector is the large-scale introduction of new generation facilities based on renewable energy sources (RES) [1]. According to the report of the International Energy Agency [2], the growth of installed RES capacity in 2020 was 280 GW, which is almost 45% more than in 2019, the record growth was also due to an increase of 23% of new photovoltaic installations of almost 135 GW of capacity.

Common to RES facilities is the use of power converters (PC) for connection to the network, which leads to the absence of direct coupling with the network and, accordingly, a contribution to the overall inertia of the system. The mentioned features of devices based on power semiconductor technology significantly change the dynamic properties of electric power systems (EPS) due to the different dynamics of PC functioning, especially its automatic control system (ACS), in comparison with traditional EPS equipment. As a result, the continuous growth of the implementation level of RES facilities, which will last until at least 2030 according to the Paris Agreement [3], leads to a significant decrease in the reliability of modern EPS functioning in normal and especially emergency modes [4-7].

One of the main problems is to ensure the frequency stability of EPS [8, 9]. The emergence of this problem is associated with the introduction of inertia-free RES facilities, including by replacing conventional generation, which leads to a decrease in the available power reserve and overall system inertia. This leads to an increase in the rate of voltage frequency change in the occurrence of power imbalance [10]. As a result, in power systems with low inertia, the depth of frequency reduction is much greater for a similar perturbation compared to traditional EPS [11, 12].

In order to ensure the reliable operation of EPS with low inertia and to reduce the negative effects from the implementation of RES facilities, it is necessary to adapt their ACS to the requirements of conventional generation as part of EPS [13]. Due to the necessary mass use of frequency control algorithms, developed solutions must be simple and reliable. Currently, many approaches have been developed to solve this problem and provide the formation of the so-called synthetic inertia. One such approach, which is applicable to all dominant types of RES, is the introduction of a synthetic inertia (SI) algorithm into the ACS, as well as

.

the correct tuning of the phase locked loop (PLL) [14-16]. The PLL is usually used to measure the network frequency, due to its simple structure and reliability, the PLL is the most popular and widely used [17].

In addition, during the operation of RES objects, it is necessary to take into account the heterogeneity of the magnitude of inertia, which leads to different rates of change and, accordingly, the values of frequency reduction in different parts of the network, which causes serious difficulties in setting up systems of protection against frequency reduction and increase. The problem of modeling transients in "weak" networks when implementing RES is worth mentioning separately [16, 18]. Due to the more oscillatory nature of transients in such networks, quite often there is a situation that after perturbations begin to oscillate with increasing amplitude, and also the PLL requires more fine-tuning, in contrast to networks with "strong" links [16]. In this paper [16, 18] it is shown that the coefficients of the PLL, especially in networks with "weak" links, strongly affect the operation of the power converter.

This paper deals with this issue and is organized as follows. First, the SI algorithm under consideration is described with the peculiarities of its application and the "underloading" mode of the photovoltaic plant (PV). Next, the mathematical model of the PV object used and the EPS test scheme are presented. The final section presents the results of the experiments with a corresponding description. The conclusions on the performed research are presented in the conclusion.

1. Approach to the implementation of the SI algorithm and the "deloading" mode PV

One of the main approaches to the formation of synthetic inertia is the use of SI [8, 15] Implementation of SI is usually considered in relation to wind turbines (WT) [8, 15, 19-21]. This is due to the possibility of using the stored energy of the rotating wind wheel for a short-term increase in the power output of the WT during the occurrence of frequency sag in the EPS. At the same time, there are 2 variants of implementation of the synthetic inertia algorithm: single-loop and double-loop control scheme (Figure 1). The double-circuit scheme has an obvious advantage over the single-circuit one [22] because it reacts not only in the process of frequency change, but also at the actual frequency deviation from the set value, thus providing a return to a higher frequency level after the occurrence of imbalance. Further we will consider the double-circuit circuit.

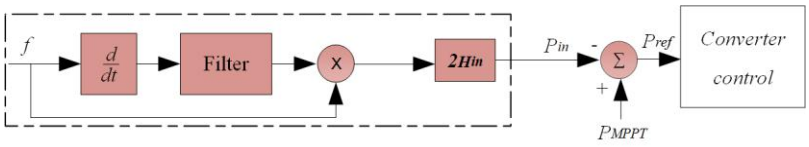

a)

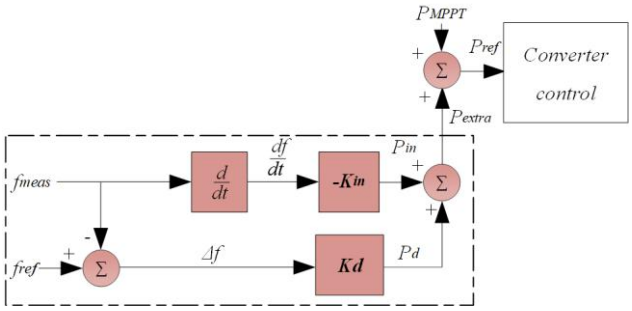

b)

Fig. 1. Schematic diagram of the synthetic inertia algorithm: a) single-loop control, b) double-loop control

The double-loop circuit works as follows: when frequency fluctuations occur in the power system, the WT plant output power control system adds a Pextra frequency response signal to the active power setpoint. This signal is formed by a two-loop control circuit, including a frequency derivative control circuit df/dt and a frequency deviation circuit Δf. At the same time, the contribution in the formation of Pextra of the first loop is greatest in the initial stage of the transient process and does not imply the return of the network frequency to the nominal value. In order to ensure the return of frequency to the acceptable region, the second circuit is used, which imitates the effect of damped windings in a classical synchronous generator and provides linear frequency smoothing [23].

Application of PV for frequency control in emergency modes is possible in two ways. The first way is to use electric energy storage devices to deliver additional power, the second way is to "deloading" PV in steady-state mode and to use full power in emergency modes. In [24] it was proved that the first method has a higher cost, in this connection the widespread and currently main option is the "deloading" mode of PV. In this case, the use of synthetic inertia in the ACS PV allows the formation of an optimal frequency response and effective maintenance of stable operation of the EPS as a whole, including at different levels of illumination. Figure 2 shows the power dependence of the PV DC voltage. The Maximum Power Point Tracking (MPPT) controller normally changes the DC voltage of the panels to achieve maximum efficiency (point A1 in Figure 2).

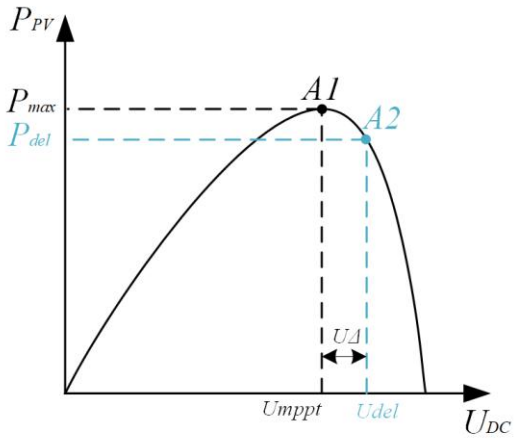

Fig. 2. Dependence of power on the DC voltage of the PV.

The Maximum Power Point and the corresponding DC voltage depend on solar insolation, ambient temperature, and solar cell temperature. There are many MPPT methods [25] to maximize PV power output. To unload the PV, the PV cell voltage is raised above the MPPT point by ΔU [26], the output power is reduced (point A2 in Figure 2) and a power reserve is created that can be used to provide inertial response and participate in frequency control. In view of the above, the research further uses a scheme that provides "deloading" of the PV and SI algorithm (Figure 3).

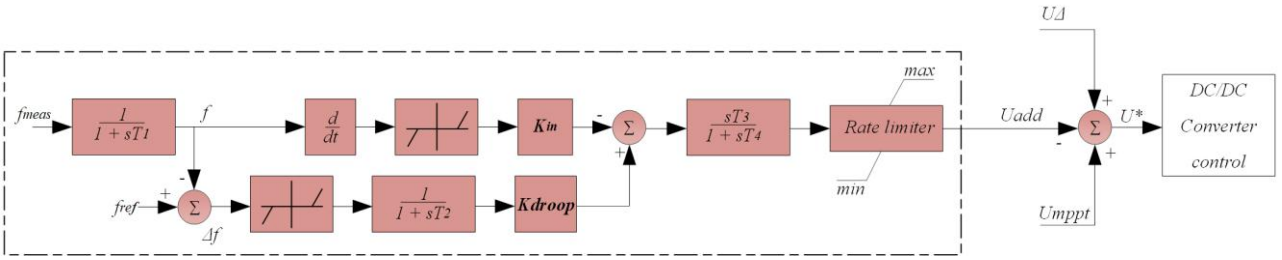

Fig. 3. Modification of ACS PV which includes a synthetic inertia algorithm with two-channel control [8, 15, 24, 26].

2. Description of test circuit EPS and the scheme of the PV used

For the research, a three-machine EPS was implemented as shown in Figure 4. The PV is implemented in bus 5 (Fig. 5), which is connected to the network by means of a static voltage converter (inverter). With a PV capacity of 25 MW, its share corresponds to 40% of the installed capacity. In the "deloading" mode of PV, there is a power reserve of 2.5 MW, which is 10% of the installed power [26]. For the presented network topology (Fig. 4), the following perturbation was carried out: load surge at busbar 3. The load surge allows to estimate the influence of the SI algorithm on the inertial response of the network.

.

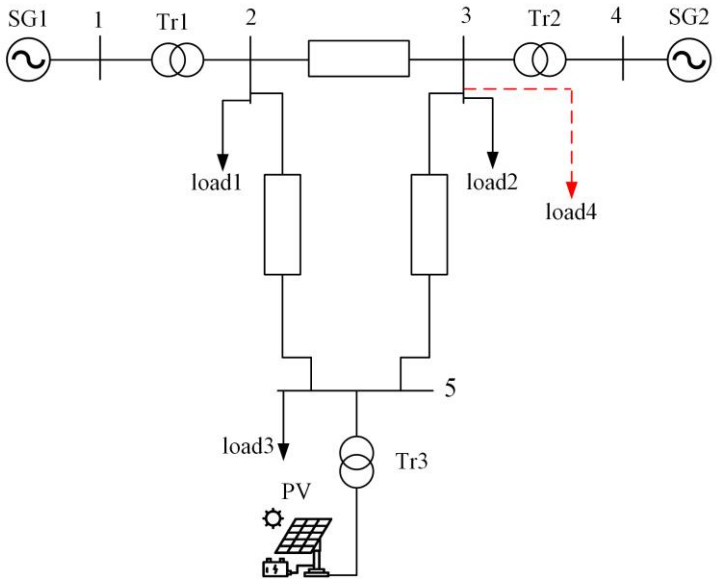

Fig. 4. Test three-machine power system.

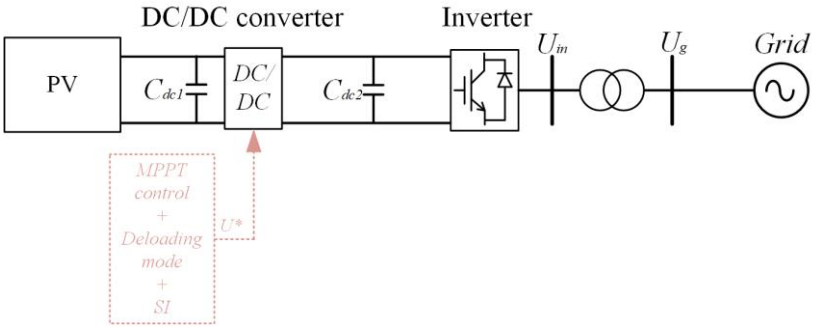

Fig. 5. Structural diagram of PV with upgraded ACS

To investigate the influence of the SI algorithm on the frequency stability, 2 variants of circuit-mode conditions are realized: "strong" and "weak" network. The strong network means that the short circuit ratio (SCR) of this network is more than 10 o.u. (SCR of "strong" network = 14,36), respectively SCR of weak network is less than 10 o.u. (SCR of "weak" network = 7,54) [27]. The calculation is made according to formula (1):

$$SCR = \frac{S_{\min}}{P_{RES}} \text{ [o.e.]}, \tag{1}$$

where, $S_{\min}$ - is the minimum value of short-circuit power at the RES connection point to the mains without RES influence, P_{RES} - is the rated power of RES.

3. Study of the influence of SI algorithm and PLL settings on EPS frequency stability

For the synthetic inertia algorithm (SI) coefficients were taken according to the analyzed literature: [28, 29] "Kin" differential coefficient we take equal to 2H (Kin=40) [28]. "Kdpoop" proportional coefficient is calculated according to the formula, relative to the network topology (2) [29].

$$Kdroop = \frac{Pg}{R} = 20 \text{ [p.u.]}, \tag{2}$$

where, Pg - power of PES (p.u.), R - equivalent droop coefficient of synchronous generators.

3.1 Study of the effect of the proportional and differential coefficient of the synthetic inertia algorithm on the stability of the power system by frequency.

Figure 6 and 7 show the oscillograms of frequency changes when varying the differential coefficient of the SI algorithm. From Fig. 6 and 7 we can see that increasing the differential coefficient leads to a decrease in the frequency sag, as is observed the damping of oscillations in both "strong" and "weak" network. The use of a larger differential coefficient has a positive effect on the transient process during load surge.

The proportional coefficient of the SI algorithm was varied in a similar way, the results are shown in Figures 8 and 9.

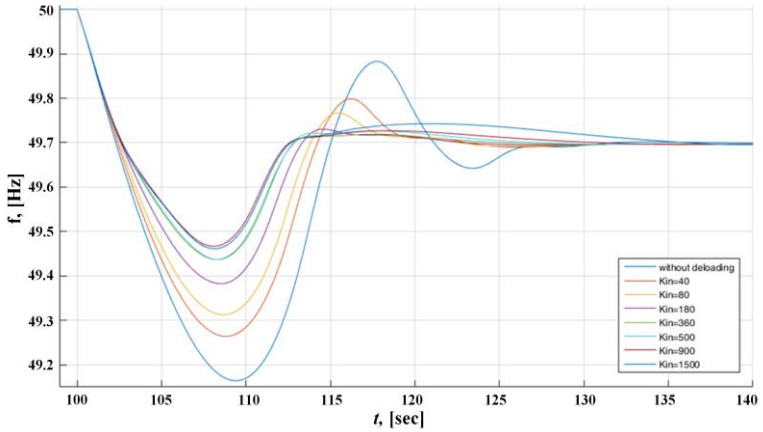

Fig. 6. Oscillograms of frequency changes when varying the "Kin" coefficient of the SI algorithm (Kdroop=const=20; SCR network = 14,36)

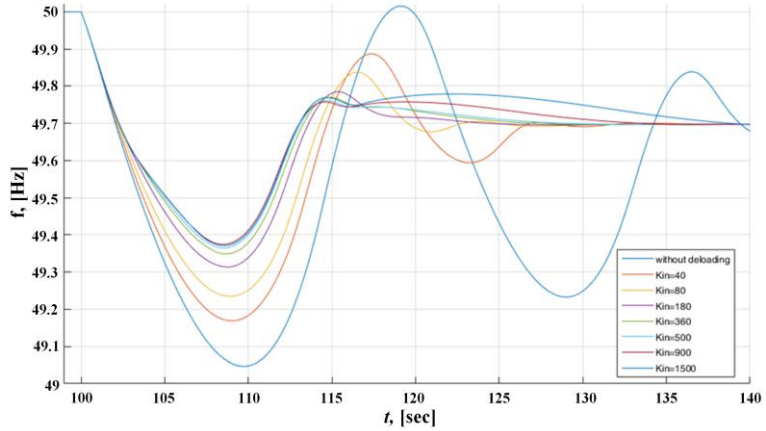

Fig. 7. Oscillograms of frequency changes when varying the "Kin" coefficient of the SI algorithm (Kdroop=const=20; SCR network = 7,54).

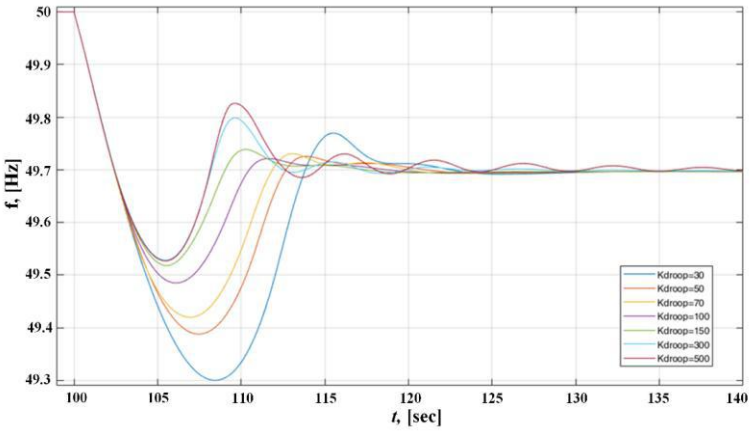

Fig. 8. Oscillograms of frequency changes when varying the coefficient "Kdroop" of the SI algorithm (Kin=const=40; SCR network = 14,36)

.

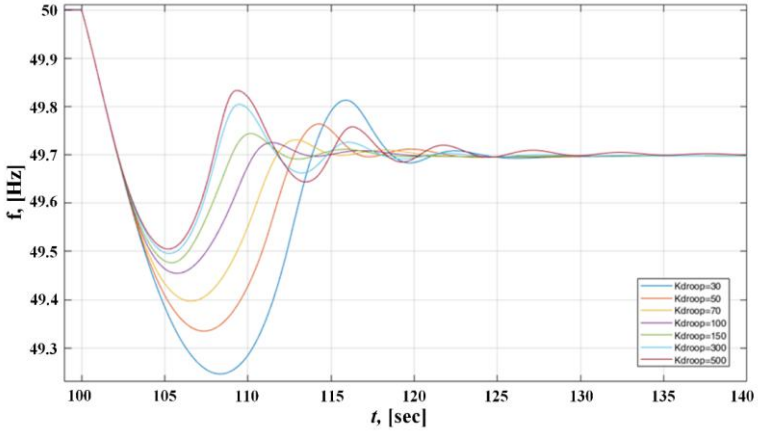

Fig. 9. Oscillograms of frequency changes when varying the coefficient "Kdroop" (Kin=const=40; SCR network = 7,54)

Figure 8 and 9 show that increasing the proportional coefficient leads to decreasing the frequency sag in both "strong" and "weak" networks. Increasing the proportional coefficient up to the value of 300 has a positive effect on the transient process in the "strong" network, a further increase in the coefficient leads to overshooting, which in turn leads to a decrease in network stability. This process has the same tendency for the "weak" network. Increasing the coefficients of the SI algorithm has a positive effect on the frequency stability of the EPS. However, the variation of coefficients should be within acceptable limits, in order to avoid a negative trend of frequency change, which can lead to an emergency situation and unstable state of EPS, respectively with the correct adjustment of the SI algorithm it is possible to maintain and improve the stability of EPS, which is confirmed by the obtained experimental results.

3.2. Study of the influence of the PLL bandwidth on the performance of the SI algorithm

As mentioned above, the study was conducted for "strong" and "weak" network, changing the PLL bandwidth in networks with different SCR led to different results. Calculation of the bandwidth of the PLL was performed according to [30]. The bandwidths for the studies were taken as follows: 0.3 Hz (Ki=0.83; Kp=1.2), 30 Hz (Ki=8390; Kp=130) and 50 Hz (Ki=20500; Kp=240) and SI algorithm coefficients were taken Kin=40; Kdpoop=20. Figures 10 and 11 show oscillograms of frequency changes and oscillograms of signal changes of SI algorithm at different PLL bandwidths in the "strong" and "weak" networks, respectively.

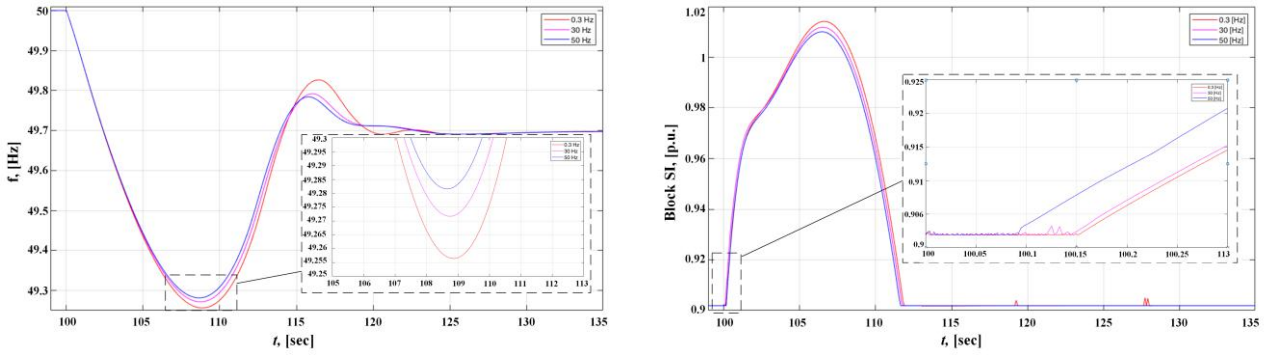

a *b*

Fig. 10. Oscillograms of the transient process in the "strong" network, where: a) frequency change at different bandwidth of the PLL, b) signal change of the SI algorithm at different bandwidth of the PLL

In a "strong" network, as the bandwidth of the PLL increases, the amount of frequency sag decreases (Figure 10a). This process occurs due to the fact that the PLL, with the entrainment of the bandwidth, increases the response speed of the SI algorithm (Figure 10b). In the "weak" network, the opposite picture is observed (Figure 11a), the PLL, with increasing bandwidth, decreases the response speed of the SI algorithm (Figure 11b), which leads to an increase in frequency droop.

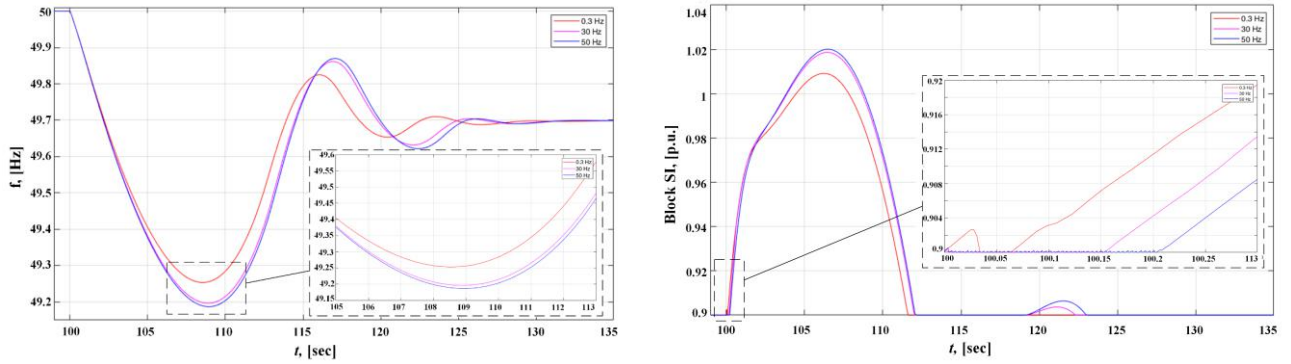

a *b*

Fig.11. Oscillograms of the transient process in the "weak" network, where: a) frequency change at different bandwidth of the PLL, b) signal change of the SI algorithm at different bandwidth of the PLL

Figures 12 and 13 show oscillograms of frequency changes and oscillograms of signal changes of SI algorithm on the differential channel when the "Ki" factor of the PLL increases in the "strong" network and "weak" network, respectively.

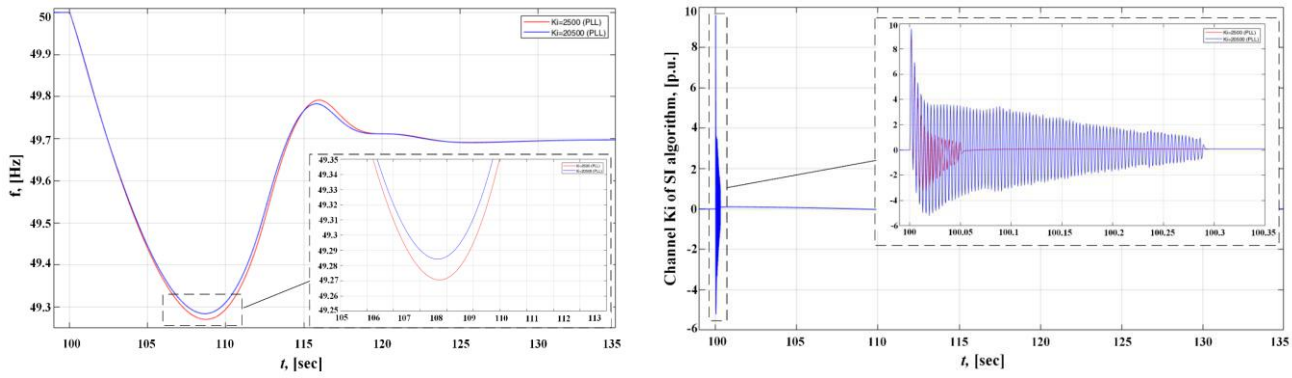

a *b*

Fig.12. Oscillograms of the transient process in the "strong" network, where: a) frequency change at different bandwidth of PLL, b) change of the SI algorithm signal on the differential channel when the "Ki" coefficient of the PLL increases

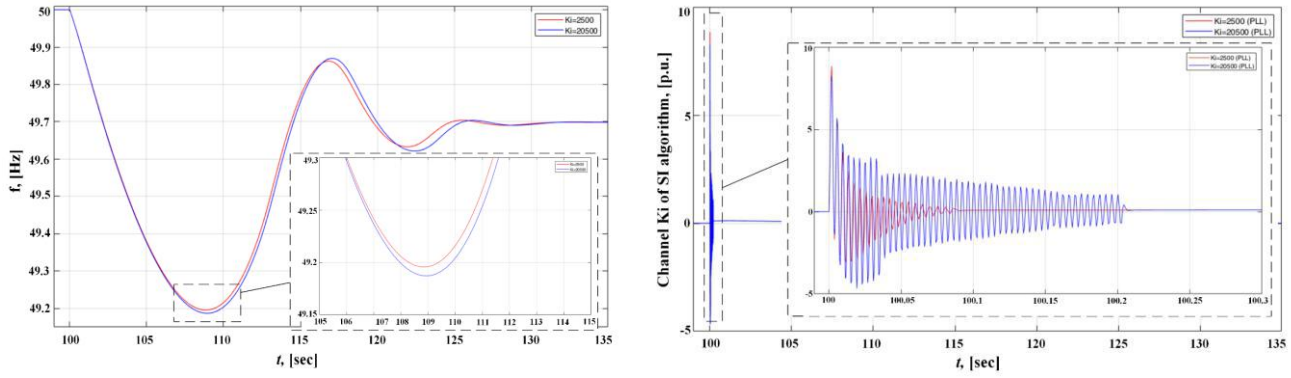

a *b*

Fig. 13. Oscillograms of the transient process in the "weak" network, where: a) frequency change at different bandwidth of PLL, b) change of the SI algorithm signal on the differential channel when the "Ki" coefficient of the PLL increases

At the moment of perturbation when the "Ki" coefficient of the PLL is larger, a signal of larger amplitude is generated in the differential channel of the SI algorithm (Fig. 12b), which leads to a smaller EPS frequency sag (Fig. 12a), in the "weak" network results in the opposite process (Figure 13 a, b). Figures 14 and 15 show oscillograms of frequency changes and oscillograms of signal changes of the SI algorithm on the differential channel when the "Kp" factor of the PLL increases in the "strong" and "weak" network, respectively.

.

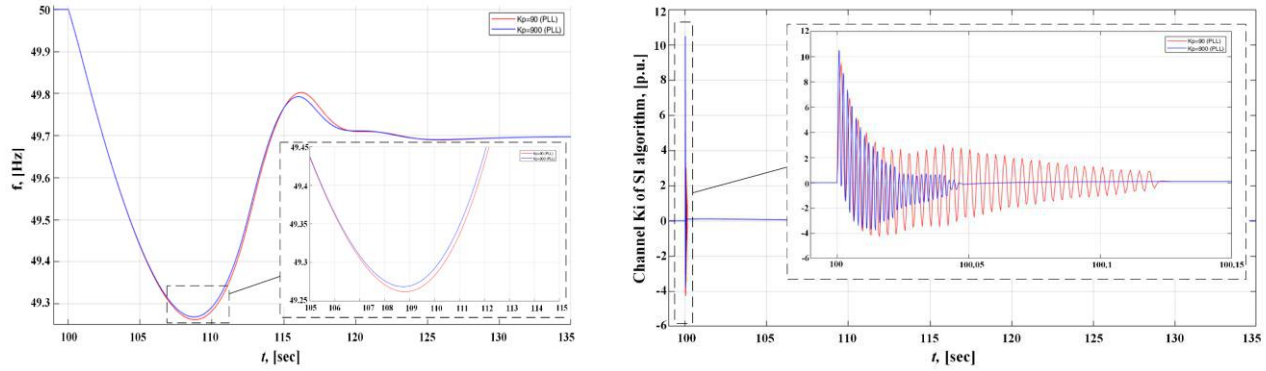

a *b*

Fig.14. Oscillograms of the transient process in the "strong" network, where: a) change of frequency at different bandwidth of PLL, b) change of signal of SI algorithm on differential channel when increasing the coefficient "Kp" of PLL

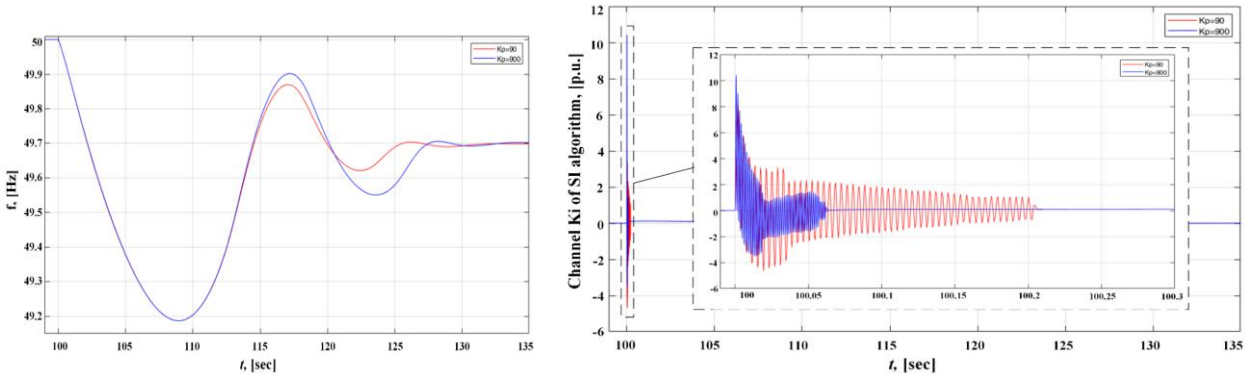

a *b*

Fig.15. Oscillograms of the transient process in the "weak" network, where: a) frequency change with different bandwidth of PLL, b) change of the SI algorithm signal on the differential channel when the "Kp" coefficient of the PLL increases

With the increase of "Kp" coefficient in the "strong" network, there is a positive tendency of frequency change: the level of frequency sag decreases (Figure 14a) due to the fact that the differential channel of SI algorithm generates a signal of larger amplitude (Figure 14b). With the increase of "Kp" coefficient in the "weak" network, the trend of frequency change has a negative character (Fig. 15a, b), there is an effect of overshoot on the second oscillation cycle, which is associated with the intensity of signal generation of differential channel of SI algorithm. Changing the settings of the PLL in the power converter control system allows to influence the characteristics of the frequency reduction process, but for the "strong" and "weak" network a different approach in setting is required.

3.3. A study of the effect of PLL bandwidth on the performance of an SI algorithm in a large-scale EPS

The study was conducted on a test power system of large-scale, which contains 177 bus (Figure 16). PV is being implemented in bus 176. The introduction of PV in this area is justified by suitable climatic conditions, the area is located near the zone of maximum intensity of solar radiation. The introduction of PV allows to solve the problems of the deficit energy district, and is one of the possible solutions to improve the reliability and sustainability of electricity supply. Also, this area is "weak" (SCR<10 o.u.), so in it is important to consider the identified patterns as in Section 4.2. To investigate the effect of the PLL bandwidth on the performance of the SI algorithm, load shedding at bus 170 was performed. The connection of the power district with the rest of the power system is carried out by a two-chain transmission line. The coefficients of the SI algorithm are calculated similarly to [28, 29], the bandwidths of the PLL are taken as in Section 4.2. Figure 17 shows the oscillograms of transients in the power system of large-scale.

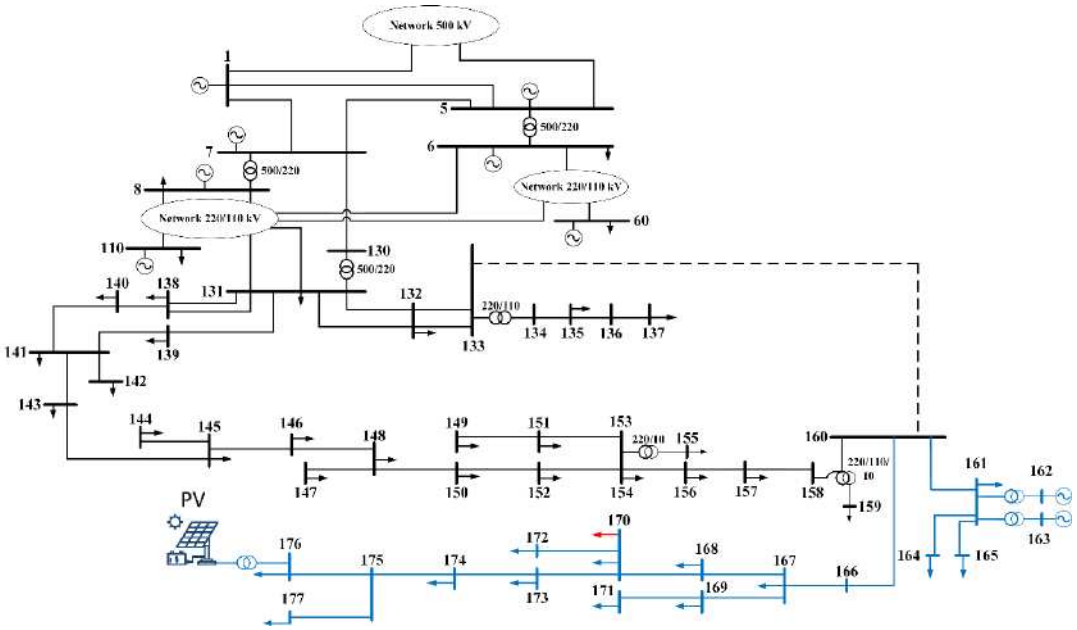

Fig. 16. Scheme of a large-scale EPS.

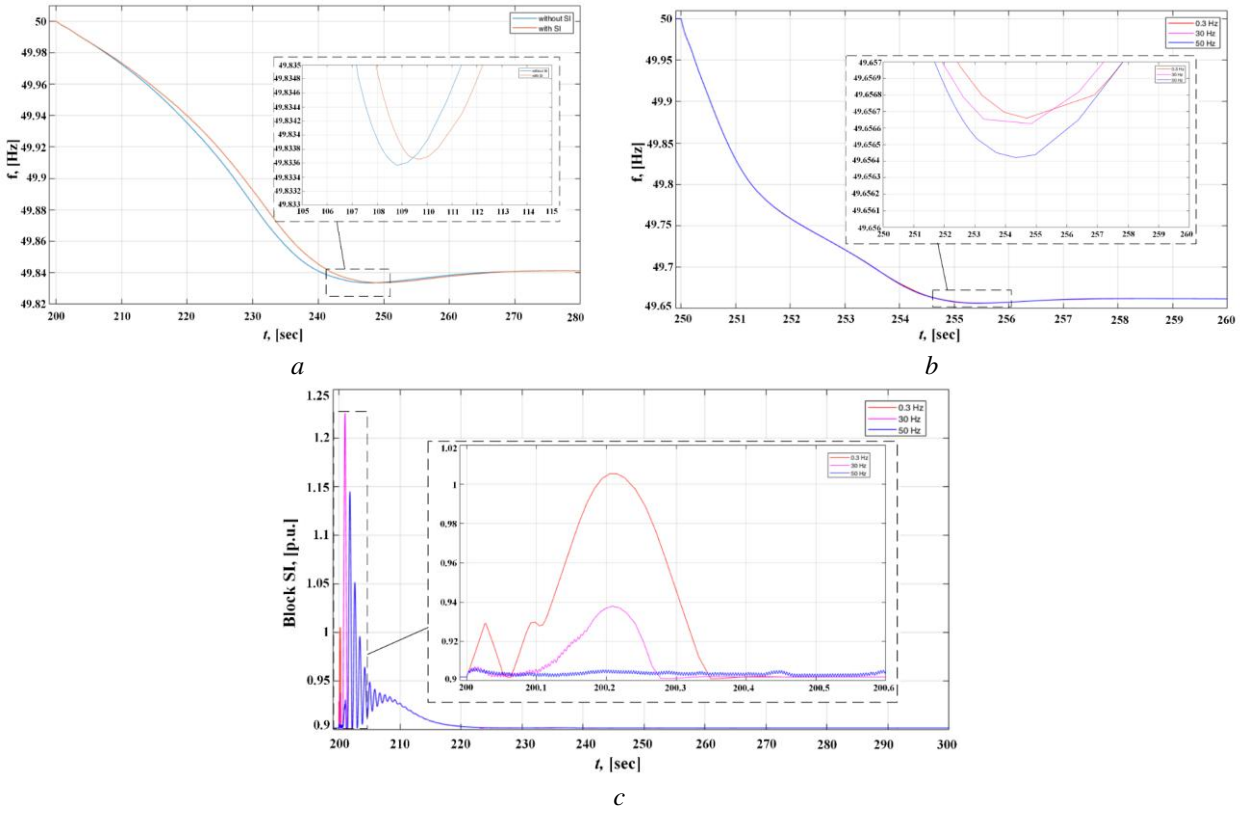

a *b* *c*

Fig. 17. Oscillograms of the transient process in the power system of large-scale where: a) frequency change in bus 176 when operating PV with and without SI algorithm; b) frequency change in bus 176 when varying the bandwidth of PLL; c) signal changes of SI algorithm when varying the bandwidth of PLL

Obviously, in large-scale EPS, the introduction of PV in general does not have a significant effect on the transients and does not dramatically reduce the overall inertia, but for a remote power district the contribution of PV including the SI algorithm and different setting of the PLL can have an impact on the transients. Figure 17a shows that the use of the SI algorithm has a positive effect on the frequency stability of the EPS, the frequency sag is reduced. Figure 17b shows that increasing the bandwidth PLL, leads to an

.

increase in the frequency sag in the EPS, this process occurs due to the fact that with increasing bandwidth PLL, decreases the response rate SI algorithm (Figure 17c). The regularities obtained in section 4.2. for the test EPS are also observed in large-scale EPS.

Conclusion

In the article the influence of SI algorithm on the frequency stability of EPS is investigated. It is noted that the correct adjustment of the SI algorithm has a significant impact on the dynamic stability of the network, especially in networks with a predominant fraction of RES. For the EPS test scheme, the results clearly show the possibility of a positive effect of SI algorithm on the dynamic stability of EPS. It is noted that varying the coefficients of the SI algorithm affects the transient process.

With a certain adjustment of the SI algorithm it is possible not only to provide the required inertial response, but also to extend the stability boundaries. It is also worth noting the effect of the PLL on the performance of the SI algorithm. The results show that changing the bandwidth of the PLL in the ACS PV allows to influence the process characteristics of both decreasing and increasing the frequency during the transient process, depending on the network topology. Accordingly, in a "strong" network, as the PLL bandwidth increases, the frequency sag decreases, while in a "weak" network, the opposite situation is observed. The same patterns obtained for the "weak" network in the test EPS are also observed in the high-dimensional EPS. The research proves that the problem of modeling transients in "weak" networks when implementing RES is relevant. Due to the more oscillatory nature of transients in such networks, quite often there is a situation that after perturbations begin to oscillate with increasing amplitude, and also the PLL requires more accurate tuning, in contrast to networks with "strong" links.

Acknowledgements

The reported study was funded by the Russian Science Foundation, project number 21-79-00129.

References

1 Wu J. Z., Yan J. Y., Jia H. J., Hatziargyriou N., Djilali N., Sun H. B. Integrated energy systems. *Applied Energy,* 2016, Vol. 167, pp. 155– 157. doi:10.1016/j.apenergy.2016.02.075

2 Renewable Energy Market Update 2021. Available at: https://www.iea.org/reports/renewable-energy-market-update-2021

3 OECD. World electricity generation by source of energy: Terawatt hours (TWh). Paris: OECD Publishing; 2016. // Available: https://doi.org/10.1787/factbook-2015-en

4 Sinsel, S. R., Riemke, R. L., Hoffmann, V. H. Challenges and solution technologies for the integration of variable renewable energy sources—a review. *Renewable Energy,* 2020, Vol. 145, pp. 2271 - 2285. https://doi.org/10.1016/j.renene.2019.06.147

5 National Grid, Voltage and Frequency Dependency. National Grid, 2018. Available: https://www.nationalgrid.com/sites/default/files/documents/SOFReport-Fr%ment.pdf

6 Huang S., Schmall J., Conto J., Adams J., Zhang Y., Carter C. "Voltage control challenges on weak grids with high penetration of wind generation: ERCOT experience." *IEEE Power and Energy Society General Meeting*, 2012, pp. 1-7. doi: 10.1109/PESGM.2012.6344713

7 Liu H., et al. Subsynchronous Interaction between Direct-Drive PMSG Based Wind Farms and Weak AC Networks. *IEEE Transactions on Power Systems,* 2017, Vol. 32, No. 6, pp. 4708-4720.

8 Cheng Y., Azizipanah-Abarghooee R., Azizi S., Ding L., Terzija V. Smart frequency control in low inertia energy systems based on frequency response techniques: A review. *Applied Energy,* 2020, vol. 279, 115798. https://doi.org/10.1016/j.apenergy.2020.115798.

9 JWG C2/C4.41: Impact of High Penetration of Inverter-based Generation on System Inertia of Networks. Available at: https://e-cigre.org/publication/wbn022-impact-of-high-penetration-of-inverter-based-generation-on-system

10 Johnson S.C, Rhodes J.D, Webber M.E. Understanding the impact of nonsynchronous wind and solar generation on grid stability and identifying mitigation pathways. *Applied Energy,* 2020, Vol. 262, pp. 114492.

11 Seneviratne, Chinthaka, Ozansoy C. Frequency response due to a large generator loss with the increasing penetration of wind/PV generation – A literature review. *Renewable and Sustainable Energy Reviews*, 2016, Vol. 57, pp. 659-668. DOI: 10.1016/j.rser.2015.12.051.

12 Razzhivin I., Askarov A., Rudnik V., Suvorov A. A Hybrid Simulation of Converter-Interfaced Generation as the Part of a Large-Scale Power System Model. *International Journal of Engineering and Technology Innovation,* 2021, Vol. 11, No. 4, pp. 278–293.

13 Arani M.F.M., El-Saadany E.F. Implementing virtual inertia in DFIG-based wind power generation. *IEEE Transactions on Power Systems,* 2013, Vol. 28, pp. 1373–84. https://doi.org/10.1109/TPWRS.2012.2207972

14 Zhong C, Zhou Y, Yan G. Power reserve control with real-time iterative estimation for pv system participation in frequency regulation. *International Journal of Electrical Power and Energy Systems*, 2021, Vol. 124, 106367. https://doi.org/10.1016/j.ijepes.2020.106367 .

15 Nguyen H. T., Yang G., Nielsen A. H., Jensen P. H. Frequency stability enhancement for low inertia systems using synthetic inertia of wind power. *IEEE Power and Energy Society General Meeting*, 2017, pp 1-5. doi: 10.1109/PESGM.2017.8274566

16 Qi Hu, Lijun Fu, Fa, Ma, Fen, Ji. Large Signal Synchronizing Instability of PLL-Based VSC Connected to Weak AC Grid. *IEEE Transactions on power systems*, 2019, Vol. 99. doi:10.1109/TPWRS.2019.2892224

17 Wan, Y. F., We, Li Y. Analysis and Digital Implementation of Cascaded Delayed-Signal-Cancellation PLL. *IEEE Transactions on Power Electronics*, 2011, Vol. 26, No. 4, pp. 1067-1080. doi: 10.1109/TPEL.2010.2091150

18 Zho, J Z., Ding H., Fan S., Zhang Y., Gole A.M. Impact of short-circuit ratio and phase-locked-loop parameters on the small-signal behavior of a VSC-HVDC converter. *IEEE Transactions on Power Delivery,* 2014, Vol.29, No. 5, pp. 2287–2296. doi: 10.1109/TPWRD.2014.2330518

19 Magnus D.M., et al. A novel approach for robust control design of hidden synthetic inertia for variable speed wind turbines. *Electric Power Systems Research,* 2021, Vol.196. doi:10.1016/j.epsr.2021.107267

20 Gutierrez F., Riquelme E., Barbosa K.A., Chavez H. State estimation for synthetic inertia control system using kalman filter. *Proceeding of the IEEE Intern. Conference on Automation 24th Congress of the Chilean Association of Automatic Control,* ICA-ACCA. 2021. doi:10.1109/ICAACCA51523.2021.9465316

21 Nguyen H.T., Chleirigh M.N., Yang G. A technical economic evaluation of inertial response from wind generators and synchronous condensers. *IEEE Access,* 2021, Vol. 9, pp.7183-7192.

22 Mohammad D, Mokhlis H., Mekhilef S. Inertia response and frequency control techniques for renewable energy sources: A review. *Renewable and Sustainable Energy Reviews,* 2017, Vol. 69, pp. 144-155. https://doi.org/10.1016/j.rser.2016.11.170

23 Bevran, H., Is, T., Miur, Y. Virtual synchronous generators: A survey and new perspectives. *International Journal of Electrical Power and Energy Systems*, 2014, Vol. 54, pp. 244-254. https://doi.org/10.1016/j.ijepes.2013.07.009

24 Zarina P.P., Mishra S., Sekhar P.C. Exploring frequency control capability of a PV system in a hybrid PV-rotating machine-without storage system. *International Journal of Electrical Power and Energy Systems,* 2014, Vol. 60, pp. 258-267. https://doi.org/10.1016/j.ijepes.2014.02.033

25 Karami N., Moubayed N., Outbib R. General review and classification of different MPPT techniques. *Renewable and Sustainable Energy Reviews*, 2017, Vol. 68, No. 1, pp. 1–18. https://doi.org/10.1016/j.rser.2016.09.132

26 Tielens P. *Operation and control of power systems with low synchronous inertia*. PhD diss. thesis, 2017.

27 Lingling Fan. Modeling Type-4 Wind in Weak Grids. *Proceeding of the IEEE Transactions on sustainable energy,* 2019, Vol.10, No. 2, pp. 853-864. doi: 10.1109/TSTE.2018.2849849

28 Zhang S., Jiao L., Zhang H., Shi L., Yang H. A new control strategy of active participation in frequency regulation of photovoltaic system. *Proceeding of the IEEE 4th Conference on Energy Internet and Energy System Integration: Connecting the Grids Towards a Low-Carbon High-Efficiency Energy System,* 2020, pp. 2314-2318. doi: 10.1109/EI250167.2020.9347015

29 Qiaoming Shi, Gang Wang, Weiming Ma, Lijun Fu, You Wu, Pengxiang Xing. Coordinated Virtual Inertia Control Strategy for D-PMSG Considering Frequency Regulation Ability. *Journal of Electrical Engineering and Technology,* 2016, Vol. 11, No. 6, pp. 1556-1570. http://dx.doi.org/10.5370/JEET.2016.11.6.1556

30 Sun Yin, (Erik) de Jong, E. C. W., Wang, Xiongfei, Yang, Dongsheng, Blaabjerg, Frede , Cuk, Vladimir, and (Sjef) Cobben, J. F. G. The Impact of PLL Dynamics on the Low Inertia Power Grid: A Case Study of Bonaire Island Power System. *Energies*, 2019, Vol. 12, No. 7, pp. 1259. https://doi.org/10.3390/en12071259.

Article accepted for publication 02.03.2022

.

DOI 10.31489/2022No2/86-92

UDC 535.55; 535.343

SPECTRAL DEPENDENCIES OF MAGNETOOPTICAL EFFECTS IN MAGNETIC FLUIDS

Yerin C.V.*, Vivchar V.I., Belykh S.S.

Department of Physics and Technology, North-Caucasus Federal University, Stavropol, Russian Federation, exiton@inbox.ru

The spectral dependences of the transmittance and optical anisotropy effects in magnetic fluid have been investigated. It is shown that the refractive index spectra of bulk magnetite known are of little use for the quantitative and qualitative interpretation of optical effects in magnetic fluids. The transmission, birefringence, and dichroism spectra are calculated using the known refractive index spectra of magnetite. The best agreement with the experiment was obtained using the experimental spectra of the complex refractive index of the powder of magnetite nanoparticles. It is concluded that there is a significant difference in the spectra of the complex refractive index for bulk and nanosized magnetite.

Keywords: magnetic fluids, optical anisotropy, magnetite, complex refractive index.

Introduction

Magnetic fluids (ferrofluids, magnetic nanofluids) are colloids of nanoparticles of ferro- and ferrimagnets in various liquid media. To prevent coagulation under the action of van der Waals and magnetic dipole-dipole interactions, the surface of the particles is coated with molecules of a surfactant. Due to stabilization, magnetic fluids remain stable for a long time. Such media are unique systems in which the interaction of particles with an external magnetic field leads to interesting physical effects [1-2]. They were first developed in the early 1960s at NASA to control the flow of propellant under weightless conditions [3]. Subsequently, magnetic fluids have received a wide range of applications, such as: magnetic fluid dampers, bearings and seals [4], micromechanical systems [5], non-destructive testing devices [6], microfluidics devices [7], biosensors for studying cellular toxicity, and systems for treating oncological diseases by the method of hyperthermia [11], etc. Magnetic fluids under the influence of a magnetic field exhibit some different optical effects, such as birefringence [12-13], linear and circular dichroism [14], Faraday rotation and ellipticity [15], changes in the intensity of transmitted, scattered and reflected light [16-17], etc. Due to these effects, magnetic fluids are used in various magneto-optical devices: optical filters, limiters and gates, waveguides and fiber-optic modulators, diffraction gratings with a controlled period, optical sensors of magnetic field, static and dynamic displays, etc. [18]. When studying magneto-optical effects in magnetic colloids, monochromatic radiation sources, lasers, are usually used. When studying the spectral dependences of optical effects in magnetic fluids, transmission spectra are mainly studied [19]. The spectra of the effects of magnetic birefringence and dichroism were studied in [13, 20]. For the theoretical interpretation of optical effects in magnetic colloids and predicting the properties of magneto-optical devices, accurate data on the optical properties of colloidal particles and a dispersion medium are required. Such information can be obtained based on data from studies of the spectra of optical effects.

In this work, we present the results of experimental studies of the spectral dependences of optical effects in kerosene based magnetic fluids in the visible region. Earlier, in [18], we determined the spectra of the complex refractive index of magnetic colloids with different concentrations of the solid phase. This work aims to interpret the spectral dependences of optical effects in magnetic colloids using our data and those known from the literature on the spectra of the complex refractive index of magnetite.

1 Experimental technique

To study optical effects in magnetic fluids, a setup based on the Ellips-1891 spectral ellipsometer was used. We measured the ellipsometric parameters in transmitted light, as well as the transmission spectra of

samples in the wavelength range of 350-1050 nm, in 5 samples of magnetic fluid with volume concentrations from 0.01% to 1%. All samples were obtained by dilution from the original magnetic fluid with a concentration of about 10%. For research, the samples were placed in rectangular glass cuvettes with a thickness of 1 to 5 mm. We investigated the following optical parameters of the samples: transmittance (the ratio of the intensities of the incident and transmitted light $T=I/I_0$) and, at the same time, optical density (D), change in optical density under the action of a field $(D_H-D_0)/D_0$, as well as ellipsometric parameters Ψ and Δ, determining the state of the polarization ellipse of the transmitted or reflected light. Using Δ, the main parameter of birefringence was calculated - the difference between the refractive indices of the extraordinary and ordinary rays $\Delta n = n_{\parallel} - n_{\perp}$, and according to Ψ data - the dichroism parameter $\Delta k = k_{\parallel} - k_{\perp}$. Helmholtz coils mounted on a sample stage in an ellipsometer were used to create a magnetic field.

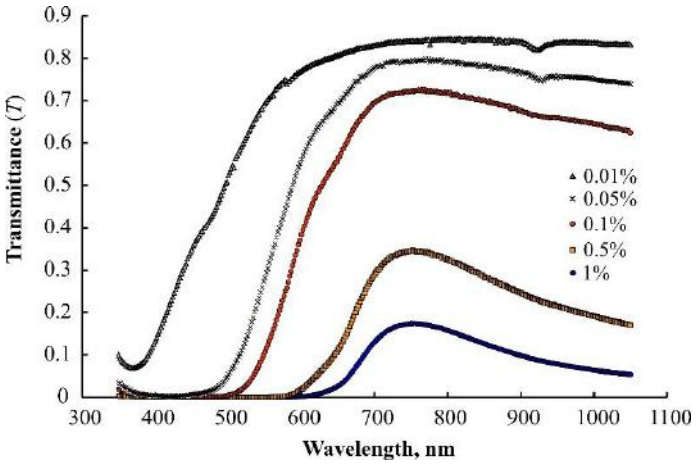

Fig. 1. Transmission spectra of magnetic fluids with different concentrations in a 1 mm thick cuvette.

Also, by the method of ellipsometry in reflected light, a sample of a powder of magnetite nanoparticles 10 nm in size, pressed into a tablet with a diameter of about 13 mm under a pressure of 100 MPa, were investigated. The density of the compressed nanoparticle powder was 2360 kg/m^3, which corresponds to a volume concentration of about 37%. The nanoparticle powder was obtained by prolonged drying of a magnetic fluid based on kerosene, which suggests the presence of a certain amount of oleic acid in it. In Fig. 1 shows the transmission spectra of samples of magnetic fluids with different concentrations of the solid phase. A characteristic feature of the spectra is the presence of a transmission maximum in the 720–750 nm region, which becomes more pronounced with an increase in the particle concentration.

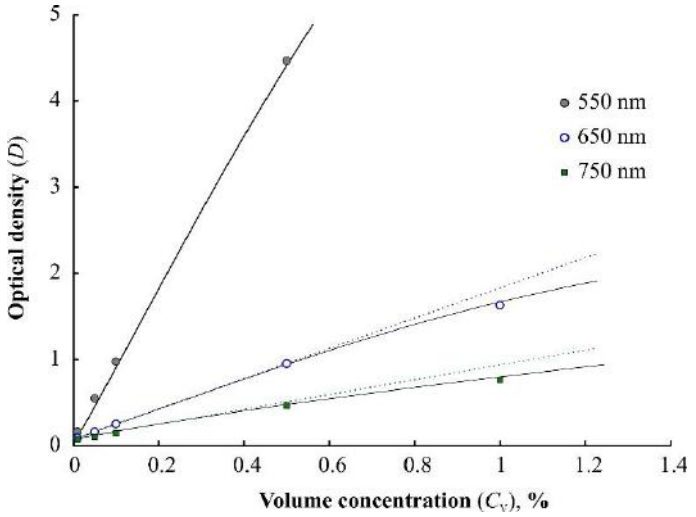

Fig 2. Dependences of the optical density of various samples of a magnetic fluid on the volume concentration of the solid phase

In Fig. 2 shows the dependences of optical density on concentration at three different wavelengths. We found that the effect of the magnetic field on the light transmission of the samples is rather weak. For samples with a concentration of less than 0.5%, within the experimental error, no changes in transparency were observed upon exposure to a field. The relative change in optical density under the action of the field did not exceed a few percent (Fig. 3). In Fig. 4 and Fig. 5 show the spectra of the effects of birefringence and dichroism in a magnetic fluid with a concentration of 0.01%.

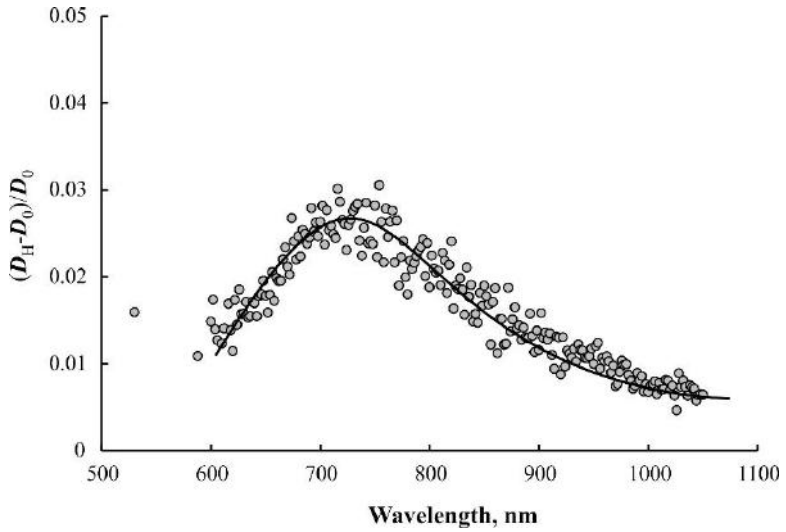

Fig. 3. Spectral dependence of the relative change in the optical density of a sample with a concentration of 1% under the influence of a constant magnetic field *H*=200 Oe

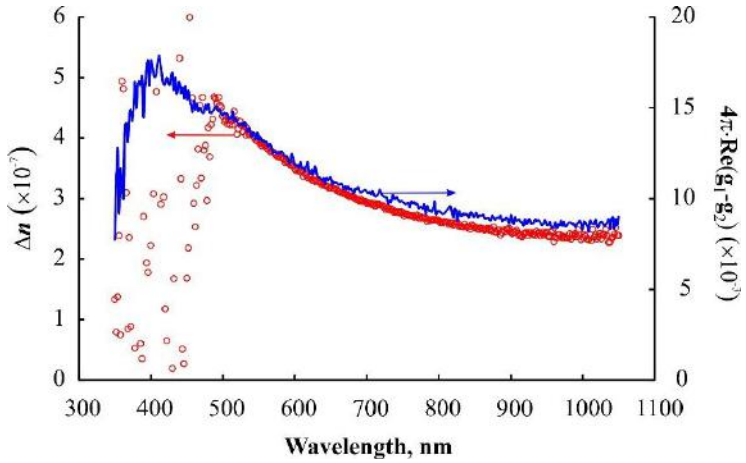

Fig. 4. Birefringence spectrum in a sample with a concentration of 0.01% when exposed to a magnetic field *H*=50 Oe and calculation of the real part of optical anisotropy

2 Results and Discussion

The interpretation of the spectral dependences of the transmittance of magnetic colloids with a not too high concentration of particles can be constructed on the basis of the Bouguer-Lambert law [19], according to which:

$$T = \frac{I}{I_0} = \exp\left(-\sigma_{ext} NL\right). \tag{1}$$

here σ_{ext} is the cross -section of light attenuation by an individual particle, N is the number concentration of particles, *L* is the light path length. From (1) it follows that the optical density of the medium should be proportional to the concentration of particles:

$$D = \lg\left(\frac{I_0}{I}\right) = 0.43\sigma_{ext}NL\,. \tag{2}$$

The validity of expression (2) for samples with a low concentration is confirmed by Fig. 2, from which it can be seen that a direct proportionality between the concentration of particles and optical density takes place up to a concentration of about 0.3-0.4%, and the linear dependence remains for different wavelengths, albeit with a different slope. With increasing concentration, increasing deviations from the linear dependence are observed, which can be explained by the effects of multiple scattering of light in dense media. When exposed to an external field, the colloid acquires optical anisotropy. The simplest anisotropy mechanism is the orientational ordering of the long axes of nonspherical particles along the direction of the external field [10]. More complex mechanisms of optical anisotropy in a magnetic colloid are associated with the formation of ordered structures under the action of a field: chains, labyrinths, or quasicrystalline formations of nanoparticles similar to a photonic crystal [15]. The uniaxial optical anisotropy induced by an external field can be described by the diagonal refractive index tensor. This leads to the appearance of birefringence in the colloid and a change in the light extinction. The refractive and extinction indices of light become different for light polarized along and across the applied field $n_{\parallel} \neq n_{\perp}$ and $k_{\parallel} \neq k_{\perp}$, where indices $\parallel$ и $\perp$ denote the orientation of the polarization of light with respect to the direction of the optical axis, i.e. direction of the external field.

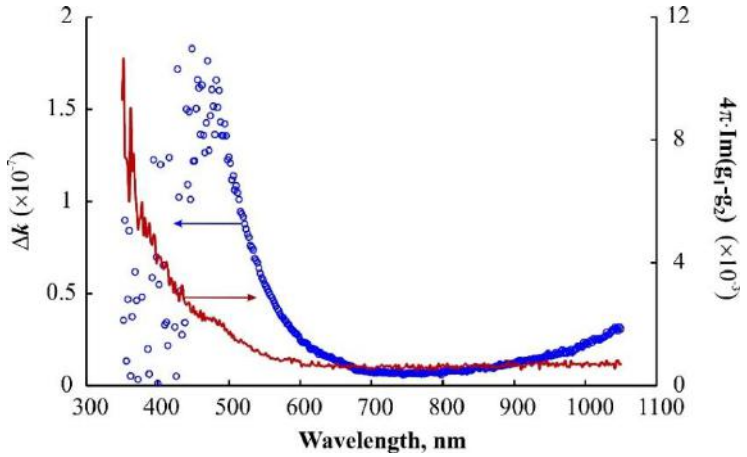

Fig. 5. Dichroism spectrum in a sample with a concentration of 0.01% when exposed to a constant magnetic field *H*=50 Oe and calculation of the imaginary part of optical anisotropy.

Following [10, 20], birefringence and dichroism in a colloid of single-domain magnetic particles under the action of an external magnetic field can be described by the expressions:

$$\Delta n = \frac{2\pi C_V}{n_k}\mathrm{Re}(g_1 - g_2)\cdot\Phi(\xi,\sigma), \qquad \Delta k = \frac{2\pi C_V}{n_k}\mathrm{Im}(g_1 - g_2)\cdot\Phi(\xi,\sigma), \tag{3}$$

where C_V is the volume concentration of particles, $g_1 - g_2$ is the optical anisotropy of the particle, $\Phi(\xi,\sigma)$ is the orientation function determined by the ratio of the energy of the particle in the magnetic field and the energy of anisotropy to the thermal energy: $\xi = mH/kT$ and $\sigma = KV/kT$. In expression (3), only the optical anisotropy is dependent on the wavelength of light, the formula for the components of which has the form:

$$g_{1,2} = \frac{n_k^2}{4\pi}\cdot\frac{\tilde{n}_m^2 - n_k^2}{n_k^2 + N_{1,2}(\tilde{n}_m^2 - n_k^2)}, \tag{4}$$

where $N_{1,2}$ are demagnetizing factors along the short and long axes of the particle, respectively, n_k is the refractive index of the dispersion medium (kerosene). Fig. 4 and 5 shows the dependencies $\mathrm{Re}(g_1 - g_2)$ and

$\mathrm{Im}(g_1 - g_2)$ as a functions of the wavelength calculated for the spectrum of the complex refractive index of the powder of magnetite nanoparticles. It can be seen that the shape of the dependence is in very good agreement with the results of birefringence measurements. However, the agreement between the experimental and calculated curves for dichroism is only qualitative.

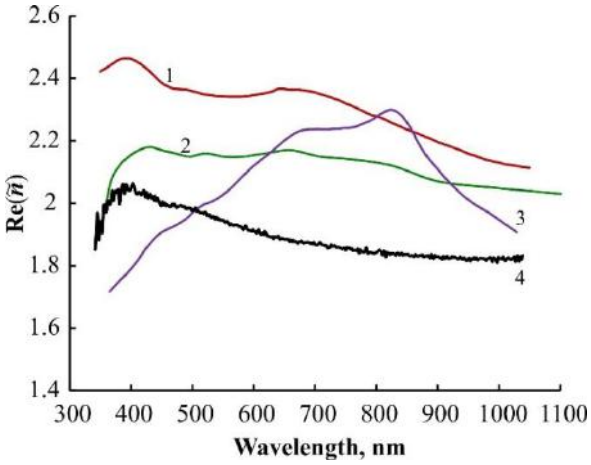

Fig. 6. Spectra of the real part of the refractive index of magnetite, plotted from the known data: 1 – [21], 2 – [22], 3 – [23], 4 – our data for magnetite nanoparticle powder.

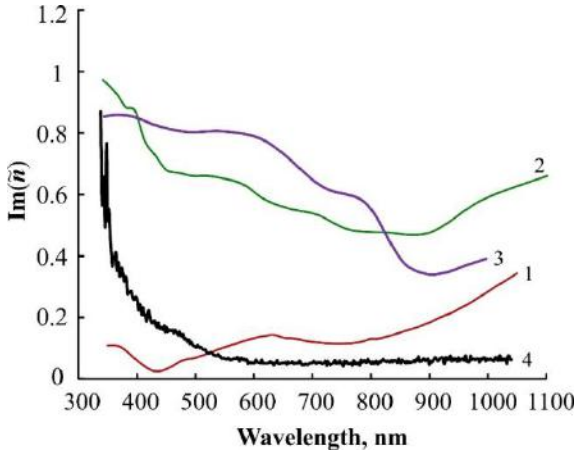

Fig. 7. Spectra of the imaginary part of the refractive index of magnetite, plotted from the known data: 1 – [21], 2 – [22], 3 – [23], 4 – our data for magnetite nanoparticle powder.

The key parameter in (3) and (4) is the dependence of the complex refractive index of magnetite on the wavelength of light $\tilde{n}_m(\lambda) = n_m(\lambda) - i \cdot k_m(\lambda)$. At least 6 spectral dependences of the complex refractive index for magnetite are known in the literature [21-23]. Figures 6 and 7 shows some of these dependencies for real and imaginary parts of refractive index of magnetite. The same graphs show the data obtained by us for the powder of magnetite nanoparticles by the ellipsometric method. It can be seen from the graphs that the spectra of both real and imaginary parts differ significantly. The spread in the values of the real part is from 50% in the short-wavelength part of the visible spectrum to 20% in the near-IR region. The difference in the values of the imaginary part is about 20%. This shows that it is incorrect to use data on optical parameters obtained for macroscopic magnetite crystals to interpret the spectra of magneto-optical effects. A comparison of the experimental and calculated spectra makes it possible to refine the data on the spectral dependence of the real and imaginary parts of the refractive index of nanosized magnetite.

The spectra of the real and imaginary parts of the refractive index of nanosized magnetite can be used to calculate the spectral dependences of the transmission of colloids (Fig. 1). For liquids with a low concentration of particles, to calculate the light extinction, one can use the Rayleigh approximation, which is valid under the condition $x = 2\pi a/\lambda << 1$. For such particles, the attenuation cross-section can be written in the form [19]:

$$\sigma_{ext} = \pi a^2 4x \operatorname{Im}\left\{\frac{\tilde{m}^2-1}{\tilde{m}^2+2}\left[1+\frac{x^2}{15}\left(\frac{\tilde{m}^2-1}{\tilde{m}^2+2}\right)\frac{\tilde{m}^4+27\tilde{m}^2+38}{2\tilde{m}^2+3}\right]\right\}+\frac{8}{3}x^4 \operatorname{Re}\left\{\left(\frac{\tilde{m}^2-1}{\tilde{m}^2+2}\right)^2\right\}, \quad (5)$$

where $\tilde{m} = \tilde{n}_2 / \tilde{n}_k$ is the relative complex refractive index of the particle material and the dispersion medium.

In Fig. 8 shows a comparison of the experimental transmission spectrum of a weakly concentrated magnetic fluid and calculations by formulas (1) and (5), for which different dependences $\tilde{n}_m(\lambda)$ are used. Calculations show that reasonable agreement with the experiment can be achieved only when using the dependence for the powder of magnetite nanoparticles. To take into account the influence of the dispersion medium of the colloid on the transmission spectra of our samples, we measured the transmission spectra of kerosene. The results were in good agreement with the known data [24].

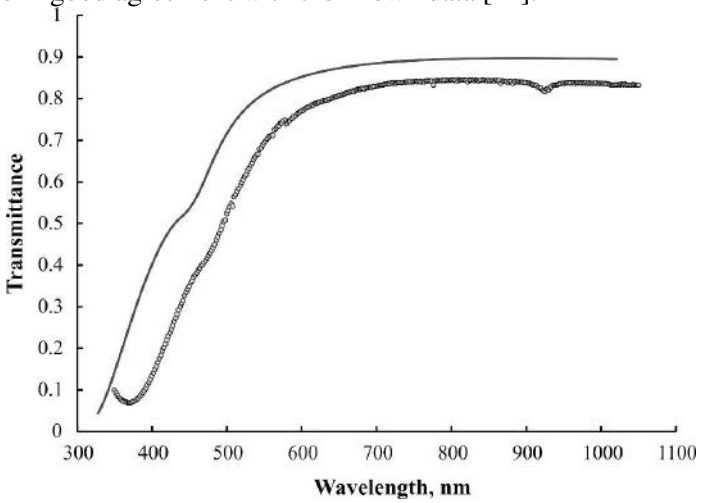

Fig. 8. Calculations of the transmission spectra of a magnetic fluid with a concentration of 0.01% (points - experiment, curve - calculation using the data for powder of magnetite nanoparticles (line 4 on Fig. 6 and Fig. 7).

The transmission spectrum of kerosene does not have any features in the spectral region from 350 to 890 nm. A small absorption band in the near IR region at 890–950 nm is determined by the third overtones of the stretching vibrations of the methyl $–CH_3$ and methylene $–CH_2$ groups. It can be assumed that the transmission spectrum of kerosene does not affect the features of the transmission spectra and spectra of magneto-optical effects in magnetic colloids. The rest of the literature and the results of our experiment on measuring the refractive index of a natural magnetite crystal give transmission spectra that differ significantly from the experimental ones both in the magnitude of the transparency and in the shape of the dependence on the wavelength.

Conclusions

The results of experimental studies of the spectral dependences of birefringence and transparency in magnetic colloids allow us to conclude that the known spectra of the refractive index of bulk magnetite are of little use for quantitative and even qualitative interpretation of optical effects in magnetic fluids based on magnetite. The best agreement with the experiment is obtained from calculations of the magnitudes of optical effects using the experimental spectra of the refractive index of a powder of magnetite nanoparticles. This may indicate that the spectral dependences of the optical parameters of bulk and nanosized magnetite differ significantly. Especially significant is the difference in the imaginary parts of the refractive index, which can reach 2-5 times, depending on the wavelength.

Acknowledgments

This work was supported within a State assignment of the Ministry of Science and Higher Education of the Russian Federation for research contract (project no. 0795-2020-0007). Measurements were carried out using equipment at the Shared Research Facilities Center, North-Caucasus Federal University, and was supported by the Russian Federation Ministry of Science and Higher Education (RF-2296.61321X0029, agreement no. 075-15-2021-687).

REFERENCES

1 Zahn M. Magnetic fluid and nanoparticle applications to nanotechnology. *J. Nanopart. Res.*, 2001, Vol. 3, pp. 73-78.

2 Odenbach S. Magnetic fluids. *Adv. Coll. Int. Sci.*, 1993, Vol. 46, pp. 263-282.

3 Philip J., Laskar J.M. Optical Properties and Applications of Ferrofluids – A Review. *J. Nanofluids*, 2012, vol. 1, pp. 3-20.

4 Szczęch M. Theoretical analysis and experimental studies on torque friction in magnetic fluid seals. *Proc. Inst. Mech. Eng., Part J: J. Eng. Tribol.*, 2020, vol. 234(2), pp. 274-281.

5 Saga N., Nakamura T. Elucidation of propulsive force of microrobot using magnetic fluid. *J. Appl. Phys.,* 2002, vol. 91, 7003.

6 Mahendran V., Philip J. Nanofluid based optical sensor for rapid visual inspection of defects in ferromagnetic materials. *Appl. Phys. Lett.*, 2012, Vol. 100, 073104.

7 Hesselbach J., Abel-Keilhack C. Active hydrostatic bearing with magnetorheological fluid. *J. Appl. Phys.*, 2003, Vol. 93, 8441.

8 Das P., Colombo M., Prosperi D. Recent advances in magnetic fluid hyperthermia for cancer therapy. *Colloids and Surfaces B: Biointerfaces.*, 2019, Vol. 174, pp. 42-55.

9 Davies H.W., Llewellyn J.P. Magneto-optic effects in ferrofluids. *J. Phys. D: Appl. Phys.*, 1980, Vol. 13, pp. 2327-2336.

10 Llewellyn J.P. Form birefringence in ferrofluids. *J. Phys. D: Appl. Phys.*, 1983, Vol. 16, pp. 95-104.

11 Jennings B.R., Xu M., Ridler P.J. Ferrofluid structures: a magnetic dichroism study. *Proc. Royal Soc. A,* 2000, Vol. 456, pp. 891-907.

12 Donatini F., Neveu S., Monin J. Measurements of longitudinal magneto-optic effects in ferrofluids: dynamical method. *J. Magn. Magn. Mater.*, 1996, Vol. 162, pp. 69-74.

13 Yerin K.V., Kunikin S.A. Change in the intensity of light scattering in a magnetite colloid under the simultaneous action of electric and magnetic fields. *Optics and Spectroscopy*, 2007, Vol. 102, No 5, pp. 765-770.

14 Yerin C.V., Vivchar V.I. Ellipsometry of magnetic fluid in a magnetic field. *J. Magn. Magn. Mater.*, 2020, Vol. 498, 166144.

15 Torres-Diaz I., Rinaldi C. Recent progress in ferrofluids research: Novel applications of magnetically controllable and tunable fluids. *Soft Matter*, 2014, Vol. 10, pp. 8584-8605.

16 Pandey B.K., Shahi A. K., Shah J., et al. Optical and magnetic properties of Fe_2O_3 nanoparticles synthesized by laser ablation/fragmentation tech-nique in different liquid media. *Applied Surface Science*, 2014. Vol. 289, pp. 462–471.

17 Donatini F., Jamon D., Monin J., Neveu S. Experimental Investigation of Lon-gitudinal Magneto-optic Effects in Four Ferrite Ferrofluids in Visible-Near Infrared Spectrum. *IEEE Trans. Magn.*, 1999, Vol. 35, No. 5, pp. 4311–4317.

18 Yerin C.V., Lykhmanova V.I., Yerina M.V. Spectral dependences of the complex refractive index of concentrated magnetic fluids. *Magnetohydrodynamics*, 2018, Vol. 54, No. 1-2, pp. 155-159.

19 Bohren C.F., Huffman D. R. *Absorption and Scattering of Light by Small Particles*. Wiley, 2007, 530 p.

20 Yerin C., Vivchar V. Field dependence of magnetooptic effect in magnetic colloid with superparamagnetic particles. *J. Phys.: Conference Series*, 2019, Vol. 1389, Issue 1, 012055.

21 Queery M.R. *Optical Constants, Contractor report*, US Army Chemical Research, Development and Engineering Center (CRDC), Aberdeen, 1985. 418 p.

22 Buchenau U., Muller I. Optical properties of magnetite. *Solid State Communication,* 1972, Vol. 11, Issue 9, pp.1291-1293.

23 Dyakov S.A., Fradkin I.M., Gippius N.A., et al. Wide-band enhancement of the transverse magneto-optical Kerr effect in magnetite-based plasmonic crystals. *Physical Review B*., 2019, Vol. 100, pp.214411.

24 Kanyathare B., Peiponen K.E. Wavelength-dependent excess permittivity as indicator of kerosene in diesel oil. *Applied Optics*, 2018, Vol. 57, No. 12, pp. 2997-3002.

Article accepted for publication 15.03.2022

DOI 10.31489/2022No2/93-100

UDC 523.2/.7, 52-13, 52-14

SPECTRAL OBSERVATIONS OF GEOSTATIONARY SATELLITES

Serebryanskiy A.V.[1], Omarov Ch.T.[1], Aimanova G.K.[1], Krugov M.A.[1], Akniyazov Ch.B.[1,2]

[1]Fesenkov Astrophysical Institute, Almaty, Kazakhstan, akniyazov@aphi.kz
[2]al-Farabi Kazakh National University, Almaty, Kazakhstan

One of the main tasks of the situational awareness system in near-Earth space is to determine the type and class of observed objects by analyzing its reflection spectra. This paper proposes a methodology and interpretation of the spectral observational data of geostationary orbit satellites obtained at the Tian Shan Astronomical Observatory (Kazakhstan) from June-December 2021. 8 geostationary objects, the type and design features of which are known were selected as observation targets. The selected satellites are stable (no fast rotation of these objects was detected) and have large reflecting surface areas. An analysis of the obtained reflection spectra shows the dependence on the phase angle of the object. The studies carried out are especially relevant for objects in high orbits, where the only currently available methods of detection and study are ground-based optical photometry and spectroscopy using meter-class telescopes.

Keywords: Optical measurements, geosynchronous Earth orbit, spectroscopy, artificial Earth satellites, orbital mechanics, observations, material spectra.

Introduction

Despite the rapid development of satellite fleets in low orbit (LEO), the geosynchronous orbit (GSO) band remains one of the most sought-after resources in near-Earth space, used by most commercial telecommunications and military satellites, each of which can cost several hundred million dollars.

One of the main tasks of the situational awareness system in near-Earth space is to determine the type and class of observed objects. One of the methods for obtaining these characteristics is the analysis of reflection spectra. This task is especially relevant for objects in high orbits, where the only methods of detection and research currently available are ground-based optical photometry and spectroscopy using meter-class telescopes (as the most effective tool, given their prevalence, availability, operating costs, etc.). Spectroscopy methods have a number of advantages over traditional multicolor photometry, since, in addition to much more information contained in the spectra, it allows one to obtain object brightness estimates simultaneously in all spectral bands, which is very important for objects in the geostationary zone [1,3,15]. Most of the objects in the GEO zone are fragments of space debris (uncontrolled objects of artificial origin), which include upper stages, parts of the fragmentation of the spacecraft, uncontrolled satellites, etc., often showing a rapid change in brightness (due to proper rotation). The rate of such a change can be from fractions of a second to minutes. It becomes clear that it is not possible to determine the color index (as one of the main indicators of the optical characteristics of the reflective surface) from the brightness values in different filters obtained by the traditional method of multicolor photometry. In addition, as shown in [2,11,12], different materials used in the space industry exhibit a variety of changes due to the effects of outer space conditions, which leads to unique spectral characteristics of each of the materials. This, in turn, also makes it possible to identify the object and determine its state.

The method of reflection spectroscopy has a number of complexities, the main of which is the inability to study small-sized objects with low brightness. However, this difficulty can be solved by using an efficient low-resolution spectrograph equipped with EMCCD in combination with a large aperture instrument, which is the AZT-20 telescope of the Assy-Turgen observatory. Such a spectrograph was developed and installed at AZT-20 at the end of 2021, and it is planned to be operational from 2022. To refine the methodology for analyzing reflectance spectra, selecting the initial class of objects of study, and developing the methodology for obtaining and preprocessing CCD spectral observation data, it was decided to conduct a series of observations of selected GSS using the Zeiss-1000 “West” telescope of the Tian Shan Observatory (TShAO), using low-resolution slit spectrograph.

1 Observations

The GSO objects with a known type, design features, stable (no fast rotation of these objects was detected), having large reflective surfaces, which is, the brightness of objects in the V-band is not higher than magnitude 11 were selected as observational targets. Another criterion was the observational visibility of these objects at the TShAO observatory. A list of these objects is shown in Table 1.

Table 1. List of objects selected for observations.

NORAD ID	Shape	Mean cross-sectional area, m^2
30793	Box + 2 Pan	13.8
32404	Box + 1 Dish + 2 Pan	458.1
38098	Box + 2 Pan	56.1
39460	Box + 2 Pan	22.2
28899	Box + 1 Dish + 2 Pan	57.2
39728	Box + 2 Pan	17.0
37749	Box + 2 Pan	10.7
29230	Box + 2 Pan	15.9

A series of five spectroscopic observations of satellites of the KazSat constellation and several GSSs were carried out using the low-resolution spectrograph of the Zeiss-1000 "Western" telescope of the TShAO. The spectrograph is equipped with a diffraction grating of 300 lines/mm, and a SBIG STT 3200 CCD camera with a size of 2184×1472 pixels (pixel size 6.8 μm) as a detector was used, which made it possible to obtain spectra in the wavelength range from ~4000 Å to ~ 8000 Å, with a dispersion of about 3Å. To obtain the optimal signal-to-noise ratio, the mode of averaging the signal over 2×2 pixels (2nd binning) was used, and the exposure time for different objects was chosen in the range from 60 seconds to 1800 seconds. The observations were carried out on the following nights: June 29, November 6, 24, 30 and December 1, 2021.

1.1 Preliminary data reduction

Data preprocessing was performed using standard procedures utilizing the Image Reduction and Analysis Facility (IRAF) package which includes dark frame subtraction, cosmic ray removal, and wavelength calibration. An example of the reduced spectra is shown in Fig.1.

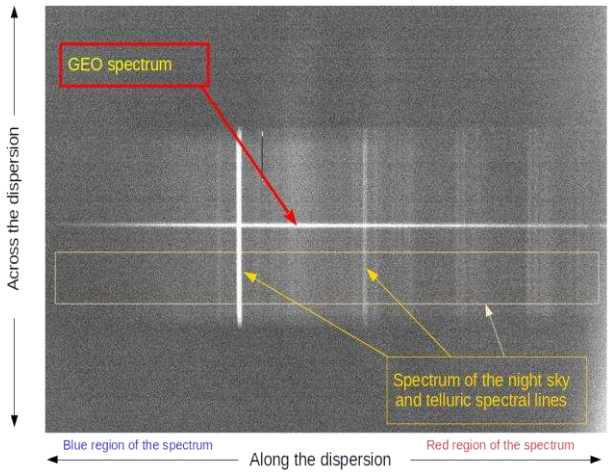

Fig. 1. An example of a CCD frame of the GSS spectrum obtained on the Zeiss-1000 "Western" slit spectrograph of TShAO. Range from ~4500Å to 7600Å

For wavelength calibration, after each spectrum of the GSO object, the spectra of a standard source - a He-Ne-Ar lamp - were obtained. Preprocessing is identical for both the GSS spectra and the spectra of standard stars. To take into account the effect of changes in the air mass during observations, the effect of flux absorption in each wavelength range (extinction) was taken into account. The resulting GSS reflectance spectra were obtained by dividing the GSS spectrum by the spectrum of the standard star.

1.2 Reference stars selection

For the task of analyzing the reflection spectra of the GSS, it is important to choose standard stars whose spectral type is as close as possible to the solar one. Additional criteria are available for observations on a given night, as well as sufficient brightness of the star to obtain a spectrum with a high signal-to-noise ratio. The list of standard stars selected according to these criteria is given in Table 2.

Table 2. List of selected standard stars

Standard star	RA	DEC	Sp type	V mag
HD 14754/HIP 11106	$02^h22^m56^s.65$	+08°32’43’’.65	F0	7.6
HD 11532	$01^h53^m18^s.37$	+00°22’23’’.28	G8III/IV	9.7
HD 292561	$06^h51^m33^s.73$	-00°11’31’’.52	G2V-G3V	10.7
HIP 111063/HD 213199	$22^h29^m58^s.797$	-16°28’07’’.395	G2V C	8.19
HIP 118115/HD 224383	$23^h57^m33.518$	-09°38’51’’.070	G3V C	7.88
TYCHO 4893-1379/HIP 46404/HD 81809	$09^h27^m46^s.808$	-06°04’17’’.008	G1.5IV-V C	5.42
TYCHO 5338-724/HIP 23831/HD 33093	$05^h07^m24^s.963$	-12°29’28’’.572	G0IV C	5.97

2 Methodology of spectral data analysis

2.1 Reflectance spectra

Reflectance spectroscopy is a powerful characterization tool that helps with the identification of micrometeoroid and orbital debris material (collectively referred to by space agencies as MMOD - Micrometeoroid and orbital debris), especially in the research related to asteroids since the 1970s. In the 1990s, its application expanded to the characterization of materials for orbiting spacecraft [4,13,14]. Ground-based spectral measurements are valuable references that assist remote optical observations in analyzing the composition of space debris material, object position and orbital motion. Reflectance spectroscopy has proven to be a viable tool for providing the aerospace industry with detailed data on the characteristics of materials commonly used in spacecraft construction, such as iridium aluminum, stainless steel, glass, gold, various silicone paints, and different types of solar cells [5]. Spectroscopic measurements taken on pieces of spacecraft materials in the lab can then be compared with spectroscopic or photometric data from orbital debris taken remotely with telescoping instruments. Research data are stored in the National Aeronautics and Space Administration (NASA) Johnson Space Center Spectral Database [6].

In the practice of spectral studies, an approximate, but a simpler and more convenient method for obtaining reflection spectra is widely used, which does not require registration of the spectral distribution of energy in the solar radiation spectrum at the time of observation. At the same time, despite the obvious advantages, such a simplified method also has significant disadvantages, most often associated with the low quality of the resulting reflection spectrum, i.e. the noise. If at the stage of recording the spectrum of an object, a reduction in the level of statistical noise can be achieved by simply increasing the exposure time, then the following procedure for dividing the spectral data series to obtain a reflection spectrum introduces an additional noise component into the final result. The most significant source of the additional noise component in the reflection spectra is the solar analog stars themselves.

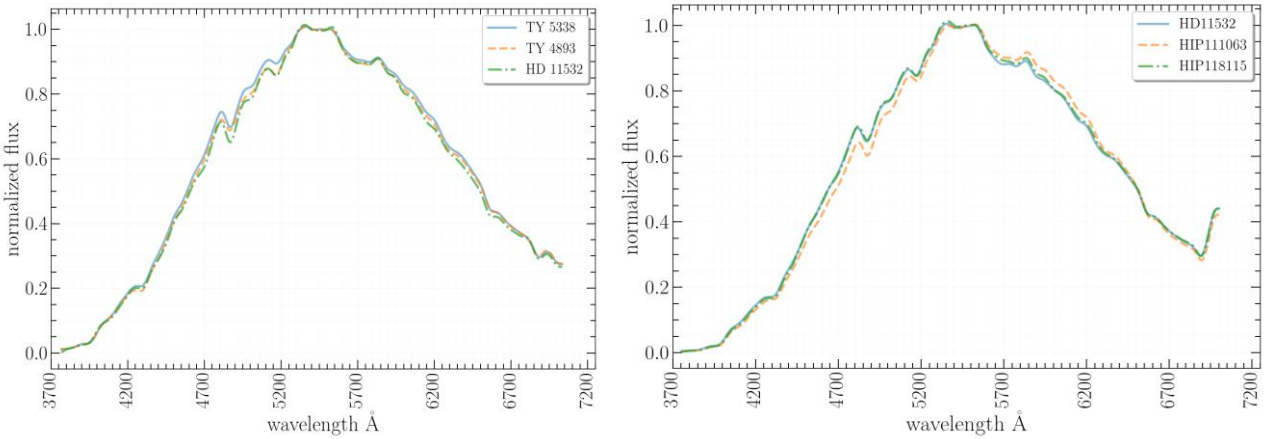

Fig. 2. Standard spectra: on the left - TYCHO 4893-1379 (HD 81809), TYCHO 5338-724 (HD 33093) and HD 11532 as of December 1, 2021; right - HD 11532, HIP 111063 and HIP 118115 as observed on November 29, 2021.

At least two solar analogue stars from Table 2 were observed every night. Examples of the spectra of the standard stars obtained on two different nights are shown in Fig.2. As a rule, we calculated the reflectance spectrum of each object with each standard by dividing its flux by the flux of the solar analog star observed on the same night in the most similar air mass conditions.

2.2 Smoothing reflectance spectra

A careful search for "ideal" standard stars, which can be considered good spectral analogues of the Sun [7,8,9], has so far only led to a list of about a dozen stars (magnitudes in the range 4^m - 6^m and spectral type G0V - G3V). Therefore, the search for methods for minimizing additional noise in the spectra is of current interest. A fairly effective way to suppress noise in the reflection spectra is their smoothing.

To smooth the reflection spectra, we used a Butterworth filter. The feature of this filter is to effectively remove unwanted noise from the data in the high-frequency range, while not affecting the data in the low-frequency region. In other words, the frequency response of this filter is constant over the passband and drops to zero in the frequency range we deem to be noise.

The Butterworth filter was implemented in the *scipy* package [10] by the *signal.butter* method, which took the filtering degree and the cutoff frequency in units of the Nyquist frequency as parameters. In our case, the filtering degree was set to 3, and the cutoff frequency was 0.055, which corresponds to smoothing the spectrum in a window of about 100Å band with a spectral resolution of about 3Å. Testing with various cutoff frequencies showed that this was the optimal value and the smoothing result, when this parameter was chosen in a reasonable range around 0.055, did not change the conclusions.

The smoothing process itself was carried out by the *signal.filtfilt* method of the *scipy* package. The results of the smoothing process are illustrated in Fig. 3-6.

In each panel of the figure, top part, the observations of the geostationary satellite spectra obtained at different phase angles are shown, below - the reflection spectra obtained for these phase angles. Reflection spectra are normalized to a wavelength of 0.55 μm. The NORAD ID number, the year of launch and the device owner country are written in the bottom line.

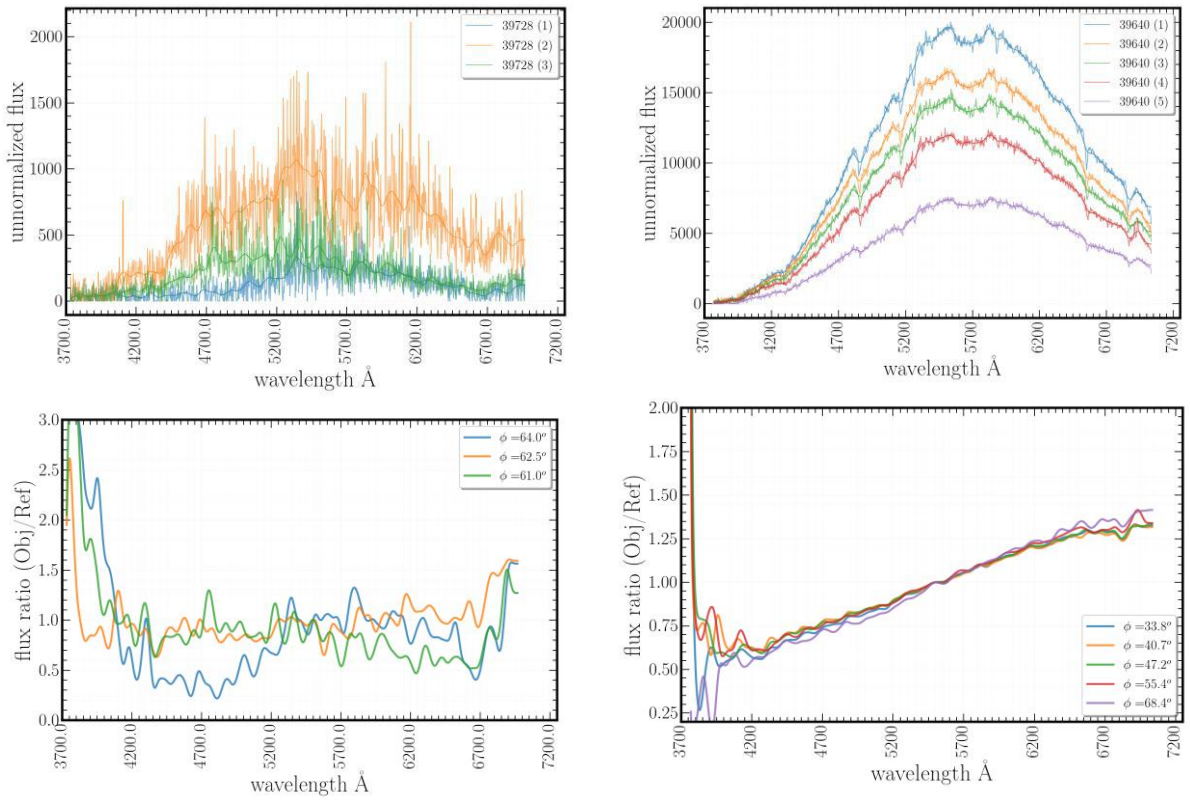

Fig. 3. Reflective spectra of GSS launched between 2013-2014 with different phase angles □. The left column shows 39728 and the right column shows 39640 with unnormalized flux (top) and normalized (bottom).

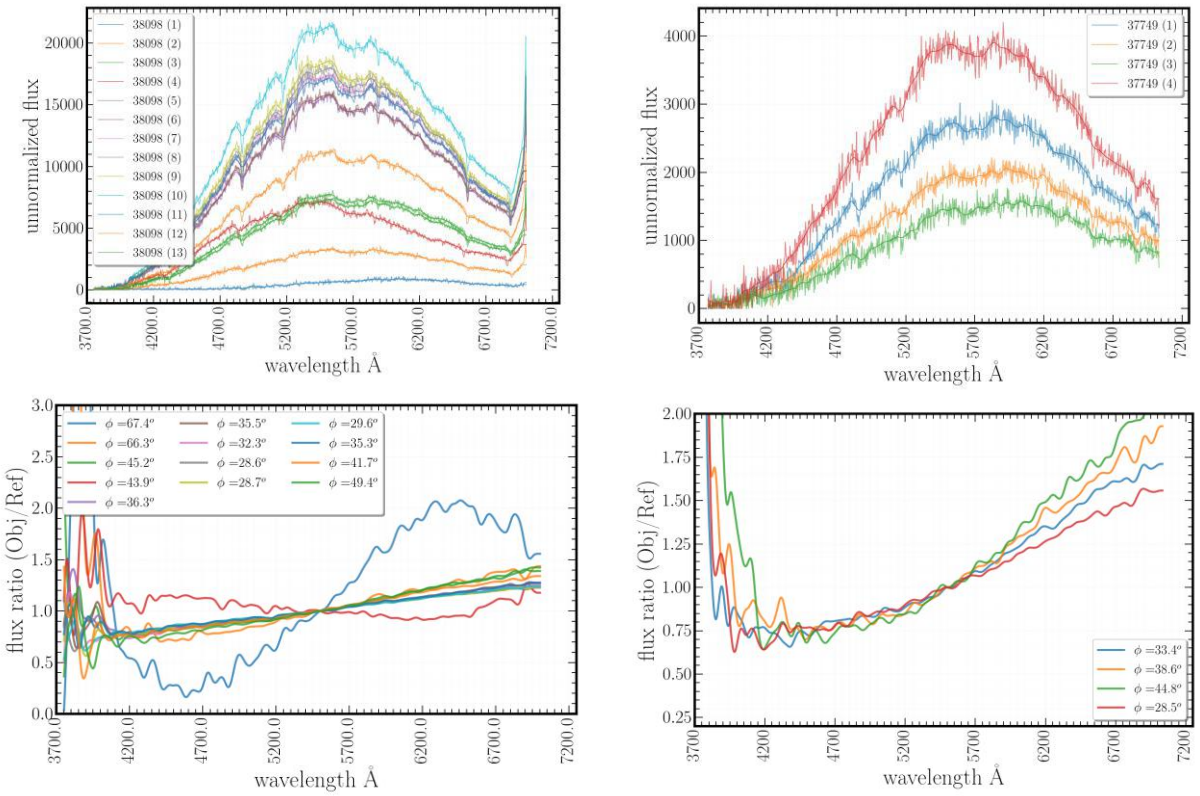

Fig. 4. Reflective spectra of GSS launched between 2011-2012 with different phase angles □. The left column shows 38098 and the right column shows 37749 with unnormalized flux (top) and normalized (bottom).

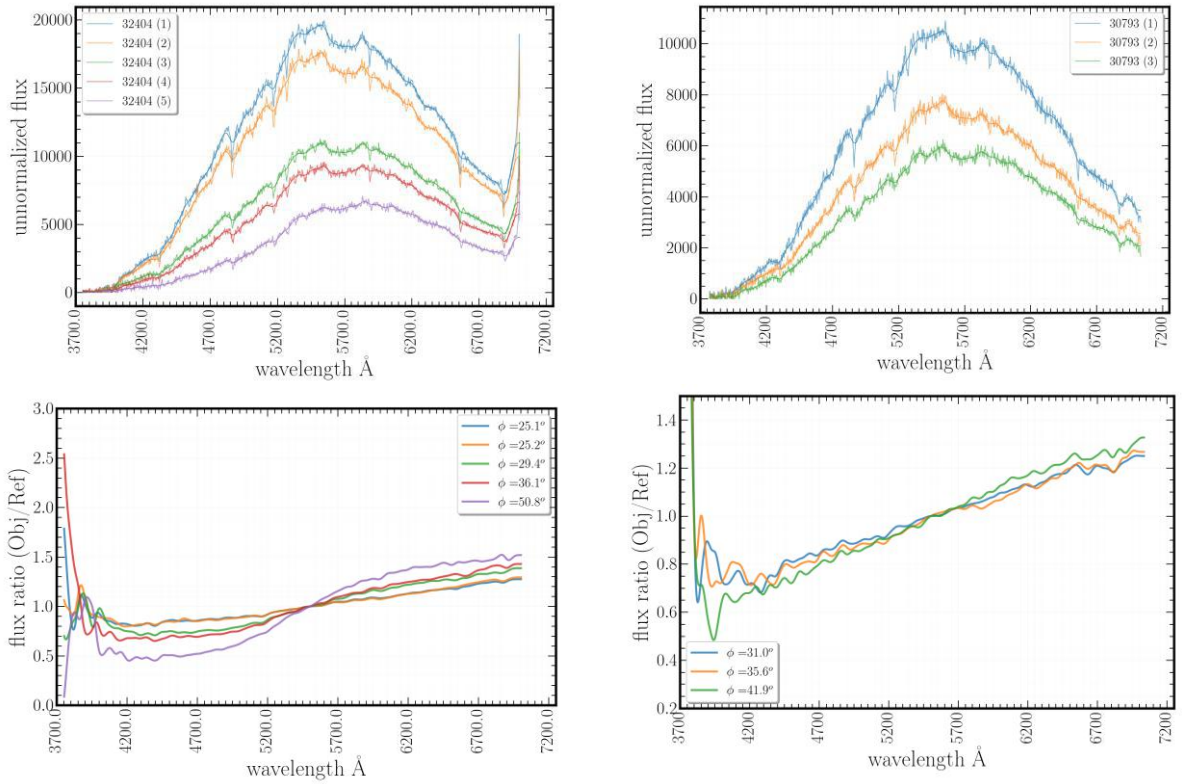

Fig. 5. Reflective spectra of GSS launched between 2007-2008 with different phase angles □. The left column shows 32404 and the right column shows 30793 with unnormalized flux (top) and normalized (bottom).

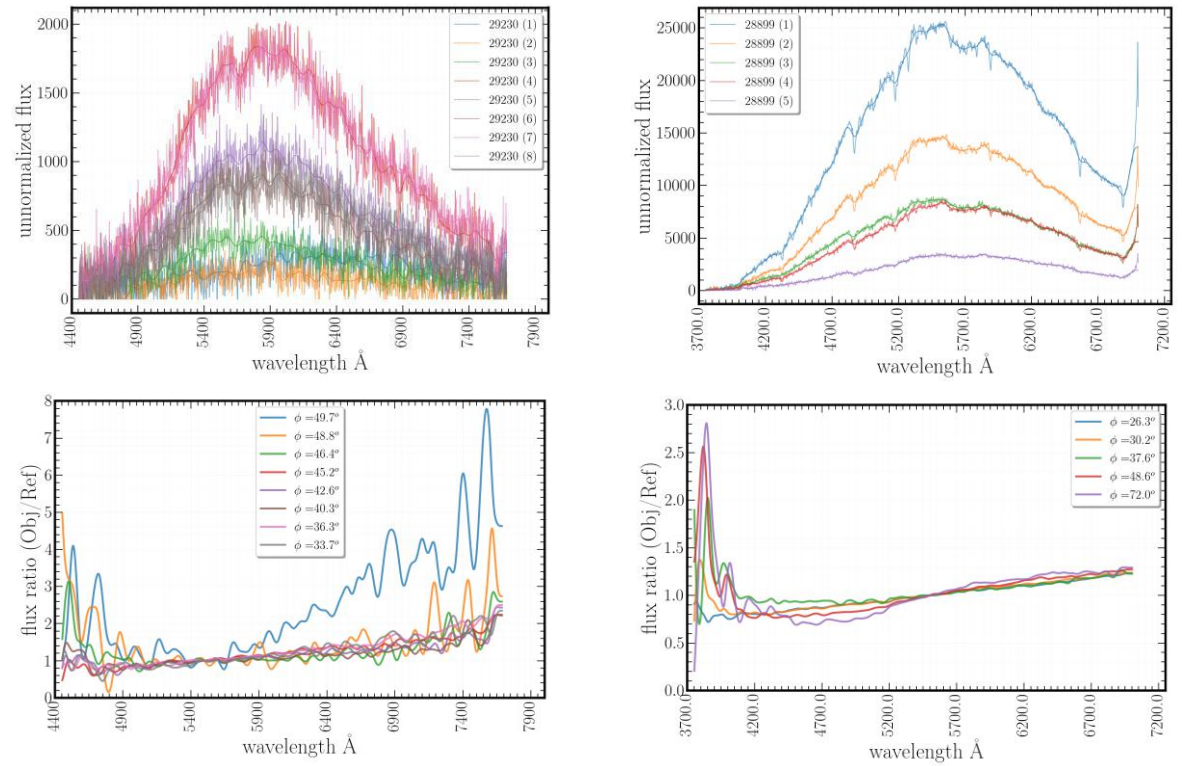

Fig. 6. Reflective spectra of GSS launched between 2005-2006 with different phase angles □. The left column shows 29230 and the right column shows 28899 with unnormalized flux (top) and normalized (bottom).

3 Discussion

It can be seen from Fig. 2 that the normalized fluxes of the selected solar analog standard stars show a good match. The resulting reflectance spectra were calculated using different standard stars observed on the same night as the object turned out to be identical in many cases along the course of change.

There is a dependence on the phase angle of the object, but at this stage, due to the limited observational material, it is impossible to trace the dependence of changes in the reflection spectrum on the lifetime of the device in orbit.

As a parameter for analyzing the change in the reflection spectrum depending on the phase angle, we have chosen the slope factor (α) of the reflection spectrum (hereinafter referred to as the "spectrum slope"), which is determined from the linear approximation of the reflection spectrum as a function of the wavelength: $flux_{fit} = \alpha \times \lambda + \beta$.

Fig. 7 shows the changes in the spectrum slope of satellites launched at different times. It can be noted that the reflectance spectra of satellites with a shorter operating time have, in general, a greater spectrum slope than satellites launched at earlier dates, but this observational material does not allow us to draw an unambiguous conclusion about the relationship between this parameter and the operating time of the apparatus. Fig. 8 shows the change in the spectrum slope of the KazSat-1 satellite, currently uncontrolled.

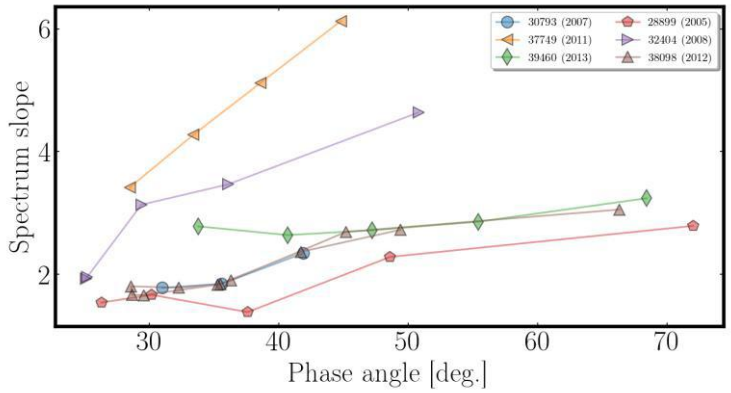

Fig. 7. Variation of the spectrum slope relative to the phase angle of the object.

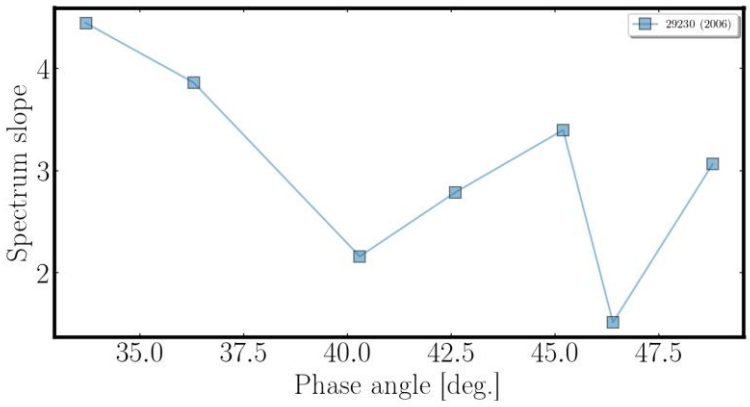

Fig. 8. The change in spectrum slope of KazSat-1 launched in 2006 and is currently uncontrolled.

Conclusion

The conducted studies have shown that the proposed method of observations and interpretation of the spectral data of the geostationary area is suitable for further research.

The analysis of the results also showed the need to obtain a large number of spectra for GSS of different configurations (geometry, platforms), for a wide range of phase angles, and different service life (after

orbital deployment). In addition, it is necessary to expand the studied spectral range into the infrared region of the spectrum. For future works, it is planned to conduct a comparative analysis of the obtained parameters of the reflection spectra of GSS with the parameters of the spectra of samples of materials and composites that are in the public domain. The preliminary result showed the possibility of obtaining the spectral characteristics of GSO, including uncontrolled spacecraft with rapidly changing illumination conditions (reflections) using an innovative spectrograph mounted on the AZT-20 telescope, which is planned to be fully operational in 2022 at the Assy-Turgen observatory.

Acknowledgements

Part of the research had been done by Ch. Akniyazov with the support grant AP08052884 "The degradation and lifetime estimation for the geostationary satellites by its photometric observations" funded by the Committee of Science of the Ministry of Education and Science of the Republic of Kazakhstan.

This research has been funded by the Aerospace Committee of the Ministry of Digital Development, Innovations and Aerospace Industry of the Republic of Kazakhstan BR11265408 "Development of the National System for Space Situational Awareness: Monitoring of Near-Earth and Deep Space and Space Weather".

The authors cordially thank the anonymous reviewer for the attention to this study and for providing valuable remarks.

REFERENCES

1 Alberto B., et. al. Physical characterization of the deep-space debris WT1190F: A testbed for advanced SSA techniques. *Advances in Space Research*, 2019, Vol. 63, pp. 371–393.

2 Reyes J.A., et. al. Spectroscopic behavior of various materials in a GEO simulated environment. *Acta Astronautica*, 2021, Vol. 189, pp. 576-583, doi: https://doi.org/10.1016/j.actaastro.2021.09.014

3 Bengtson M., et. al. Optical Characterization of Commonly Used Thermal Control Paints in a Simulated GEO Environment. *The Advanced Maui Optical and Space Surveillance Technologies Conference*, 2018, Proceedings, Hawaii, id.33.

4 Bedard M.D., Levesque M., Wallace B. Measurement of the photometric and spectral BRDF of small Canadian satellites in a controlled environment. *DRDC-VALCARTIER-SL*, 2011, Vol. 343, No 7, pp. 2011.

5 Cowardin H. et al. Observations of Titan IIIC Transtage fragmentation debris. *Proceedings of the Advanced Maui Optical and Space Surveillance Technologies Conference,* 2013, doi: https://amostech.com/2013-technical-papers/

6 NASA JSC Spacecraft Materials Spectral Database. 2018. Available at: https://ntrs.nasa.gov/ (Dec 10, 2021).

7 Farnham T.L., Schleiche D.G., A'Hearnc M.F. The HB Narrowband Comet Filters: Standard Stars and Calibrations. *Icarus*, 2000, Vol. 147, pp. 180–204. doi: https://doi.org/10.1006/icar.2000.6420.

8 Tedesco E.F., Tholen D.J., Zellner B. The eight-color asteroid survey - Standard stars. *Astronomy & Astrophysics*, 1982, Vol. 642, No A80, pp. 29.

9 Cayrel de Strobel G. *Stars resembling the Sun*. Available at https://doi.org/10.1007/s001590050006 (Jan 22, 2022)

10 Virtanen P., Gommers R., Oliphant T.E., et.al. SciPy 1.0: Fundamental Algorithms for Scientific Computing in Python. *Nature Methods*, 2022, Vol. 17, No 3, pp. 261-272.

11 Reyes J.A., Darren C. Characterization of Spacecraft Materials using Reflectance Spectroscopy. *The Advanced Maui Optical and Space Surveillance Technologies Conference Proceedings*, 2018, Hawaii, Ed.: S. Ryan, The Maui Economic Development Board, id.57.

12 Reyes J.A., et. al. Understanding optical changes in on-orbit spacecraft materials. *Proceedings of the SPIE*, 2019, Vol. 11127, id. 111270I, pp. 13, doi: 10.1117/12.2528926

13 Plis E.A., et. al. Solar panel coverglass degradation due to the simulated GEO environment exposure. *Proceedings of the SPIE*, 2021, Vol. 11727, id. 117270W, pp. 8. doi: 10.1117/12.2588655

14 Plis E.A., et. al. Effect of Simulated GEO Environment on the Properties of Solar Panel Coverglasses. *IEEE Transactions on Plasma Science*, 2021, Vol. 49, No 5, pp. 1679-1685. doi: 10.1109/TPS.2021.3070196

15 Fedorenko D.S., Legkov K.E., Modeling of the high-orbital satellite reflection spectrum. *T-Comm: Telecommunications and transport*, 2020, Vol. 14, No 11, pp. 14-20. doi: 10.36724/2072-8735-2020-14-11-14-20

Article accepted for publication 30.03.2022

DOI 10.31489/2022No2/101-106

UDC 537.533.34

USE OF COLLIMATION REGIME OF CHARGED PARTICLE BEAM FOR EXPAND THE FUNCTIONAL CAPABILITIES OF CORPUSCULAR OPTICAL SYSTEMS

Saulebekov A.O.[1], Kambarova Zh.T.[2]

[1] Kazakhstan branch of Lomonosov Moscow State University, Nur-Sultan, Kazakhstan

[2] E.A. Buketov Karaganda University, Karaganda, Kazakhstan, kambarovazht@gmail.com

The approach for the modeling of corpuscular-optical systems for the analysis of charged particle flows is considered. For all the methods considered and used earlier, the condition of spatial focusing of the particle beam was required. However, this strict condition is not always feasible in combination with other requirements. When a cylindrical electrostatic mirror analyzer is used as the main element, spatial focusing of the beam is incompatible with focusing in time of flight in terms of energy. In the paper the possibility of using the collimation regime of charged particle beam is considered, thereby eliminating the need to fulfill the focusing condition.

Keywords: electron spectroscopy, collimation, energy analyzer, corpuscular-optical systems.

Introduction

At present, electron and ion optics have not lost their relevance and continue to develop. The use of electron spectroscopy methods in microelectronics, diagnostics of materials, processing and control of surfaces has a significant impact, while these methods are used in solving technological and scientific problems. For fully solve the problems of studying the surface of a solid body, it is necessary to use a set of mutually complementary methods. Methods such as X-ray photoelectron spectroscopy (XPS) or electron spectroscopy for chemical analysis, slow electron diffraction, Auger electron spectroscopy, secondary mass spectroscopy allow, in combination, to obtain complex information about the chemical, energy state and structure of the surface of a solid [1-7]. The XPS or ESCA method occupies a special place here [8-10].

Previously, the problems and existing directions for modeling energy analyzers of charged particle flows were considered. Since the limits of energy change in electron spectroscopy methods lie in the range from units of keV to eV, electrostatic systems are mainly used as energy analyzers. The choice of electrode configurations is dictated by the ease of fabrication, small dimensions, and evaluation of the expected electron-optical characteristics of the device.

Basically, when modeling and calculating corpuscular-optical systems, two directions were used, arising from the following formula $R = \frac{\Delta L}{D}\Gamma$, where R, ΔL, D, Γ are energy resolution, linear smearing of the image, linear energy dispersion and coefficient of linear longitudinal magnification, respectively. By varying these three parameters, problems were solved to achieve certain purposes. The first direction of research was related to reducing image smearing, that is, improving the quality of focusing a beam of charged particles or increasing the focusing order. For widely used analyzers of the type of cylindrical and spherical electrostatic mirrors (CM and SM), the limits and regions of angular focusing were found. For further development of this direction, it was necessary either to complicate the field-forming electrodes [11-16] or to use additional elements.

The second direction is associated with an increase in the magnitude of the linear energy dispersion [17, 18]. The basic principle in this case was as follows. An element with increased angular energy dispersion was used, which was converted into linear dispersion by subsequent cascades in a cylindrical mirror.

Accounting for the coefficient of linear longitudinal magnification in calculations also makes it possible to improve the quality of beam focusing. When modeling analyzers of charged particle beam, the imposition of additional conditions can significantly expand the functionality of the systems. Additional conditions are imposed for each system individually, based on the specific problems for which the device is created.

In multi-cascade systems used to increase the linear energy dispersion with each cascade, the aberrational smearing of the image also increases. Accordingly, it is not possible to improve the energy resolution of the analyzer.

1 Collimating devices based on cylindrical and spherical electrostatic mirrors

One of the functions of electron-optical elements of practical interest is the collimation of charged particle beams. In corpuscular optics, this problem makes it possible to drastically reduce the intensity loss during the transport of charged particle beams and is technically realized by using electrostatic lenses and mirrors. The collimator makes it possible to obtain parallel trajectories of charged particles, which can be transmitted over long distances and fixed on the detector at any point. According to the perturbation theory approach, the quality of collimation can be described by the order, the value of which is determined by the number of simultaneously vanishing derivatives $\frac{d^n\alpha_1}{d\alpha^n} = 0$. α and α_1 are the angles of inclination of the particle trajectories at the exit from the source and after reflection from the mirror, respectively.

In work [19], the problem of collimating charged particles in SM in the inner reflection regime was considered. The conditions for collimation in this regime are determined. It is shown that a high quality of parallelism of trajectories in the beam is achieved under conditions of second-order collimation.

The collimating properties of the SM were studied by the methods of perturbation theory in [20]. The conditions for collimating charged particle beams in SM with outer reflection of the beam are determined. It is shown that the second-order collimation regime is also achieved. Charged particle beam coming from a source and located on the axis of a spherical mirror becomes parallel under certain conditions after outer reflection from the mirror (Fig.1) [21].

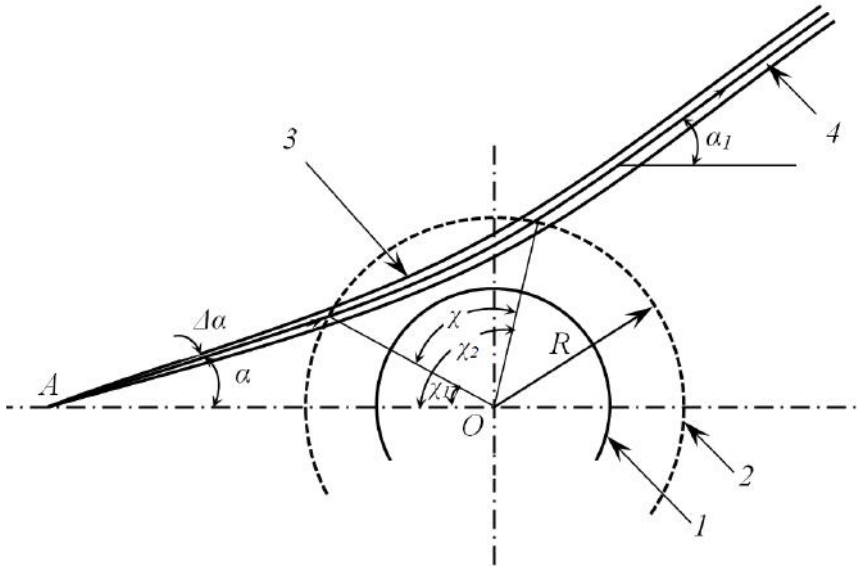

A – point source, 1 – inner spherical electrode, 2 –outer spherical electrode,
3 – trajectories of particles, 4 – parallel beams

Fig.1. The course of trajectories in the spherical mirror at the collimating regime

In Ref. [22], the collimating regime of charged particle beam at a symmetry angle in cylindrical, spherical, and hyperbolic (HM) electrostatic mirrors were calculated. The system of sequentially located CM and SM (Figs. 2 and 3), as well as a system of CM and GM in the regime of collimating charged particles at an angle to the symmetry axis of the system, is considered. It has been determined that the angular energy dispersion of the system of SM and CM significantly exceeds the angular dispersion of a single SM. This makes it possible to use it both independently and as an element with a large angular energy spread with its subsequent transformation into a linear dispersion by means of cylindrical mirrors (Fig. 4). Since, in the future, in this work, the GM is not used, then the regimes and schemes with this mirror are not presented in the work.

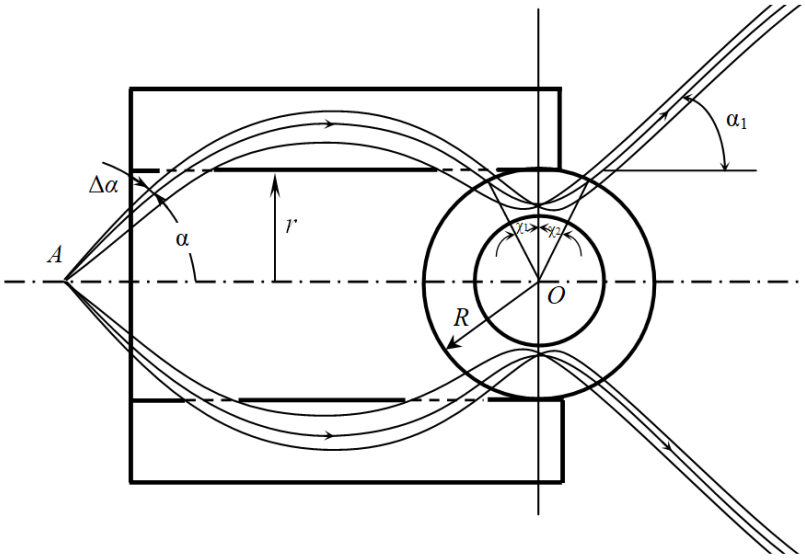

Fig.2. The system of CM and SM in the collimating regime of charged particle beam at an angle to the axis, the angular dispersion in energy is 4.6° per one percent change in the kinetic energy of the particle, the theoretical broadening of the beam at a path length of 1 m after the collimator is 0.6 mm.

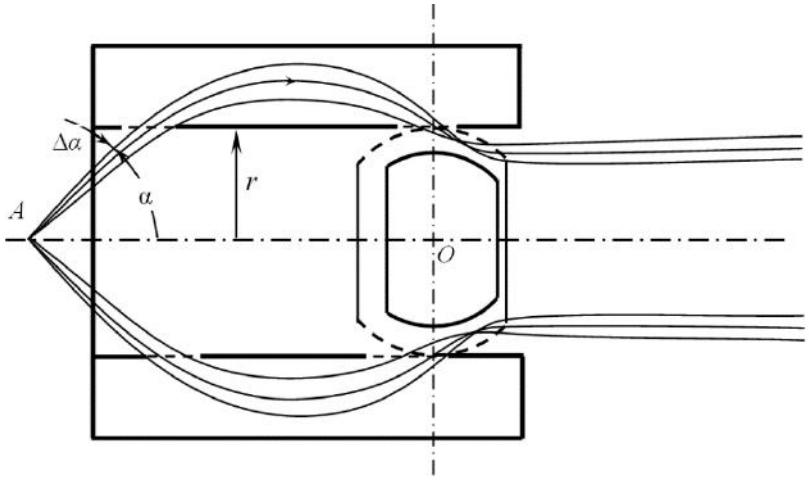

Fig.3. The system of CM and SM in the collimating regime of charged particle beam along the axis, the angular dispersion in energy is 5.4° per one percent of the change in the kinetic energy of the particle

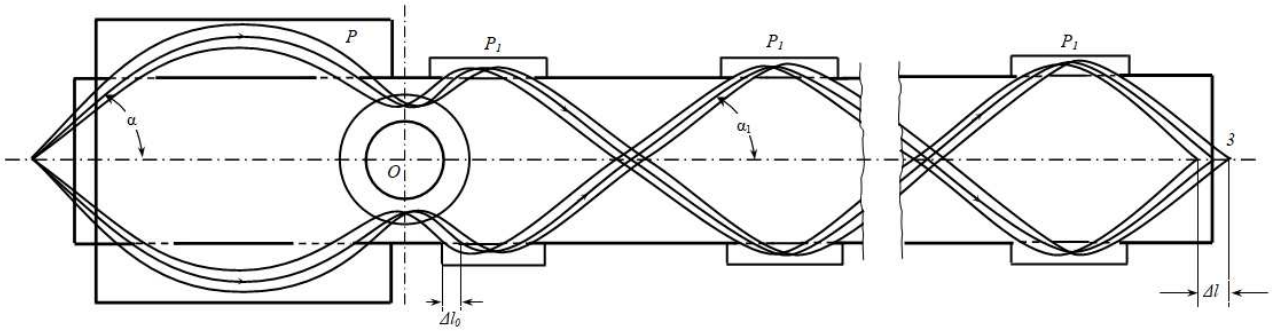

Fig.4. The energy analyzer of charged particle beam
with high energy dispersion in the collimated regime, energy resolution 0.038% in the case of one cascade, with two stages 0.024% at luminosity 1.665% of 4π

2 Application of the collimation regime for provide the possibility of carrying out time-of-flight mass analysis in a system of SM and CM

Let's show that the condition of spatial focusing of charged particle beam is incompatible with focusing in time of flight in terms of energy. Let's consider the time-of-flight properties of the trajectories of charged particles in the CM. According to [22], the time of flight T of a charged particle with an initial velocity υ, in the section between the points of entrance and exit from the CM field from "n" reflection cascades, is

$$T = 2\frac{r}{\upsilon}\sqrt{1+ctg^2\alpha}\; n\left[1-\frac{\delta}{2n}+2P\theta\right], \tag{1}$$

where δ is radius of ring source, α is angle of inclination of the trajectory to the symmetry axis of the system, W is particle kinetic energy, $p=\sqrt{\frac{W}{qv}\ln\frac{r}{r_0}}\sin\alpha$ is reflection parameter of CM, $\theta(p)=e^{p^2}\int_0^{p^2}e^{-x^2}dx$, q is particle charge [23].

Let's demand the independence of time from the energy in the first approximation with respect to ε, where $\varepsilon=\frac{W-W_0}{W_0}$ [24]. It follows from this condition that

$$1-\frac{\delta}{2n}=2P^2(1+2P\theta)\cdot \tag{2}$$

Since $0\le\delta\le1$, then all solutions of equation (2) are contained within the boundaries from P=0.5404 (δ=0) to P=0.4222 (δ=1, n=1). The time-of-flight changes due to the spread in the angle of inclination of the trajectories are determined by the derivatives of T with respect to α. Differentiating (1) twice with respect to α, we obtain [24]

$$\frac{\upsilon}{r}\frac{dT}{d\alpha}=2ctg\alpha\sqrt{1+ctg^2\alpha}\; n\left[-1+\frac{\delta}{2n}+2P^2(1+2P\theta)\right], \tag{3}$$

$$\frac{\upsilon}{r}\frac{d^2T}{d\alpha^2}=2\sqrt{1+ctg^2\alpha}\; n\left\{-(1+2ctg^2\alpha)\left(1-\frac{\delta}{2n}+2P\theta\right)+\right. \tag{4}$$

$$\left.+4P^2ctg^2\alpha\left[(1+2P\theta)(1+P^2)+P\theta\right]\right\}$$

If condition (2) is satisfied, then, as follows from Eq. (3):

$$dT/d\alpha=0.$$

Thus, in the CM, in the first approximation in ε and α, temporal focusing is carried out, both in energy and in the angle of inclination of the trajectories.

Let us now turn to angular focusing in terms of the opening angle of beam at the source exit. Let's take the derivative with respect to the angle α of the axial path function [23]

$$L=2n\,ctg\alpha\left[1-\frac{\delta}{2n}+2P\theta\right] \tag{5}$$

and equate it to zero, then we obtain the condition for spatial focusing of charged particles beam in the first approximation in the divergence angle [24,25]

$$ctg^2\alpha = \frac{1-\frac{\delta}{2n}+2P\theta}{2P^2\left(1+2P\theta\right)-1+\frac{\delta}{2n}} \tag{6}$$

When condition (2) is satisfied, when $2P^2\left(1+2P\theta\right)\to 1-\frac{\delta}{2n}$, $ctg^2\alpha\to\infty$ and $\alpha\to 0$. Consequently, in a CM, the spatial focusing of the beam is incompatible with the time-of-flight- focusing in terms of energy. If the analyzed beam has an initial angular divergence, then the time-of-flight mass-analysis under conditions of temporary energy focusing is accompanied by a longitudinal smearing of the beam, which increases with an increase in the number of cascades "*n*".

To avoid increasing smearing of the image at the entrance to the CM, narrow beams collimated at an angle to the symmetry axis of the CM should be formed; then, even with multiple reflections from the CM, the longitudinal smearing will be small.

Conclusions

Thus, method is presented that expands the functionality of the CM by implementing the function of time-of-flight mass analysis with a wide transmission range of charged particle energies. This became possible by replacing the condition of spatial focusing of the beam, which is impossible in this case, by the collimation regime. As a collimator placed at the entrance to the CM, the systems shown in Fig. 1 and 2 can be used.

The trajectories of charged particles beam of the same energy W_0 collimated at an angle α to the CM symmetry axis must be identical. The time of flight along these trajectories of charged particles of mass *m* must be the same. Since the condition of temporal focusing in energy is satisfied in the CM, then for a collimated beam of charged particles of mass *m*, but of a different energy, in the first approximation in ε, the time of flight remains the same. Due to the linear dispersion in energy *D*, the collimated energy *W* beam at the entrance to the slit of the receiving diaphragm will shift along the symmetry axis. This shift is proportional to *D* and the energy range ε in the particle beam passing through the analyzer. Charged particles of the same mass but different energies arrive at different parts of the receiving slit at the same time. This significantly increases the transmission of the analyzer in the time-of-flight mass analysis regime.

Acknowledgements

The research was supported by the Ministry of Education and Science of the Republic of Kazakhstan, Grant number AP09058188

REFERENCES

1 Woodruff D.P., Delchar T.A. *Modern Techniques of Surface Science*. Cambridge University Press; 2nd edition: 1994, 608 p.

2 Siladi M. *Electron and ion optics*. Moscow. Mir. 1990, 639 p. [in Russian]

3 Weiland C., Rumaiz A.K., Pianetta P. Recent applications of hard x-ray photoelectron spectroscopy. Journal of Vacuum Science & Technology A, 2016, Vol.34, Is.3, pp. 030801. doi: 10.1116/1.4946046

4 Chen L.X., Zhang X., Shelby M.L. Recent advances on ultrafast X-ray spectroscopy in the chemical sciences. *Chemical science,* 2014, Vol.5, Is.11, pp. 4136-4152. doi: 10.1039/c4sc01333f

5 HON, DNS. Fourier-Transform IR Spectroscopy And Electron-Spectroscopy For Chemical-Analysis - Use In The Study Of Paper Documents**.** *Advances in chemistry series.* 1986, Is. 212, pp. 349-361.

6 Baer D.R., Gaspar D.J., Nachimuthu P., et al. Application of surface chemical analysis tools for characterization of nanoparticles. *Analytical and Bioanalytical Chemistry,* 2010, Vol. 396, Is. 3, pp. 983-1002. doi: 10.1007/s00216-009-3360-1

7 Barthes-Labrousse, MGV. Auger electron spectroscopy and X-ray photoelectron spectroscopy - Principle and applications*. Vide-Science Technique Et Applications,* 2003, Vol.58, Is.308, pp. 353.

8 Zigban K., Nordling K., Falman A., et al. *Electron Spectroscopy*. Moscow, Mir, 1971, 493 p. [in Russian]

9 Penent F, Lablanquie P, Hall RI . Coincidence Auger spectroscopy. *Journal of Electron Spectroscopy and Related Phenomena, 2005,* Vol. 144, pp. 7-11. doi: 10.1016/j.elspec.2005.01.187

10 Ohno, Masahide. Many-body theory of the Auger Auger-electron coincidence spectroscopy (AAECS) spectra of solids. Chemical Physics, 2012, Vol.393, Is.1, pp. 74-79. doi: 10.1016/j.chemphys.2011.11.028

11 Saulebekov A.O., Vénos D., Kambarova Zh.T., et al. Development of energy analyzer of charged particles based on the basis non-uniform electrostatic field. *Eurasian Physical Technical Journal*, 2019, Vol.16, No.1 (31), pp. 24-29.

12 Kambarova Zh.T., Saulebekov A.O. Development of a mirror energy analyzer of charged particles beams based on a modified electrostatic field. *«Book Series: 7th International Congress «Energy Fluxes and Radiation Effects» (IEEE Xplore Digital Library).,* pp.1028-1030. doi: 10.1109/EFRE47760.2020.9242029

13 Kambarova Zh.T., Saulebekov A.O. Analyzer of charged particles based on the electrostatic quadrupole-cylindrical field in the «axis-ring» focusing regime. *«Book Series: 7th International Congress «Energy Fluxes and Radiation Effects» (IEEE Xplore Digital Library)*, pp.1031-1033. doi: 10.1109/EFRE47760.2020.9242088

14 Kambarova Zh.T., Trubitsyn A.A., Saulebekov A.O. Axially symmetric energy analyzer based on the electrostatic decapole-cylindrical field. *Technical Physics,* 2018, Vol.63, No.11, pp.1667–1671. doi: 10.1134/S1063784218110142

15 Baranova L.A. Charged particle energy analyzer based on a modified cylindrical mirror in the ring-axis focusing mode. *Technical physics,* 2014, Vol. 59. Iss. 3, pp. 463-465. doi:10.1134/s1063784214030049

16 Baranova L.A. Cylindrical mirror energy analyzer with the input of charged particles through end-surface diaphragm. *Technical physics*, 2016, Vol. 61, Iss. 8, pp. 1272-1274.

17 Ashimbaeva B.U., Chokin, K.Sh., Saulebekov A.O., Kambarova Zh.T. The combined energy analyzer composed of electrostatic mirror fields. *Journal of Electron Spectroscopy and Related Phenomena*, 2012, V.185, №11, pp.518-522.

18 Ashimbaeva B.U., Chokin, K.Sh., Saulebekov A.O., Kambarova Zh.T. Modeling of an electrostatic system from cylindrical and hyperbolic mirrors. *Prikladnaya fizika,* 2012, № 4, pp . 73-78. [in Russian].

19 Zashkvara V.V., Yurchak L.S., Bylinkin A.F. Electron-optical properties of electrostatic spherical mirror and systems based on it (I). *Zh. Tekh. Phys.,* 1989, V.58, № 10, pp. 2010-2020. [in Russian].

20 Zashkvara V.V., Saulebekov A.O., Ashimbaeva B.U. Electron-optical properties of electrostatic spherical mirror and systems based on it. II. The electrostatic spherical mirror in external reflection of charged particles beam. *Zh. Tekh. Phys.,* 1989, V.59, № 7, pp.1-9. [in Russian].

21 Saulebekov A.O., Assylbekova S.N., Kambarova Zh.T., Orakbai A. Modeling of electrostatic collimator of charged particles beams on the basis of spherical mirror. *Eurasian phys. tech. j.,* 2016, V.13, No 1 (25), pp. 22-26.

22 Saulebekov A.O., Assylbekova S.N., Tazhibaeva S.D., et al. Collimation of charged particles beam in electrostatic cylindrical, spherical and hyperbolic mirrors. *Bulletin of University of Karaganda*, 2004, №2 (34), pp.50-55.

23 Zashkvara V.V., Ilyin A.M., Ashimbaeva B.U. Time-of-flight mass separator based on electrostatic cylindrical mirrors. *Zh. Tekh. Phys.,* 1980, T.50, №7, pp.1464-1470. [in Russian].

24 Gurov V.S., Saulebekov A.O., Trubitsyn A.A. *Approximate-Analytical and Numerical Methods in the Design of Energy Analyzers/ Advances in imaging and electron physics*. Analytical Editor-in-chief Peter W. Hawkes CEMES-CNRS Toulouse, France. - Academic Press is an imprint of Elsevier, 2015. - Volume 192.- 224p.

25 Ashimbaeva B.U., Chokin K.Sh., et al. Energy analysis and time-flight mass- analysis of spherical and cylindrical mirrors system. *Eurasian phys. tech. j.,* 2007, V.4., No 2(8), pp.45-51.

Article accepted for publication 16.05.2022

SUMMARIES	ТҮСІНІКТЕМЕЛЕР	АННОТАЦИИ

Ишков А.А., Маликов В.Н., Тихонский Н.Д., Гуляренко А.А., Ремшев Е.Ю., Войнаш С.А., Соколова В.А., Ореховская А.А.

ГФҚ негізіндегі $Al+B_2O_3$ қоспасын қыздырумен бірге ӨЖС әдісімен алынған беріктейтін жабындылардың рентгенфазалық және микроқұрылымдық талдауы.

Мақалада **ӨЖС** процесін іске асыру кезінде алынған беріктейтін боридті жабындыларды зерттеу нәтижелері сипатталған. Бұл жабындылар алюминий оксиді мен борға негізделген композициялық материалдар болып табылады. Алынған жабындылар рентгендік фазалық және микроқұрылымдық талдаудан өтті, нәтижесінде алынған композициялардың негізгі құраушылары анықталып, жабынды-негізгі өтпелі аймағының қалыңдығы мен құрылымын бағалауға мүмкіндік берді. Кремний мен темірдің әртүрлі мөлшері ГФҚ негізіндегі базалық қоспаның үлгілерін қыздыру кезінде ӨЖС процестерін іске асыру кезінде беттік химиялық және металлургиялық процестердің жүруін бағалауға мүмкіндік берді. Беріктейтін жабындыны сапалы тозаңдату үшін ӨЖС процесімен бірге ГФҚ қыздыруды пайдаланудың орындылығы көрсетілген. Жабындағы екі аймағының пайда болуы көрсетілген, олар жабынның әр түрлі қалыңдығы мен құрылымына ие үлгіні ГФҚ негізіндегі қыздырумен бірге жүретін ӨЖС процесін жүзеге асыру кезінде пайда болды.

Кілт сөздері: болатты беріктендіру, микроқұрылымды талдау, өздігінен таралатын жоғары температуралық синтез, жабындылар, жоғары жиілікті тоқтар.

Ишков А.А., Маликов В.Н., Тихонский Н.Д., Гуляренко А.А., Ремшев Е.Ю., Войнаш С.А., Соколова В.А., Ореховская А.А.

Рентгенофазовый и микроструктурный анализ упрочняющих покрытий, полученных методом СВС в сочетании с нагревом смеси $Al+B_2O_3$ на основе ГФУ.

В статье описаны результаты исследований упрочняющих боридных покрытий, полученных при реализации процесса СВС. Эти покрытия представляли собой композитные материалы на основе оксида алюминия и бора. Полученные покрытия были подвергнуты рентгенофазовому и микроструктурному анализу, который показал основные компоненты полученных композиций и позволил оценить толщину и структуру переходной зоны покрытие-основной металл. Различное содержание кремния и железа позволяет оценить протекание поверхностных химических и металлургических процессов при осуществлении процессов СВС при нагреве образцов базовой смеси на основе ГФУ. Показана целесообразность использования нагрева ГФУ в сочетании с процессом СВС для более качественного распыления упрочняющего покрытия. Показано появление двух областей в покрытии, которые образовались при осуществлении процесса СВС в сочетании с нагревом образца на основе ГФУ с разной толщиной и структурой покрытия.

Ключевые слова: упрочнение стали, анализ микроструктуры, самораспространяющийся высокотемпературный синтез, покрытия, высокочастотные токи.

Козловский А.Л., Абишев Б., Жумадилов К.Ш., Шлимас Д.И.

Литий цирконатты керамикасындағы фазалық процестердің беріктік пен термофизикалық қасиеттерге әсерін зерттеу

Мақала қатты фазалық синтез әдісімен алынған литий цирконатты керамикасының қасиеттерін зерттеуге арналған. Литий цирконатты керамикасын зерттеу нысаны ретінде таңдау оларды тритийдің таралуы үшін материалдар ретінде пайдаланудың үлкен перспективаларымен байланысты. $LiO/ZrO_2/Li_2ZrO_3 \rightarrow LiO/Li_2ZrO_3 \rightarrow Li_2ZrO_3$ типті керамикадағы фазалық түрлендірулердің керамиканың беріктік және жылу-физикалық параметрлеріне әсер етуін зерттеу нәтижелері алынды. Зерттеулер барысында қаттылық пен жарыққа төзімділіктің өзгеруі керамика құрамындағы қоспа фазаларының фазалық құрамына және концентрациясына тікелей тәуелді екені анықталды. Литий оксиді және цирконий диоксиді қоспалық фазаларының ығысуы қаттылықтың жоғарылауына және бір рет сығылған кезде жарықшақтың пайда болуына төзімділіктің жоғарылауына әкелетіні анықталды. 900°С-тан жоғары температурада беріктік пен термофизикалық параметрлердің өзгеруі минималды болатындығы анықталды. Бұл жағдайда $LiO/ZrO_2/Li_2ZrO_3 \rightarrow Li_2ZrO_3$ типті керамиканың фазалық құрамының өзгеруі жылу өткізгіштік коэффициентінің 15-20%-ға артуына әкеледі.

Кілт сөздері: құрамында литий бар керамика, фазалық түрленулер, қаттылық, жылу өткізгіштік, ядролық материалдар.

Козловский А.Л., Абишев Б., Жумадилов К.Ш., Шлимас Д.И.

Изучение влияния процессов фазообразования в литиевых керамиках на прочностные и теплофизические свойства

Статья посвящена изучению свойств керамик на основе цирконата лития, полученных методом твердофазного

синтеза. Выбор в качестве объектов исследования керамик на основе цирконата лития обусловлен большими перспективами использования их в качестве материалов для размножения трития. Получены результаты исследования влияния фазовых превращений в керамиках типа $LiO/ZrO_2/Li_2ZrO_3 \rightarrow LiO/Li_2ZrO_3 \rightarrow Li_2ZrO_3$ в зависимости от температуры отжига на прочностные и теплофизические параметры керамик. В ходе проведенных исследований установлено, что изменение твердости и трещиностойкости имеют прямую зависимость от фазового состава и концентрации примесных фаз в составе керамик. Определено, что вытеснение примесных фаз оксида лития и диоксида циркония приводит к увеличению твердости и повышению устойчивости к трещинообразованию при однократном сжатии. Установлено, что при температурах отжига выше 900°С изменение прочностных и теплофизических параметров минимально. При этом изменение фазового состава керамик типа $LiO/ZrO_2/Li_2ZrO_3 \rightarrow Li_2ZrO_3$ приводит к увеличению коэффициента теплопроводности на 15-20 %.
Ключевые слова: литий содержащие керамики, фазовые превращения, твердость, теплопроводность, ядерные материалы.

Кучеренко М.Г., Кручинин Н.Ю., Неясов П.П.

Сыртқы электр өрісінде көлденең поляризацияланған металл наносым бетіндегі полиэлектролиттердің конформациялық өзгерістерін модельдеу

Бетінде адсорбцияланған полиэлектролиттері бар алтын наносымдар әр түрлі биомедициналық зерттеулерде кеңінен қолданылады. Берілген жұмыста алғаш рет сыртқы электр өрісінде көлденең поляризацияланған алтын наносым бетіндегі полилектролиттердің конформациялық өзгерістері қарастырылған. Наносым осіне көлденең сыртқы электр өрісіндегі цилиндрлік металл наносым бетіне адсорбцияланған гаусстық макромолекулалық тізбектің конформациялық қайта құрулардың арнайы құрастырылған аналитикалық моделінің қасиеттері зерттелген. Молекулалық динамика әдісін қолдана отырып, көлденең поляризацияланған алтын наносым бетіндегі біртекті зарядталған полипептидтердің конформациялық өзгерістері зерттелген. Аналитикалық модель мен молекулалы-динамикалық модельдеу нәтижелерінің негізінде наносым бетіндегі полиэлектролит буындар тығыздығының кеңістіктік таралуы құрастырылған. Сыртқы электр өрісінің кернеулігінің артуымен көлденең поляризацияланған наносымның диполь моментінің бағытында полиэлектролитті жиектің асимметриялық созылуы байқалған.
Кілт сөздері: металл наносымы, полиэлектролит, конформациялық өзгерістер, молекулалық динамика.

Кучеренко М.Г., Кручинин Н.Ю., Неясов П.П.

Моделирование конформационных изменений полиэлектролитов на поверхности поперечно поляризованного во внешнем электрическом поле металлического нанопровода

Золотые нанопровода с адсорбированными на их поверхности полиэлектролитами широко используются в различных биомедицинских исследованиях. В данной работе впервые рассмотрены конформационные изменения полиэлектролитов на поверхности золотого нанопровода, поперечно поляризованного во внешнем электрическом поле. Исследованы свойства специально созданной аналитической модели конформационных перестроек гауссовой макромолекулярной цепи, адсорбированной на поверхности цилиндрического металического нанопровода во внешнем электрическом поле, поперечном к оси нанопровода. С использованием метода молекулярной динамики исследованы конформационные изменения однородно заряженных полипептидов на поверхности поперечно поляризованного золотого нанопровода. На основе аналитической модели и результатов молекулярно-динамического моделирования построены пространственные распределения плотности звеньев полиэлектролита на поверхности нанопровода. При увеличении напряженности внешнего электрического поля наблюдалось асимметричное вытягивание полиэлектролитной опушки в направлении дипольного момента поперечно поляризованного нанопровода.
Ключевые слова: металлический нанопровод, полиэлектролит, конформационные изменения, молекулярная динамика.

Селиверстова Е.В., Ибраев Н.Х., Алихайдарова Э.Ж.

Графеннің кванттық нүктелерінің қасиеттеріне лазер энергиясы тығыздығының әсері

Әр түрлі энергия тығыздығымен лазерлік сәулелену абляция арқылы алынған графен оксидінің (GO) негізіндегі нүктелердің құрылымдық және оптикалық қасиеттері зерттелді. Лазерлік абляциядан кейін лазерлік сәулелену энергиясының тығыздығы сәйкесінше, E~15 және 21 Дж/см^2 бойынша дайындалған үлгілер үшін GO жапырақшаларының орташа бүйірлік өлшемі 1280 – 1900 нм-ден 230 ± 95 нм-ге және 110 ± 42 нм-ге дейін төмендейтіні көрсетілген. Раман спектроскопиясының деректері абляциядан кейін I_D/I_G қатынасының 1,04-тен 0,97-ге дейін төмендегенін көрсетті, бұл абляциядан кейін GO-да sp^2 гибридтелген домендер санының артуын көрсетеді. Қуаттың өзгеруі оның функционализациясының өзгеруіне, сондай-ақ GO жапырақшаларының ішіндегі sp^2-домендерінің реттелуіне іс жүзінде әсер етпейді. GO дисперсиясының оптикалық тығыздығы және олардың флуоресценциясының қарқындылығы абляция шарттарына байланысты. Абляцияланбаған дисперсия үшін 450 нм шамасында люминесценция жолағымен бірге спектрде максимумы шамамен 600 нм болатын

қосымша жолақ пайда болады. Абляциядан кейін бөлшектердің таралуы біркелкі болады, бұл GO люминесценция диапазонының пішінінің өзгеруімен де, әр түрлі толқын ұзындықтарында тіркеу кезіндегі флуоресценцияның өмір сүру ұзақтығының тұрақтылығымен де дәлелденеді.
Кілт сөздері: графен оксиді, графен нүктелері, абляция, құрылым, оптикалық қасиеттер.

Селиверстова Е.В., ИБраев Н.Х., Алихайдарова Э.Ж.
Влияние плотности энергии лазерного излучения на свойства графеновых квантовых точек
Изучены структурные и оптические свойства точек на основе оксида графена (GO), полученных при абляции лазерным излучением с различной плотностью энергии. Показано, что после лазерной абляции средний латеральный размер листов GO уменьшается с 1280 – 1900 нм до 230±95 nm и 110±42 нм для образцов, приготовленных при плотности энергии лазерного излучения E~15 и 21 Дж/см^2, соответственно. Данные Раман-спектроскопии показали, что после абляции отношение I_D/I_G уменьшилось с 1,04 до 0,97, что свидетельствует о росте числа sp^2-гибридизированных доменов в GO после аблирования. Изменение мощности практически не влияет на изменение его функционализации, а также упорядоченность sp^2-доменов внутри листа GO. Оптическая плотность дисперсий GO и интенсивность их флуоресценции зависят от условий аблирования. Для неаблированных дисперсий наряду с полосой люминесценции около 450 нм в спектре появляется дополнительная полоса с максимумом около 600 нм. После абляции распределение частиц становится более равномерным, о чем свидетельствует как изменение формы полосы люминесценции GO, так и постоянство времени жизни флуоресценции при регистрации на разных длинах волн.
Ключевые слова: оксид графена, графеновые точки, абляция, структура, оптические свойства.

Аймуханов А. К., Рожкова К. С., Ильясов Б. Р., Омарбекова Г.И., Сейсембекова Т.Е.
Төмен атмосфералық қысымда күйдірілген PEDOT:PSS полимерлі қабыршақтарының құрылымдық, оптикалық және электрфизикалық сипаттамаларына спирттік еріткіштердің әсері
Жұмыста сынап бағанасы 10^{-3} миллиметр болатын төмен атмосфералық қысымда күйдірілген поли(3,4-этилендиокситиофен) полистирол сульфонатының беттік құрылымына, оптикалық және электрофизикалық сипаттамаларына спирттік еріткіштердің әсерін зерттеу нәтижелері көрсетілген. Полимерлі қабықша бетін этил және изопропил спирттерімен модификациялау бетінің морфологиясының, полимердің оптикалық және электртасымалдаушы қасиеттерінің өзгеруіне әкелетіні анықталды. Поли(3,4-этилендиокситиофен) полистирол сульфонаты қабыршағын спирт еріткіштерімен модификациялау кезінде жұтылу спектрінде полистирол сульфонатының хош иісті фрагментінің жұтылуының төмендеуі байқалған. Поли(3,4-этилендиокситиофен) полистирол сульфонаты беттік морфологиясының құрылымдық ерекшеліктері қабыршақтың поли(3,4-этилендиокситиофен) полистирол сульфонаты қабыршағының кедергісі, поли(3,4-этилендиокситиофен) полистирол сульфонат /электрод аралығында заряд тасушылардың тасымалдану кедергісі, заряд тасушылардың тиімді жылдамдығы және тиімді ұшу уақыты тәрізді электртасымалдаушы параметрлеріне әсер ететіндігі көрсетілген. Төмен атмосфералық қысымда күйдірілген поли(3,4-этилендиокситиофен) полистирол сульфонаты қабыршақтарының электрлік тасымалдау қасиеттері жақсаратын қабыршақтарды алудың оңтайлы технологиялық параметрлері анықталды.
Кілт сөздері: PEDOT:PSS, Изопропанол, Этанол, төмен атмосфералық қысым, беттік морфология, оптикалық спектроскопия, импеданстық спектроскопия.

Аймуханов А. К., Рожкова К. С., Ильясов Б. Р., Омарбекова Г. И., Сейсембекова Т. Е.
Влияние спиртовых растворителей на структурные, оптические и электрофизические характеристики пленок полимера PEDOT:PSS, отожженных при низком атмосферном давлении
В работе представлены результаты исследования влияния спиртовых растворителей на структуру поверхности, оптические и электрофизические характеристики пленок Поли(3,4-этилендиокситиофен) полистирол сульфоната, отожженных при низком атмосферном давлении 10^{-3} миллиметров ртутного столба. Установлено, что модификация поверхности полимерной пленки этиловым и изопропиловым спиртами приводит к изменению морфологии поверхности, оптических и электротранспортных свойств полимера. Показано, что при модификации пленки Поли(3,4-этилендиокситиофен) полистирол сульфоната спиртовыми растворителями, в спектрах поглощения наблюдается уменьшение поглощения ароматического фрагмента полистирол сульфоната. Показано, что структурные особенности морфологии поверхности Поли(3,4-этилендиокситиофен) полистирол сульфоната оказывают влияние на электротранспортные параметры пленок, такие как сопротивление пленки Поли(3,4-этилендиокситиофен) полистирол сульфоната, сопротивление переноса носителей заряда на границе Поли(3,4-этилендиокситиофен) полистирол сульфонат /электрод, эффективная скорость извлечения и эффективное время пролета носителей заряда. Определены оптимальные технологические параметры получения пленок, при которых повышаются электротранспортные свойства пленок Поли(3,4-этилендиокситиофен) полистирол сульфоната, отожженных при низком атмосферном давлении.
Ключевые слова: PEDOT:PSS, Изопропанол, Этанол, низкое атмосферное давление, морфология поверхности,

оптическая спектроскопия, импедансная спектроскопия.

Қасенов Б.Қ., Қасенова Ш.Б., Сағынтаева Ж.И., Қуанышбеков Е.Е., Бектұрғанов Ж.С., Зейниденов А.К.
Жаңа наноқұрылымды мыс-мырышты лантан мен магний манганитінің электрофизикалық қасиеттері
Лантан (III), мыс (II), мырыш (II), марганец (III) және магний карбонаты оксидтерінің 800-1200°С аралығында алғашқы рет қатты фазалық өзара әрекеттесу әдісімен поликристалды мыс-мырыш манганиті синтезделді, оны "Retsch" (Германия) діріл диірменінде ұнтақтау арқылы оның наноқұрылымды бөлшектері алынды. Рентгенографиялық зерттеулер наноқұрылымды манганит кубтық сингонияда кристалданатынын анықтады. LCR (Тайвань) қондырғысында 1,5 және 10 кГц – ке тең жиіліктер кезінде 293-483 К интервалында диэлектрлік тұрақтылар мен электр кедергісі зерттелді және осы қосылыс 293-353 К интервалында жартылай өткізгішті, 353-373 К – металдық және 373-483 К-де қайтадан жартылай өткізгішті көрсетеді. Тыйым салынған аймақтың ені есептелген. 483 К диэлектрлік тұрақтылық уш жилікте де үлкен мәндерге жетеді. Жоғарыда айтылғандарға сәйкес бұл жұмыстың мақсаты жаңа наноқұрылымды лантан мен магнийдің мыс-мырышты манганитінің диэлектірлік өтімділігі мен электрқарсылығының температураға тәуелділігін зерттеу болып табылады.
Түйін сөздер: мыс-мырышты манганит, лантан, магний, наноқұрылымды бөлшектер, электронды микроскопия, рентгенография, электрфизика, жартылай өткізгіш.

Касенов Б.К., Касенова Ш.Б., Сагинтаева Ж. И., Куанышбеков Е.Е., Бектурганов Ж.С., Зейниденов А.К.
Электрофизические свойства нового наноструктурированного медно-цинкового манганита лантана и магния
Методом твердофазного взаимодействия в интервале 800-1200°С оксидов лантана (III), меди (II), цинка (II), марганца (III) и карбоната магния впервые синтезирован поликристаллический медно-цинковый манганит, измельчением которого на вибрационный мельнице «Retsch» (Германия) получены его наноструктурированные частицы. Рентгенографическими исследованиями установлено, что наноструктурированный манганит кристаллизуется в кубической сингонии. На установке LCR (Тайвань) в интервале 293-483 К при частотах, равных 1,5 и 10 кГц исследованы диэлектрические проницаемости и электросопротивления и выявлено, что данное соединение в интервале 293-353 К проявляет полупроводниковую, при 353-373 К – металлическую и при 373-483 К – опять полупроводниковую проводимость. Рассчитаны ширины запрещенной зоны. Диэлектрическая проницаемость при 483 К достигает гигантских величин при всех частотах. В связи с вышеизложенными цель настоящей работы исследование температурной зависимости диэлектрической проницаемости и электросопротивления нового наноструктурированного медно-цинкового манганита состава лантана и магния.
Ключевые слова: медно-цинковый манганит, лантан, магний, наноструктурированные частицы, электронная микроскопия, рентгенография, электрофизика, полупроводник.

Комаров И.И., Вегера А.Н., Брызгунов П.А., Махмутов Б.А., Смирнов А.О.
Осьтік көмірқышқыл турбиналары қалақшаларының салқындату арналарының топологиясын әзірлеу және зерттеу
Қазіргі уақытта энергия секторынан көміртегі диоксидінің шығарындыларын азайту жөніндегі перспективті шешім оттегі-отын циклдерін енгізу болып табылады. Оттегі-отын циклі - Аллама циклі болып табылады. Бұл циклде жұмыс денесі аса сындық көмірқышқыл газы болып табылады. Турбинаның алдындағы CO_2 –нің температурасы 1150 °С, ал қысымы 30 МПа құрайды. Жұмыс ортасының жоғары температурасымен байланысты көмірқышқыл турбинаның бастапқы кезеңдерін салқындату қажет. Берілген турбинаның салқындату жүйесінің ерекшелігі - көміртегі диоксиді салқындатқыш ретінде қолданылады. Бұл жұмыста көмірқышқыл турбинасының шүмек қалақшасының конвективті салқындату жүйелерінің екі топологиясы зерттелген, сонымен бірге цилиндрлік салқындатқыш арнасында бұрандалы қабырғалауды қолдану арқасында жылуалмасу қарқындылығын арттыру нұсқасы қарастырылған. ANSYS бағдарламалық пакетінің көмегімен шүмек қалақшасының денесінде салқындататын арналардың орналасуының екі топологиясының математикалық модельдеуі жүргізілді: 1 – конфигурация – диаметрі 1 мм 17 арнамен, 2-конфигурация-қалақша профилі пішінді үш арнамен. 1 конфигурация тиімдірек болды: Нуссельт саны 117, ал салқындатқыш жағынан жылу беру коэффициентінің орташа мәні - 6413 Вт/м^2·К. Зерттелетін қалақшаның салқындатқыш цилиндрлік арнасында бұрандалы қабырғалауды қолданудың әсері зерттелген, бұл металл температурасын орташа есеппен 54 °С-қа төмендетуге және жылу беру коэффициентін 2 есе арттыруға мүмкіндік берді.
Кілт сөздері: салқындататын қалақшалар, аса критикалық көміртегі диоксиді, оттегі-отын энергетикалық циклі, көмір қышқыл турбинасы, қабырғалық турбулизаторлар, жылу алмасу

Комаров И.И., Вегера А.Н., Брызгунов П.А., Махмутов Б.А., Смирнов А.О.
Разработка и исследование топологии охлаждающих каналов лопаток осевых углекислотных турбин
В настоящее время перспективным решением по сокращению выбросов диоксида углерода от энергетического

сектора является ввод кислородно-топливных циклов. Наиболее кислородно-топливным циклом является цикл Аллама. В данном цикле рабочим телом является сверхкритический диоксид углерода. Температура CO_2 перед турбиной равна 1150 °C, а давление 30 МПа. Вследствие высокой температуры рабочей среды появляется необходимость охлаждения первых ступеней углекислотной турбины. Особенностью системы охлаждения данной турбиной является то, что в роли хладогента применяется диоксид углерода. В данной работе проведено исследование двух топологий систем конвективного охлаждения сопловой лопатки углекислотной турбины, а также рассмотрен вариант увеличения интенсивности теплообмена благодаря применению винтового оребрения в цилиндрическом охлаждающем канале. Проведено математическое моделирование с помощью программного пакета ANSYS двух топологий расположения охлаждающих каналов в теле сопловой лопатки: конфигурация 1 – с 17 каналами диаметром 1мм, конфигурация 2 – с тремя каналами в форме профиля лопатки. Конфигурация 1 оказалась более эффективной: число Нуссельта имеет значение 117, а среднее значение коэффициента теплоотдачи со стороны хладагента равно 6413 Вт/м^2·К. Исследовано влияние применения винтового оребрения в охлаждающем цилиндрическом канале исследуемой лопатки, что позволило снизить температуру металла в среднем на 54 °C и увеличить коэффициент теплоотдачи в 2 раза.

Ключевые слова: охлаждаемые лопатки, сверхкритический диоксид углерода, кислородно-топливный энергетический цикл, углекислотная турбина, реберные турбулизаторы, теплообмен

Омарова Ж.Б., Ережеп Д.Е., Алдияров А.У., Голиков О., Токмолдин Н.С.

$CH_3NH_3SNI_3$ негізіндегі экологиялық таза күн элементтерінің өнімділігін модельдеу

$CH_3NH_3PbI_3$ сияқты жоғары тиімді материалдарды пайдалана отырып, перовскиттік фотоэлектрлік технологияны кең ауқымда ендіру болашақта күрделі экологиялық мәселелерге әкелуі мүмкін. Коммерцияландыру үшін балама шешім Sn негізіндегі перовскит күн батареясын енгізу болып табылады. Бұл жұмыста қорғасынсыз, экологиялық таза күн батареясы, яғни жарықты сіңіретін қабат ретінде $CH_3NH_3SnI_3$ қолданылуымен теориялық зерттеу нәтижелері көрсетілген. Перовскит негізіндегі күн батареясының сипаттамаларын модельдеу SCAPS-1D бағдарламасы арқылы жүзеге асырылды. Сіңіргіш қабаттың әр түрлі қалыңдықтары талданды және қоршаған орта температурасында 28%-ға дейін жоғары қуатты түрлендіру тиімділігін (PCE) көрсететін оңтайландырылған құрылғы құрылымы ұсынылды. Нәтижесінде, $CH_3NH_3SnI_3$ сіңіргіш қабатының әртүрлі қалыңдығын талдағаннан кейін, 500 нм қалыңдығында қуатты түрлендіру ПӘК-і 27,41 %, толтыру коэффициенті 85,92 % және қысқа тұйықталу тоғының тығыздығы 32,60 мА/см^2 және ашық тізбектегі кернеу 0,98 В кезінде оңтайлы өнімділік көрсетілгені анықталды. Алынған сандық нәтижелер $CH_3NH_3SnI_3$ сіңіргіш қабатын пайдалану перовскит негізіндегі экологиялық таза күн батареясының жоғары тиімді технологиясын жасау үшін балама алмастырғыш бола алатынын көрсетеді.

Кілт сөздері: қорғасынсыз перовскит күн батареялары, электронды-тасымалдау қабаты, тесік-тасымалдау қабаты, сіңіру қабаты, SCAPS-1D.

Омарова Ж.Б., Ережеп Д.Е., Алдияров А.У., Голиков О., Токмолдин Н.С.

Моделирование производительности экологически чистых солнечных элементов на основе $CH_3NH_3SnI_3$

Широкомасштабное внедрение перовскитной фотоэлектрической технологии с использованием таких высокоэффективных материалов, как $CH_3NH_3PbI_3$, в будущем может столкнуться с серьезными экологическими проблемами. Альтернативным решением для коммерческой реализации может являться внедрение перовскитного солнечного элемента на основе Sn. В данной работе представлены результаты теоретического исследования без свинцового, экологически чистого солнечного элемента, с использованием $CH_3NH_3SnI_3$ в качестве светопоглощающего слоя. Моделирование характеристик солнечного элемента на основе перовскита было проведено с помощью программы SCAPS-1D. Проанализированы различные толщины поглощающего слоя, и была предложена оптимизированная структура устройства, показывающая высокую эффективность преобразования энергии (PCE) до 28% при температуре окружающей среды. В результате, после анализа различных толщин поглощающего слоя $CH_3NH_3SnI_3$, было выявлено, что при толщине 500 нм демонстрируются оптимальная производительность с КПД преобразования мощности 27,41 %, коэффициентом заполнения 85,92%, плотность тока короткого замыкания 32,60 мА/см^2 и напряжение холостого хода 0,98 В. Полученные численные результаты свидетельствуют о том, что использование поглощающего слоя $CH_3NH_3SnI_3$ может быть альтернативной заменой для создания высокоэффективной технологии экологически чистого солнечного элемента на основе перовскита.

Ключевые слова: бессвинцовые перовскитные солнечные элементы, электронно-транспортный слой, дырочно-транспортный слой, поглощающий слой, SCAPS-1D.

Супрун Т.Т.

Қорытқы кептіру процесінің аэродинамикалық сипаттамаларын жақсартудың жергілікті тәсілі

Энергия үнемдейтін технологиялар әр түрлі технологиялық процестерде, атап айтқанда өсімдік қалдықтарын кептіру үшін кеңінен қолданылады. Зерттеудің мақсаты - ағындардың оңтайлы таралуын қамтамасыз ету және термоанемометрия әдісімен кеңістіктің сипаттамалық нүктелеріндегі жергілікті жылдамдықты өлшеу негізінде

салқындатқышты беру жүйесінің конструкциясына мақсатты өзгерістер енгізу болып табылады. Өлшеулер кезең-кезеңмен жүргізілді және қондырғының сегіз модификациясын қамтыды. Алынған мәліметтерді талдау негізінде жылу беру жүйесі конструкциясын жетілдіру бойынша нақты шаралар жасалды.
Кілт сөздері: жылу тасымалдағышты беру жүйесі, жергілікті аэродинамикалық сипаттамалар.

Супрун Т.Т.
Локальный подход к улучшению аэродинамических характеристик процесса окончательной сушки
Энергосберегающие технологии широко используются в различных технологических процессах, в частности для досушивания растительных отходов. Целью исследования является обеспечение оптимального распределения потоков и внесение целенаправленных изменений в конструкцию системы подачи теплоносителя на основе измерений локальных скоростей в характерных точках пространства методами термоанемометрии. Измерения проводились поэтапно и охватили восемь модификаций установки. На основе анализа полученных данных были разработаны конкретные мероприятия по совершенствованию конструкции системы подачи теплоносителя.
Ключевые слова: система подачи теплоносителя, местные аэродинамические характеристики.

Карабекова Д.Ж., Қисабекова П.Ә., Кучерук В.Ю., Мусенова Э.К., Азатбек Ш.
Жылу ағынын өлшеуге арналған құрылғының негізгі сипаттамалары
Жұмыста жылу желілері мен әр түрлі технологиялық объектілердің жағдайын техникалық диагностикалау үшін бұзылмайтын бақылау әдістерін қолдану мәселелері мен перспективалары қарастырылады. Шығын өлшегіштің көмегімен жылу процестерінің температуралық жағдайын тіркеу оның жылу физикалық сипаттамаларының өзгеруі сезімталдығына, сыртқы энергия көзін пайдаланбай басқару мүмкіндігіне және т.б. байланысты. Жылу ағынының жылуэлектрлік түрлендіргіші негізінде арнайы құрылымын пайдалану негізінде жылу ағынын өлшеуге арналған құрылғының сипаттамасы ұсынылған. Құрылғының қыздырғыш элементі тірек беті ретінде қызмет ететін оқшаулағыш қабатқа орнатылуы оның ерекшелігі болып табылады. Құрылғыны калибрлеуді зерттелетін объектіден жылу ағынын ол арқылы электр тогы өткен кезде қыздырғыш элементінде бөлінетін жылу ағынымен ауыстыру арқылы жүргізу ұсынылады. Әзірленген құрылғы жылу ағынының тығыздығының өзгеруін (25-100) Вт/м^2 диапазонында тіркеуге мүмкіндік береді, ал бұл жылу оқшаулаудың бұзылуын анықтауға мүмкіндік береді.
Кілт сөздері: жылу ағынын өлшегіш, термоэлектрлік батарея түрлендіргіші, жылу ағынын өлшегіштерінің интегралды сезімталдығы, мыс-константан терможұбы, жылу энергиясы.

Карабекова Д.Ж., Кисабекова П.А., Кучерук В.Ю., Мусенова Э.К., Азатбек Ш.
Основные характеристики измерителя теплового потока
В работе рассматриваются проблемы и перспективы применения методов неразрушающего контроля для технической диагностики состояния тепловых сетей и различных технологических объектов. Регистрация температурного состояния тепловых процессов с помощью расходомера обусловлено его чувствительностью к изменению теплофизических характеристик, возможностью управления без использования внешнего источника энергии и др. Приведено описание разработанного устройства для измерения теплового потока на основе использования термоэлектрического преобразователя теплового потока специальной конструкции. Отличительная особенность устройства в том, что нагревательный элемент установлен на изоляционном слое, служащем опорной поверхностью. Калибровку прибора предлагается проводить путем замены теплового потока от исследуемого объекта тепловым потоком, выделяющимся в нагревательном элементе при прохождении через него электрического тока. Разработанное устройство позволяет регистрировать изменение плотности теплового потока в диапазоне (25 -100) Вт/м^2, что позволяет обнаружить малейшее нарушение теплоизоляции.
Ключевые слова: измеритель теплового потока, термоэлектрический батарейный преобразователь, интегральная чувствительность измерителей теплового потока, медно-константановая термопара, тепловая энергия.

Рудник В.Е., Суворов А.А., Разживин И.А., Рубан Н.Ю., Андреев М.В.
Әр түрлі тығыздықты электр желілеріндегі синтетикалық инерция алгоритмінің жұмысын зерттеу
Синтетикалық инерция алгоритмін қолдану мүмкіндігі қуат түрлендіргіші арқылы желіге қосылатын жаңартылатын энергия көздері негізінде генерациялайтын қондырғылардың маңызды қасиеттерінің бірі болып табылады. Синтетикалық инерцияны қолдану арқасында мұндай қондырғылардың инерциялық және демпфирлеу қасиеттерін арттыруға болады. Синтетикалық инерция алгоритмінің тиімділігі қуат түрлендіргішінің басқару жүйесінің ажырамас бөлігі болып табылатын жиілікті фазалық автоматты түрде баптау контурының көмегімен қалыптасатын желінің кернеу жиілігінің кіріс мәніне байланысты. Алайда, жиілікті фазалық автоматты түрде баптау тізбегінің жұмыс істеуі әлсіз электр желілеріне қуат түрлендіргіші орнатқан кезде әртүрлі жиіліктегі тербелістерге әкелуі мүмкін және сәйкесінше синтетикалық инерция

алгоритмінің жұмысына теріс әсер етуі мүмкін. Зерттеулер көрсеткендей, фотоэлектрлік қондырғыны басқару жүйесіндегі жиілікті фазалық автоматты түрде баптау тізбегі синтетикалық инерция алгоритмінің жұмысына әсер етеді, бірақ бұл әсердің сипаты - электр желісінің тығыздығына байланысты және оң немесе теріс болуы мүмкін. Сынақты электр энергия жүйесінде алынған әсер нақты өлшемділікті энергия жүйесі үшін де расталған.
Кілт сөздері: фазалық жиілікті автоматты түрде реттеу, синтетикалық инерция, фотоэлектрлік қондырғы, жаңартылатын энергия көздері, электр энергия жүйесі.

Рудник В.Е., Суворов А.А., Разживин И.А., Рубан Н.Ю., Андреев М.В.

Исследование функционирования алгоритма синтетической инерции в электрических сетях разной плотности

Возможность использования алгоритма синтетической инерции является одним из важнейших свойств генерирующих установок на базе возобновляемых источников энергии, подключаемых к сети через силовой преобразователь (ГУСП). Благодаря применению синтетической инерции появляется возможность повысить инерционные и демпфирующие свойства таких установок. Эффективность функционирования алгоритма синтетической инерции зависит от входного значения частоты напряжения сети, которое формируется с помощью контура фазовой автоподстройкой частоты, являющегося неотъемлемой частью системы управления силового преобразователя. Однако функционирование контура фазовой автоподстройкой частоты может приводить к колебаниям с различной частотой при установке ГУСП в слабые электрические сети и, соответственно, негативно сказаться на работоспособности алгоритма синтетической инерции. Проведенные исследования показали, что контур фазовой автоподстройкой частоты в системе управления фотоэлектрической установки позволяет влиять на функционирование алгоритма синтетической инерции, но характер этого влияния зависит от плотности электрической сети и может быть положительным или отрицательным. Полученное на тестовой электроэнергетической системе влияние также подтверждено для энергосистемы реальной размерности.
Ключевые слова*:* фазовая автоподстройка частоты, синтетическая инерция, фотоэлектрическая установка, возобновляемые источники энергии, электроэнергетическая система.

Ерин К.В., Вивчарь В.И, Белых С.С.

Магниттік сұйықтықтардағы магниттік-оптикалық әсерлердің спектрлік тәуелділіктері

Магниттік сұйықтықтағы өткізу пен оптикалық анизотропия әсерлерінің спектрлік тәуелділіктері зерттелген. Көлемді магнетиттің сыну көрсеткішінің белгілі спектрлері магниттік сұйықтықтардағы оптикалық эффектілерді сандық және сапалық түсіндіруге жарамсыз екендігі көрсетілген. Эксперименттің ең жақсы үйлесімі - магнетиттің нанобөлшектері ұнтағының кешенді сыну көрсеткішінің эксперименттік спектрлерін қолдану арқылы алынды. Көлемді және наноөлшемді магнетиттің кешенді сыну көрсеткішінің спектрлеріндегі айтарлықтай айырмашылық туралы қорытынды жасалды.
Кілт сөздері: магниттік сұйықтықтар, оптикалық анизотропия, магнетит, кешенді сыну көрсеткіші.

Ерин К.В., Вивчарь В.И, Белых С.С.

Спектральные зависимости магнитооптических эффектов в магнитных жидкостях

Исследованы спектральные зависимости эффектов пропускания и оптической анизотропии в магнитной жидкости. Показано, что известные спектры показателя преломления объемного магнетита малопригодны для количественной и качественной интерпретации оптических эффектов в магнитных жидкостях. Наилучшее согласие с экспериментом было получено при использовании экспериментальных спектров комплексного показателя преломления порошка наночастиц магнетита. Найдены существенные различия спектров комплексного показателя преломления объемного и наноразмерного магнетита.
Ключевые слова: магнитные жидкости, оптическая анизотропия, магнетит, комплексный показатель преломления.

Серебрянский А.В., Омаров Ч.Т., Айманова Г.К., Кругов М.А., Акниязов Ч.Б.

Геотұрақты аймақтағы серіктердің спектрлік бақылаулары

Жер маңындағы ғарыш кеңістігінің жағдайынан хабардар болу жүйесінің басты міндеттерінің бірі - бақыланатын объектілердің класын және типін анықтау болып табылады. Бұл сипаттамаларды алу әдістерінің бірі – шағылдырушы спектрлерді талдау болып табылады. Берілген жұмыста 2021 жылдың шілде-желтоқсан аралығында Тянь-Шань астрономиялық обсерваториясында (Қазақстан) алынған геотұрақты аймақтағы аппараттардың спектрлік бақылау мәліметтерінің талдаулары және әдістемесі ұсынылған. Бақылауға типі және құрылымдық ерекшеліктері белгілі 8 объектісі таңдап алынды. Таңдап алынған аппараттар тұрақты, шағылдырушы беттің ауданы ауқымды (бұл объектілердің тез айналулары бақыланбады). Алынған шағылдырушы спектрлерін талдаулары объектінің фазалық бұрыштан тәуелділігін көрсетті. Жүргізілген зерттеулер әсіресе жоғары орбитадағы объектілер үшін өте маңызды, себебі қазіргі уақытта қол жетімді жалғыз анықтау және зерттеу әдісі - бұл метрлік классты телескоптарды қолдануымен жердегі оптикалық фотометрия

және спектроскопия болып табылады.
Кілт сөздері: оптикалық өлшеулер, жерге жақын геосинхронды орбита, спектроскопия, жердің жасанды серіктері, орбиталық механика, астрономиялық бақылаулар, материалдық спектрлер.

Серебрянский А.В., Омаров Ч.Т., Айманова Г.К., Кругов М.А., Акниязов Ч.Б.

Спектральные наблюдения спутников геостационарной области

Одной из главных задач системы ситуационной осведомленности в околоземном космическом пространстве является определение типа и класса наблюдаемых объектов. Одним из методов для получения этих характеристик является анализ отражательных спектров. В данной работе предлагается методика и интерпретация спектральных данных наблюдений аппаратов геостационарной области, полученных на Тянь-Шанской астрономической обсерватории (Казахстан) в июне-декабре 2021 года. В качестве объектов наблюдений выбраны 8 объектов, тип и конструктивные особенности которых известны. Выбранные аппараты стабильные (не обнаружено быстрых вращений этих объектов), имеют большие площади отражающей поверхности. Анализ полученных спектров отражения, показывает зависимость от фазового угла объекта. Проведенные исследования особенно актуальны для объектов на высоких орбитах, где единственным доступным на данный момент методом обнаружения и исследования является наземная оптическая фотометрия и спектроскопия с использованием телескопов метрового класса.
Ключевые слова: оптические измерения, геосинхронная околоземная орбита, спектроскопия, искусственные спутники Земли, орбитальная механика, астрономические наблюдения, материальные спектры

Сәулебеков А.О., Қамбарова Ж.Т.

Корпускулалы-оптикалық жүйелердің функционалдық мүмкіндіктерін кеңейту үшін зарядталған бөлшектер шоғын коллимирлеу режимін қолдану

Зарядталған бөлшектердің ағындарын талдау үшін корпускулалы-оптикалық жүйелерді модельдеудің жаңа тәсілі қарастырылған. Бұрын қарастырылған және қолданылған барлық әдістер үшін бөлшектер шоғын кеңістіктік тоғыстау шарты міндетті болды. Алайда, бұл қатаң шарт басқа талаптармен бірге әрдайым орындала бермейді. Негізгі элемент ретінде цилиндрлік электрстатикалық айналы талдағыштың қолданған кезде, шоқтың кеңістіктік тоғысталуы энергия бойынша ұшу уақытында тоғыстаумен үйлеспейді. Жұмыста зарядталған бөлшектердің шоғын коллимирлеу режимін қолдану мүмкіндігі қарастырылған, осылайша тоғыстау шартын орындау қажеттілігін жояды.

Саулебеков А.О., Камбарова Ж.Т.

Использование режима коллимирования пучка заряженных частиц для расширения функциональных возможностей корпускулярно-оптических систем.

Рассмотрен еще один подход при моделировании корпускулярно-оптических систем для анализа потоков заряженных частиц. Обязательным для всех рассмотренных и использованных ранее методов было выполнение условия пространственной фокусировки пучка частиц. Однако это строгое условие не всегда выполнимо в сочетании с другими требованиями. При использовании в качестве основного элемента цилиндрического электростатического зеркального анализатора пространственная фокусировка пучка несовместима с фокусировкой во времени пролета по энергии. В работе рассмотрена возможность использовать режим коллимирования пучка заряженных частиц, тем самым исключив необходимость выполнения условия фокусировки.

INFORMATION ABOUT AUTHORS | **АВТОРЛАР ТУРАЛЫ МӘЛІМЕТТЕР** | **СВЕДЕНИЯ ОБ АВТОРАХ**

Abyshev, B. – PhD student, L.N. Gumilyov Eurasian National University, Nur-Sultan, Kazakhstan

Aimanova, G.K. - Candidate of phys.-math. sciences, Leading Researcher, Fesenkov Astrophysical Institute, Almaty, Kazakhstan; Scopus Author ID: 16482414800, Orcid ID: 0000-0002-3869-8913

Aimukhanov, A.K. – PhD, Associate Professor, Professor, Department of Radiophysics and Electronics, Scientific Center for Nanotechnology and Functional Nanomaterials, E.A. Buketov Karaganda University, Karaganda, Kazakhstan; Scopus Author ID: 35321945000; ORCID ID: 0000-0002-4384-5164; a_k_aitbek@mail.ru

Akniyazov, Ch.B. - PhD student, Acting Head of the Laboratory, Fesenkov Astrophysical Institute, Almaty, Kazakhstan; Scopus Author ID: 57208627555; Orcid ID: 0000-0002-6325-0213, akniyazov@yahoo.com

Aldiyarov, A.U. – Candidate of Phys. and math. sciences, Associate Professor, al-Farabi Kazakh National University, Almaty, Kazakhstan; Scopus Author ID:16201950600; Orcid ID: 0000-0002-5091-7699

Alikhaidarova, E. – Master (Scie.), Junior Research Fellow**,** PhD student, Institute of Molecular Nanophotonics, E.A. Buketov Karaganda University, the Republic of Kazakhstan; Scopus Author ID: 57218136924, ORCID ID: 0000-0003-3024-8237

Andreev M.V. – Candidate of technical sciences, Docent, Associate professor, School of Energy and Power Engineering, Tomsk Polytechnic University, Tomsk, Russia; andreevmv@tpu.ru, Scopus AuthorID: 56473722500, ORCID ID: 0000-0002-6420-4374

Azatbek Sh. – Master student, E.A. Buketov Karaganda University, Karaganda, Kazakhstan

Bekturganov, Zh.S. - Doctor of chem. sciences, Professor, Department of radiophysics and electronics, E.A. Buketov Karaganda University, Karaganda, Kazakhstan, zhbekturganov@gmail.com

Belykh, S.S. – Master (Sci.), Engineer-physicist, Department of Physics and Technology, North-Caucasus Federal University, Stavropol, Russian Federation; Scopus Author ID: 57202009427, ORCID ID: 0000-0001-9133-0192

Bryzgunov, P.A. – PhD student**,** National Research University “Moscow Power Engineering Institute", Moscow, Russian Federation; BryzgunovPA@mpei.ru

Golikov O., Master (Eng.), PhD student, Kazakh National University. al-Farabi, Almaty, Kazakhstan, Orcid ID: 0000-0002-6691-8346, golikov@physics.kz

Gulyarenko, A.A. – PhD, Associate Professor, Kazakh Agrotechnical University named after S. Seifullin, Nur-Sultan, Kazakhstan; Scopus Author ID: 57201112442, gulyarenko@mail.ru

Ibrayev, N.Kh. - Doctor of phys.-math. sciences, Professor, Director of the Institute of Molecular Nanophotonics, E.A. Buketov Karaganda University, the Republic of Kazakhstan; Scopus Author ID: 9333698600, ORCID ID: 0000-0002-5156-5015; niazibrayev@mail.ru

Ilyassov, B.R. - PhD, Associate Professor, Professor, Department of Intelligent Systems and Cyber Security, Astana IT University, Nur-Sultan, Kazakhstan; Scopus Author ID: 56669724700, ORCID ID: 0000-0003-4563-2004; baurdinho@mail.ru

Ishkov, A.A. – Doctor of techn. sciences, Professor, Department of Technology of Structural Materials and Machine Repair, Altai State Agrarian University, Barnaul, Russia; Scopus Author ID: 6603935969, mirotnas@gmail.com

Kambarova, Zh.T. - PhD, Associate Professor, Physical and Technical Faculty, E.A Buketov Karaganda University, Karaganda, Kazakhstan, ORCID ID: 0000-0001-9808-5484, Scopus ID: 55543382800, WoS Researcher ID: AAV-8669-2020, kambarovazht@gmail.com

Karabekova, D.Zh. - PhD, Associate Professor, E.A. Buketov Karaganda University, Karaganda, Kazakhstan; Scopus Author ID: 57191485660, karabekova71@mail.ru

Kasenov, B.K. - Doctor of chem. sciences, Professor, Head of the Laboratory of Thermochemical Processes, Abishev Chemical-Metallurgical Institute, Karaganda, Kazakhstan, ORCID ID: 0000-0001-9394-0592, kasenov1946@mail.ru

Kasenova, Sh.B. - Doctor of chem. sciences, Professor, Chief researcher, Laboratory of Thermochemical Processes, Abishev Chemical-Metallurgical Institute, Karaganda, Kazakhstan; ORCID ID: 0000-0001-9755-7478, kasenovashuga@mail.ru

Kissabekova P.A. - PhD student, E.A. Buketov Karaganda University, Karaganda, Kazakhstan, pika_1666@mail.ru

Komarov, I.I. - Candidate of phys.-math. sciences, Associate Professor, National Research University "Moscow Power Engineering Institute", Moscow, Russian Federation; Scopus Author ID: 56105319600, komarovII@mpei.ru

Kozlovskiy, A.L. - PhD, Associate Professor, Head of Solid State Physics Laboratory, Astana branch of the Institute of Nuclear Physics of the Ministry of Energy of the Republic of Kazakhstan; Scopus Author ID: 55632118900, kozlovskiy.a@inp.kz

Kruchinin, N.Yu. – Candidate of phys.-math. sciences, Associate Professor, Department of radiophysics and electronics, Orenburg State University, Orenburg, Russia; Scopus Author ID: 35170029600, kruchinin_56@mail.ru

Krugov, M.A. – Master (Eng.), Engineer, Fesenkov Astrophysical Institute, Almaty, Kazakhstan; Scopus Author ID: 57193113641; Orcid ID: 0000-0002-2788-2176

Kuanyshbekov, E.E. - Master (Eng.), Leading Engineer, Laboratory of Thermochemical Processes, Abishev Chemical-Metallurgical Institute, Karaganda, Kazakhstan; ORCID ID: 0000-0001-9172-9566; mr.ero1986@mail.ru

Kucherenko, M.G. - Doctor of phys.-math. sciences, Professor, Director of the Laser and Information Biophysics Centre, Orenburg State University, Orenburg, Russia; Scopus Author ID: 7003581468, clibph@yandex.ru

Kucheruk, V.Yu. — Doctor of techn. sciences, Professor, Head of the Department of Metrology and Industrial Automation, Vinnytsia National Technical University, Vinnytsa, Ukraine, vladimir.kucheruk@gmail.com

Makhmutov, B.A. – PhD student**,** National Research University "Moscow Power Engineering Institute", Moscow, Russian Federation; Scopus Author ID: 57211781560, makhmutovBA@mpei.ru

Malikov, V.N. – Candidate of techn. sciences, Associate Professor, Department of General and Experimental Physics, Altai State University, Barnaul, Russia; Scopus Author ID: 57217258853, osys11@gmail.com

Musenova, E.K. - Candidate of phys.-math. sciences, Associate Professor, E.A. Buketov Karaganda University, Karaganda, Kazakhstan, emusenova@mail.ru

Neyasov, P. P. – Leading Engineer, Department of the Physics and Methods of Teaching Physics**,** Orenburg State University, Orenburg, Russia; Scopus Author ID: 57222337052, nejapetr@yandex.ru

Omarbekova, G. – PhD student, Researcher, Scientific Center for Nanotechnology and Functional Nanomaterials, E.A. Buketov Karaganda University, Karaganda, Kazakhstan; ORCID ID - 0000-0002-0755-6832; gulnur_130983@mail.ru

Omarov, Ch.T. - PhD (Sci.), Director, Fesenkov Astrophysical Institute, Almaty, Kazakhstan; Scopus Author ID: 8655858100, Orcid ID: 0000-0002-1672-894X

Omarova, Zh.B. – Master (Eng.), PhD student, al-Farabi Kazakh National University, Almaty, Kazakhstan; Orcid ID: 0000-0002-1101-7735; zhansaya_o@mail.ru

Orekhovskaya, A.A. - Candidate of Agricult. sciences, Head of Department for Work with Grants and REC, Belgorod State Agrarian University, Belgorod, Russia; Scopus ID: 57211231389, ORCID: 0000-0001-8149-7191, orehovskaja_aa@bsaa.edu.ru

Razzhivin, I.A. – Candidate of technical sciences, Associate professor, School of Energy and Power Engineering, Tomsk Polytechnic University, Tomsk, Russia; Scopus Author ID: 57192890811, ORCID ID: 0000-0001-7024-0198

Remshev, E.Yu. – Candidate of techn. sciences, Associate Professor, Baltic State Technical University named after D.F. Ustinov «Voenmeh», Russia, St. Petersburg; Scopus Author ID: 56731054600

Rozhkova, X.S. – PhD student, Researcher, Scientific Center for Nanotechnology and Functional Nanomaterials, E.A. Buketov Karaganda University, Karaganda, Kazakhstan; ORCID ID: 0000-0003-3048-6171; ksusharogovaya@mail.ru

Ruban, N.Yu. – Candidate of technical sciences, Docent, Associate Professor, School of Energy and Power Engineering, Tomsk Polytechnic University, Tomsk, Russia, Scopus Author ID: 56485819800, ORCID ID: 0000-0003-1396-9104, rubanny@tpu.ru

Rudnik, V. E. – Research engineer, School of Energy and Power Engineering, Tomsk Polytechnic University, Tomsk, Russia; Scopus AuthorID: 57201883080, ORCID ID: 0000-0002-6181-2497, ver3@tpu.ru.

Sagintaeva, Zh.I. - Candidate of chem. sciences, Associate Professor, Leading Researcher, Laboratory of Thermochemical Processes, Abishev Chemical-Metallurgical Institute, Karaganda, Kazakhstan; ORCID ID: 0000-0001-8655-356, kai_sagintaeva@mail.ru

Saulebekov, A.O. – Doctor of phys.-math. sciences, Professor, Professor, Kazakhstan branch of Lomonosov Moscow state University, Nur-Sultan, Kazakhstan, saulebekovarman@gmail.com

Seisembekova, T. - PhD student, Junior Researcher, Scientific Center for Nanotechnology and Functional Nanomaterials, E.A. Buketov Karaganda University, Karaganda, Kazakhstan; ORCID ID: 0000-0002-1497-0759; tosh_0809@mail.ru

Seliverstova, E. – PhD, Senior Research Fellow, Institute of Molecular Nanophotonics, E.A. Buketov Karaganda University, the Republic of Kazakhstan; Scopus Author ID: 35323255400, ORCID ID: 0000-0002-9507-8825; genia_sv@mail.ru

Serebryanskiy, A.V. - PhD (Sci.), Head of Observational Astronomy Department, Fesenkov Astrophysical Institute, Almaty, Kazakhstan; Scopus Author ID: 6506120160; Orcid ID: 0000-0002-4313-7416

Shlimas, D.I. - PhD, Researcher of Solid State Physics Laboratory, Astana branch of the Institute of Nuclear Physics of the Ministry of Energy of the Republic of Kazakhstan; Scopus Author ID: 57189516212, shlimas@mail.ru

Smirnov, A.O. - PhD student**,** National Research University "Moscow Power Engineering Institute", Moscow, Russian Federation; smirnovAOl@mpei.ru

Sokolova, V.A. – Candidate of techn. sciences, Associate Professor, Lecturer, Military Academy of Communications named after marshal of the Soviet Union S.M. Budyonny, St. Petersburg, Russia; WoS Researcher ID: AAK-6062-2020, ORCID: 0000-0001-6880-445X, sokolova_vika@inbox.ru

Suprun, T.T. - Candidate of tech. Sciences, Senior Researcher, Institute of Engineering Thermophysics, National Academy of Sciences of Ukraine, Kyiv, Ukraine; WoS Researcher ID: AAH-6957-2020; ORCID iD: 0000-0002-5360-388X; suprun@secbiomass.com

Suvorov A.A. – Candidate of technical sciences, Associate professor, School of Energy and Power Engineering, Tomsk Polytechnic University, Tomsk, Russia; Scopus AuthorID: 56959954100, ORCID ID: 0000-0003-3896-3921, lionrash@tpu.ru

Tikhonsky, N.D. –Master student, Altai State University, Barnaul, Russia; Scopus Author ID: 57439736100, svaritrffi@gmail.com

Tokmoldin, N.S. - PhD, Postdoctoral Researcher, University of Potsdam, Potsdam, Germany (Scopus Author ID 16043572900; Orcid ID: 0000-0002-0663-0228

Vegera, A.N. - Candidate of phys.-math. sciences, Associate Professor, National Research University "Moscow Power Engineering Institute", Moscow, Russian Federation; Scopus Author ID: 57194569459, VegeraAN@mpei.ru

Vivchar, V.I. – Post Graduate student, Department of Physics and Technology, North-Caucasus Federal University, Stavropol, Russian Federation

Voinash, S.A. – Master, Engineer, PRO FERRUM LLC, St. Petersburg, Russia; WoS Researcher ID: AAK-2987-2020, ORCID: 0000-0001-5239-9883, sergey_voi@mail.ru

Yerezhep, D. – PhD, Senior Lecturer, al-Farabi Kazakh National University, Almaty, Kazakhstan, Scopus Author ID: 57194012596; Orcid ID: 0000-0002-2232-2911, darhan_13@physics.kz

Yerin, C.V. – Doctor of phys.-math. sciences, Professor, Department of Physics and Technology, North-Caucasus Federal University, Stavropol, Russian Federation; Scopus Author ID: 56305531700, ORCID ID: 0000-0002-2426-4225

Zeinidenov, A.K. – PhD, Associate professor, Dean of the Physical-Technical Faculty, Scientific Center for Nanotechnology and Functional Nanomaterials, E.A. Buketov Karaganda University, Karaganda, Kazakhstan; ORCID ID: 0000-0001-9780-5072, Scopus Author ID: 56386144000, asyl-zeinidenov@mail.ru

Zhumadilov, K.Zh. – PhD, Professor, Head of Department of nuclear physics, new materials and technologies, L.N. Gumilyov Eurasian National University, Nur-Sultan, Kazakhstan; Scopus Author ID: 12646415800, kassymz@mail.ru

GUIDELINES FOR AUTHORS

Eurasian Physical Technical Journal (Eurasian phys. tech. j.) is a peer-reviewed open access international scientific journal publishing original research results on actual problems of technical physics and other related fields. Since 2004 «Eurasian phys. tech. j.» is published in English.

Acceptance of the manuscript for publication in the Eurasian phys. tech. j. is carried out online through website - https://phtj.buketov.edu.kz/index.php/EPTJ. Authors should check that their submissions meet all of the following requirements, as submissions may be returned to authors that do not comply with these guidelines.

Scientific article topic and content

A scientific article should contain the results of original scientific research previously unpublished and not intended for publication in other publications.

Manuscript of the article should contain at least 75% of the original text.

All articles are published **in English in 4 scientific areas of physics: Energy, Engineering, Materials Science, Physics and Astronomy.**

Publication Ethics and Malpractice Statement

Submission of an article to the Eurasian phys. tech. j. implies that the paper described has not been published previously, that it is not under consideration for publication elsewhere, that its publication is approved by all authors and tacitly or explicitly by the responsible authorities where the paper was carried out, and that, if accepted, it will not be published elsewhere in the same form, in English or in any other language, including electronically without the written consent of the copyright holder. In particular, translations into English of papers already published in another language are not accepted.

For information on Ethics in publishing and Ethical guidelines for journal publication see http://www.elsevier.com/publishingethics and http://www.elsevier.com/journal-authors/ethics.

The Eurasian phys. tech. j. follows the Code of Conduct of the Committee on Publication Ethics (COPE), and follows the COPE Flowcharts for Resolving Cases of Suspected Misconduct (http://publicationethics.org/files/u2/New_Code.pdf).

To verify originality, your article may be checked by the originality detection service Cross Check http://www.elsevier.com/editors/plagdetect.

Pre-publication process

Authors are responsible for the content of their publications. No other forms of scientific misconduct are allowed, such as plagiarism, falsification, fraudu-lent data, incorrect interpretation of other works, incorrect citations, etc. Authors are obliged to participate in peer review process and be ready to provide corrections, clarifications, retractions and apologies when needed. All authors of a paper should have significantly contributed to the research.

Reviewers should provide objective judgments and should point out relevant published works which are not yet cited. Reviewed articles should be treated confidentially. The reviewers will be chosen in such a way that there is no conflict of interests with respect to the research, the authors and/or the research funders.

Editors have complete responsibility and authority to reject or accept a paper, and they will only accept a paper when reasonably certain. They will preserve anonymity of reviewers and promote publication of corrections, clarifications, retractions and apologies when needed.

The acceptance of a paper automatically implies the copyright transfer to the Eurasian phys. tech. j.

All submitted papers will the sent for reviewing to leading experts in the given area.

The Editorial Board of the Eurasian phys. tech. j. will monitor and safeguard publishing ethics.

The editors reserve the right to accept or reject manuscripts.

The article and all documentation must be identified by the name of the 1st author: Akhmetov AA_et al_paper; Akhmetov AA_et al_fig.1; Akhmetov AA_et al_Cover letter; …

The article text must be formatted according to the **Template**, font - Times New Roman, size -11 pt; line spacing-single; alignment-in width, see https://phtj.buketov.edu.kz/index.php/EPTJ/about/submissions#authorGuidelines

An article should consist:

Title: includes a separate line on the left the **UDC** index, Title of the article, information about the authors-surname and initials, name of institution, city, country, e-mail of a corresponding author. The author* who submitted an article for publication will be considered as a corresponding author.

Abstract should consist of at least 5-6 sentences, not exceeding 200-250 words without formula, references, abbreviations. An abstract is a short and powerful summary that describes the focus and subject of a research paper. It could contain the information about why the research study was done, background, what the methodology was and something about the findings of the author(s).

Keywords: at least 3-10 basic terms or short phrases used in the article.

The text should be divided on structural parts: Introduction, Main part (Theoretical part, Methods and materials or Experimental technique), Results and Discussion, Conclusions.

Conclusions: formulating main results; a comparison of the results with the existing data on this topic; assessment of scientific novelty and practical value of the results.

Acknowledgments or Funding may be shown at the end of the article text, before References.

References: a bibliographic list is compiled according to the requirements:

- Books, abstracts, patents: Surname and initials of the authors (it is enough to indicate the first three or one surnames, et al), ***Title of the book*** in italics, publish house or city, year and total number of pages.
- Journals, collections of papers, conference proceedings - Surname and initials of the authors (the first three are enough), the title of the article, the ***Title of the journal*** in italics (you can use the abbreviated title), city and / or country, year, volume, issue number, pages of the "begining and end" (pp. … - … .).
- Internet links also must to indicated the authors, the title and URL

The authors should represent References according to the requirements of international journals on physics, but should to consult preliminarily for standard abbrevi¬ations of journal's names. More information on references guidelines for journal publication you can see in Harvard reference system - http://www.emeraldgrouppublishing.com /authors/guides/write/harvard.htm?part=2/

All references must be numbered in the text (for example, [1], [2-4]) and listed in numerical order.

The manuscript volume, including text, formulas, figures, bibliography, should not exceed 10-12 pages including tables, figures (no more than 6-8) and references (no more than 30-35) of text typed on a computer (Microsoft Word editor. A review paper must not be more than 10-12 pages (including no more than 15 figures).

All abbreviations and acronyms, with the exception of obviously well-known, should be deciphered at first use in the text.

Equations in your paper have to be written using the Microsoft Equation Editor or the MathType.

Tables, numbered and titled, should be inserted into the text (Times New Roman, size - 10 pt) or have been presented as an appendix at the end of the article.

Figures should be prepared in a digital form suitable for direct reproduction. Figures shall be submitted on the separate sheets or can be included into the text.

The manuscript volume, including text, formulas, figures, bibliography, should not exceed 12 pages including tables, figures (no more than 8) and references (no more than 35) of text typed on a computer using Microsoft Word editor. The overview article should not exceed 20 pages with no more than 15 figures.

List of required documents

The following files must be uploaded to the journal's website:

1. Text of the article, with pictures (*.doc);
2. Figure, Picture, Photo (fig1.jpg, fig2.pcx, …);
3. Figure captions (*.doc);
4. A **Cover letter** - from a university, research institute or an organization licensed to conduct research activities, must be issued on an official letterhead and / or certified by the organization seal. The management officially confirms by this letter that the article (the title of the article and the names of the authors are indicated in English) doesn't contain any information constituting state or commercial secrets, and the article can be published in the Open Press. Authors must upload a copy of the signed Cover Letter in PdF format to the Journal website.

It's necessary to upload by separately 2 files in English (and in Russian for authors from Russia, and in Kazakh for authors from Kazakhstan):

5. **Article's data**: Surname and initials of the authors, the article title, abstract, keywords.
6. **Information about each co-author**: full name, academic degree, academic title, place of work or study, , title of organization, city, country, SCOPUS Author ID or ORCID iD; and contact details (e-mail, phone).

7. **Receipt of payment.** Authors should pay for the publication only after receiving notification about a positive decision of the reviewers.